

TECHNOLOGY PLATFORMS FOR TRANSFORMING COMPLEX BIOLOGICAL STUDIES

By

Christina C. Marasco

Dissertation

Submitted to the Faculty of the  
Graduate School of Vanderbilt University  
in partial fulfillment of the requirements

for the degree of

DOCTOR OF PHILOSOPHY

in

Biomedical Engineering

August, 2012

Nashville, Tennessee

Approved:

Professor John P. Wikswo

Professor Kevin T. Seale

Professor John A. McLean

Professor David E. Cliffel

Professor Hak-Joon Sung

Professor Danny G. Winder

In memory of Ben Liesch and Dean Paras

Without loss, we would lack the drive to save.

## ACKNOWLEDGEMENTS

This work has been financially supported by the Defense Threat Reduction Agency (DTRA), the National Institute on Drug Abuse (NIDA), the Searle Systems Biology and Bioengineering Undergraduate Research Experience (SyBBURE-Searle), and the Vanderbilt Institute for Integrative Biosystems Research and Education (VIIBRE).

The work herein represents a highly collaborative multidisciplinary, inter-institutional research effort that spans the work of undergraduate students, graduate students, staff scientists and engineers, research associates, and faculty from Vanderbilt University, Duke University, and Cornell University. An exhaustive list of contributors and their affiliations can be found in Appendix A. I am overwhelmingly appreciative for all of their efforts, though this is not a sufficient display of gratitude for all of their indispensable work. I particularly thank Jeff Enders and Cody Goodwin for their sizeable contributions to this body of work, for their friendship, for their commiseration, and for their humor. To the many SyBBURE students who have endured working alongside me, burdened by my lofty expectations; I thank you for your hard work, for talking through problems, and for quitting on me or graduating when I needed you, forcing me to come to terms with my lack of knowledge. These projects also could not have been completed without the support and expertise of the VIIBRE scientists, engineers, and support staff. The opportunity to participate in this research was afforded to me at critical time in my graduate career and without it I would not have achieved this goal. I sincerely thank Kevin Seale, John Wikswo and John McLean for allowing me to work with SyBBURE and on these projects. Your continued support has and will continue to be appreciated on many levels.

Finally, I wish to acknowledge those who have supported this eight-year journey. I will show you my gratitude through my renewed presence in your lives.

## TABLE OF CONTENTS

	Page
ACKNOWLEDGEMENTS .....	III
LIST OF TABLES .....	VII
LIST OF FIGURES.....	VIII
CHAPTER I.....	1
1    INTRODUCTION .....	1
1.1    Objective .....	1
1.2    Specific Aims.....	2
1.2.1    Specific Aim 1 .....	2
1.2.2    Specific Aim 2 .....	3
1.3    Technology Innovation, Background and Significance.....	3
1.3.1    Microfluidics for the Study of Cellular Response .....	3
1.3.2    Mass Spectrometry for Cell State Assessment .....	11
1.3.3    Combining Microfluidics with Mass Spectrometry .....	14
1.3.4    Computational Modeling of Complex Biological Systems .....	15
1.3.5    Systems Biology Approach for Automated Science .....	17
1.3.6    Summary.....	18
1.4    Biological Background and Significance .....	19
1.4.1    Cocaine Effects .....	19
1.5    References.....	41
CHAPTER II.....	60
2    REAL-TIME CELLULAR EXOMETABOLOME ANALYSIS WITH A.....	60
MICROFLUIDIC-MASS SPECTROMETRY PLATFORM .....	60
2.1    Abstract.....	61
2.2    Introduction.....	62
2.3    Methods.....	69
2.3.1    Microfluidic Bioreactor Design and Fabrication.....	69
2.3.2    PDMS Surface Modification .....	69
2.3.3    Cell Culture and “In Culture” Cocaine Exposure .....	72
2.3.4    Metabolomics Sample Preparation and UPLC-ESI-IM-MS Analysis .....	73
2.3.5    Online Cell Loading and Experimentation .....	74
2.3.6    Solid Phase Extraction Desalter.....	75
2.3.7    Online Cell Effluent Desalting and Mass Spectrometry Analysis .....	77
2.3.8    Data Processing and Multivariate Statistical Analysis .....	78
2.4    Results and Discussion .....	78
2.4.1    Platform Integration and Evaluation .....	78
2.4.2    Cocaine Metabolism in Naïve and Experienced T cells .....	84
2.5    Conclusions.....	90
2.5.1    Platform Capabilities and Shortcomings .....	90

2.5.2	Cellular Memory of Cocaine Experience.....	92
2.6	References.....	94
CHAPTER III.....		97
3	PROGRESS TOWARDS A HETERODYNE FRAMEWORK FOR THE GENERATION AND DETECTION OF OSCILLATORY CHEMICAL SIGNALS IN NONLINEAR LIGHT-PRODUCING SYSTEMS	97
3.1	Abstract.....	98
3.2	Introduction.....	99
3.3	Heterodyne Chemistry Theory .....	100
3.3.1	Heterodyne Models of Nonlinear Reactions.....	103
3.4	Development of Hardware and Data Analysis Methods for Heterodyne Chemistry.....	110
3.4.1	Sinusoidal Concentration Generation .....	111
3.4.2	Chemical Signal mixing with a Microfluidic Reactor.....	123
3.4.3	Detection of Light as Reaction Products.....	123
3.4.4	Fourier Transform Analysis.....	128
3.5	Nonlinear Chemical Reaction Exploration.....	129
3.5.1	Fluorescence Quenching.....	129
3.5.2	Peroxyoxalate Chemiluminescence.....	137
3.6	Summary, Pitfalls, and Problems.....	146
3.7	Future Solutions.....	150
3.8	References.....	152
CHAPTER IV.....		156
4	SUMMARY, FUTURE WORK AND ETHICAL IMPACT.....	156
4.1	MF-SPE-nESI-IM-MS.....	157
4.1.1	Microfluidic Device Design and Control .....	158
4.1.2	Online Desalting .....	158
4.1.3	Data Analysis.....	160
4.1.4	MTNP-SPE-nESI-IM-MS.....	161
4.2	Heterodyne Framework.....	162
4.2.1	Sinusoidal Concentration Generation .....	163
4.2.2	Upstream Chemical Signal Mixing.....	165
4.2.3	Downstream Chemical Signal Detection .....	166
4.2.4	Data Analysis Techniques .....	166
4.2.5	Modeling Heterodyne Chemistry.....	167
4.2.6	Probing Biochemical Reactions.....	167
APPENDIX A ALPHABETICAL LIST OF CONTRIBUTORS.....		168
APPENDIX B MTNP-SPED-NESI-IM-MS USE AND TROUBLESHOOTING GUIDE .....		169
APPENDIX C MEDI HEAT MAPS.....		197
APPENDIX D CHEMICAL REACTION MODELS.....		200
APPENDIX E RPPM CODE.....		219

APPENDIX F HETERODYNE DATA ANALYSIS CODE .....	227
APPENDIX G PUMP CALIBRATION ANOVA .....	238
APPENDIX H HETERODYNE FREQUENCY TABLES .....	241

## LIST OF TABLES

Table		Page
1	Methods of Cellular Communication.....	8
3.1	Methods of Cellular Communication.....	99
3.2	Fluorescein Quenching Frequencies.....	106
3.3	Peroxyoxalate Chemiluminescence Frequencies.....	109
3.4	Input Speed and Average Resulting Flow Rates for Constant Speed Calibration.....	121
3.5	Input and Output Parameters for Sinusoidal Calibration.....	121
3.6	Fluorescein Quenching Experimental Variable Flow Frequencies.....	133
3.7	Fluorescein Quenching Experimental Corrected Frequencies.....	135
3.8	Reservoir Contents and Sample Input Parameters for Peroxyoxalate Reaction.....	138
3.9	Pre- and Post-calibration Results for Peroxyoxalate Reaction.....	142
3.10	Comparison of Model and Experimental Peroxyoxalate Reaction Frequencies.....	145
3.11	Heterodyne chemistry hardware performance metrics.....	147

## LIST OF FIGURES

Figure	Page
1.1 Device Fabrication, Design and Cell Loading .....	6
1.2 Examples of Microfluidic Sinusoidal Concentration Generators .....	10
1.3 Ion Mobility Mass Spectrometry .....	12
1.4 Waters Synapt G2 .....	13
1.5 Conceptual Pathway from Experimental Data to Discovery of Conservation Laws .....	16
1.6 A Comparison of Substances of Abuse .....	20
1.7 Potential Mechanisms of the $\sigma_1$ Receptor .....	26
1.8 Summary of Effects of Cocaine on Immune Function .....	28
1.9 Brain-immune Bi-directional Connections .....	37
2.1 Cocaine Metabolic Pathways .....	67
2.2 Experimental Scheme Showing the Potential Cell Fates .....	68
2.3 Device Fabrication and Design .....	70
2.4 PDMS Silanization .....	71
2.5 Cocaine Exposure Scheme .....	72
2.6 Solid Phase Extraction Desalter Setup .....	76
2.7 MTNP-SPE-nESI-IM-MS Platform .....	79
2.8 Insulin Treatment of Silanized PDMS Channels .....	83
2.9 Walking Principal Component Analysis of Exometabolomic Profiles .....	85
2.10 Benzoyllecgonine Time Course and Fragmentation Spectrum .....	86
2.11 Additional Metabolite Time Course Data .....	88
2.12 Metabolite Expression Dynamics Inspector Heat Maps .....	89



2.13	In Culture Principal Component Analysis of Exometabolomic Profiles .....	91
3.1	Heterodyne Chemistry Basics .....	101
3.2	Reaction Rate Equations for Fluorescein Quenching .....	104
3.3	Fluorescein Quenching Model Data .....	105
3.4	Reaction Rate Equations for Peroxyoxalate Chemiluminescence .....	107
3.5	Peroxyoxalate Chemiluminescence Model Data .....	108
3.6	Examples of Microfluidic Sinusoidal Concentration Generators .....	112
3.7	Multiple Pump Sinusoidal Concentration Profile Generation .....	113
3.8	Y-offset Contributions to Frequency Spectrum .....	114
3.9	Rotary Planar Peristaltic Micropump .....	116
3.10	Single Pump Sinusoidal Flow Rate .....	118
3.11	Pump Calibration .....	120
3.12	Sinusoidal Pump Calibration .....	122
3.13	Microfabrication Procedure .....	124
3.14	Continuous Flow Photometer .....	125
3.15	CFP Evaluation .....	127
3.16	CFP Detection of Sinusoidal Concentration Profiles .....	128
3.17	Experimental Setup for Fluorescein Quenching .....	131
3.18	Fluorescein Quenching Sample Data Set .....	132
3.19	Corrected Fluorescein Quenching Sample Data Set .....	134
3.20	3D Plot of Varying FL Drive Frequencies .....	136
3.21	Experimental Setup for Peroxyoxalate Chemiluminescence .....	139
3.22	Pre- and Post-calibration Peroxyoxalate Chemiluminescence Experimental Data .....	141
3.23	3D Plot of Varying H <sub>2</sub> O <sub>2</sub> Drive Frequencies .....	143

3.24	Model versus Experimental Peroxyoxalate Chemiluminescence.....	144
------	--	-----

## CHAPTER I

### 1 INTRODUCTION

#### 1.1 Objective

The progression of science and medicine is often predicated by advancements in technology. Particularly, automation has played a large role in many of these technological advancements, allowing for progress to occur at a more rapid pace. For example, high impact technological driving forces, such as gene sequencing<sup>1,2</sup>, microarray technology<sup>3,4</sup>, and high-throughput screening<sup>3,5</sup>, have led to a genomic revolution that has fueled not only the mapping of the human genome, but also drug discovery, epigenetics, biomarker discovery, systems biology and basic science research as a whole<sup>6-8</sup>. As popularity in approaching scientific issues from a systems biology perspective continues to grow, the need for new tools capable of rapidly producing data has become evident. The development of technology platforms for complex biological studies will be twofold. The first, a platform for assessing the metabolic state of a population of cells under highly controllable environmental parameters, could provide significant insight as to the underlying biological phenomenon leading to potential advancement in both clinical and academic systems biology research. This work, as described within, discusses a platform comprised of the Vanderbilt Institute for Integrative Biosystems Research and Education (VIIBRE) Multitrap Nanophysiometer (MTNP) paired with a solid phase extraction desalter (SPED), and an Ion Mobility-Mass Spectrometer (IM-MS). Through the use of this platform, it is hypothesized that new insight into cellular behavior, particularly under challenge-based conditions such as cocaine exposure may result and potentially lead to the ability to predict and control cellular dynamics. The second technology framework developed will be for

the generation and receiving of oscillatory chemical signals and will consist of parallel Rotary Planar Peristaltic Micropumps (RPPMs) for the generation of sinusoidal concentrations of chemical signals, a microfluidic mixer for the combination the oscillatory signals, the Continuous Flow Photometer (CFP) for the collection of light from reaction products, and data analysis techniques for describing the frequency domain of the raw data. This framework stands to provide unique information regarding nonlinear reaction dynamics and is transferrable to more complex biochemical signaling pathways.

## 1.2 Specific Aims

The following aims will lead to the creation and testing of these two novel platforms for real-time analysis of dynamic cellular exometabolomes and investigation of oscillatory chemical reaction networks.

### 1.2.1 Specific Aim 1

The development of an instrumentation platform for real-time systems biology measurements of small populations of cells will be carried out through the integration of microfluidic bioreactors, a solid phase extraction desalter and nano-electrospray ionization-ion mobility-mass spectrometry (nESI-IM-MS). Validation of this instrumentation platform will be carried out through assessing the exometabolomic profiles of naïve and cocaine-experienced Jurkat T cells through online cocaine challenge. Successful completion of this instrumentation platform with inaugural biological experimentation will include comparison of this platform to the current mass spectrometry standard for analysis of complex biological samples as well as principal component analysis of the resulting online biological data for the identification of differential exometabolomic profiles.

### 1.2.2 Specific Aim 2

The complexities of biological regulatory networks provide motivation for the inclusion of advanced mathematical techniques and instrumentation for the investigation of nonlinear reaction dynamics. The development of instrumentation for producing oscillatory upstream signal generation and data analysis techniques for assessing downstream signaling could provide a means of more closely regulating and interpreting cell signal response. In order to validate this technique without the added complexity of a biological system, two non-cellular non-linear chemical reaction networks will be used, specifically Fluorescein quenching and peroxyoxalate chemiluminescence. Successful development of this framework will include the production and analysis of a sinusoidal concentration generator, signal mixer, reaction product receiver, and frequency domain data analysis techniques.

## 1.3 Technology Innovation, Background and Significance

The technology platform developed and integrated for the work described in the **Specific Aims** will be a joint microfluidics/mass spectrometry/computational modeling construct including the VIIBRE Multitrap Nanophysiometer, the Waters Synapt G2 HDMS and co-evolutionary algorithms developed by the Cornell Computational Synthesis Laboratory. These technologies, while innovative in their own respect, will be incorporated to form a unique and technologically advanced approach for automated systems biology research.

### 1.3.1 Microfluidics for the Study of Cellular Response

Microfluidic devices are becoming increasingly popular and several designs have translated to market. The field of microfluidics incorporates skills and techniques from a variety of disciplines such as engineering, physics, chemistry, and biology. This technology is often

referred to as lab-on-a-chip (LOC) as it seeks to transform or often replicate the traditional experimental techniques of cell and molecular biology and biochemistry into small-scale on-chip experiments. Since there is a reduction in experimental scale, compared to traditional techniques, decreased reagent volume is necessary and is based on microfluidic device size and length of experiment. Microfluidic technology benefits from easier fluid handling, thus allowing for better control of experimental parameters and reduced sample loss. Experiments conducted with microfluidic devices are typically inexpensive not only due to the decreased cost of reagents, but also because of the low material cost as the devices are typically comprised of poly(dimethylsiloxane) and a glass slide or cover slip<sup>9,10</sup>. The design and fabrication procedures allow for meticulous control of the device features. Because devices can be designed on a smaller scale with less volume surrounding cells, extracellular contents, including autocrine and paracrine signaling molecules, are not diluted by the large volumes of traditional techniques such as cell culture and titer plates<sup>11</sup>. An important factor in working on the microscale is the physical phenomena that become influential on the experimental results. These factors include diffusion, laminar flow, and surface area-to-volume ratio, among others, and have significant repercussions in physiological processes and can greatly contribute to in vitro/in vivo correlation. By taking advantage of the numerous benefits of microfluidics many researchers have been able to make measurements at the micro scale that would otherwise not be possible<sup>12</sup>.

Microfluidics and LOC techniques have shown remarkable promise in various biological measurements, such as immunoassays<sup>13-17</sup>, protein and DNA separations<sup>18-21</sup>, capillary electrophoresis<sup>22-26</sup>, and cell sorting<sup>27-29</sup>. There also exists a wealth of bioreactors designed to culture cells in an environment more closely replicating in vivo conditions<sup>11,30-36</sup>. Some microfluidic devices have also been combined with microfabricated multi electrode arrays for

electrochemical measurements of the metabolic activity of small numbers of cells and their rapid response to drugs and other perturbations. Combined optical and electrochemical technologies allowed for the recording of acidification rate, oxygen and glucose consumption, lactate release, intracellular calcium concentrations, transmembrane potentials and NADH concentrations with sensitivities to monitor single cells in nanophysiometers<sup>37-41</sup>. On-chip strategies for both cell culture and biochemical assays have taken great strides in the past decade, yet room for improvement of both on- and off-chip analysis techniques remains.

The Vanderbilt Institute for Integrative Biosystems Research and Education (VIIBRE) Multitrap Nanophysiometer (MTNP), a microfluidic device used as miniature bioreactor, allows for studies on small populations of cells or simple organisms ( $<10^5$ ). This is contrast to traditional cell biology techniques which often require populations several orders of magnitude larger. The MTNP has been used for long-term optical measurements of the dynamic behavior of cells, including fluorescent labeling of cells to determine type and activation state and detect signaling dynamics<sup>11,38,42</sup>. This device is ideally suited for studying immune cells, i.e., T cells, B cells, and natural killer cells as it traps non-adherent cells with structural barriers instead of with chemical surface modification that may allow cells to be exposed to higher shear stresses resulting from fluid flow. Design of the MTNP is done through the use of AutoCAD to create drawings of the device which will then be transferred to a chrome mask. Device parameters such as trap size, spacing and number, as well as chamber dimensions and inlet and outlet features, can be manipulated in AutoCAD for the optimization of devices as needed for specific experiments. Construction of microfluidic devices from these chrome masks occurs as previously described<sup>10,43</sup> with photolithography performed to produce a silicon master from which numerous polydimethylsiloxane (PDMS) devices can be replica molded. After their inlet and outlet ports have been punched, the PDMS is plasma-bonded to glass cover slips. Prior to cell

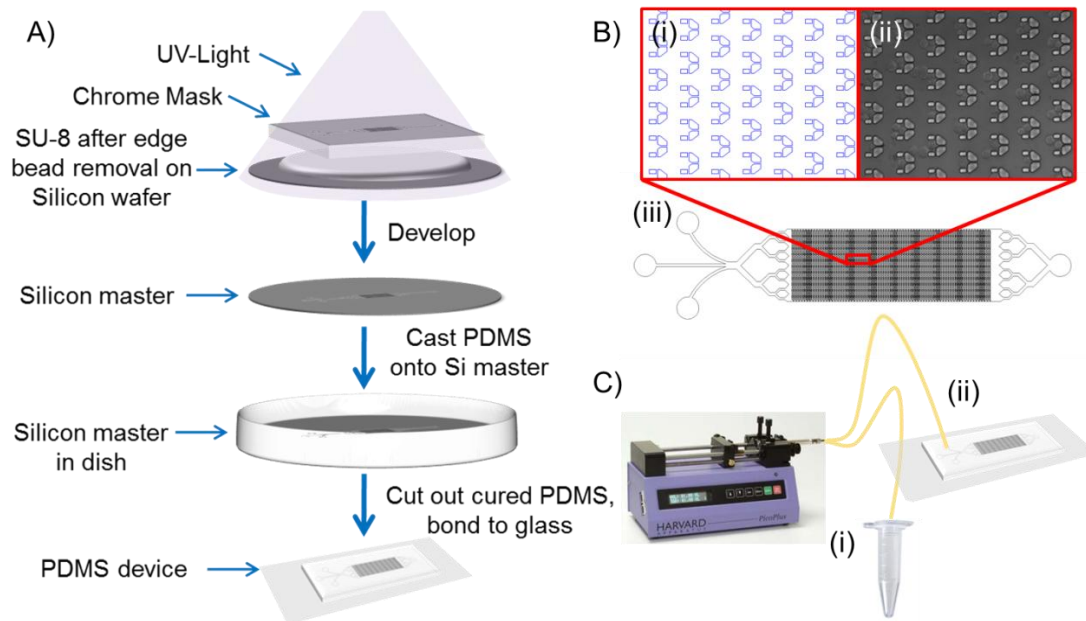


Figure 1.1 Device Fabrication, Design and Cell Loading A) PDMS device fabrication method involving photolithography and replica molding techniques. B) Design of the MTNP with (i)  $18\mu\text{m} \times 12\mu\text{m}$  cell traps capable of (ii) trapping 2-3 cells each in a device with a 2nL volume and 7056 cells traps. C) Cell loading procedure using a Harvard Apparatus syringe pump to (i) first aspirate cells from a pellet in a microcentrifuge tube, then (ii) reverse the flow of the pump to push cells into the MTNP.

loading, devices are primed with warmed culture media to prevent air bubble formation, a detrimental complication in any microfluidic device. As shown in Figure 1.1, cell loading is accomplished by first aspirating cells into a length of PEEK tubing using an automated Harvard Apparatus syringe pump and then, after inserting the tubing into the device inlet, reversing the direction of flow to pump the cells into then device. An alternate loading method that employs a manual or motorized rotary on-chip microfluidic pump<sup>44</sup> is also permissible. The loading of cells is easily monitored with an inverted microscope, and once cells are loaded, the desired experiments can be performed. Visualization of the experiment can continue with microscopy, allowing for optical measurements to be conducted as needed.



The MTNP is not only well suited to detect autocrine and paracrine signaling molecules in cellular effluent, but it is also unique in its ability to provide a system for investigating dynamic response of a cell population to a stimulus. The constant perfusion design of the experimental setup gives rise to platform capable of real time monitoring of alterations in species transport across the cell membrane, whether small molecule, protein, etc. Knowledge concerning changes in species transport provides information on the current state of the cell population which can lead to a more thorough understanding of the particular cell's biology and the ability to control this cell's behavior.

#### *1.3.1.1 Complex Cell Signaling Dynamics*

Central to the field of systems biology is the effort to both model and understand the complex cell signaling pathways that govern biological networks. Table 3.1 lists the various types of cellular signaling that comprise the breadth of response of a cell to its environment. Experimental and computational biologists alike often use wiring diagram analogies to represent these molecular interaction networks. Biological regulatory networks have been shown to be comprised of simple motifs, such as cycles and cascades, controlled by positive and negative feedback loops, described by linear, hyperbolic, sigmoidal, and oscillatory signal-response dynamics, which when taken together to form an integrated network, can drive the parametric state of the cell into one or more attractor states<sup>45,46</sup>. With such complexities in signaling systems, experimental determination of dynamical properties must be coupled with mathematical models to avoid error in the interpretation of the results. The dynamics of nonlinear biochemical networks under oscillatory stimulus conditions has been modeled by Ingalls as an extension of metabolic control analysis<sup>47</sup>. Tyson describes a means of combining simple signal-response elements consisting of sigmoidal switches, transient responses,

hysteretic switches and oscillators to computationally model any complex regulatory network<sup>46</sup>. Interested readers are directed towards numerous excellent reviews<sup>45,46,48-50</sup> that have been written detailing the finer points of cell signaling, state stability and modeling of complex networks that are tangential to the scope of this work.

Table 1 Methods of Cellular Communication

Intercellular Signaling	Target	Example
Method		
<b>Endocrine</b>	Distant cells	Insulin on hepatocytes
<b>Paracrine</b>	Nearby cells	Coagulation factors in platelets
<b>Juxtacrine</b>	Adjacent cells	Membrane-bound growth

Paramount to this work is in the exploration of sinusoidal signaling dynamics. Sinusoidal stimulus-response has been shown to provide valuable information in dynamical biological systems ranging from neuronal networks<sup>51-55</sup> and the human visual response<sup>56-59</sup> to insulin secretion in pancreatic islets<sup>60-62</sup> and yeast regulation<sup>63-67</sup>. Oscillatory glucose levels have been shown to synchronize pancreatic islets in vitro<sup>68</sup>. Bird et al. report constant frequency sinusoidal calcium oscillations resulting from the stimulation of mouse lacrimal acinar cells with submaximal methacholine dose which are dependent on a negative feedback loop driven by protein kinase C<sup>69</sup>. Berthoumieux et al. reported oscillatory concentration dynamics on a three state enzyme system following Michaelis-Menten kinetics<sup>70</sup>.

### *1.3.1.2 Sinusoidal Flow Generation for Environmental Control in Microfluidic Devices*

While much of the neuronal network studies are performed through the application of oscillatory electrical pulses, the generation of sinusoidal concentration gradients for simulating in vivo non-linear dynamics requires sophisticated and expensive flow systems. Several groups have pioneered work on producing microfluidic variable concentration generators, often incorporating valves and pumps (examples shown in Figure 1.2). Mosadegh et al. produced a microfluidic oscillator using switch valves and check valves to convert a constant infusion of fluid into an oscillating output<sup>71</sup>. Azizi and Mastrangelo created a microfluidic pulsed waveform generator capable of simulating rat striatum dopamine release, beta cell intracellular calcium oscillations and beta cell extracellular insulin secretion<sup>72</sup>. A microfluidic device for the production of sinusoidal glucose concentrations has been shown to allow for the entrainment of pancreatic islets<sup>68,73</sup>. The same research group has also produced a microfluidic multi-analyte gradient generator capable of independent sinusoidal control of up to four different chemical species<sup>74</sup>. Through the use of these or similar non-linear concentration generators, it is possible to more closely simulate upstream signaling dynamics, leading to a cellular response to stimulus that more closely mimics the in vivo response. With a sinusoidal concentration generator paired with a method of analyzing cell response data, the influence of the sinusoidal signal component could be revealed, providing another tool for describing, modeling and analyzing complex biological systems.

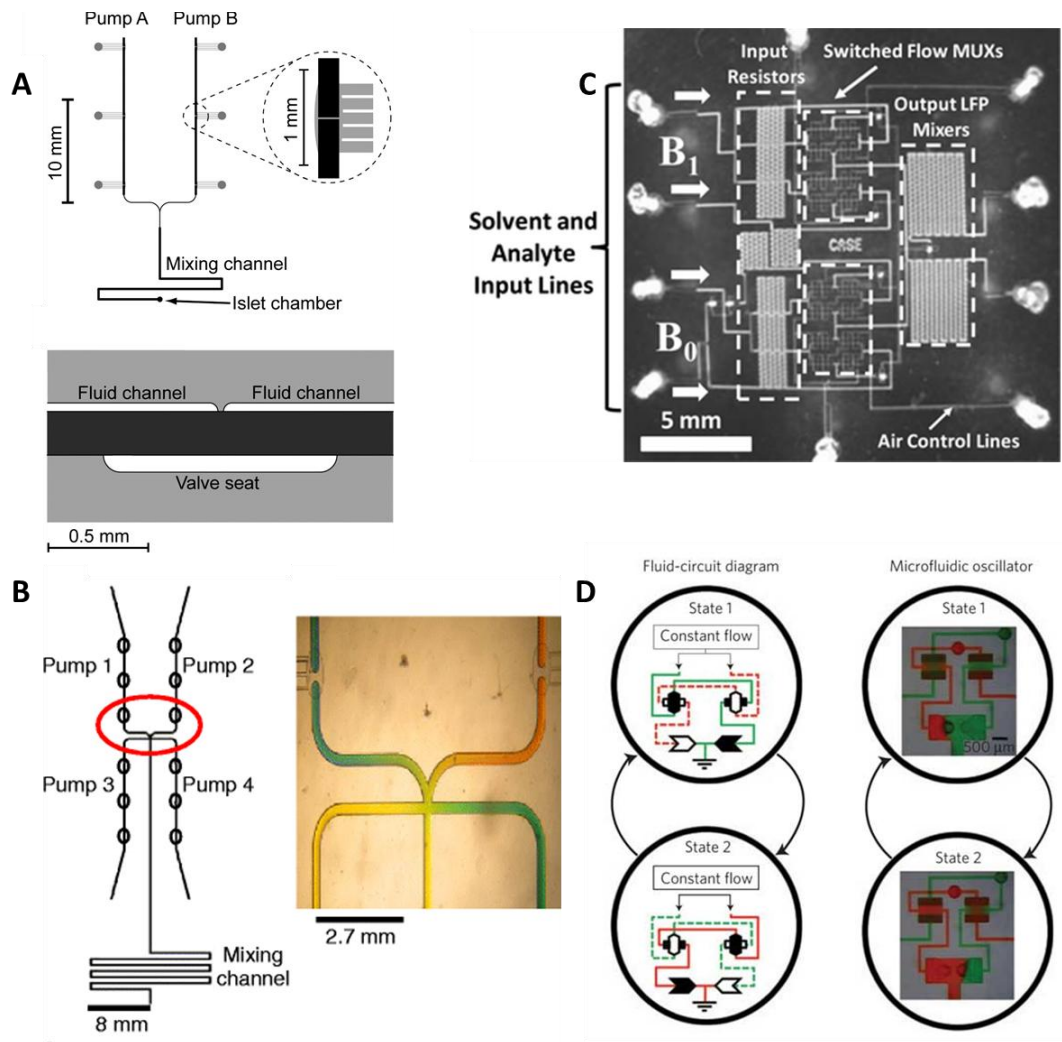


Figure 1.2 Examples of microfluidic sinusoidal concentration generators. (A) and (B) are designs from the same group incorporating pumps and a series of valves to produce independently controllable sinusoidal concentrations<sup>68,73,74</sup>. (C) employs a pulse code modulator comprised of a multiplexer with a low pass filter and digitally encoded clock signals to generate a variety of waveforms<sup>72</sup>. (D) depicts a design for a microfluidic oscillator capable of converting constant flow into an oscillating output through the use of both switch valves and check valves<sup>71</sup>.

### 1.3.2 Mass Spectrometry for Cell State Assessment

The complexity of biological samples often exacerbates standard screening techniques to the detriment of most attempts to discover biomarkers of disease or to rapidly screen drug efficacy. This unique problem warrants an analytical technique capable of rapid, yet non-destructive screening of samples. The need for sensitivity in this screening is an additional complicating factor characteristic of this type of experimental work as it is plagued by low abundance of analytes. The move towards mass spectrometry (MS) as the powerhouse of proteomic<sup>75</sup>, lipidomic<sup>76</sup>, glycomic<sup>77</sup> and metabolomic studies has led to many advances in elucidating the complexity of the cell.

Mass spectrometry is a technique for determining sample composition by using an ion source to create charged particles from the sample, separating those particles based on their mass to charge ratio ( $m/z$ ) in a mass analyzer and then recording the relative abundance of ions of a particular  $m/z$  present in the sample through the use of a detector. Ion sources include electrospray ionization (ESI)<sup>78</sup>, which ionizes and volatilizes liquid sample, and matrix-assisted laser desorption/ionization (MALDI)<sup>79</sup>, which involves firing a laser at a dried sample co-crystallized with an organic matrix molecule. While MALDI has the advantage of reducing issues caused by salts in biological samples and also gives a means of storing temporally resolved data when an immediate MS scan is unavailable, ESI can handle liquid samples and thus is capable of additional separation methods, rendering it preferred for more complex samples<sup>80</sup>. A variety of mass analyzers have been developed, such as ion trap (IT), time-of-flight (TOF), quadrupole and Fourier transform (FT), and are reviewed elsewhere<sup>80,81</sup>. MS is frequently coupled with chromatography techniques such as liquid chromatography (LC) and gas chromatography (GC) for additional separation of analytes. Recently, MS has also been paired with ion mobility (IM), a technology that separates ions in a drift tube, which is filled with a neutral gas and surrounded

by parallel ring electrodes in series, connected by resistors. A voltage difference applied across the resistors produces an electrostatic field which causes ions to collide with the drift gas. Ions with a larger collision cross section move slowly through the drift tube, while those with a smaller collision cross section are able to pass quickly. This allows IM-MS to provide an

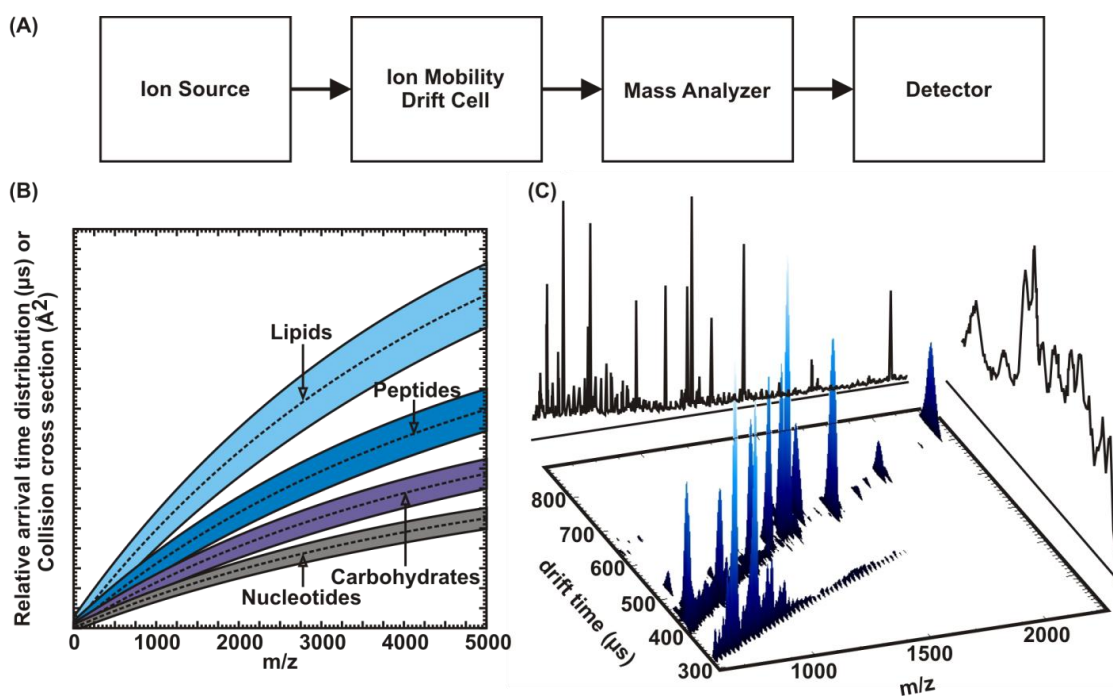


Figure 1.3 Ion Mobility Mass Spectrometry (A) Schematic of IM-MS procedure, (B) Separation of classes of biomolecules based on collision cross section and  $m/z$ , (C) Sample combined IM-MS spectra showing 3D information. Enders et al.<sup>75</sup>

additional dimension of information: relative abundance and collision cross section as a function of  $m/z$ , a distinct advantage over LC- or GC-MS (Figure 1.3). IM-MS has further benefits of separation speed ( $\mu\text{s}$ - $\text{ms}$ ), decreased chemical noise and enhanced peak identification<sup>82,83</sup>.

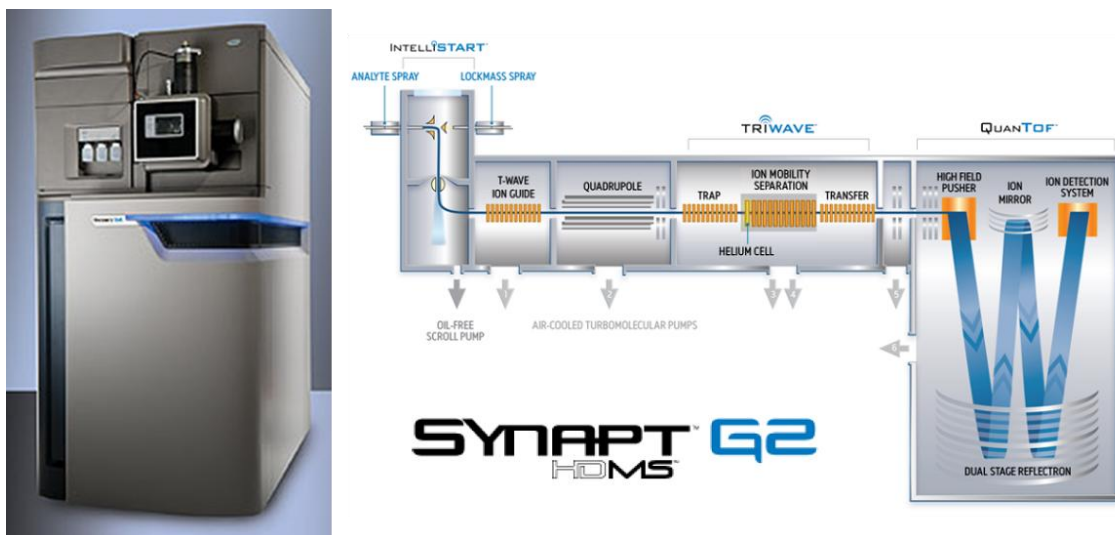


Figure 1.4 Waters Synapt™ G2, a state of the art, commercially available IM-MS, showing external image (left) and internal details (right)<sup>86</sup>. This instrument is outfitted with ESI, nano-ESI and MALDI sources. The ion mobility separation cell contains three consecutive traveling wave ion guides to increase resolution: the ion trap in which ions are held and periodically released into the next region, the ion mobility separation (IMS) guide that exploits the mobility of the ions to achieve separation and the transfer region which maintains the ion separation and directs them to the analyzer. Once ions travel through these regions, they move into the time-of-flight analyzer with a high field ion pusher, dual stage reflectron and ion detection system.

Because of these advantages, IM-MS is well suited for the rapid analysis of complex biological samples<sup>84,85</sup>.

The Waters Synapt™ G2 HDMS (Figure 1.4)<sup>86</sup> is a state-of-the-art, commercially available IM-MS residing in the McLean Laboratory for Structural Mass Spectrometry. This instrument is outfitted with nano-ESI and is capable of direct fluid input, bypassing the built-in fluidics system. The ion mobility separation cell called Triwave™ Technology contains three consecutive traveling wave ion guides to increase resolution: the ion trap in which ions are held and periodically released into the next region, the ion mobility separation (IMS) guide that exploits the mobility of the ions to achieve separation and the transfer region which maintains the ion separation and directs them to the analyzer. Once ions travel through these regions,

they move into the QuanTof™ time-of-flight analyzer with a high field ion pusher, dual stage reflectron and ion detection system. The Synapt G2 is managed through the use of MassLynx™ software and DriftScope™ Mobility Environment software is used for 2- and 3D visualization of data and peak labeling and identification.

### 1.3.3 Combining Microfluidics with Mass Spectrometry

Combining microfluidic constant perfusion bioreactors with mass spectrometry has the potential to rapidly screen cell effluent and even cell contents for proteins, lipids, carbohydrates and oligonucleotides. Several studies have taken on the challenge of the integration of these two technologies to produce a powerful analytical platform. In an early experiment, Chan et al. verified that using PDMS devices to transfer samples into the ESI-MS did not contaminate the samples<sup>87</sup>. On-chip ultrafiltration and analyte pre-concentration for high-throughput small molecule screening with ESI-MS were performed with the resulting detection sensitivity shown to increase by 1-2 orders of magnitude over off-chip screening strategies<sup>88</sup>. Kim and Knapp validated a fabrication method for producing on-chip ESI emitters, as opposed to direct spraying from channels ending at the edge of the device<sup>89</sup>. Silica capillaries were also used as on-chip electrospray nozzles and shown to be comparable to commercially available nanospray tips<sup>90</sup>. Huikko et al. used microfluidic channels and ESI-MS to analyze pharmaceuticals and amino acids, and based on these experiments, recommended a fabrication protocol for avoiding background noise caused by device fabrication procedures<sup>91</sup>. The development of an on-chip capillary electrophoresis device capable of direct ESI-MS from the channel edge was reported by Mellors et al<sup>92</sup>. The coupling of microfluidic devices for enzymatic protein digestions to MALDI- and ESI-MS has seen success<sup>93,94</sup>. A significant impairment in coupling microfluidic devices with online-MS is in the saturation of signals with salts present in biological samples. To avoid this issue,



MALDI-TOF MS was paired with a microfluidic bioreactor capable of trypsin digestion for proteomic analysis of *Esherichia coli*<sup>94</sup>. MALDI may provide a means of partially circumventing the issue caused by salts, but it is not a solution. While most of the work has just begun, many groups are poised to begin using these combined techniques for inspection of biological samples.

#### 1.3.4 Computational Modeling of Complex Biological Systems

Modeling complex biological systems is a challenging task due to poor understanding of the biochemical pathways under investigation. Kitano describes biological systems as “functionally diverse, and frequently multifunctional, sets of elements [that] interact selectively and nonlinearly to produce coherent rather than complex behaviours”<sup>95</sup>. With the growing realization of complexity and amount of experimental biological data produced, many computational modeling methodologies have struggled to remain on the forefront of systems biology.

##### *1.3.4.1 Cornell Computational Synthesis Laboratory Co-evolutionary Algorithms*

One promising technique for the analysis of non-linear systems developed by the Cornell Computational Synthesis Laboratory (CCSL) is a co-evolutionary method combining symbolic regression algorithms (SRA) and estimation-exploration algorithms (EEA). The SRA, as shown in Figure 1.5, calculates partial derivatives for every combination of variables, searches for possible invariance, predicts and compares partial derivatives based on the invariance and generates candidate models along with the estimation phase of the EEA. The EEA compares the candidate models and proposes an experiment based on the extent to which it would cause disagreement between candidate models<sup>96</sup>. The benefit of symbolic regression lies in its ability to concurrently search for both forms of equations and parameters<sup>97</sup>. The data generated from

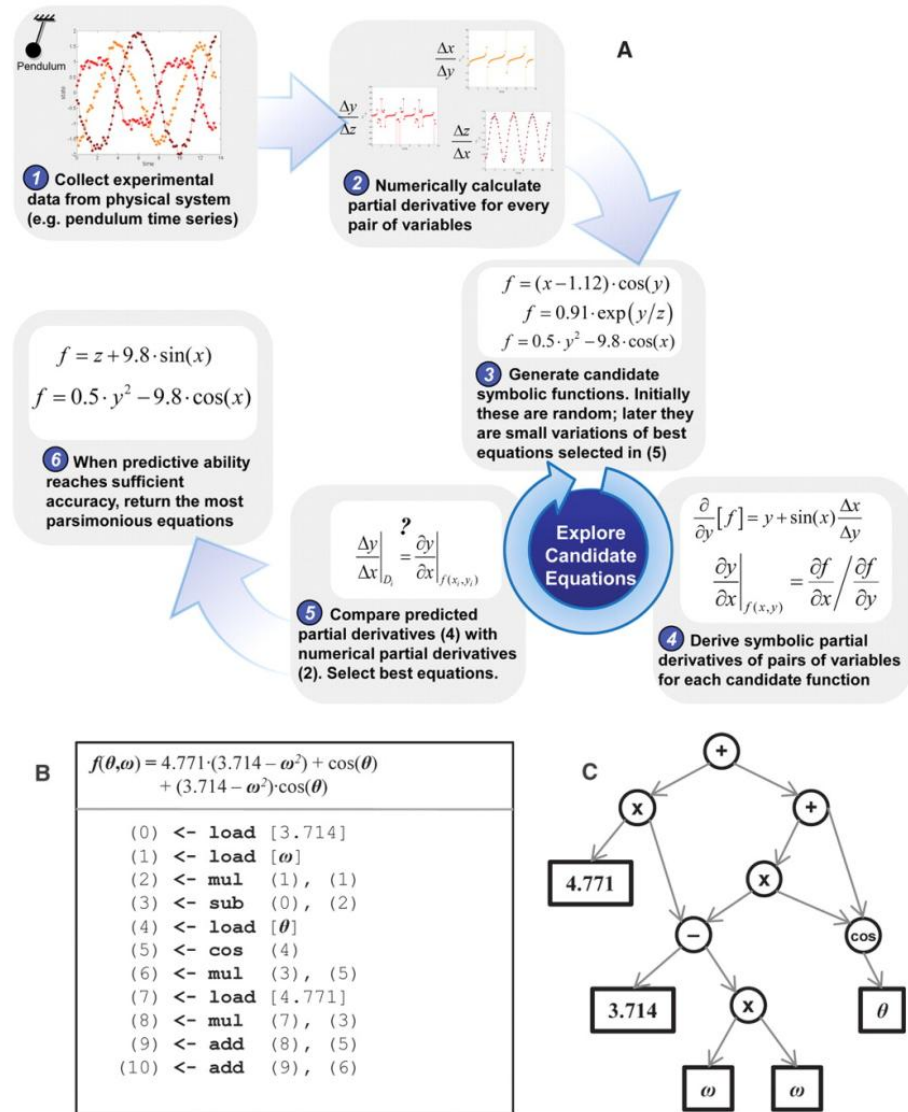


Figure 1.5. Conceptual pathway from experimental data to discovery of conservation laws. A) Shows the process of partial derivative calculation from which candidate functions are explored. B) List of mathematical operations as stored in the computer. C) Tree figure representing the equation in B. Schmidt and Lipson<sup>97</sup>.

the proposed experiments would again be mined by the SRA, reducing the candidate models. The candidate model synthesis and experiment proposal eventually lead to model inference<sup>96</sup>. These algorithms display the capabilities of determining models of complex biological systems with model reduction.

#### *1.3.4.2 Incorporation of Computational Modeling*

Modeling biological processes is a daunting task that can be overcome but often leaves the researcher with a purely theoretical, mathematical model that cannot be validated due to insufficient experimental data. While some experimentalists are dedicated to studying the cellular response one perturbation at a time, this method may not be capable of determining non-linear response, especially when a large number of variables is considered. Additionally, some experiments are capable of simultaneous adjustment of multiple experimental parameters, yet they may suffer from limitations in detecting cellular response as low sampling rates or signal amplitudes force the averaging of data over time or cell population<sup>98</sup>. Validating complex mathematical models with averaged, incomplete or biased data sets restricts model accuracy. Rapid detection of complex, dynamic biological response to multivariable perturbations will prove necessary to characterize the true cellular response. Since the fusion of microfluidics and mass spectrometry has the capability of detecting such responses, the use of these technologies for experimental data production is well suited. Spectral and optical data produced by this experimental platform is capable of being electronically transferred to Cornell for data mining and eventual model inference.

#### 1.3.5 Systems Biology Approach for Automated Science

With the wealth of data the combination of microfluidics and mass spectrometry for the analysis of complex samples is likely to produce, taking a systems biology approach to the determination of biological models would be advantageous. Systems biology seeks to understand living organisms by studying the interactions of numerous levels of biochemical networks comprising that organism and does so frequently through the use of computational modeling to understand existing experimental results. The key innovation of the combined

MTNP – IM-MS – SRA/EEA approach lies in the opportunity for automation. In the matter of minutes, a population of cells can be exposed to a certain set of experimental conditions in the MTNP, effluent from these cells can be analyzed by IM-MS, spectral and optical data can be electronically transferred to Cornell for data mining and experimental parameters for a subsequent experiment on the same population of cells can be delivered and implemented. All of these steps can occur in the absence of the researcher and allows for the testing of a greater number of system variables than any human is able to control. Pioneers of automated science introduced the community of researchers to the possibilities of a robot scientist and tested its capabilities in functional genomics<sup>99-101</sup>. Our approach builds on this idea that the scientific process is capable of automation and, with the powerful data generation, analysis and computational modeling capabilities, extends this idea to experimental designs humans are unable to perform alone.

#### 1.3.6 Summary

The microfluidic/analytical chemistry/model inference platform discussed applied to the problem of cocaine-induced immune suppression would serve to quickly and effectively discover any permanent or long-term changes in immune function. While technology resulting from the proposed work is poised to revolutionize basic science research on cellular or small organism populations, it may also result in a platform for developing personalized treatment strategies.

## 1.4 Biological Background and Significance

Humans have the ability to fight off infections and disease with the aid of the immune system. When this vital component is diminished, a host of health problems can arise including cardiovascular disease and cancer. While some individuals are born with an immunodeficiency, others may acquire immune issues as a result of their lifestyle or exposure to hazardous substances. Many toxins and elicit substances are known to affect the immune system, leading to serious health complications. Cocaine, one such substance shown to suppress the immune system, will be discussed herein along with various biological toxins, T cell activators and basic factors in metabolic regulation. All effectors of cell state are experiments suited for analysis with the advanced technology platform discussed in the previous section to be developed for assessing and characterizing the effects drugs and toxins on the immune system.

### 1.4.1 Cocaine Effects

Drug use is widespread and is blind to cultural, societal, or economic diversity. Cocaine, isolated from the *Erythroxylum coca* plant, is a central nervous system stimulant that affects the reward center of the brain by blocking the reuptake of dopamine, norepinephrine and serotonin causing mood-stimulating effects, with chronic use leading to permanent changes in levels of certain uptake transporters<sup>102</sup>. The effects of cocaine reach far beyond the central nervous system, into the immune system through mechanisms not fully understood, resulting in a suppression of immune function discussed in more detail later in this proposal. Figure 1.6, based on the findings of Nutt et al., shows cocaine to be the second most harmful and addictive substance of those commonly abused<sup>103</sup>. In 2008, the National Survey on Drug Use and Health (NSDUH) estimates that 36.8 million Americans over the age of 12 have used cocaine at least once in their lives, with 1.9 million having done so in the previous month<sup>104</sup>. The prevalence of

use combined with the severe physical effects, including suppression of the immune system, make cocaine a worthy candidate for further investigation. A more complete understanding of the actions of this drug on the immune system can lead not only to potential testing methods, but also to more effective treatment strategies for addiction.

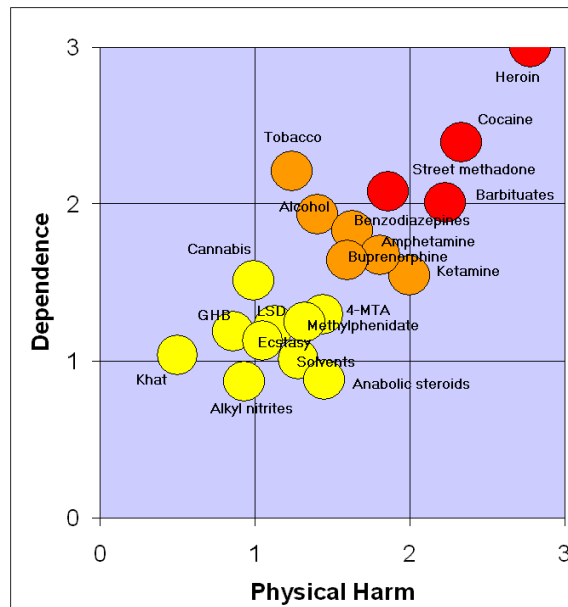


Figure 1.6 A comparison of substances of abuse based on addictive quality and physical harm caused by use is shown. From Nutt et al.<sup>103</sup>

#### 1.4.1.1 Drug testing

Exact statistics of a population's cocaine use can be difficult to determine and are currently accomplished through surveys as mentioned previously. The accuracy of this method is questionable as no drug testing is performed on survey participants. Wastewater analysis using a gas chromatography-mass spectrometer for determining population use by amount of cocaine and its metabolites present has been suggested and tested in Belgium<sup>105</sup> and in Florence, Italy<sup>106</sup>. While this method provides total amounts used, assumptions of amounts of individual

use would need to be made in order to determine percentages of the population using cocaine. The results from such testing are valuable in that they can be used to assess public tactics for reducing drug use in a population.

Drug testing on an individual level is accomplished by analyzing bodily fluids and materials such as urine, blood, hair, sweat, and saliva with urine being the most commonly used based on ease of acquisition and cost of analysis. The initial urine screening is typically done with the enzyme-multiplied immunoassay technique and can be confirmed with gas chromatography-mass spectrometry (GC-MS)<sup>107</sup> or liquid chromatography-mass spectrometry (LC-MS)<sup>108</sup> for cocaine and/or its major metabolite, benzoylecgonine, with detection capabilities of 300 ng/mL, 1 ng/mL and 25 ng/mL, respectively. Since both substances are metabolized and cleared relatively quickly from the body (cocaine's half-life is about an hour and benzoylecgonine's is about 6 hours), the urine test would have to be performed soon after drug use<sup>109</sup>. Typical time limits for urine screening are on the order of days. Urine testing is also easily adulterated with the addition of bleach, vinegar, Visine and hand soap<sup>110,111</sup>. While urine testing is the standard, some aspects of other testing procedures are advantageous. For instance, the use of hair for drug testing allows for an extended time limit for detection and also provides information on use patterns based on hair growth rates. While adulterating hair samples is more complex, the removal of hair altogether is simple. Blood can also be tested, but due to the short half-life of cocaine, testing must be done within hours of drug use<sup>109</sup>.

Significant advances in cocaine testing methods have not occurred in over 15 years as the tradeoff between cost and sensitivity has not been worthwhile. With just a few  $\mu\text{L}$  of blood from a finger stick, the proposed research could lead to a testing method rivaling a standard urine screening in cost, with none of the detection time limitations or sample adulteration issues, and with sensitivities on the order of those used in more expensive GC-MS or LC-MS

conformational analysis. Instead of testing directly for cocaine or its metabolites, the proposed method seeks to detect changes in metabolic dynamics of cells of the blood, particularly immune cells, as a result of in vivo cocaine exposure which could produce subsequent biomolecular signatures of drug use, thus detecting permanent changes in cellular biochemistry that may accompany single use, recreational use or chronic use of illicit drugs (John McLean, personal communication).

#### *1.4.1.2 Effects of Cocaine Use on the Central Nervous System*

Cocaine is a stimulant of the central nervous system, and as a result, most research on cocaine use and addiction in the past few decades has been focused on neurological effects, with less attention given to the more systemic physiological effects and the secondary effects of changes in neurobiology. Though many pharmacological actions of cocaine in the nervous system have been explored, not all are completely understood. A synopsis of the mechanisms of cocaine action in the nervous system will add to the classic view of cocaine and begin to associate the drug with its broad range of actions.

##### 1.4.1.2.1 Monoamine Reuptake Inhibition

The most well-known and studied action of cocaine is its role in blocking the reuptake of monoamine (norepinephrine, serotonin and dopamine) neurotransmitters. As a small xenobiotic molecule exhibiting both lipophilic and hydrophilic properties, cocaine, upon administration, can cross the blood-brain barrier. Much of the cocaine localizes to areas of the brain that are rich in neurotransmitter transporters, such as the nucleus accumbens, ventral tegmental area, and amygdala<sup>112,113</sup>, where it becomes concentrated in the synapses between neurons and binds to these transporters, which are responsible for the recycling of the transmitters back into the



presynaptic neuron where they are stored in vesicles. This blockade increases levels of monoamines (norepinephrine, serotonin, and dopamine) in the synaptic cleft, allowing greater ligand binding to their respective receptors on the postsynaptic neuron. With increased dopamine signaling and subsequent binding to the G-protein-coupled dopamine receptor, comes an increase in cyclic AMP in postsynaptic neurons<sup>114</sup>, leading to increased neuronal firing and maintenance of an activated state in the pleasure center of the brain, perpetuating the euphoric feeling of the user<sup>112,115</sup>. Prolonged exposure to cocaine leads to a downregulation in postsynaptic receptors for dopamine that causes desensitization to the effects of the drug, and thus a higher dose is required to achieve the same results<sup>116</sup>. Upregulation of dopamine transporters is evident up to 30 days post-cocaine use; however, results also show that these levels return to normal after 90 days, indicating that monoamine reuptake inhibition is not permanently modified<sup>117</sup>. Dopamine signaling plays a fundamental role in learning and memory systems, and as such, cocaine addiction is hypothesized to result from adaptations in these systems as a result of Pavlovian and operant conditioning<sup>114,118,119</sup>. In a recent review, Wise and Kiyatkin discuss the ultra-fast rewarding action associated with cocaine use in chronic users: a spike in dopamine that occurs prior to cocaine reaching the brain<sup>120</sup>. This pre-use stimulus represents evidence of a conditioned response caused by release of glutamate and acetylcholine<sup>120-122</sup>. Reuptake inhibition, however, is not the only method of cocaine neuromodulation, as is evident by the fact that many medications designed to block monoamine reuptake do so without the psychotic and depressive effects linked to repeated cocaine stimulation<sup>123</sup>. Thus, cocaine must interact with other receptors to elicit these additional effects.

#### 1.4.1.2.2 Non-monoaminic Nervous System Substrates: Sigma-1 Receptor

Dopamine reuptake inhibition has received great attention from the scientific community as it is the main pathway leading to the reward associated with cocaine use. Investigation of the role of cocaine binding to additional neural substrates also has the potential to contribute to our understanding of cocaine's complex pharmacological actions. For example, although it is still unidentified, an additional neuronal receptor was discovered by Rothman et al. to be a potential binding site for cocaine, as the binding affinity of the drug to this receptor is within the concentration range of cocaine found in brain membrane preparations post-administration<sup>123</sup>. Smirnov et al. have implicated peripheral non-monoamine neural substrates in the immediate physiological response (EEG and EMG changes) to cocaine prior to stimulation of the central nervous system<sup>124</sup>. Secondary effects of increased dopamine signaling may also occur. For instance, prolonged cocaine administration leads to upregulation of  $\mu$  opioid receptors in the nucleus accumbens and  $\kappa$  opioid receptors in the olfactory tubule, caudate putamen, and cingulate cortex as a result of increased dopamine transmission<sup>125</sup>. The sigma-1 ( $\sigma_1$ ) receptor is one of the more extensively studied of the additional substrates for cocaine and will be reviewed here in greater detail.

As mentioned above, cocaine has complex mechanisms of action, some of which are a direct result of receptor-mediated binding to the  $\sigma_1$  receptor, which is found in high density in the central nervous system, and also throughout peripheral organs, tissues, and even immune cells. While the existence of this receptor as an opioid receptor was first suggested in 1976<sup>126</sup> and subsequently reclassified upon discovery of the lack of naloxone or naltrexone binding affinity to this receptor<sup>127</sup>, a complete understanding of the  $\sigma_1$  mechanism of action has remained elusive. It has, however, been implicated in addiction, cognition, pain, depression and a wealth of human diseases, including cancer and cardiovascular disease<sup>128</sup>. This receptor is an

endoplasmic reticulum (ER) ligand-gated molecular chaperone<sup>129</sup>, also associated with the control and modulation of voltage-regulated and ligand-gated ion channels, such as Ca<sup>+2</sup>, K<sup>+</sup>, Na<sup>+</sup>, and Cl<sup>-</sup> channels, as well as NMDA and IP3 receptors, thus playing a role in Ca<sup>+2</sup> signaling<sup>130,131</sup>. Through these actions, it is postulated that  $\sigma_1$  receptors control neuronal firing and neurotransmitter release<sup>132</sup> and play a role in the behavioral and locomotor stimulus response associated with cocaine use<sup>133</sup>.

The affinity level of cocaine for the  $\sigma_1$  receptor is 2-10 $\mu$ M, which is within typical blood concentrations of cocaine users<sup>128,132</sup>. Cocaine also augments the expression of the immediate early gene fos-related antigen 2 (*fra-2*), which in turn potentiates the gene expression of the  $\sigma_1$  receptor and its subsequent protein expression<sup>134,135</sup>. As a  $\sigma_1$  agonist, cocaine is capable of inhibiting voltage-gated ion channels while enhancing the ligand-gated ion channels<sup>130</sup>. Hayashi and Su give evidence that stress to the endoplasmic reticulum causes  $\sigma_1$  receptors to redistribute to the entire ER and postulate that they may play a role in the suppression of misfolded proteins that leads to or is part of the unfolded protein response (UPR)<sup>129</sup>. Recently, some advances have been made that give insight into the workings of this complicated receptor chaperone. These results suggest that the concentration of agonists may cause the  $\sigma_1$  receptor to leave the endoplasmic reticulum and translocate to the cell membrane, where it can potentially alter the function of the ion channels (Figure 1.7)<sup>129,136-139</sup>. NMDA receptors, ion channels involved in memory and learning, were one of the first cell membrane receptors to be associated with the  $\sigma_1$  receptor, and although discrepancies exist between studies<sup>140-142</sup>, the interaction between these two receptors is evident. Regardless of the suggested membrane-translocation, the  $\sigma_1$  receptors regulate neighboring ion channels in the endoplasmic reticulum as well. For instance,  $\sigma_1$  agonists administered in neural cell lines caused a rise in Ca<sup>+2</sup> flux through the IP3 receptor (IP3R) even in the presence of an IP3R inhibitor<sup>143</sup>. Sigma-1 receptors

have been shown to regulate the interorganelle  $\text{Ca}^{+2}$  signaling between the mitochondria and the ER<sup>129</sup>. The relationship between calcium and cocaine is far from new information; however,

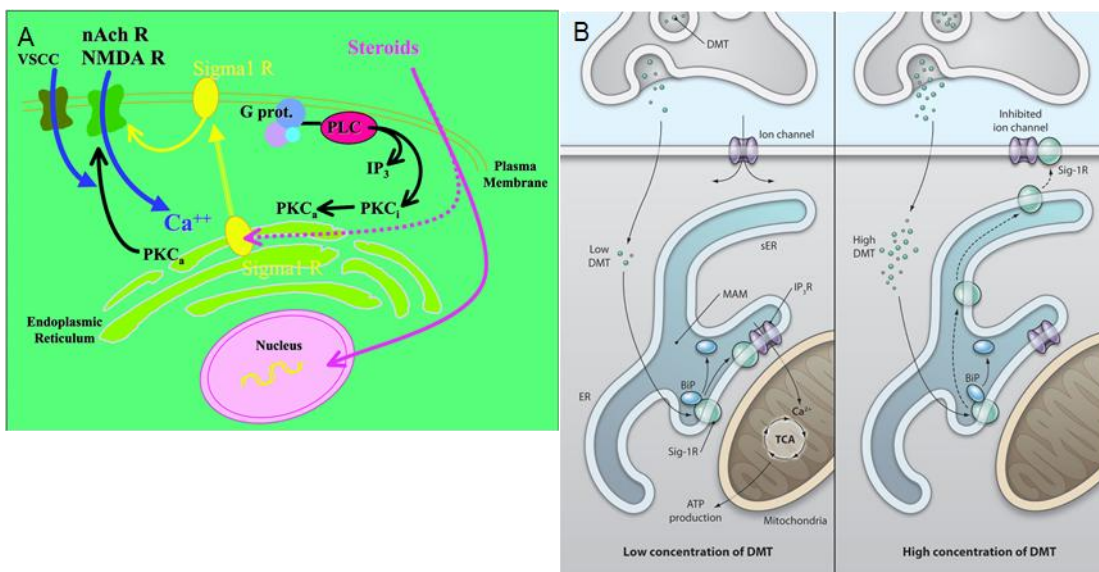


Figure 1.7 Representations of the potential mechanisms by which the  $\sigma_1$  receptor mediates both ER and plasma membrane (PM) ion channels: A) Steroids binding to  $\sigma_1$  receptors cause translocation to the PM. From Monnet et al.<sup>138</sup> B) High concentrations of *N,N*-dimethyltryptamine (DMT) causes signaling in neurons leading to  $\sigma_1$  receptor translocation. From Su et al.<sup>139</sup>

the details of the relationship, beyond that of cocaine causing a decrease in mobilized cytosolic  $\text{Ca}^{+2}$ , potentially through a mechanism involving the  $\sigma_1$  receptor, are unclear.

These studies of both monoamine and non-monoamine targets for cocaine binding give rise to the complex nature of the drug's pharmacological and behavioral effects. While many of these substrates, such as dopamine transporters, are well characterized, others are still in the early stages of identification and characterization. Understanding the diverse actions of cocaine will allow for the development of innovative methods for treatment of addiction or cocaine

toxicity, yet investigating only the nervous system effects of the drug leaves an untapped resource for potential treatment strategies. One must also consider the immune effects of cocaine, as well as how the immune and nervous systems interact to truly understand the complete physiological reaction to the drug.

#### *1.4.1.3 Immunological Effects of Cocaine Use*

Investigation of the effects of cocaine on immune response began slowly in the 1980s with a study showing the suppressive effects of cocaine on the immune response of mice to sheep red blood cells<sup>144</sup>, followed by 10-15 studies published per year from the early 1990s through the present day. As the link between cocaine use and immune function has become stronger, the expectation of permanent immune changes grows more plausible, but it has not yet been investigated directly. Extensive research on the role of cocaine in the susceptibility to and progression of HIV, cancer, and cardiovascular diseases has been conducted and will be reviewed here alongside general immune function changes due to cocaine exposure.

##### 1.4.1.3.1 Direct Immunomodulatory Effects

Cocaine is described as an immune suppressor that acts directly on the  $\sigma_1$  receptor in a wide range of leukocyte populations, including T cells, B cells, and natural killer (NK) cells. Numerous peripheral mechanisms of action via the neuro-immune connection that result in immune function changes are also suspected (Figure 1.8). In one of the earliest studies of the effects of cocaine on the immune system, Watson et al. described a suppression of the immune system following cocaine administration in mice as measured by ear swelling and plaque-forming cell (PFC) splenic assay<sup>144</sup>. As time progressed, more direct measures of immune function were incorporated. Change in white blood cell count post cocaine exposure was one of

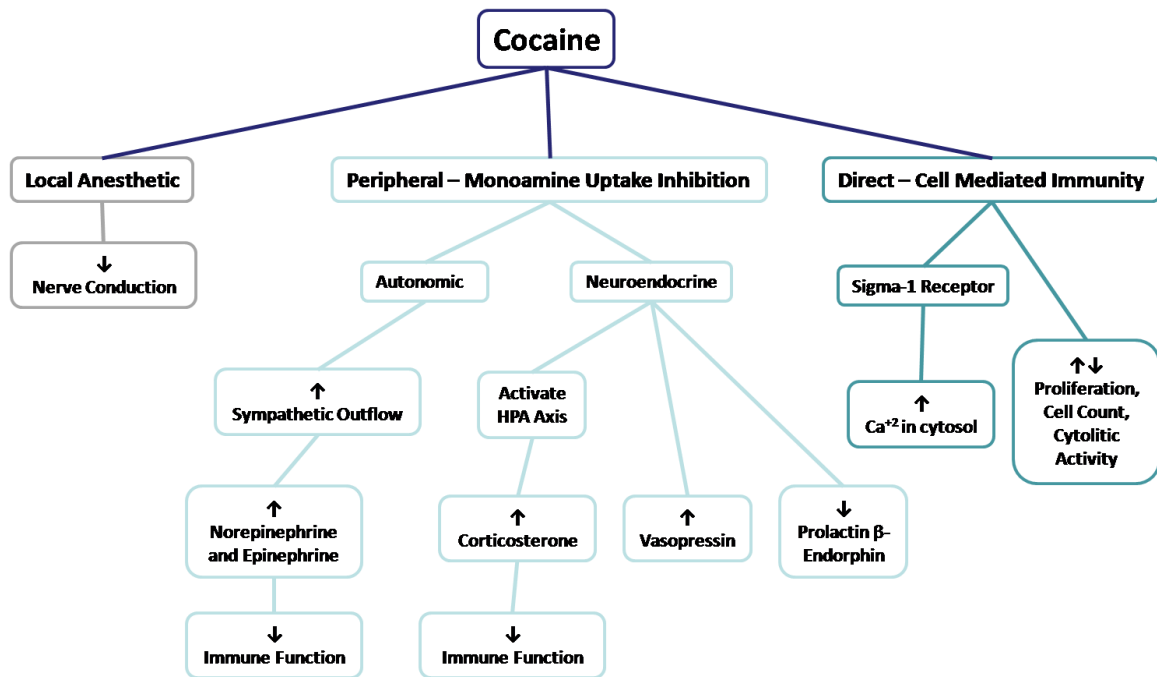


Figure 1.8. Summary of effects of cocaine on immune function, both up and down arrows indicate mixed results. Cocaine also alters antibody and cytokine production, though it is not clear by which route these alterations occur. Adapted from Pellegrino and Bayer.<sup>154</sup>

these more direct immune differences, although there is some discrepancy in the nature of that change, with some reports of decrease<sup>145</sup> and even no change<sup>146,147</sup> in cell count or viability. When exposed to cocaine, and to a greater degree when incubated with cocaine for 24 hours, phytohemagglutinin (PHA)-induced proliferation of T cells is suppressed and associated with a decrease in the cytosolic free  $Ca^{+2}$  and diminished production of IL-2<sup>148</sup>, although other studies show no link between decreased T cell proliferation and  $Ca^{+2}$  flux or IL-2 production<sup>149</sup>. Disagreement between findings suggests a more complex signaling cascade, with  $Ca^{+2}$  most likely playing a critical role in need of further investigation. Faraj et al. report that lymphocytes possess a high affinity dopamine uptake process that cocaine blocks in a concentration-dependent manner<sup>150</sup>. Cytokine secretion has been shown to be altered in response to cocaine

exposure in various leukocytes, including NK cells, T cells, neutrophils and macrophages<sup>151,152</sup>. Specifically, cocaine may increase T helper type 1 (Th1) cytokines and decrease T helper type 2 (Th2) cytokines, and thus promote Th1-mediated immune responses and degrade Th2-mediated responses<sup>152,153</sup>. This range of results is perhaps a result of varying exposure parameters (chronic and acute administration are known even to cause differential effects in the central nervous system), experimental model or cell population, and potential tolerance to cocaine<sup>154,155</sup>. Pellegrino et al. released a compelling study on lymphocyte proliferation after exposure to cocaine and demonstrated that suppression of proliferation occurred as a result of peripheral activities of cocaine<sup>156</sup>. They additionally report that the need for high dose cocaine in vitro in order to elicit a decrease in immune function, points to indirect methods of immune modulation, potentially through alterations on neurotransmitters or the neuroendocrine system. Disagreement between results from numerous studies indicates the complexity of this biological system and drives the need for a more systematic approach that includes studies on both the humoral and cell-mediated immune responses in single and mixed immune cell populations from various animal models, and especially from humans, under tightly controlled and easily adjustable experimental conditions.

#### 1.4.1.3.2 Serum Protein Alteration and Resulting Immune Response

The body's responses to any foreign substance include non-specific innate immune responses and primary and secondary adaptive immunological responses. These will occur if the foreign body, in this case cocaine, elicits an immune response. Upon entry into the bloodstream, non-specific esterases in the plasma of the blood, part of the humoral immune system, hydrolyze cocaine to two primary metabolites: benzoylecgonine and ecgonine methyl ester<sup>157</sup>.

As a result, cocaine has been found to be detectable in blood for only 4-6 hours after ingestion<sup>158</sup>.

Immunological responses to antigen presentation should not occur in response to cocaine alone as it is a small molecule. However, cocaine can elicit an immune response when attached to a large carrier molecule, such as a protein. Cocaine has been shown to covalently modify endogenous proteins (e.g., albumin) present in the plasma through the acylation of the  $\epsilon$ -amino group of the protein lysine residues through a nucleophilic attack by benzoylecgonine<sup>159</sup>. These modified proteins are recognized as foreign antigens through binding with major histocompatibility complexes (MHC) located on antigen-presenting cells (e.g., macrophages, dendritic cells). Binding, depending on whether the proteins are endogenous or exogenous, will occur on either MHC class I or MHC class II, respectively, for any antigen that is recognized. The modified proteins that have been documented are treated as exogenous, as they are highly abundant plasma proteins, such as albumin and IgG proteins. The exogenous modified proteins are endocytosed by antigen-presenting cells (APCs). This endocytosis occurs either non-specifically by dendritic cells whose primary job it is to scavenge and present any protein they encounter, by receptors on macrophages, or through surface IgM antibodies on B cells. These endosomes are digested through the fusion with lysosomes, which contain proteases and an acidic medium. Meanwhile, MHC II complexes are synthesized in the ER of the APC and combined with an invariant chain that allows for the transportation of the MHC molecule to the endolysosome, while preventing any binding in the antigen binding region prior to reaching the endolysosome. The resultant digested peptides from the endolysosome have a high affinity for the binding region of the MHC II. These are conjugated with class II MHC molecules through vesicle fusion, as the invariant chain is degraded by proteases in the endolysosome. This MHC:peptide complex is then shipped to the plasma membrane for



presentation to CD4+ T cell recognition. Upon recognition, the CD4 cells are activated by the antigen-presenting cell, and they then stimulate B cells to produce neutralizing antibodies against the cocaine-acylated proteins.

The antigen-presenting cell and the CD4+ T cell adhere through interaction of the MHC class II molecule and the T cell receptor (located on the T cell surface). For activation to occur, antigen-specific recognition, along with co-stimulatory molecules, must be present (e.g., B7 on the antigen-presenting cell interacts with cluster of differentiation 28, or CD28, on T cells). Once the CD4+ T cell is activated, it produces IL-2, along with an increased expression of IL-2 receptor, essentially resulting in self-activation through IL-2:IL-2R interaction. This promotes T cell growth and proliferation. These T cells differentiate into T helper cells, which then differentiate into Th1 cells through IL-12 promotion, or Th2 cells through IL-4 promotion. For this discussion, Th2 cells are most important, as they promote the production of antibodies through the activation of B cells.

To accomplish this, the antigen-presenting cell and the CD4+ T cell adhere through interaction of the MHC class II molecule and the T cell receptor (located on the T cell surface). For activation to occur, antigen-specific recognition, along with co-stimulatory molecules, must be present (e.g., B7 on the antigen-presenting cell interacts with cluster of differentiation 28, or CD28, on T cells). Once the CD4+ T cell is activated, it produces IL-2, along with an increased expression of IL-2 receptor, essentially resulting in self-activation through IL-2:IL-2R interaction. This promotes T cell growth and proliferation. These T cells differentiate into T helper cells, which then differentiate into Th1 cells through IL-12 promotion, or Th2 cells through IL-4 promotion. For this discussion, Th2 cells are most important, as they promote the production of antibodies through the activation of B cells.

B cell activation occurs through a similar antigen recognition procedure: a specific antigen binds to B cell surface antibodies (IgM and IgD antibodies), is endocytosed and presented as a MHC class II complex. This MHC class II complex must then be recognized by an antigen-specific Th cell, which then activates the naïve B cell through cytokine secretion. This Th cell also expresses a CD40 receptor, which binds with the CD40 produced by the antigen-presenting B cell. These B cells then proliferate and differentiate into antibody secreting B cells. As such, both memory T and B cells specific to the modified proteins are present in the body, along with antibodies for their neutralization in the plasma.

After the initial recognition, activation, and antibody-forming cascade, cocaine-modified proteins in the bloodstream are recognized by IgM or IgG antibodies, resulting in an immunological cascade. The cocaine modified proteins are bound to extracellular IgM or IgG antibodies, which in turn activate the complement system. This is considered the classical pathway of activation and results from an antigen:antibody complex. These antibodies are produced by B-cells, each having a single specificity for a modified protein dictated by the variable region of the antibody. The activation of complements results in the opsonization of the antigen and the recruitment of inflammatory cells.

Opsonization serves to mark the complex for phagocytosis, produced through the covalent binding of complement components to the modified proteins. The binding of complements results in conformational changes that activate specific cleavages within the complement system (i.e., C1s as a serine protease), which generates C3 convertases that bind to the cocaine-modified proteins. C3 convertase is further cleaved into C3b, which serves as the opsonization agent, and C3a, which is a small peptide involved in inflammation. Phagocytes (i.e., neutrophils, monocytes, macrophages, and dendritic cells) are recruited using these chemokines produced from this complement cleavage (i.e., C3a, C4a, and C5a). These phagocytes serve to

recognize, contain, and destroy the modified protein. Macrophages recognize conjugated complement with complement receptors, which induce the phagocytosis of complexed antigen. Specifically, the binding of the C3b complement, which is covalently bound to the antibody:antigen complex, to its respective receptor (i.e., CR1 on macrophages), is the first step to phagocytosis. Phagocytosis then occurs when the inflammatory chemokine C5a activates the macrophage. This results in the formation of a phagosome in the macrophage through engulfment, bringing the modified protein into the macrophage in a vesicle, which is then fused with a lysosome. Within the phagolysosome, degradation of the protein occurs via acidification and lysing enzymes. In this manner antibody:antigen complexes are cleared from the system in a specific fashion.

Activated macrophages also secrete cytokines and other signaling factors, such as leukotrienes and prostaglandins in response to antigen recognition. These recruit and alert lymphocytes that an antigen is present, eliciting an adaptive response. As a result of activation, a cocktail of interleukins (i.e., IL-1, IL-6, IL-8, IL-12), in addition to tumor necrosis factor alpha (TNF- $\alpha$ ), are produced by macrophages. Important for this discussion is the production of IL-6, IL-8, and IL-12, as IL-6 activates lymphocytes and stimulates further antibody production, IL-12 activates Th 1 cells, and IL-8 recruits neutrophils, basophils, and T cells. Hence, as a result of cocaine's permanent covalent modification of plasma proteins, an immunological response that ultimately includes both innate and adaptive immune systems is mounted.

#### 1.4.1.3.3 Progression of Diseases and Aging

Immune suppression as a result of cocaine administration leaves the user with an increased susceptibility to infection. The relation of cocaine use and prevalence of HIV and AIDS has frequently been studied, with reports indicating that increased susceptibility to HIV infection

among cocaine users is not a result of intravenous drug use alone but of the changes in the immune system caused by cocaine<sup>154</sup>. Baldwin et al. report an increase in infectivity or HIV replication in human cells when exposed to cocaine *in vitro*<sup>151</sup>. A decrease in CD4+ counts, lower CD4:CD8 ratio, and marked increase in viral load upon cocaine administration were found in mice implanted with HIV-infected human peripheral blood leukocytes<sup>160</sup>. In a supplementary study by the same investigators of the various mechanisms through which viral load was increased 150-fold, it was shown that cocaine both increases expression of HIV chemokine coreceptors and directly binds the  $\sigma_1$  receptor of leukocytes, causing an increase in IL-10 and TGF- $\beta$  – both significant factors in the progression of HIV<sup>146</sup>. The striking impact of cocaine administration on risk and progression of HIV, along with the evidence of numerous mechanisms of action leading to these issues, necessitates further work before effective HIV treatment and prevention strategies can be developed.

HIV and other infections are not the only conditions worsened by cocaine use. Cancer progression has also been shown to be associated with the binding of cocaine to  $\sigma_1$  receptors, which alters chemokine production, specifically IL-10, leading to suppression of the antitumor response<sup>152,161</sup>. It has also been reported that macrophage inhibition of tumor growth is diminished when exposed to cocaine *in vitro*<sup>162</sup>. As the antitumor response is a feature associated with the immune system, it follows that the suppression of the immune system by cocaine would also hamper the response to tumor formation.

Cocaine use is a culprit in many cardiovascular complications, including myocardial ischemia, apparent myocardial infarction, hypertrophy, myocarditis, thrombosis, stroke and sudden cardiac death, among others. Although the mechanisms by which cocaine plays a role in cardiovascular disorders remain to be determined, many studies investigate the connection<sup>163–168</sup>. A thorough review of the role of cocaine use in cardiovascular disorders has been conducted

elsewhere<sup>169-171</sup>. It is, however, important to realize the broad range of physical effects caused by cocaine use.

In a related study on drug-induced accelerated aging, Reece reports that addicted populations of patients show higher erythrocyte sedimentation rate (ESR), C-reactive protein (CRP), globulins, globulin/albumin ratio, and lymphocyte count when compared with non-addicted medical patients and that since many of these factors are considered biomarkers of aging, it is possible that aging of addicted individuals follows a contracted time course<sup>172</sup>.

#### 1.4.1.3.4 Current Strategies of Immune Modulation Research

Much of the research to determine the effects of cocaine on immune function discussed above was performed using immune cell lines and blood samples from animal models. The assessment of immune status is typically performed by quantifying parameters such as lymphocyte proliferation, cell count, cytolytic activity, plaque-forming activity, antibody titer, cytokine production, and corticosterone levels, to name a few. Immunoassays such as enzyme-linked immunosorbent assay (ELISA) and immunohistochemistry combined with flow cytometry are the current techniques used in these types of studies. These techniques have their downfalls, though. For example, ELISA is plagued by potential complications of cross-reactivity and poor sensitivity, although digital ELISA might increase the sensitivity by orders of magnitude<sup>173</sup>. Flow cytometry, while fast and capable of detecting multiple wavelengths at a time, reports only population-based information, missing any variation between cell phenotypes and not allowing sequential measurements on individual cells. Further complicating such measurements in cultured lymphocyte cell lines are the large volumes associated with cell culture known to dilute paracrine and autocrine signaling factors that provide critical information concerning the status of the immune system<sup>42</sup>. These concerns in the determination

of immune status bring to light the need for additional analytical techniques and instrumentation to delve further into these biological matters.

#### *1.4.1.4 Neuroimmune Connection and its Role in Potential Long-Term Effects of Cocaine*

It is widely accepted that drug use, especially when repeated, leads to long-lasting behavioral sensitization in the form of psychosis or craving for the drug, which is thought to arise from potentially permanent<sup>174-177</sup> neuroplastic changes in certain areas and circuitry of the brain as a result of increased dopamine transmission<sup>178</sup>. De Vries et al. report that reinstatement of drug-seeking behavior after withdrawal is associated with this long-term behavioral sensitization<sup>179</sup>. Activation of the  $\sigma_1$  receptor has been implicated in drug-seeking relapse in mice as determined through the use of the conditioned place preference (CPP) behavioral assessment<sup>180</sup>. Ecker et al. link long-term alterations in genes typically viewed as stress- or immune-related to cocaine use and the levels of cAMP response element-binding protein (CREB), a factor in stress-induced reinstatement<sup>181</sup>. The evidence of long-term effects in the nervous system shows that permanent changes could be taking place that may have a subsequent effect on immune function either through the brain-immune communication network (Figure 1.9)<sup>182-184</sup> or by some other means. Brain-mediated immune responses involve not only neuroendocrine, neurochemical, metabolic and autonomic responses, but also changes in mood, motivational state, sleeping patterns, eating behavior, and social and locomotor activities<sup>185</sup>.

Cocaine has long been shown to increase levels of adrenocorticotropin hormone (ACTH),  $\beta$ -endorphin, and corticosterone in rats in a manner dependent upon cocaine or dopamine regulation of corticotropin-releasing hormone (CRH), the initiator of hypothalamic-pituitary-

adrenal (HPA) axis activation<sup>186–188</sup>. Likewise, cocaine use is associated with the maintenance of increased cortisol levels<sup>189</sup>. Upregulation of these stress hormones leads to alteration in gene expression and potentiates cocaine self-administration<sup>190</sup>. HPA axis activation, along with the increased secretion of these signaling molecules, leads to modulation of the immune system.

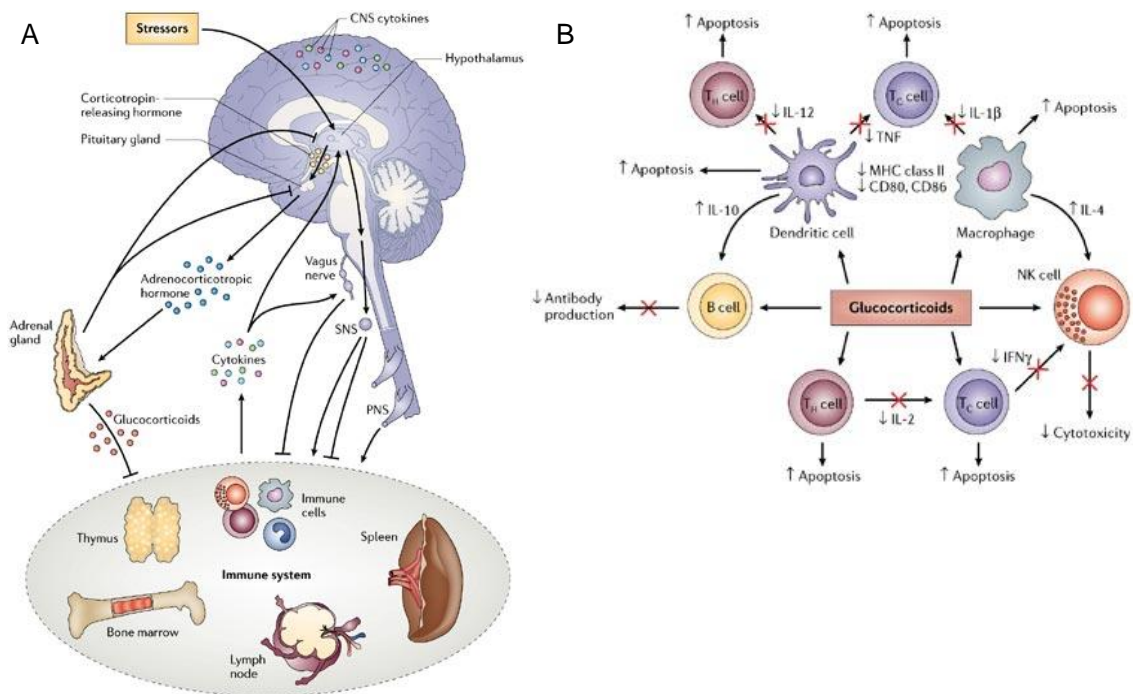


Figure 1.9 A) Brain-immune bi-directional connections: the vagus nerve, the hypothalamic–pituitary–adrenal (HPA) axis, the sympathetic nervous system (SNS) and the peripheral nervous system (PNS). B) Glucocorticoids' mechanisms of action on immune cells resulting in alteration of function. From Sternberg et al.<sup>184</sup>

Most investigations into the combined modulation of the immune system through the brain signaling in addition to cocaine are relatively short-term studies, and their findings have mixed responses due to the difficulty of controlling studies with collective cell-mediated immunity alterations and peripheral effects relating to the humoral immune response. In one of the few

long-term studies, Avila et al. suggest several valid explanations for prolonged immune suppression after withdrawal from chronic cocaine use that imply long-term or even permanent alterations in the immune system<sup>191</sup>. They discuss how the immune system vulnerability caused periodic release of corticosteroids initiated by cocaine administration, the sustained stress response release of corticosteroids during withdrawal, or the combination of the two as potential mechanisms of sustained T cell suppression after withdrawal<sup>191</sup>. In separate studies by the same group, the activated neuroendocrine stress response was implicated in the alteration of cellular immunity during the early withdrawal period<sup>192,193</sup>. Johnson et al. investigated the immune markers during acute cocaine withdrawal in pregnant women, and over this short period of data collection saw significant changes in complement receptor expression, which plays a role in the host-pathogen response<sup>194</sup>.

The interaction between the brain and the immune system is bidirectional, resulting in the brain interpreting immune cell activation as a stressor through signaling of cytokines<sup>182,183</sup>. Since cocaine is capable of eliciting an immune response by binding to serum proteins and thereby activating the release of cytokines, the effects of cocaine may be potentiated through the HPA axis.

A recent review published on the neuroimmunopharmacology of opioids provides an in-depth discussion of the role of the central immune system – i.e., astrocytes and microglial cells, which exhibit behaviors of both neural cells and immune cells – in this interconnection of the neurological and immunological systems<sup>195</sup>. Hutchinson comments that “[c]entral immune signaling cannot be thought of as a parallel system separate from that of neuronal synaptic transmission and neuronal communication,” which, taken together with the research findings of the neuro-immune connection, can be extended to include the peripheral immune signaling. Cocaine has been found to further potentiate the neuro-immune connection by serving as an



inflammatory stressor that causes leukocytes to adhere to endothelial cells of the blood-brain barrier, which leads to leaking of the tight junctions and allows leukocytes to traverse the barrier<sup>196</sup>. This connection complicates the determination of potential mechanisms of immunosuppressive effects of cocaine, but further establishes the likelihood of both direct and peripheral mechanisms of action, the interactions of which may serve as a feedback system that could lead to prolonged and long-term effects in both the immune and nervous systems.

Experienced researchers in the field of drug-modulated immunology also speculate on the matter of long-term immune effects. For instance, Pacifici et al. comment that “. . . the possibility that some kind of immune memory mechanism could also play a role cannot be discarded”<sup>197</sup>. Evidence of these potential sustained effects, however, may lie in the neuro-immune communication, including the HPA axis and the autonomic nervous system. With the increasing attention toward psychoneuroimmunology and the link between the brain and the immune system, in addition to the continuing quest to understand addiction, future studies may be able to bring to light any long-term or permanent immune effects and the connection between those of the long-lasting or permanent behavioral changes in the nervous system.

#### *1.4.1.5 Cocaine Effects Summary*

Cocaine, while often considered to plague a single physiological system, is capable of eliciting a range of effects on both the nervous and immune systems, thereby creating a cascade of physiological responses. Many of the effects on the nervous system are due to modifications of dopamine signaling, though there is evidence of additional actions through the  $\sigma_1$  receptor, as well as receptors that are still to be identified. The modulation of the immune system by cocaine is highly dependent on dose and administration frequency, and although cocaine alone does not elicit an immune response, it may lead to activation of the immune system and production of

cytokines through alterations in serum proteins. When viewing the modulations of both the immune and nervous systems in light of the bi-directional communication network, it is likely that further regulatory interactions occur, specifically through stress hormones and immune-signaling molecules, producing a complex interaction network that leads to adaptations in gene transcription. While there is no published evidence of a permanent change in immune function as a result of either chronic or acute cocaine use, the long-lasting or permanent behavioral changes, in addition to the link between the brain and the immune system, lead one to speculate regarding this possibility. Immune adaptations could further explain the relationship between cocaine use and diseases and aging.

In order to best treat addiction, it is important to understand how drugs of addiction affect not only the brain, but also the immune system. Though the recent advances in developing vaccines against cocaine addiction<sup>198</sup> could serve to benefit many individuals, they focus on preventing the neural effects of the drug, ignoring the immune response to the drug-modified serum proteins (which begins as soon as cocaine enters the bloodstream) and subsequent neuro-immune signaling capable of perpetuating addictive effects. Yet these endeavors may serve to propel interest in the effects of cocaine on the immune system in addition to the neurological effects. Continuing to look at cocaine modulations on a systems level, thus further investigating the neuro-immune connection, could lead to additional treatment strategies that ameliorate the long-term or permanent changes associated with chronic drug use.

## 1.5 References

1. Rothberg, J. M. & Leamon, J. H. The development and impact of 454 sequencing. *Nature Biotechnology* **26**, 1117–1124 (2008).
2. Martin-Sanchez, F., Maojo, V. & Lopez-Campos, G. Integrating genomics into health information systems. *Methods Inf Med* **41**, 25–30 (2002).
3. Meyer, J. M. & Ginsburg, G. S. The path to personalized medicine. *Current Opinion in Chemical Biology* **6**, 434–438 (2002).
4. Kurian, K. M. *et al.* DNA chip technology, DNA chip technology. *The Journal of Pathology, The Journal of Pathology* **187**, 267, 267–271, 271 (1999).
5. Drews, J. Drug Discovery: A Historical Perspective. *Science* **287**, 1960–1964 (2000).
6. 10 Years on, 'The Genome Revolution Is Only Just Beginning'. *WIRED* at <http://www.wired.com/wiredscience/2010/03/genome-at-10/>
7. Collins, F. Has the revolution arrived? *Nature* **464**, 674–675 (2010).
8. Frazier, M. E., Johnson, G. M., Thomassen, D. G., Oliver, C. E. & Patrinos, A. Realizing the Potential of the Genome Revolution: The Genomes to Life Program. *Science* **300**, 290–293 (2003).
9. Sia, S. K. & Whitesides, G. M. Microfluidic devices fabricated in Poly(dimethylsiloxane) for biological studies. *ELECTROPHORESIS* **24**, 3563–3576 (2003).
10. Whitesides, G. M., Ostuni, E., Takayama, S., Jiang, X. & Ingber, D. E. SOFT LITHOGRAPHY IN BIOLOGY AND BIOCHEMISTRY. *Annu. Rev. Biomed. Eng.* **3**, 335–373 (2001).
11. Faley, S. *et al.* Microfluidic platform for real-time signaling analysis of multiple single T cells in parallel. *Lab Chip* **8**, 1700–1712 (2008).
12. Whitesides, G. M. The origins and the future of microfluidics. *Nature* **442**, 368–373 (2006).

13. Linder, V., Verpoorte, E., Rooij, N. F. de, Sigrist, H. & Thormann, W. Application of surface biopassivated disposable poly(dimethylsiloxane)/glass chips to a heterogeneous competitive human serum immunoglobulin G immunoassay with incorporated internal standard. *ELECTROPHORESIS* **23**, 740–749 (2002).
14. Rossier, J. S. & Girault, H. H. Enzyme linked immunosorbent assay on a microchip with electrochemical detection. *Lab Chip* **1**, 153–157 (2001).
15. Jiang, X., Ng, J. M. K., Stroock, A. D., Dertinger, S. K. W. & Whitesides, G. M. A Miniaturized, Parallel, Serially Diluted Immunoassay for Analyzing Multiple Antigens. *Journal of the American Chemical Society* **125**, 5294–5295 (2003).
16. Bernard, A., Michel, B. & Delamarche, E. Micromosaic Immunoassays. *Analytical Chemistry* **73**, 8–12 (2001).
17. Ismagilov, R. F., Ng, J. M. K., Kenis, P. J. A. & Whitesides, G. M. Microfluidic Arrays of Fluid–Fluid Diffusional Contacts as Detection Elements and Combinatorial Tools. *Analytical Chemistry* **73**, 5207–5213 (2001).
18. Doyle, P. S., Bibette, J., Bancaud, A. & Viovy, J.-L. Self-Assembled Magnetic Matrices for DNA Separation Chips. *Science* **295**, 2237 (2002).
19. Ren, X., Bachman, M., Sims, C., Li, G. P. & Allbritton, N. Electroosmotic properties of microfluidic channels composed of poly(dimethylsiloxane). *Journal of Chromatography B: Biomedical Sciences and Applications* **762**, 117–125 (2001).
20. Effenhauser, C. S., Bruin, G. J. M., Paulus, A. & Ehrat, M. Integrated Capillary Electrophoresis on Flexible Silicone Microdevices: Analysis of DNA Restriction Fragments and Detection of Single DNA Molecules on Microchips. *Analytical Chemistry* **69**, 3451–3457 (1997).
21. Ocvirk, G. *et al.* Electrokinetic control of fluid flow in native poly(dimethylsiloxane) capillary electrophoresis devices. *Electrophoresis* **21**, 107–115 (2000).
22. Sanders, J. C., Breadmore, M. C., Mitchell, P. S. & Landers, J. P. A simple PDMS-based electro-fluidic interface for microchip electrophoretic separations. *Analyst* **127**, 1558–1563 (2002).

23. Campbell, L. C., Wilkinson, M. J., Manz, A., Camilleri, P. & Humphreys, C. J. Electrophoretic manipulation of single DNA molecules in nanofabricated capillaries. *Lab Chip* **4**, 225–229 (2004).
24. Yao, S. *et al.* SDS capillary gel electrophoresis of proteins in microfabricated channels. *Proceedings of the National Academy of Sciences of the United States of America* **96**, 5372–5377 (1999).
25. Slentz, B. E., Penner, N. A., Lugowska, E. & Regnier, F. Nanoliter capillary electrochromatography columns based on collocated monolithic support structures molded in poly(dimethyl siloxane). *ELECTROPHORESIS* **22**, 3736–3743 (2001).
26. Chen, X., Wu, H., Mao, C. & Whitesides, G. M. A Prototype Two-Dimensional Capillary Electrophoresis System Fabricated in Poly(dimethylsiloxane). *Analytical Chemistry* **74**, 1772–1778 (2002).
27. Fu, A. Y., Spence, C., Scherer, A., Arnold, F. H. & Quake, S. R. A microfabricated fluorescence-activated cell sorter. *Nat Biotech* **17**, 1109–1111 (1999).
28. Deng, T., Prentiss, M. & Whitesides, G. M. Fabrication of magnetic microfiltration systems using soft lithography. *Appl. Phys. Lett.* **80**, 461–463 (2002).
29. Huh, D. *et al.* Use of Air-Liquid Two-Phase Flow in Hydrophobic Microfluidic Channels for Disposable Flow Cytometers. *Biomedical Microdevices* **4**, 141–149 (2002).
30. Leclerc, E., Sakai, Y. & Fujii, T. Microfluidic PDMS (Polydimethylsiloxane) Bioreactor for Large-Scale Culture of Hepatocytes. *Biotechnology Progress* **20**, 750–755 (2004).
31. Heo, J., Thomas, K. J., Seong, G. H. & Crooks, R. M. A Microfluidic Bioreactor Based on Hydrogel-Entrapped *E. coli*: Cell Viability, Lysis, and Intracellular Enzyme Reactions. *Analytical Chemistry* **75**, 22–26 (2003).
32. Mehta, G. *et al.* Quantitative measurement and control of oxygen levels in microfluidic poly(dimethylsiloxane) bioreactors during cell culture. *Biomedical Microdevices* **9**, 123–134 (2007).
33. Micheletti, M. & Lye, G. J. Microscale bioprocess optimisation. *Current Opinion in Biotechnology* **17**, 611–618 (2006).

34. Sud, D. *et al.* Optical imaging in microfluidic bioreactors enables oxygen monitoring for continuous cell culture. *J Biomed Opt* **11**, 050504 (2006).
35. Balagadde, F. K., You, L., Hansen, C. L., Arnold, F. H. & Quake, S. R. Long-Term Monitoring of Bacteria Undergoing Programmed Population Control in a Microchemostat. *Science* **309**, 137–140 (2005).
36. El-Ali, J., Sorger, P. K. & Jensen, K. F. Cells on chips. *Nature* **442**, 403–411 (2006).
37. Werdich, A. A. *et al.* A microfluidic device to confine a single cardiac myocyte in a sub-nanoliter volume on planar microelectrodes for extracellular potential recordings. *Lab Chip* **4**, 357–362 (2004).
38. Warnement, M. R., Faley, S. L., Wikswa, J. P. & Rosenthal, S. J. Quantum Dot Probes for Monitoring Dynamic Cellular Response: Reporters of T Cell Activation. *NanoBioscience, IEEE Transactions on* **5**, 268–272 (2006).
39. Ges, I. A. *et al.* Thin-film IrOx pH microelectrode for microfluidic-based microsystems. *Biosensors and Bioelectronics* **21**, 248–256 (2005).
40. Ges, I. A., Ivanov, B. L., Werdich, A. A. & Baudenbacher, F. J. Differential pH measurements of metabolic cellular activity in nl culture volumes using microfabricated iridium oxide electrodes. *Biosensors and Bioelectronics* **22**, 1303–1310 (2007).
41. Ges, I., Dzhura, I. & Baudenbacher, F. On-chip acidification rate measurements from single cardiac cells confined in sub-nanoliter volumes. *Biomedical Microdevices* **10**, 347–354 (2008).
42. Faley, S. L. *et al.* Microfluidic single cell arrays to interrogate signalling dynamics of individual, patient-derived hematopoietic stem cells. *Lab Chip* **9**, 2659–2664 (2009).
43. Duffy, D. C., McDonald, J. C., Schueller, O. J. A. & Whitesides, G. M. Rapid Prototyping of Microfluidic Systems in Poly(dimethylsiloxane). *Analytical Chemistry* **70**, 4974–4984 (1998).
44. Darby, S. G. *et al.* A metering rotary nanopump for microfluidic systems. *Lab Chip* **10**, 3218 (2010).

45. Kholodenko, B. N. Cell-signalling dynamics in time and space. *Nature Reviews Molecular Cell Biology* **7**, 165–176 (2006).
46. Tyson, J. J., Chen, K. C. & Novak, B. Sniffers, buzzers, toggles and blinkers: dynamics of regulatory and signaling pathways in the cell. *Current Opinion in Cell Biology* **15**, 221–231 (2003).
47. Ingalls, B. P. A Frequency Domain Approach to Sensitivity Analysis of Biochemical Networks. *J. Phys. Chem. B* **108**, 1143–1152 (2003).
48. Ferrell, J. E. & Xiong, W. Bistability in cell signaling: How to make continuous processes discontinuous, and reversible processes irreversible. *Chaos: An Interdisciplinary Journal of Nonlinear Science* **11**, 227–236 (2001).
49. Eungdamrong, N. J., Iyengar, R., Eungdamrong, N. J. & Iyengar, R. Modeling Cell Signaling Networks, Modeling Cell Signaling Networks. *Biology of the Cell, Biology of the Cell* **96, 96**, 355, 355–362, 362 (2004).
50. Huang, S., Eichler, G., Bar-Yam, Y. & Ingber, D. E. Cell Fates as High-Dimensional Attractor States of a Complex Gene Regulatory Network. *Phys. Rev. Lett.* **94**, 128701 (2005).
51. Szűcs, A., Elson, R. C., Rabinovich, M. I., Abarbanel, H. D. I. & Selverston, A. I. Nonlinear Behavior of Sinusoidally Forced Pyloric Pacemaker Neurons. *J Neurophysiol* **85**, 1623–1638 (2001).
52. Denker, M., Szucs, A., Pinto, R. D., Abarbanel, H. D. I. & Selverston, A. I. A network of electronic neural oscillators reproduces the dynamics of the periodically forced pyloric pacemaker group. *Biomedical Engineering, IEEE Transactions on* **52**, 792–798 (2005).
53. Abarbanel, H. D. I. & Rabinovich, M. I. Neurodynamics: nonlinear dynamics and neurobiology. *Current Opinion in Neurobiology* **11**, 423–430 (2001).
54. Montana, D. J. & Davis, L. Training feedforward neural networks using genetic algorithms. *Proceedings of the 11th international joint conference on Artificial intelligence - Volume 1* 762–767 (1989).at <<http://dl.acm.org/citation.cfm?id=1623755.1623876>>
55. Hastings, H. M. & Pikelney, R. Stochastic information processing in biological systems. *Biosystems* **15**, 155–168 (1982).

56. Regan, D. & Heron, J. R. Clinical Investigation of Lesions of the Visual Pathway: A New Objective Technique. *J Neurol Neurosurg Psychiatry* **32**, 479–483 (1969).
57. Regan, D. & Regan, M. P. Objective evidence for phase-independent spatial frequency analysis in the human visual pathway. *Vision Research* **28**, 187–191 (1988).
58. Regan, D. & Regan, M. P. Nonlinearity in human visual responses to two-dimensional patterns, and a limitation of fourier methods. *Vision Research* **27**, 2181–2183 (1987).
59. Regan, M. P., Regan, D. & He, P. An audio-visual convergence area in the human brain. *Experimental Brain Research* **106**, 485–487 (1995).
60. Gilon, P., Shepherd, R. M. & Henquin, J. C. Oscillations of Secretion Driven by Oscillations of Cytoplasmic Ca<sup>2+</sup> as Evidences in Single Pancreatic Islets. *J. Biol. Chem.* **268**, 22265–22268 (1993).
61. Pørksen, N. The in vivo regulation of pulsatile insulin secretion. *Diabetologia* **45**, 3–20 (2002).
62. Pørksen, N. *et al.* Pulsatile Insulin Secretion: Detection, Regulation, and Role in Diabetes. *Diabetes* **51**, 245S–254 (2002).
63. Bennett, M. R. *et al.* Metabolic gene regulation in a dynamically changing environment. *Nature* **454**, 1119–1122 (2008).
64. Miller, J., Nawarathna, D., Warmflash, D., Pereira, F. & Brownell, W. Dielectric Properties of Yeast Cells Expressed With the Motor Protein Prestin. *Journal of Biological Physics* **31**, 465–475 (2005).
65. Nawarathna, D. *et al.* SQUID-Based Biosensor for Probing Ion Transporters in Cell Suspensions and Tissue. *IEEE Transactions on Applied Superconductivity* **17**, 812–815 (2007).
66. Nawarathna, D. *et al.* Harmonic generation by yeast cells in response to low-frequency electric fields. *Phys. Rev. E* **73**, 051914 (2006).



67. Mettetal, J. T., Muzzey, D., Gomez-Uribe, C. & van Oudenaarden, A. The Frequency Dependence of Osmo-Adaptation in *Saccharomyces cerevisiae*. *Science* **319**, 482–484 (2008).
68. Zhang, X., Grimley, A., Bertram, R. & Roper, M. G. Microfluidic System for Generation of Sinusoidal Glucose Waveforms for Entrainment of Islets of Langerhans. *Analytical Chemistry* **82**, 6704–6711 (2010).
69. Bird, G. S., Rossier, M. F., Obie, J. F. & Putney, J. W. Sinusoidal Oscillations in Intracellular Calcium Requiring Negative Feedback by Protein Kinase C. *J. Biol. Chem.* **268**, 8425–8428 (1993).
70. Berthoumieux, H., Antoine, C., Jullien, L. & Lemarchand, A. Resonant response to temperature modulation for enzymatic dynamics characterization. *Phys. Rev. E* **79**, 021906 (2009).
71. Mosadegh, B. *et al.* Integrated elastomeric components for autonomous regulation of sequential and oscillatory flow switching in microfluidic devices. *Nature Physics* **6**, 433–437 (2010).
72. Azizi, F. & Mastrangelo, C. H. Generation of dynamic chemical signals with pulse code modulators. *Lab on a Chip* **8**, 907 (2008).
73. Zhang, X. & Roper, M. G. Microfluidic Perfusion System for Automated Delivery of Temporal Gradients to Islets of Langerhans. *Anal. Chem.* **81**, 1162–1168 (2008).
74. Cao, L., Zhang, X., Grimley, A., Lomasney, A. & Roper, M. Microfluidic multi-analyte gradient generator. *Analytical and Bioanalytical Chemistry* **398**, 1985–1991 (2010).
75. Yates, J. R. Mass spectrometry: from genomics to proteomics. *Trends in Genetics* **16**, 5–8 (2000).
76. Han, X. & Gross, R. W. Global analyses of cellular lipidomes directly from crude extracts of biological samples by ESI mass spectrometry: a bridge to lipidomics. *J. Lipid Res.* **44**, 1071–1079 (2003).
77. Zaia, J. Mass spectrometry of oligosaccharides. *Mass Spectrometry Reviews* **23**, 161–227 (2004).

78. Fenn, J. B., Mann, M., Meng, C. K., Wong, S. F. & Whitehouse, C. M. Electrospray ionization for mass spectrometry of large biomolecules. *Science* **246**, 64–71 (1989).
79. Karas, M. & Hillenkamp, F. Laser desorption ionization of proteins with molecular masses exceeding 10,000 daltons. *Analytical Chemistry* **60**, 2299–2301 (1988).
80. Aebersold, R. & Mann, M. Mass spectrometry-based proteomics. *Nature* **422**, 198–207 (2003).
81. Domon, B. & Aebersold, R. Mass Spectrometry and Protein Analysis. *Science* **312**, 212–217 (2006).
82. McLean, J. A., Ruotolo, B. T., Gillig, K. J. & Russell, D. H. Ion mobility–mass spectrometry: a new paradigm for proteomics. *International Journal of Mass Spectrometry* **240**, 301–315 (2005).
83. Ruotolo, B. T., McLean, J. A., Gillig, K. J. & Russell, D. H. Peak capacity of ion mobility mass spectrometry: the utility of varying drift gas polarizability for the separation of tryptic peptides. *Journal of Mass Spectrometry* **39**, 361–367 (2004).
84. Enders, J. R. *et al.* Monitoring real-time cellular response using an integrated microfluidics-MALDI/nESI-ion mobility-mass spectrometry platform. *IET Systems Biology In Review*,
85. McLean, J. A. The Mass-Mobility Correlation Redux: The Conformational Landscape of Anhydrous Biomolecules. *Journal of the American Society for Mass Spectrometry* **20**, 1775–1781 (2009).
86. Waters SYNAPT G2 HDMS. at <[www.waters.com](http://www.waters.com)>
87. Chan, J. H., Timperman, A. T., Qin, D. & Aebersold, R. Microfabricated Polymer Devices for Automated Sample Delivery of Peptides for Analysis by Electrospray Ionization Tandem Mass Spectrometry. *Analytical Chemistry* **71**, 4437–4444 (1999).
88. Jiang, Y., Wang, P.-C., Locascio, L. E. & Lee, C. S. Integrated Plastic Microfluidic Devices with ESI-MS for Drug Screening and Residue Analysis. *Analytical Chemistry* **73**, 2048–2053 (2001).

89. Kim, J.-S. & Knapp, D. R. Microfabrication of polydimethylsiloxane electrospray ionization emitters. *Journal of Chromatography A* **924**, 137–145 (2001).
90. Chiou, C.-H., Lee, G.-B., Hsu, H.-T., Chen, P.-W. & Liao, P.-C. Micro devices integrated with microchannels and electrospray nozzles using PDMS casting techniques. *Sensors and Actuators B: Chemical* **86**, 280–286 (2002).
91. Huikko, K. *et al.* Poly(dimethylsiloxane) electrospray devices fabricated with diamond-like carbon-poly(dimethylsiloxane) coated SU-8 masters. *Lab Chip* **3**, 67–72 (2003).
92. Mellors, J. S., Gorbounov, V., Ramsey, R. S. & Ramsey, J. M. Fully Integrated Glass Microfluidic Device for Performing High-Efficiency Capillary Electrophoresis and Electrospray Ionization Mass Spectrometry. *Analytical Chemistry* **80**, 6881–6887 (2008).
93. Krenková, J. & Foret, F. Immobilized microfluidic enzymatic reactors. *ELECTROPHORESIS* **25**, 3550–3563 (2004).
94. Lee, J., Soper, S. A. & Murray, K. K. Development of an efficient on-chip digestion system for protein analysis using MALDI-TOF MS. *Analyst* **134**, 2426–2433 (2009).
95. Kitano, H. Computational systems biology. *Nature* **420**, 206–210 (2002).
96. Bongard, J. & Lipson, H. Active Coevolutionary Learning of Deterministic Finite Automata. *J. Mach. Learn. Res.* **6**, 1651–1678 (2005).
97. Schmidt, M. & Lipson, H. Distilling Free-Form Natural Laws from Experimental Data. *Science* **324**, 81–85 (2009).
98. Wikswa, J. P. *et al.* Engineering challenges of BioNEMS: the integration of microfluidics, micro- and nanodevices, models and external control for systems biology. *IEE Proc., Nanobiotechnol.* **153**, 81–101 (2006).
99. King, R. D. *et al.* Functional genomic hypothesis generation and experimentation by a robot scientist. *Nature* **427**, 247–252 (2004).
100. King, R. D. *et al.* The Automation of Science. *Science* **324**, 85–89 (2009).

101. Soldatova, L. N., Clare, A., Sparkes, A. & King, R. D. An ontology for a Robot Scientist. *Bioinformatics* **22**, e464–471 (2006).
102. Hyman, S. E. Addiction to Cocaine and Amphetamine. *Neuron* **16**, 901–904 (1996).
103. Nutt, D., King, L. A., Saulsbury, W. & Blakemore, C. Development of a rational scale to assess the harm of drugs of potential misuse. *The Lancet* **369**, 1047–1053 (2007).
104. Substance Abuse and Mental Health Services Administration *Results from the 2008 National Survey on Drug Use and Health: National Findings*. (Office of Applied Studies: Rockville, MD, 2009).at <<http://oas.samhsa.gov/nsduh/2k8nsduh/2k8Results.cfm>>
105. Nuijs, A. L. N. van *et al.* Can cocaine use be evaluated through analysis of wastewater? A nation-wide approach conducted in Belgium. *Addiction* **104**, 734–741 (2009).
106. Mari, F. *et al.* Cocaine and heroin in waste water plants: A 1-year study in the city of Florence, Italy. *Forensic Science International* **189**, 88–92 (2009).
107. Goldstein, R. A., DesLauriers, C. & Burda, A. M. Cocaine: History, Social Implications, and Toxicity--A Review. *Disease-a-Month* **55**, 6–38 (2009).
108. Dams, R., Murphy, C. M., Lambert, W. E. & Huestis, M. A. Urine drug testing for opioids, cocaine, and metabolites by direct injection liquid chromatography/tandem mass spectrometry. *Rapid Communications in Mass Spectrometry* **17**, 1665–1670 (2003).
109. Warner, E. A. Cocaine Abuse. *Annals of Internal Medicine* **119**, 226–235 (1993).
110. Mikkelsen, S. & Ash, K. Adulterants causing false negatives in illicit drug testing. *Clin Chem* **34**, 2333–2336 (1988).
111. Jaffee, W. B., Trucco, E., Levy, S. & Weiss, R. D. Is this urine really negative? A systematic review of tampering methods in urine drug screening and testing. *Journal of Substance Abuse Treatment* **33**, 33–42 (2007).
112. Robbins, T. W. & Everitt, B. J. Drug addiction: bad habits add up. *Nature* **398**, 567–570 (1999).

113. Civelli, O., Bunzow, J. R. & Grandy, D. K. Molecular Diversity of the Dopamine Receptors. *Annu. Rev. Pharmacol. Toxicol.* **33**, 281–307 (1993).
114. Dalley, J. W. & Everitt, B. J. Dopamine receptors in the learning, memory and drug reward circuitry. *Seminars in Cell & Developmental Biology* **20**, 403–410 (2009).
115. Nestler, E. J. Molecular mechanisms of opiate and cocaine addiction. *Current Opinion in Neurobiology* **7**, 713–719 (1997).
116. Henry, D. J. & White, F. J. Repeated cocaine administration causes persistent enhancement of D1 dopamine receptor sensitivity within the rat nucleus accumbens. *Journal of Pharmacology and Experimental Therapeutics* **258**, 882–890 (1991).
117. Beveridge, T. J. R., Smith, H. R., Nader, M. A. & Porrino, L. J. Abstinence from Chronic Cocaine Self-Administration Alters Striatal Dopamine Systems in Rhesus Monkeys. *Neuropsychopharmacology* **34**, 1162–1171 (2008).
118. Everitt, B. J., Dickinson, A. & Robbins, T. W. The neuropsychological basis of addictive behaviour. *Brain Research Reviews* **36**, 129–138 (2001).
119. Hyman, S. E., Malenka, R. C. & Nestler, E. J. NEURAL MECHANISMS OF ADDICTION: The Role of Reward-Related Learning and Memory. *Annu. Rev. Neurosci.* **29**, 565–598 (2006).
120. Wise, R. A. & Kiyatkin, E. A. Differentiating the rapid actions of cocaine. *Nat Rev Neurosci* **12**, 479–484 (2011).
121. You, Z.-B., Wang, B., Zitzman, D., Azari, S. & Wise, R. A. A Role for Conditioned Ventral Tegmental Glutamate Release in Cocaine Seeking. *The Journal of Neuroscience* **27**, 10546–10555 (2007).
122. You, Z.-B., Wang, B., Zitzman, D. & Wise, R. A. Acetylcholine Release in the Mesocorticolimbic Dopamine System during Cocaine Seeking: Conditioned and Unconditioned Contributions to Reward and Motivation. *The Journal of Neuroscience* **28**, 9021–9029 (2008).
123. Rothman, R. B. & Baumann, M. H. Monoamine transporters and psychostimulant drugs. *European Journal of Pharmacology* **479**, 23–40 (2003).

124. Smirnov, M. S. & Kiyatkin, E. A. Cocaine action on peripheral, non-monoamine neural substrates as a trigger of electroencephalographic desynchronization and electromyographic activation following i.v. administration in freely moving rats. *Neuroscience* **165**, 500–514 (2010).
125. Unterwald, E. M., Rubinfeld, J. M. & Kreek, M. J. Repeated cocaine administration upregulates kappa and mu, but not delta, opioid receptors. *Neuroreport* **5**, 1613–1616 (1994).
126. Martin, W. R., Eades, C. G., Thompson, J. A., Huppler, R. E. & Gilbert, P. E. The effects of morphine- and nalorphine- like drugs in the nondependent and morphine-dependent chronic spinal dog. *Journal of Pharmacology and Experimental Therapeutics* **197**, 517–532 (1976).
127. D., B. V. Naltrexone fails to antagonize the  $\sigma$  effects of PCP and SKF 10,047 in the dog. *European Journal of Pharmacology* **92**, 269–274 (1983).
128. Su, T.-P. & Hayashi, T. Understanding the Molecular Mechanism of Sigma-1 Receptors: Towards A Hypothesis that Sigma-1 Receptors are Intracellular Amplifiers for Signal Transduction. *curr med chem* **10**, 2073–2080 (2003).
129. Hayashi, T. & Su, T.-P. Sigma-1 Receptor Chaperones at the ER- Mitochondrion Interface Regulate Ca<sup>2+</sup> Signaling and Cell Survival. *Cell* **131**, 596–610 (2007).
130. Maurice, T. & Su, T.-P. The pharmacology of sigma-1 receptors. *Pharmacology & Therapeutics* **124**, 195–206 (2009).
131. Su, T.-P. & Hayashi, T. Cocaine affects the dynamics of cytoskeletal proteins via sigma1 receptors. *Trends in Pharmacological Sciences* **22**, 456–458 (2001).
132. Hayashi, T. & Su, T.-P. [sigma]-1 receptor ligands: potential in the treatment of neuropsychiatric disorders. *CNS Drugs* **18.5**, 269 (2004).
133. Matsumoto, R. R., McCracken, K. A., Pouw, B., Zhang, Y. & Bowen, W. D. Involvement of sigma receptors in the behavioral effects of cocaine: evidence from novel ligands and antisense oligodeoxynucleotides. *Neuropharmacology* **42**, 1043–1055 (2002).

134. Liu, Y. & Matsumoto, R. R. Alterations in Fos-Related Antigen 2 and  $\sigma$ 1 Receptor Gene and Protein Expression Are Associated with the Development of Cocaine-Induced Behavioral Sensitization: Time Course and Regional Distribution Studies. *Journal of Pharmacology and Experimental Therapeutics* **327**, 187–195 (2008).
135. Liu, Y., Chen, G.-D., Lerner, M. R., Brackett, D. J. & Matsumoto, R. R. Cocaine Up-Regulates Fra-2 and  $\sigma$ -1 Receptor Gene and Protein Expression in Brain Regions Involved in Addiction and Reward. *Journal of Pharmacology and Experimental Therapeutics* **314**, 770–779 (2005).
136. Morin-Surun, M. P., Collin, T., Denavit-Saubié, M., Baulieu, E.-E. & Monnet, F. P. Intracellular  $\sigma$ 1 receptor modulates phospholipase C and protein kinase C activities in the brainstem. *Proceedings of the National Academy of Sciences of the United States of America* **96**, 8196–8199 (1999).
137. Hayashi, T. & Su, T.-P. Intracellular Dynamics of  $\sigma$ -1 Receptors ( $\sigma$ 1 Binding Sites) in NG108-15 Cells. *Journal of Pharmacology and Experimental Therapeutics* **306**, 726–733 (2003).
138. Monnet, F. P. Sigma-1 receptor as regulator of neuronal intracellular Ca<sup>2+</sup>: clinical and therapeutic relevance. *Biol. Cell* **97**, 873 (2005).
139. Su, T.-P., Hayashi, T. & Vaupel, D. B. When the Endogenous Hallucinogenic Trace Amine N,N-Dimethyltryptamine Meets the Sigma-1 Receptor. *Sci. Signal.* **2**, pe12 (2009).
140. Sabeti, J., Nelson, T. E., Purdy, R. H. & Gruol, D. L. Steroid pregnenolone sulfate enhances NMDA-receptor-independent long-term potentiation at hippocampal CA1 synapses: Role for L-type calcium channels and sigma-receptors. *Hippocampus* **17**, 349–369 (2007).
141. Martina, M., Turcotte, M.-E. B., Halman, S. & Bergeron, R. The sigma-1 receptor modulates NMDA receptor synaptic transmission and plasticity via SK channels in rat hippocampus. *The Journal of Physiology* **578**, 143–157 (2007).
142. Chen, L., Dai, X.-N. & Sokabe, M. Chronic administration of dehydroepiandrosterone sulfate (DHEAS) primes for facilitated induction of long-term potentiation via sigma 1 ([sigma]1) receptor: Optical imaging study in rat hippocampal slices. *Neuropharmacology* **50**, 380–392 (2006).

143. Hayashi, T. & Su, T.-P. Regulating ankyrin dynamics: Roles of sigma-1 receptors. *Proceedings of the National Academy of Sciences of the United States of America* **98**, 491–496 (2001).
144. Watson, E. S., Murphy, J. C., ElSohly, H. N., ElSohly, M. A. & Turner, C. E. Effects of the administration of coca alkaloids on the primary immune responses of mice: Interaction with [Delta]9-tetrahydrocannabinol and ethanol. *Toxicology and Applied Pharmacology* **71**, 1–13 (1983).
145. Bagasra, O. & Forman, L. Functional analysis of lymphocytes subpopulations in experimental cocaine abuse. I. Dose-dependent activation of lymphocyte subsets. *Clinical and Experimental Immunology* **77**, 289–293 (1989).
146. Roth, M. D., Whittaker, K. M., Choi, R., Tashkin, D. P. & Baldwin, G. C. Cocaine and {sigma}-1 receptors modulate HIV infection, chemokine receptors, and the HPA axis in the huPBL-SCID model. *J Leukoc Biol* **78**, 1198–1203 (2005).
147. Chao, C. *et al.* Recreational drug use and T lymphocyte subpopulations in HIV-uninfected and HIV-infected men. *Drug and Alcohol Dependence* **94**, 165–171 (2008).
148. Klein, T. W. *et al.* Cocaine suppresses proliferation of phytohemagglutinin-activated human peripheral blood T-cells. *International Journal of Immunopharmacology* **15**, 77–86 (1993).
149. Piccotti, J. R., Brissette-Storkus, C. S., Chambers, W. H. & Bricker, J. D. Suppression of splenic T lymphocyte proliferation by acute cocaine administration. *Life Sciences* **61**, 967–976 (1997).
150. Faraj, B. A., Olkowski, Z. L. & Jackson, R. T. A cocaine-sensitive active dopamine transport in human lymphocytes. *Biochemical Pharmacology* **50**, 1007–1014 (1995).
151. Baldwin, G. C., Roth, M. D. & Tashkin, D. P. Acute and chronic effects of cocaine on the immune system and the possible link to AIDS. *Journal of Neuroimmunology* **83**, 133–138 (1998).
152. Gardner, B. *et al.* Cocaine modulates cytokine and enhances tumor growth through sigma receptors. *Journal of Neuroimmunology* **147**, 95–98 (2004).



153. Gan, X. *et al.* Cocaine Infusion Increases Interferon-[gamma] and Decreases Interleukin-10 in Cocaine-Dependent Subjects. *Clinical Immunology and Immunopathology* **89**, 181–190 (1998).
154. Pellegrino, T. & Bayer, B. M. In vivo effects of cocaine on immune cell function. *Journal of Neuroimmunology* **83**, 139–147 (1998).
155. Kubera, M. *et al.* The effect of cocaine sensitization on mouse immunoreactivity. *European Journal of Pharmacology* **483**, 309–315 (2004).
156. Pellegrino, T. C., Dunn, K. L. & Bayer, B. M. Mechanisms of cocaine-induced decreases in immune cell function. *International Immunopharmacology* **1**, 665–675 (2001).
157. Jeong, T. C. *et al.* Immunosuppression induced by acute exposure to cocaine is dependent on metabolism by cytochrome P-450. *Journal of Pharmacology and Experimental Therapeutics* **276**, 1257–1265 (1996).
158. Van Dyke, C., Barash, P., Jatlow, P. & Byck, R. Cocaine: plasma concentrations after intranasal application in man. *Science* **191**, 859–861 (1976).
159. Deng, S.-X., Bharat, N., Fischman, M. C. & Landry, D. W. Covalent modification of proteins by cocaine. *Proceedings of the National Academy of Sciences* **99**, 3412–3416 (2002).
160. Roth, M. D. *et al.* Cocaine Enhances Human Immunodeficiency Virus Replication in a Model of Severe Combined Immunodeficient Mice Implanted with Human Peripheral Blood Leukocytes. *The Journal of Infectious Diseases* **185**, 701–705 (2002).
161. Zhu, L. X. *et al.* IL-10 Mediates Sigma1 Receptor-Dependent Suppression of Antitumor Immunity. *J Immunol* **170**, 3585–3591 (2003).
162. Xu, W., Flick, T., Mitchel, J., Knowles, C. & Ault, K. Cocaine effects on immunocompetent cells: an observation of in vitro cocaine exposure. *International Journal of Immunopharmacology* **21**, 463–472 (1999).
163. Fischman, M. W., Schuster, C. R., Javaid, J., Hatano, Y. & Davis, J. Acute tolerance development to the cardiovascular and subjective effects of cocaine. *Journal of Pharmacology and Experimental Therapeutics* **235**, 677–682 (1985).

164. Pitts, D. K., Udom, C. E. & Marwah, J. Cardiovascular effects of cocaine in anesthetized and conscious rats. *Life Sciences* **40**, 1099–1111 (1987).
165. Foltin, R. W. & Fischman, M. W. Smoked and intravenous cocaine in humans: acute tolerance, cardiovascular and subjective effects. *Journal of Pharmacology and Experimental Therapeutics* **257**, 247–261 (1991).
166. Mendelson, M. D., Sholar, M., Mello, P. D., Teoh, M. D. & Sholar, J. W. Cocaine Tolerance: Behavioral, Cardiovascular, and Neuroendocrine Function in Men. *Neuropsychopharmacology* **18**, 263–271 (1998).
167. Karch, S. B. Cocaine Cardiovascular Toxicity. *Southern Medical Journal* **98**, 794 (2005).
168. Restrepo, C. *et al.* Cardiovascular complications of cocaine: Imaging findings. *Emergency Radiology* **16**, 11–19 (2009).
169. Knuepfer, M. M. Cardiovascular disorders associated with cocaine use: myths and truths. *Pharmacology & Therapeutics* **97**, 181–222 (2003).
170. Afonso, L., Mohammad, T. & Thatai, D. Crack Whips the Heart: A Review of the Cardiovascular Toxicity of Cocaine. *The American Journal of Cardiology* **100**, 1040–1043 (2007).
171. Lange, R. A. & Hillis, L. D. Cardiovascular Complications of Cocaine Use. *N Engl J Med* **345**, 351–358 (2001).
172. Reece, A. Evidence of accelerated ageing in clinical drug addiction from immune, hepatic and metabolic biomarkers. *Immunity & Ageing* **4**, 6 (2007).
173. Rissin, D. M. *et al.* Single-molecule enzyme-linked immunosorbent assay detects serum proteins at subfemtomolar concentrations. *Nature Biotechnology* **28**, 595–599 (2010).
174. Berke, J. D. & Hyman, S. E. Addiction, Dopamine, and the Molecular Mechanisms of Memory. *Neuron* **25**, 515–532 (2000).
175. Robinson, T. E. & Berridge, K. C. The neural basis of drug craving: an incentive-sensitization theory of addiction. *Brain Res. Brain Res. Rev* **18**, 247–291 (1993).

176. Self, D. W. & Nestler, E. J. Molecular Mechanisms of Drug Reinforcement and Addiction. *Annu. Rev. Neurosci.* **18**, 463–495 (1995).
177. Kuhar, M. J. & Pilotte, N. S. Neurochemical changes in cocaine withdrawal. *Trends in Pharmacological Sciences* **17**, 260–264 (1996).
178. Kalivas, P. W. & Stewart, J. Dopamine transmission in the initiation and expression of drug- and stress-induced sensitization of motor activity. *Brain Res. Brain Res. Rev* **16**, 223–244 (1991).
179. De Vries, T. J., Schoffelmeer, A. N. M., Binnekade, R., Mulder, A. H. & Vanderschuren, L. J. M. J. Drug induced reinstatement of heroin- and cocaine- seeking behaviour following long-term extinction is associated with expression of behavioural sensitization. *European Journal of Neuroscience* **10**, 3565–3571 (1998).
180. Romieu, P. *et al.* The sigma 1 ( $\sigma_1$ ) receptor activation is a key step for the reactivation of cocaine conditioned place preference by drug priming. *Psychopharmacology* **175**, 154–162 (2004).
181. Ecke, L. E. *et al.* CREB-Mediated Alterations in the Amygdala Transcriptome: Coordinated Regulation of Immune Response Genes Following Cocaine. *The International Journal of Neuropsychopharmacology* **14**, 1111–1126 (2011).
182. Maier, S. F. & Watkins, L. R. Cytokines for psychologists: implications of bidirectional immune-to-brain communication for understanding behavior, mood, and cognition. *Psychol Rev* **105**, 83–107 (1998).
183. Anisman, H. Cascading effects of stressors and inflammatory immune system activation: implications for major depressive disorder. *J Psychiatry Neurosci* **34**, 4–20 (2009).
184. Sternberg, E. M. Neural regulation of innate immunity: a coordinated nonspecific host response to pathogens. *Nat Rev Immunol* **6**, 318–328 (2006).
185. Tilders, J. H. & Schmidt, E. D. Cross-Sensitization Between Immune And Non-Immune Stressors. *Cytokines, Stress, and Depression* 179–197 (1999).at  
<[http://dx.doi.org/10.1007/978-0-585-37970-8\\_11](http://dx.doi.org/10.1007/978-0-585-37970-8_11)>

186. Goeders, N. E. The HPA axis and cocaine reinforcement. *Psychoneuroendocrinology* **27**, 13–33 (2002).
187. Goeders, N. E. A neuroendocrine role in cocaine reinforcement. *PSYCHONEUROENDOCRINO* **22**, 237–259 (1997).
188. BIENVENU, O. & GOEDERS, N. CHRONIC COCAINE ADMINISTRATION ALTERS CORTICOTROPIN-RELEASING FACTOR RECEPTORS IN THE RAT-BRAIN. *BRAIN RES* **531**, 322–328 (1990).
189. NEGUS, B. & HEESCH, C. EFFECTS OF COCAINE ON CORTISOL SECRETION IN HUMANS. *AM J MED SCI* **310**, 61–64 (1995).
190. Ambroggi, F. *et al.* Stress and addiction: glucocorticoid receptor in dopaminergic neurons facilitates cocaine seeking. *Nat Neurosci* **12**, 247–249 (2009).
191. Avila, A. H., Alonzo, N. C. & Bayer, B. M. Effects of Cocaine and Morphine Withdrawal on the Immune Response. *Infectious Diseases and Substance Abuse* 1–11 (2005).at <[http://dx.doi.org/10.1007/0-306-48688-1\\_1](http://dx.doi.org/10.1007/0-306-48688-1_1)>
192. Avila, A. H., Morgan, C. A. & Bayer, B. M. Stress-Induced Suppression of the Immune System after Withdrawal from Chronic Cocaine. *Journal of Pharmacology and Experimental Therapeutics* **305**, 290–297 (2003).
193. Avila, A. H., Alonzo, N. C. & Bayer, B. M. Immune cell activity during the initial stages of withdrawal from chronic exposure to cocaine or morphine. *Journal of Neuroimmunology* **147**, 109–113 (2004).
194. Johnson, T. R., Knisely, J. S., Christmas, J. T., Schnoll, S. H. & Ruddy, S. Changes in Immunologic Cell Surface Markers during Cocaine Withdrawal in Pregnant Women. *Brain, Behavior, and Immunity* **10**, 324–336 (1996).
195. Hutchinson, M. R. *et al.* Exploring the Neuroimmunopharmacology of Opioids: An Integrative Review of Mechanisms of Central Immune Signaling and Their Implications for Opioid Analgesia. *Pharmacological Reviews* **63**, 772–810 (2011).
196. Gan, X. *et al.* Cocaine Enhances Brain Endothelial Adhesion Molecules and Leukocyte Migration. *Clinical Immunology* **91**, 68–76 (1999).

197. PACIFICI, R. *et al.* Cell-Mediated Immune Response in MDMA Users After Repeated Dose Administration. *Annals of the New York Academy of Sciences* **965**, 421–433 (2002).
198. Hicks, M. J. *et al.* Cocaine Analog Coupled to Disrupted Adenovirus: A Vaccine Strategy to Evoke High-titer Immunity Against Addictive Drugs. *Mol Ther* **19**, 612–619 (2011).

## CHAPTER II

### 2 REAL-TIME CELLULAR EXOMETABOLOME ANALYSIS WITH A MICROFLUIDIC-MASS SPECTROMETRY PLATFORM

Christina C. Marasco<sup>1,2,3</sup>, Jeffrey R. Enders<sup>1,2,4</sup>, Kevin T. Seale<sup>1,2,3</sup>, John A. McLean<sup>1,4</sup>,  
and John P. Wikswo<sup>1,2,3,5</sup>

<sup>1</sup>Vanderbilt Institute for Integrative Biosystems Research and Education

<sup>2</sup>The Searle Systems Biology and Bioengineering Undergraduate Research Experience

<sup>3</sup>Department of Biomedical Engineering

<sup>4</sup>Department of Chemistry, Vanderbilt Institute of Chemical Biology

<sup>5</sup>Departments of Physics & Astronomy and Molecular Physiology & Biophysics

Vanderbilt University, Nashville, TN

## 2.1 Abstract

The inherent complexity of biological systems inhibits predictability, and therefore understanding, on levels ranging from cells to systems and even to whole organisms. This complexity presents challenges to the study of systems at the cellular level that lead to conflicting and often unexplainable results. For significant progress in the biological revolution to endure, technological innovation must precede and stimulate biological advancement. Herein is described such a technological progression capable of expanding the palette of cell biology techniques. Using a combination of microfluidics, online desalting, and nanoelectrospray ionization-ion mobility-mass spectrometry (nESI-IM-MS) technologies, a platform adept at the sampling of the cellular microenvironment with robust temporal specificity has been constructed. The cellular response to stimuli in the microenvironment, in conjunction with the cell's metabolic processes, results in the secretion and excretion of a suite of biomolecules, known as the exometabolome, for the purpose of communication with other cells or tissues and elimination of waste materials. Naïve and cocaine-experienced T cell metabolism of cocaine is used as an exemplary system to confirm the capability of the platform, highlight its potential for metabolite discovery applications, and explore immunological memory of T cell drug exposure.

## 2.2 Introduction

Cellular response is a complex phenomenon that manifests both physically and chemically. While physical responses can most often be analyzed visually, chemical responses are difficult to characterize even with modern detection methods. Adding to the difficulty is the influence of timing when dealing with cellular response. When responding to a biochemically altering stimulus, such as naïve T cell response to an antigen presented by a dendritic cell, a cell undergoes a series of biochemical pathway shifts that allow it to adapt to its new conditioned state. The cell's temporal response, therefore, provides insight into the interspersed pathway shifts that occur throughout the various stages of stimulus exposure. Temporal response is especially relevant to toxicology, where, despite experiencing a toxin and undergoing numerous metabolic shifts, an organism may not show observable external symptoms until much later, when effective treatments are no longer as useful.

Nonetheless, time remains a largely underappreciated or neglected variable in most comprehensive cellular response experiments, not as much for its perceived lack of value as for its difficulty of precise temporal resolution and control of measurements. Biological measurements typically take one of two forms; either they sample a small number of targets very frequently (as in immunoassay or fluorescence measurements, *e.g.*) or they sample a plethora of targets over a broad time span (*e.g.*, proteomic workup). The limitations of current methodological strategies and detection technologies stymie the combination of these two approaches. The most comprehensive analysis would track as many analytes as possible and sample these analytes as frequently as possible to capture the truly dynamic properties of metabolic responses. As the frequency of sample collection is increased, previously unidentified patterns in signal response may begin to emerge, according to the Shannon-Nyquist theorem, which states that in order to properly characterize a pattern containing a frequency of  $Y$ , the



sampling must occur at an interval greater than  $1/(2Y)$ . Also, increasing the sampling frequency may reduce the possibility of aliasing, wherein rapidly varying phenomena are undersampled in violation of the Shannon/Nyquist theorem to produce misleading results.

With the approach in place, a major logistical problem still remains: how does one sample a biological system multiple times over the course of an experiment without destroying, or even perturbing, that system? The exometabolome, or suite of biomolecules that are secreted or excreted from a cell into the surrounding matrix, represents a promising target. The exometabolome has been demonstrated as a viable indicator of internal cellular processes and can be easily assessed without any disturbance of the system from which it originates<sup>1</sup>. Changes in exometabolomic species transport provide information on the current state of the cell population, which can lead to a more thorough understanding of the particular cell's biology and to the ability to control the cell's behavior.

The cell is constantly surveilling the surrounding environment. Perceived changes in this microenvironment lead to alterations of intracellular and intercellular signaling, which in turn lead to shifts in gene regulation and modifications in protein and metabolite production. Depending on the signal received, the intracellular processes enacted may lead to the secretion of another signaling factor to extend the complex web of communication. These signaling factors are produced by a given cell for communication with 1) nearby cells of the same type (autocrine signaling), 2) adjacent cells (juxtacrine signaling), 3) nearby cells of a different type (paracrine signaling), and 4) distant cells (endocrine signaling). The exometabolome not only includes traditional signaling molecules, but also enzymatically produced metabolites of xenobiotics (*i.e.*, drugs, toxins) introduced to cells.

The Vanderbilt Institute for Integrative Biosystems Research and Education (VIIBRE) Multitrap Nanophysiometer (MTNP) is a polydimethylsiloxane (PDMS) microfluidic device that

functions as a miniature bioreactor. In contrast to traditional cell biology techniques that often require cellular populations on the order of  $>10^8$ , the MTNP allows for studies on small populations of cells or simple organisms ( $<10^5$ ). The MTNP has been used for long-term optical measurements of the dynamic behavior of cells, including fluorescent labeling of cells to determine type and activation state and detect signaling dynamics<sup>2-4</sup>. This device provides a framework on which to study numerous cells, *i.e.*, T cells, beta cells, and breast cancer cells, as it traps both non-adherent and adherent cells with structural barriers instead of with chemical surface modification that may cause cells to be exposed to higher shear stresses resulting from direct contact with fluid flow. The MTNP is well suited to detect secreted molecules in cellular effluent, and it is also unique in its ability to provide a system for investigating the dynamic response of a cell population to a stimulus. The constant perfusion design of the microfluidic bioreactor gives rise to a platform component capable of real-time alteration and control of the cellular microenvironment, in addition to providing an opportunity for monitoring the effluent output from the device.

The use of a biological model for testing the instrumentation platform does have a major downside in the form of potential loss of metabolite signal due to adsorption to PDMS bioreactor surfaces. Rectification of these types of issues requires changing the microfluidic device material or modification of PDMS surface properties. Switching device materials, and thus the techniques for producing such devices, often requires substantial changes in infrastructure as well as loss of desirable PDMS properties such as optical clarity and low feature size. Surface modification is more plausible, as procedures can be added onto existing fabrication or experimental methods. A variety of types of surface modification of PDMS microfluidic devices have been investigated, such as chemical vapor deposition, sol-gel coating, silanization, surfactant coating and dynamic coating (reviewed elsewhere<sup>5,6</sup>). Due to the nature

of this combined technology platform with mass spectrometry downstream of the microfluidic device, care must be exercised in the selection of a surface modification method. The presence of species in the bioreactor effluent necessary for the alteration of the PDMS surface can lead to complications in the detection of desired cell secretions due to issues of dynamic range. Instability of species used in surface modification can additionally lead to adsorption of secreted cellular materials to PDMS. A stable, inert coating is crucial for downstream mass spectrometry. Surfactants and dynamic coating methods are not appropriate for this application as the presence of electrostatically bound polymer or added analytes to the solution are not compliant with detecting low levels of cellular signals. One method leading to a covalently bound surface modifier is silanization. Though silanes are often deposited on surfaces through chemical vapor deposition and can result in the production of chlorine gas, ethoxy- and methoxy-silanes can be purchased in a liquid form, resulting in ease of application to PDMS surfaces for the prevention of non-specific adsorption.

The complexity of biological samples often overwhelms standard screening techniques seeking to discover biomarkers of disease or rapidly assess drug efficacy. This unique problem warrants an analytical technique capable of both rapid screening of samples and sufficient sensitivity to account for the many analytes in low abundance that typically comprise metabolomic and signaling experiments, which often either defy detection or appear collectively as chemical noise. The use of mass spectrometry (MS) as the leading detection method of proteomic<sup>7</sup>, lipidomic<sup>8</sup>, and glycomic<sup>9</sup> studies has led to many advances in elucidating the complexity of the cell.

The combination of constant microfluidic perfusion bioreactors with mass spectrometry has the potential to rapidly screen cell effluent for secreted species indicative of internal metabolic perturbations. Several studies have taken on the challenge of integrating these

technologies to produce a powerful analytical platform. In an early experiment, Chan *et al.* verified that using PDMS bioreactor devices to transfer samples into the electrospray ionization mass spectrometer (ESI-MS) did not contaminate the samples<sup>10</sup>. On-chip ultrafiltration and analyte pre-concentration for high-throughput small molecule screening with ESI-MS were performed with the resulting detection sensitivity shown to increase by one to two orders of magnitude over off-chip screening strategies<sup>11</sup>. A significant impairment in coupling cellular bioreactor microfluidic devices with online-MS is in the suppression of signals of interest by salts present in biological samples. To combat this problem, some form of desalting is typically performed offline, using either a solid phase extraction (SPE) column and vacuum manifold or some form of liquid chromatography. These techniques desalt samples by providing a functionalized surface for which salts and analytes have differing affinities. For example, liquid chromatography (LC) typically uses C18 columns, which provide good affinity binding sites for non-polar molecules but lack sufficient interaction prospects for salts, thereby allowing for an aqueous rinse to clear the column of salts and a subsequent organic elution of analytes without the suppressing contributions from salts. These methods, while providing an efficient means of desalination, come at the expense of temporal resolution, and they are not designed for online analysis. One recent development in the online desalting of effluent from a microfluidic bioreactor is the work of Chen *et al.*, which incorporates a packed micro-solid phase extraction column<sup>12</sup>.

We have previously demonstrated the ability to rapidly desalt a continuous sample stream using online SPE<sup>13</sup>. This work directly translates to the processing of continuous sample streams originating from a MTNP. Using online SPE for such applications provides a surface for which analytes of interest have affinities but unwanted salts do not. This allows for variable duration periods of pre-concentration of the analytes.

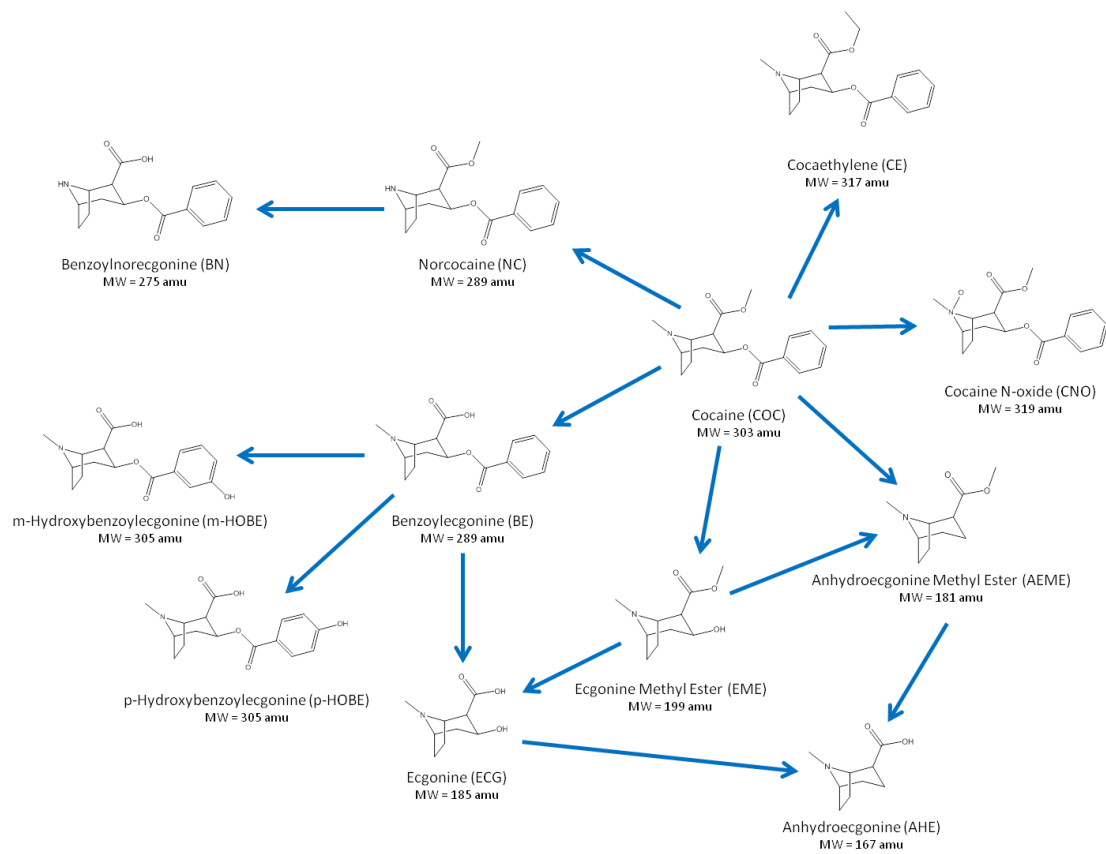


Figure 2.1 Cocaine metabolic pathways. Each compound is labeled with name, abbreviation and molecular weight.

As an initial proof of concept experiment for this integrated platform, we selected cellular memory of drug exposure, specifically Jurkat T cell memory of cocaine, for ease in identification of known drug metabolites and for its unique biological information. The choice of cell type was based upon cocaine's classification as an immunosuppressive agent, whether by mechanisms of direct and/or indirect actions on immune cells. Findings from experiments tying cocaine to immune function suppression have been contradictory at times<sup>14-18</sup>, most likely because of the complex biological systems under investigation and wide variety of experimental procedures. A major hurdle in determining these mechanisms is the lack of an assay capable of tightly controlled environmental parameters, temporal robustness to avoid loss of intermittent

changes, and multi-parameter sampling for unique evidence of experimental variable interconnection. The platform proposed herein allows for such an assay to be conducted. Through the comparison of naïve Jurkat T cells and those with prior cocaine exposure on this platform, differences in cocaine metabolism (general pathways shown in Figure 2.1) may be detected. Figure 2.2 demonstrates the experimental concept. Exposure of a naïve cell to cocaine may lead to a certain exometabolomic profile which defines the state of the cell. However, when a cell with prior cocaine experience receives a subsequent dose, the exometabolomic profile may either be identical to that of the naïve cell under exposure or distinguish the cell as unique. With a near real-time readout of cellular metabolic events on our integrated

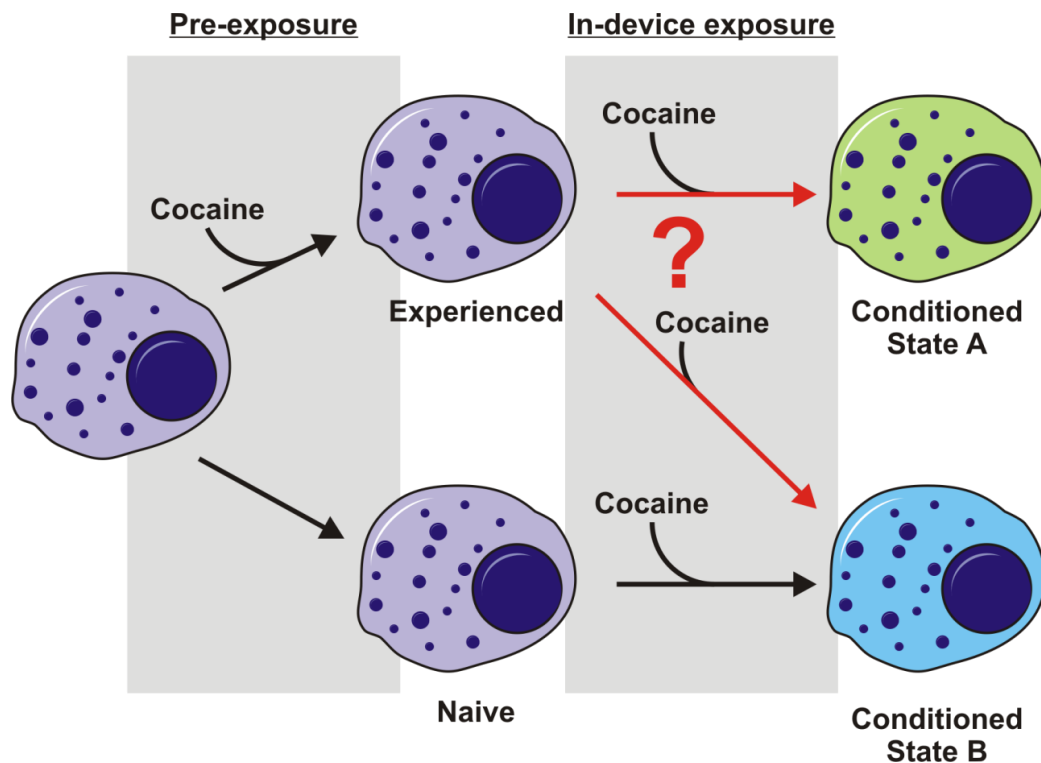


Figure 2.2 Experimental Scheme showing the potential cell fates (in terms of exometabolomic profiles) demonstrated as color change in the above image for naïve and cocaine-experienced cells upon exposure to cocaine in a microfluidic bioreactor.

microfluidic-solid phase extraction-ion mobility-mass spectrometry platform, it may be possible to determine variations in exometabolomic profiles that will provide evidence of cellular memory of cocaine exposure.

## 2.3 Methods

### 2.3.1 Microfluidic Bioreactor Design and Fabrication

The VIIBRE Multitrap Nanophysiometer (MTNP) was previously designed in AutoCAD and converted to a chrome mask on glass (Advance Reproductions, North Andover, MA). A silicon master was produced through photolithography methods which include spinning a negative photoresist, SU-8, onto silicon wafers, exposing them to UV light through the desired mask to crosslink the SU-8, then developing to remove non-cross-linked polymer<sup>19</sup>. Polydimethylsiloxane (PDMS) (Sylgard 184 Elastomer Kit, Dow Corning, Midland, MI) was then cast onto the silicon and SU-8 master, cured, and removed from the master. Inlet and outlet ports were punched and PDMS replicas were bonded to glass coverslips by O<sub>2</sub> plasma treatment (Harrick Plasma Cleaner, Ithaca, NY). A representation of this fabrication method is shown in Figure 2.3.

### 2.3.2 PDMS Surface Modification

Liquid 2-[methoxy(polyethyleneoxy)<sub>6-9</sub>propyl]trimethoxysilane (PEG-silane) was obtained from Gelest (Morrisville, PA). Immediately following plasma treatment, devices were intubated and a 2% solution of PEG-silane in 95% ethanol, 5% H<sub>2</sub>O, and 11mM acetic acid was injected until the device interior was filled. Devices were allowed to site at room temperature for 10 minutes followed by a rinse with ethanol, then water. A final incubation on a hot plate at

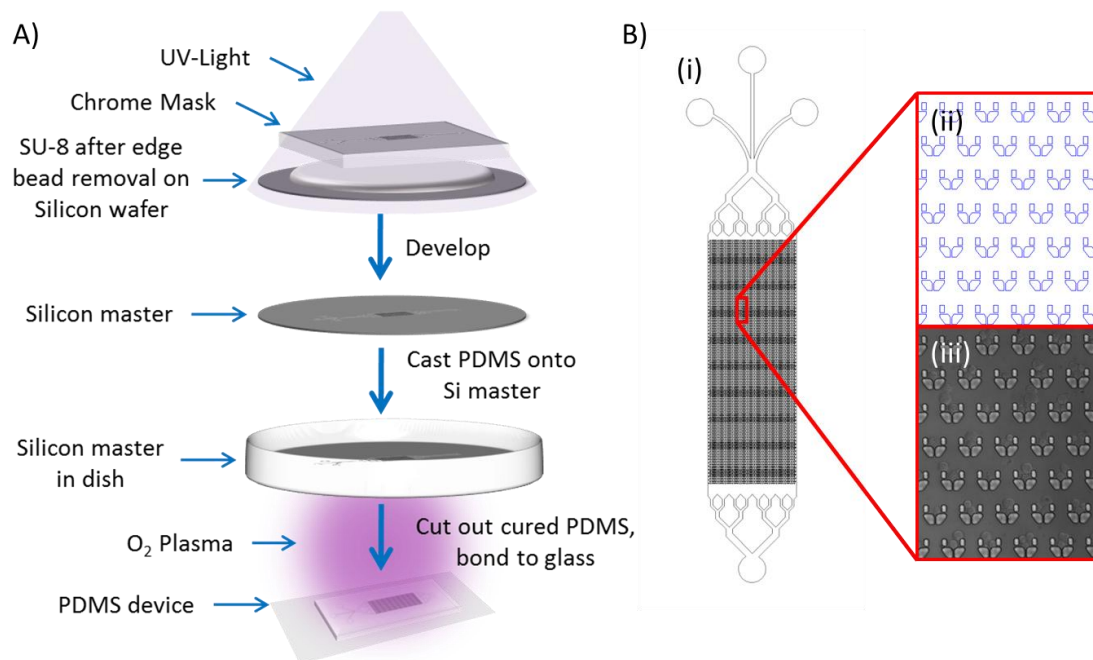


Figure 2.3 A) Microfluidic device fabrication procedure involving photolithography and replica molding techniques. B) Design of the MTNP (i) with 18 μm x 12 μm cell traps (ii) capable of trapping 2-3 cells each (iii) in a device with a 234 nL volume and 7056 cells traps.

110°C for 10 minutes was then performed to evaporate any remaining solvent and complete the surface modification. Figure 2.4 portrays the steps in the covalent surface modification of PDMS.

After at least 24 hours at room temperature, each device was perfused with fluorescently labeled insulin at a rate of 500 nL/min for 30 minutes and then rinsed with Ringer's buffer (118 mM NaCl, 5.4 mM KCl, 2.5 mM CaCl<sub>2</sub>, 1.2 mM MgSO<sub>4</sub>, 1.2 mM KH<sub>2</sub>PO<sub>4</sub>, 20 mM HEPES) for another 30 minutes. Images were collected every 15 seconds during the perfusion and rinsing stages with an inverted Nikon Eclipse Ti-e fitted with a 495 nm/521 nm excitation/emission filter set for fluorescent imaging of adsorbed insulin. Images were aligned and processed with Image J for comparison of total fluorescence intensity.



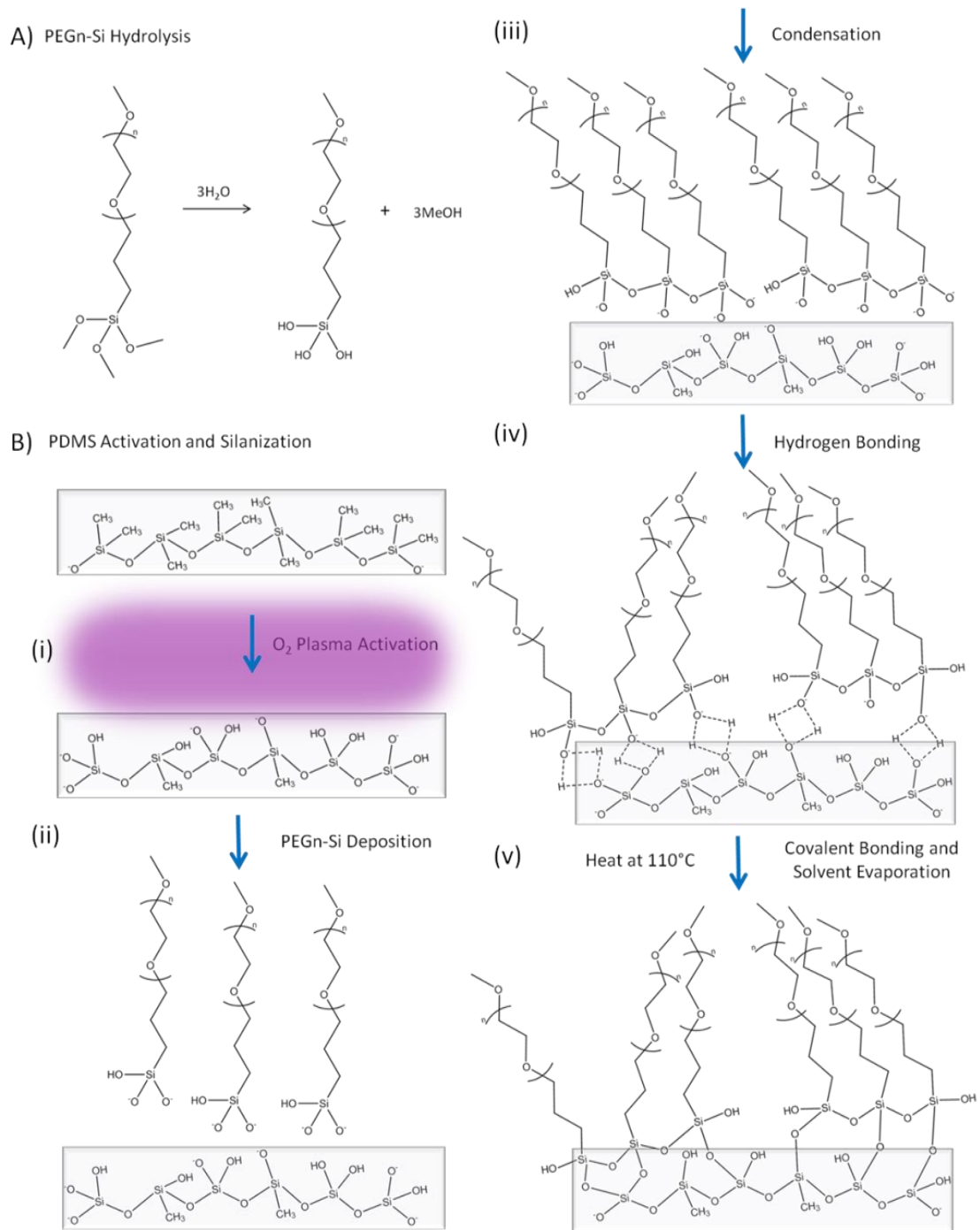


Figure 2.4 PDMS Silanization scheme showing hydrolysis of methoxy group from PEGn trimethoxysilane to form silanol groups (A) and the steps of PDMS activation (B(i)), silane deposition (B(ii)), condensation of the silane into chains (B(iii)), hydrogen bond formation between silanol and oxidized PDMS surface (B(iv)) and covalent bond formation between silane and PDMS surface (B(v)).

### 2.3.3 Cell Culture and “In Culture” Cocaine Exposure

Jurkat T cells (clone E6-1, TIB-152) (ATCC, Manassas, VA) were cultured in 90% RPMI 1640, 10% fetal bovine serum (FBS, heat inactivated) (Lonza, Allendale, NJ) at 37°C, 5% CO<sub>2</sub> according to the manufacturer’s instructions.

In-culture cocaine exposure experiments were performed as follows (Figure 2.5). Two populations of Jurkat T cells (passage 6, 2 million cells/ml, 500 µL, in biological triplicate) from the same culture flask were added to two separate microcentrifuge tubes. Both tubes were centrifuged at 200 × g for 2 minutes and supernatant was removed. Cells in tube one were

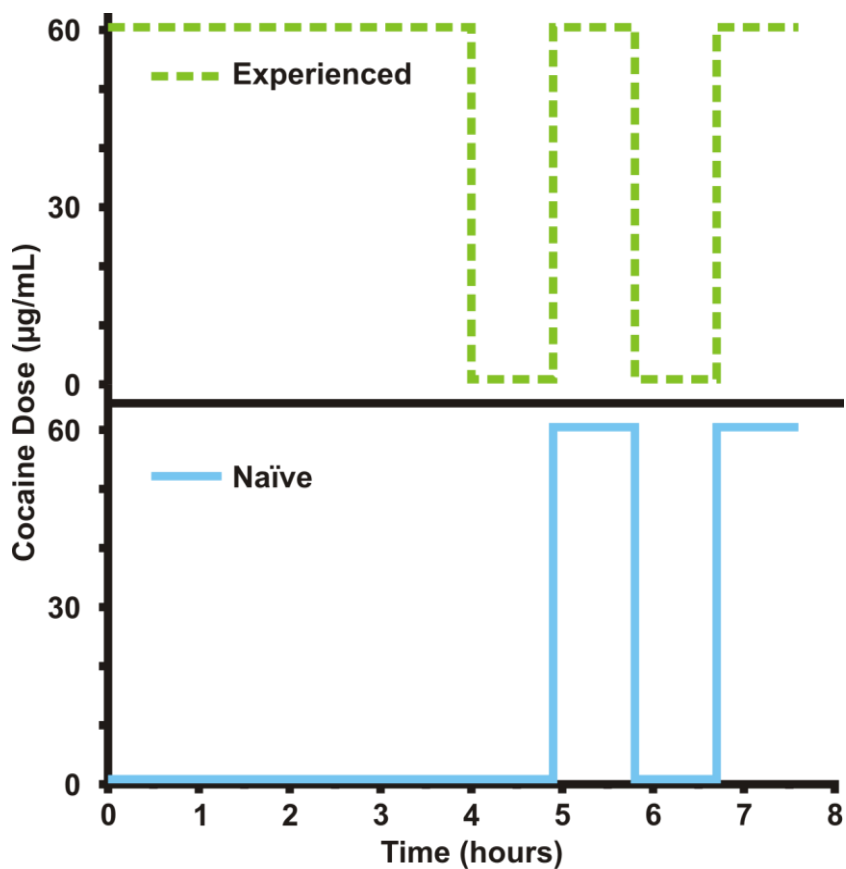


Figure 2.5 Cocaine exposure scheme for both in culture and online cell experiments showing the time course of cocaine administration to naïve (blue) and experienced (green) T cell populations. Experienced cells received a pre-exposure dose of cocaine for 4 hours while the naïve cells did not.

resuspended in 500  $\mu\text{L}$  of RPMI 1640 and incubated for 54 minutes at 37°C, 5%  $\text{CO}_2$ . The cells were then centrifuged as above and resuspended in RPMI with cocaine at 60  $\mu\text{g}/\text{ml}$ , then incubated for another 54 minutes. This cell population received two more steps of media switching, RPMI then cocaine, for a total of four 54-minute exposure periods. Each time the cells were centrifuged, the supernatant was reserved for protein precipitation and metabolomic analysis. Since these cells lacked pre-exposure to cocaine, they were termed “naïve.”

Cells in the second tube were resuspended in 500  $\mu\text{L}$  of cocaine in RPMI 1640 (60  $\mu\text{g}/\text{ml}$ ) and incubated for 216 minutes at 37°C, 5%  $\text{CO}_2$ . After this period, cells were again centrifuged and then exposed in the same manner as tube one with alternating exposure to plain RPMI 1640 and cocaine. Supernatant from these samples was also kept for metabolomic analysis. Since these cells had an extended cocaine pre-exposure period, they were termed “experienced.”

In order to investigate the cocaine degradation over the time course of the experiment, samples of cocaine in RPMI were incubated in the same conditions as the cells and sampled at each 54-minute time point starting at time zero and ending at 10.5 hours.

#### 2.3.4 Metabolomics Sample Preparation and UPLC-ESI-IM-MS Analysis

As each 54-minute time point was taken, supernatant was placed on ice to halt any continued metabolite modifications and immediately processed for protein removal with cold methanol. To each 300  $\mu\text{L}$  supernatant sample, 900  $\mu\text{L}$  of cold methanol was added, vortexed, allowed to sit for 10 minutes at 4°C and then centrifuged at maximum speed for 10 minutes in a Heraeus Fresco 21 temperature-controlled centrifuge (Thermo Scientific). Supernatant was transferred to a new microcentrifuge tube and kept at 4°C until all samples were collected and processed. All samples were then dried down in a Savant DNA 110 Speedvac overnight with low heat and reconstituted in 300  $\mu\text{L}$  5% methanol/95% water (0.01% formic acid).

Samples were placed in the sample tray of the nanoAcquity UPLC with autosampler (Waters, Milford, MA), which remains cooled to 4°C to prevent sample degradation. Ultraperformance liquid chromatography was performed on 1 µL samples loaded on a HSS C18, 1.8 µm particle size column with mobile phase A (0.1% formic acid in H<sub>2</sub>O) by ramping from 100% mobile phase A to 100% mobile phase B (0.1% formic acid in MeOH) over 11 minutes, then holding at 100% mobile phase B for 2 minutes. Ion mobility-mass spectrometry and MS<sup>°</sup> were then performed on the eluted analytes using the Synapt G2 ion mobility-mass spectrometer (Waters, Milford, MA). Quality control samples were dispersed every 10 samples in the Waters Masslynx v4.1 software sample list among technical triplicates of each biological sample.

### 2.3.5 Online Cell Loading and Experimentation

Prior to experimentation, 500-1000 µL of cell suspension was removed from culture flasks. Cells at passage 6 were used for experiments. Cells were then gently pelleted and aspirated into polyether ether ketone (PEEK) tubing connected to pump-controlled syringes. The flow direction of the pump was reversed upon intubation of the MTNP and cells were collected into microfluidic traps for experimentation. Cell-loaded devices were then perfused with selected media components and bright-field images were collected by an inverted Nikon Eclipse Ti-e (Nikon Instruments, Melville, NY). Cells in the MTNP were maintained at 37°C and 5% CO<sub>2</sub> during experimentation.

For T cell cocaine metabolism studies, populations of naïve T cells and experienced T cells (exposed to cocaine at 60 µg/mL in RPMI 1640 for 4 hours) were stimulated with either cocaine (60 µg/ml in RPMI 1640) or RPMI 1640. Cells were initially exposed to plain RPMI media for 54 minutes, followed by exposure to cocaine at 60 µg/mL in RPMI for 54 minutes. Both steps

were repeated for a total of four steps. Experiments with naïve and experienced cells were performed on the same day, in series, to exclude any variation in cell population from day to day. The cocaine exposure scheme is the same as the in-culture exposure, shown in Figure 2.5.

### 2.3.6 Solid Phase Extraction Desalter

Columns are made of 360  $\mu\text{m}$  OD/100  $\mu\text{m}$  ID fused silica tubing and are bomb-loaded in house with 3  $\mu\text{m}$ , 300 Å, C18 phase Jupiter Bulk Packing (Phenomenex, Torrance, CA) using a PIP-500 Pressure Injection System (New Objective, Woburn, MA). Three 10-port Nanovolume UPLC Valves with 360  $\mu\text{m}$  fittings, C72MH-4690ED (VICI Valco Instruments Co. Inc., Houston, TX) were used for the valve arrangement (Figure 2.6). The aqueous solvent and both organic solvent lines, running at 500 nL/min, were supplied with an Eksigent Nanoflow Metering System (AB SCIEX, Framingham, MA), which has four independent flow channels. The output lines from the two downstream valves were connected with a micro-T junction and fed directly into the mass spectrometer via a nano-electrospray ionization (nESI) source. Cheminert 360  $\mu\text{m}$  unions (with 100  $\mu\text{m}$  bore) were used for all tubing-to-tubing connections (not shown). Only fittings for 360  $\mu\text{m}$  OD tubing were used as the more popular 1/16" fittings requiring sleeves to connect to smaller bore tubing instigated leakage at high backpressures. Other than the columns, which were made of fused silica, 360  $\mu\text{m}$ /50  $\mu\text{m}$  PEEK tubing was used. Prior to experimental use a 2  $\mu\text{g}/\text{mL}$  solution of polyarginine was run through the system to bind all non-reversible interaction sites. Elution cycles were then run overnight to ensure all reversibly bound material was removed before experimentation. Sample loops were added to the system (as seen in Figure 2.6) to reduce backpressure buildup.

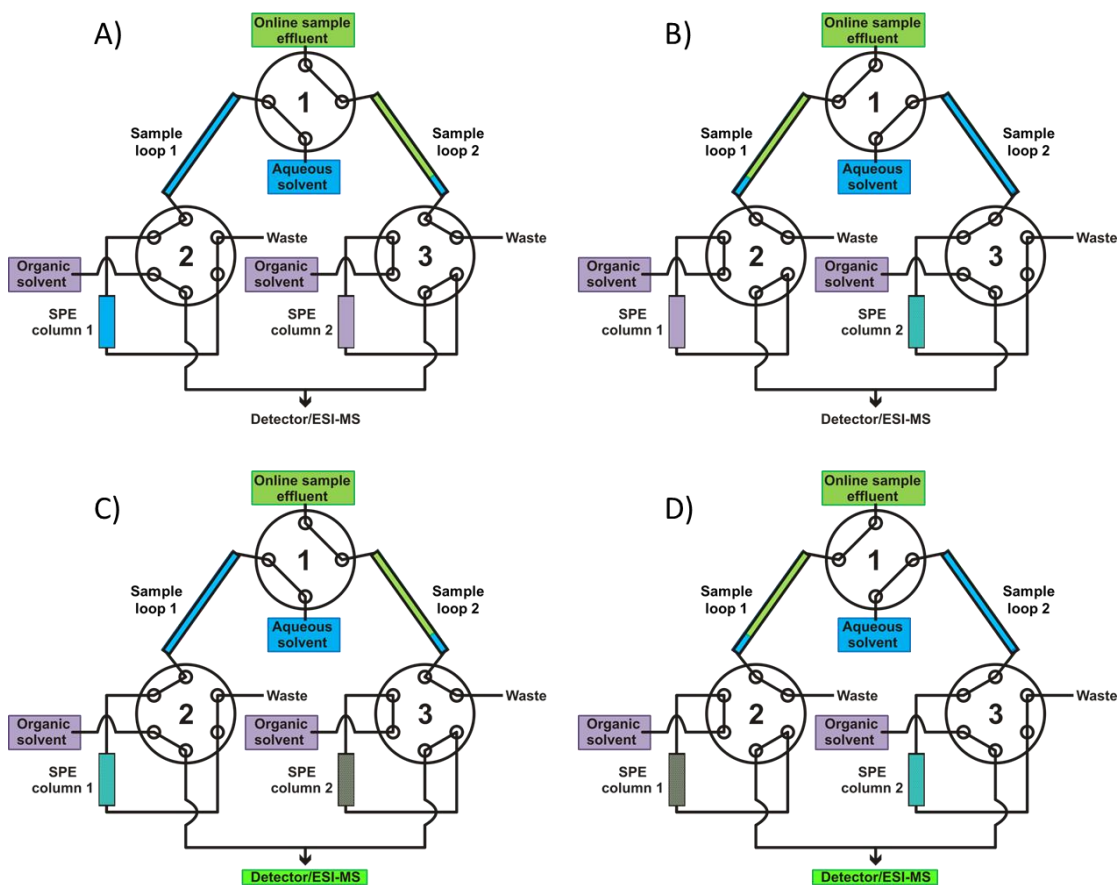


Figure 2.6 Solid phase extraction desalter setup starting from initial sample effluent flow incorporates 2 sample loops, 3 valves, and 2 C18 columns. During (A), sample effluent fills sample loop 2 for 9 minutes, while the aqueous solvent flows through sample loop 1, over column 1 and to waste. The organic solvent flows over column 2 and to the mass spectrometer. B) Upon switching of the valves, the sample effluent fills sample loop 1 for 9 minutes. Aqueous solvent forces the 1.5  $\mu\text{L}$  head of aqueous solvent, the 4.5  $\mu\text{L}$  of sample effluent, and an additional 2.1  $\mu\text{L}$  of aqueous solvent over column 2 to equilibrate the column, load the sample, and rinse away the salts. Organic solvent runs through column 1 and to the detector. C) The next valve switch again exchanges the sample loop filled by effluent, while column 1 is equilibrated, loaded, and rinsed. The analytes captured on column 2 are eluted by the organic solvent and sent to the detector. D) When the valves switch again, the sample effluent fills the opposite loop, column 2 is equilibrated, loaded, and rinsed, and column 1 is eluted with organic solvents and those analytes are sent to the detector. The pattern repeats until the experiment is completed.

### 2.3.7 Online Cell Effluent Desalting and Mass Spectrometry Analysis

All online cell effluent experiments were conducted using PDMS MTNP devices. Cellular effluent from the device was processed online prior to mass spectrometry analysis using the online SPE desalter in Figure 2.6. Cell effluents, driven by syringe pumps upstream of the bioreactor, were filtered with an inline filter (1  $\mu\text{m}$  stainless steel frit, followed by a 0.5  $\mu\text{m}$  polymer mesh, IDEX Health & Science, Oak Harbor, WA) and loaded into each sample loop. Sample loops, which were made of 360  $\mu\text{m}$  OD/250  $\mu\text{m}$  ID tubing, were 12.2 cm long, providing a sample loop volume of 6  $\mu\text{L}$ . The continuous sample stream was diverted into each sample loop for exactly 9 minutes at 500 nL/min, thus filling the sample loop to 75% capacity. Because water was always flowing through these sample loops immediately prior to sample flow, a plug of 1.5  $\mu\text{L}$  of water preceded each sample effluent plug. This plug served to quickly and roughly equilibrate the column with an aqueous solvent. Once the loop was filled to 75% with online sample effluent, the small water plug and sample effluent were passed over the column, using the aqueous solvent line to generate the necessary backpressure. Once the effluent had cleared the sample loop and had been entirely passed over the column, an additional 2.3 minutes or 2.1  $\mu\text{L}$  of aqueous solvent ( $\text{H}_2\text{O}$  with 0.1% formic acid) was run over the column to serve as the rinsing/purging step to remove residual salts. Following the salt purge, the column was eluted with organic solvent (90% methanol, 10%  $\text{H}_2\text{O}$ , 0.1% formic acid). Each step of this process from the initial effluent flow through the SPE desalter is illustrated in Figure 3. Data were collected using MassLynx software (Waters Corp., MA) by Data Dependent Analysis (DDA) method cycle files, where each column elution was collected as an individual file. Collecting each column elution as individual data files aided sample analysis, as explained later.

### 2.3.8 Data Processing and Multivariate Statistical Analysis

Resulting data sets from both online and in-culture experiments were processed using Waters MarkerLynx software along with Umetrics Extended Statistics software for multivariate statistical analysis (Waters Corp., MA). All spectra were corrected to sodiated HEPES buffer ( $[M+Na]^+$  exact mass 261.0888), centroided, and peaks were normalized to 10,000 counts per sample. Only spectra from samples analyzed through UPLC were deisotoped and underwent chromatographic peak detection. Data from online experiments were processed by a combined scan range. An intensity threshold was set for all data at 1000. Principal component analysis (PCA) with Pareto scaling was performed to verify initial sample grouping. Further statistical analysis with orthogonal partial least squares-discriminate analysis (OPLS-DA) was performed to identify significant contributors for group separation.

Metabolite Expression Dynamics Inspector (MEDI), a free java-based program, was used to create metabolite expression profiles from the raw metabolite data obtained from the online experiments. Respective media standard profiles (cocaine in RPMI and plain RPMI) were subtracted from each experimental profile. Naïve profiles were subtracted from the experienced profiles according to their experimental timing to produce a difference map of metabolite expression unique to the experienced cell population.

## 2.4 Results and Discussion

### 2.4.1 Platform Integration and Evaluation

Successful integration of the platform has been achieved as shown in Figure 2.7. The microfluidic bioreactor (MTNP) is controlled upstream by Harvard Apparatus syringe pumps and viewed under the Nikon Eclipse Ti-e, for optional fluorescent and brightfield imaging acquisition,



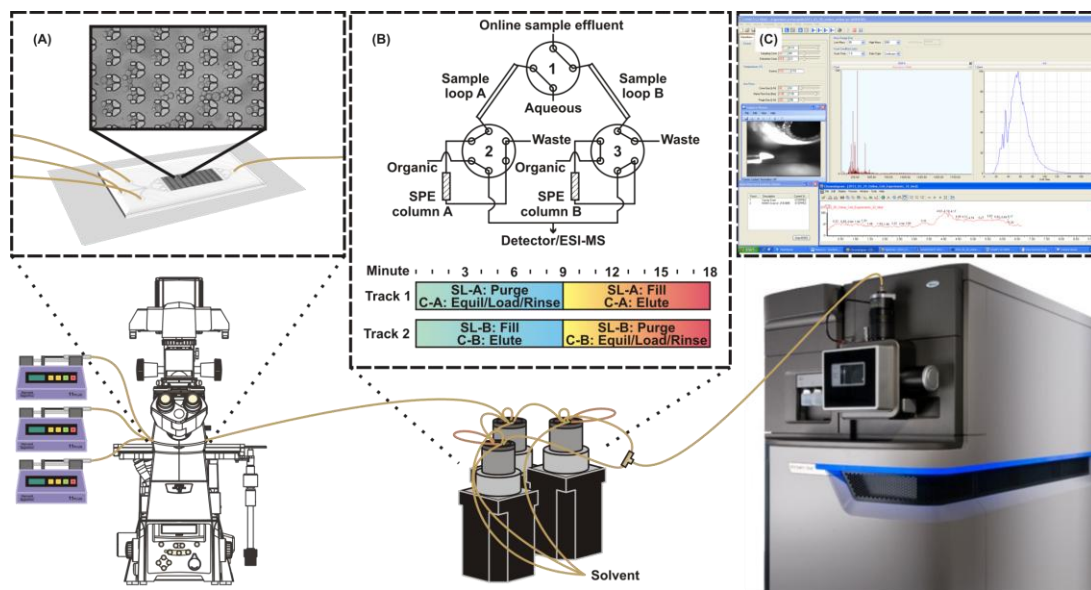


Figure 2.7 MTNP-SPE-nESI-IM-MS platform with Harvard Apparatus syringe pumps, Nikon Eclipse Ti-e inverted fluorescence microscope with stage incubator, solid phase extraction desalter with Eksigent and nanoAcquity pumps for solvent flow control, nanoelectrospray ionization source for continuous flow sample analysis in the Waters Synapt G2 ion mobility-mass spectrometer. Beyond the initial experimental setup, all components are fully automated and capable of running multi-hour experiments limited by the lifetime of cells in the MTNP.

and outfitted with a stage incubator for control of temperature, gas and humidity. The effluent exiting from the MTNP flows through two inline filters for catching cell debris (1  $\mu\text{m}$  stainless steel frit, followed by a 0.5  $\mu\text{m}$  polymer mesh, IDEX Health & Science, Oak Harbor, WA). Once through the filters, the effluent fills one of the two sample loops vented to open air to avoid high backpressures in series with the compliant microfluidic device. After the effluent undergoes salt removal by the solid phase extraction desalting system, it is directed into the nESI source and sprayed into the Waters Synapt G2 nESI-IM-MS. A complete use and troubleshooting guide is available in Appendix B.

Initial work, which paired a previous arrangement of the online SPE design<sup>20</sup> with MTNPs, resulted in ruptured devices. When LC pumps were used to rinse and elute the SPE

columns, pressure would build up behind the column. When the valve was switched so that the MTNP was directly in series with the column, this high backpressure (>200psi), would cause massive flow reversal and induce the PDMS device to physically delaminate from the glass to which it was bonded. This problem was mitigated by altering the valve arrangement to incorporate sample loops. By cutting off the direct pathway between the columns and the microfluidics, the buildup of pressure that occurred during rinsing/eluting was unable to take the least resistive path to the compliant microfluidic device and would instead be vented to the waste port, as shown in Figure 2.6. Although in extreme cases the inline filters downstream of the microfluidic device may become clogged with cells, thus interfering with effluent flows, this is a rare occurrence and can be prevented by using new filters for each experiment in addition to open-outlet cell loading (allowing cells to exit the device during loading before attaching to the downstream components).

The sample loop addition to the valve arrangement allowed for a two-step valve configuration, a simplification of the previous version. The new two-step arrangement generated a saw-toothed pattern as opposed to the rise-and-fall delta-function pattern observed with previous arrangements<sup>20</sup>. In this 180-minute experiment, an 18-minute-long cycle was used, producing an elution peak every 9 minutes. The sample loop volume was designed specifically to hold 9 minutes of sample effluent (4.5  $\mu$ L at 500 nL/min flow rate). This cycle duration was determined to be optimal based on analyte concentrations. The file acquisition was set to account for the delay time from the device to the nESI source such that one column elution was captured per file while accounting for the roughly 12-second software delay between file acquisitions. Pump switching for control of the MTNP perfusion media was also timed with the SPE desalter valve switching.

Removal of salts in an online manner greatly increases signal-to-noise ratio. Yet with the low number of cells and high concentration of media components, detecting low concentrations of analytes is challenging. The signals are also affected by the dynamic range ( $\sim 10^5$ ) of the mass spectrometer<sup>21</sup>. Presumably, post-desalting, and given cellular utilization of nutrients in the media, HEPES at 10 mM is the analyte of greatest concentration. The high concentration of this species limits the lower range of detection of exometabolomic contents to roughly five orders of magnitude lower. This HEPES concentration can be reduced if necessary, but as its purpose is to buffer the media to maintain a physiological pH, there could perhaps eventually be a tradeoff. While detection of low concentration species remains a challenge, the ongoing advances in mass spectrometry technology will increase the detection capabilities of this system.

#### *2.4.1.1 PDMS Surface Passivation for Increased Signal-to-Noise Ratio*

Using fluorescently labeled insulin, the adsorption of insulin to the surface of PDMS could be visualized. Figure 2.8 provides both pictorial and graphical representations of the adsorption of insulin to PDMS and PEG-Si-PDMS. During the 30 minutes of fluorescent insulin exposure, the intensity increases drastically for the control PDMS and less drastically for the silanized PDMS with a relative maxima of 4:1.

While insulin is not necessarily a prime target of these experiments, it serves as an example of the potential complications from non-specific adsorption. Though high sensitivity is characteristic of mass spectrometry, this system seeks to identify secreted molecules from roughly  $10^5$  cells. Detecting these low-level signals becomes a greater challenge when a portion of the signal is lost due to interactions with seemingly inert materials. Although the PDMS passivation schemes returned positive results, some metabolite, peptide or protein species, such as insulin, are particularly “sticky” to most polymer and glass. In testing the capabilities of

the system, we have noticed drastic reduction in and even absence of signal from insulin standards over time, even at low temperatures. Additionally, insulin hysteresis in the combined platform has been discovered after as long as 4 days of continuous perfusion of the SPE desalter tubing and columns. While the columns may be a source of insulin retention, this particular hysteresis occurred with freshly made columns, pointing to an alternate source of contamination as the culprit. The remaining sources of contamination could be from insulin retention in the PEEK and/or fused silica tubing lines, the valve rotors, or even on the source block or cone of the mass spectrometer. Insulin adsorption does not merely lead to a contamination problem; it also leads to reduction in the overall insulin signal.

#### *2.4.1.2 Comparison of UPLC-ESI-IM-MS to MTNP-SPE-nESI-IM-MS*

A significant reduction in time is among the benefits of continuous sample flow from the microfluidic bioreactor to the solid phase extraction desalter and into the nESI-IM-MS. This integrated platform allows for the setup (~2-3 hours), execution (~4-8 hours), and data collection (no additional time) in the course of a day. Traditional in-culture experiments with UPLC-ESI-IM-MS analysis possibly require less initial setup (~1 hour), roughly the same execution time (~4-8 hours), significant additional sample processing time (~15-20 hours including overnight sample evaporation), and data collection (~50 hours for 120 samples with a 25-minute UPLC time per sample) for a total of about 4 days until data are ready for processing compared to 1 day for the platform developed in this work.

Another advantage of the integrated platform compared to in-culture experiments is in the ease of obtaining mass spectra at multiple time points. Our process is automated with constant media perfusion control timed with the switching of the SPE desalter valves as well as the data file collection timing. With the in-culture experiments, a lengthier process is required to

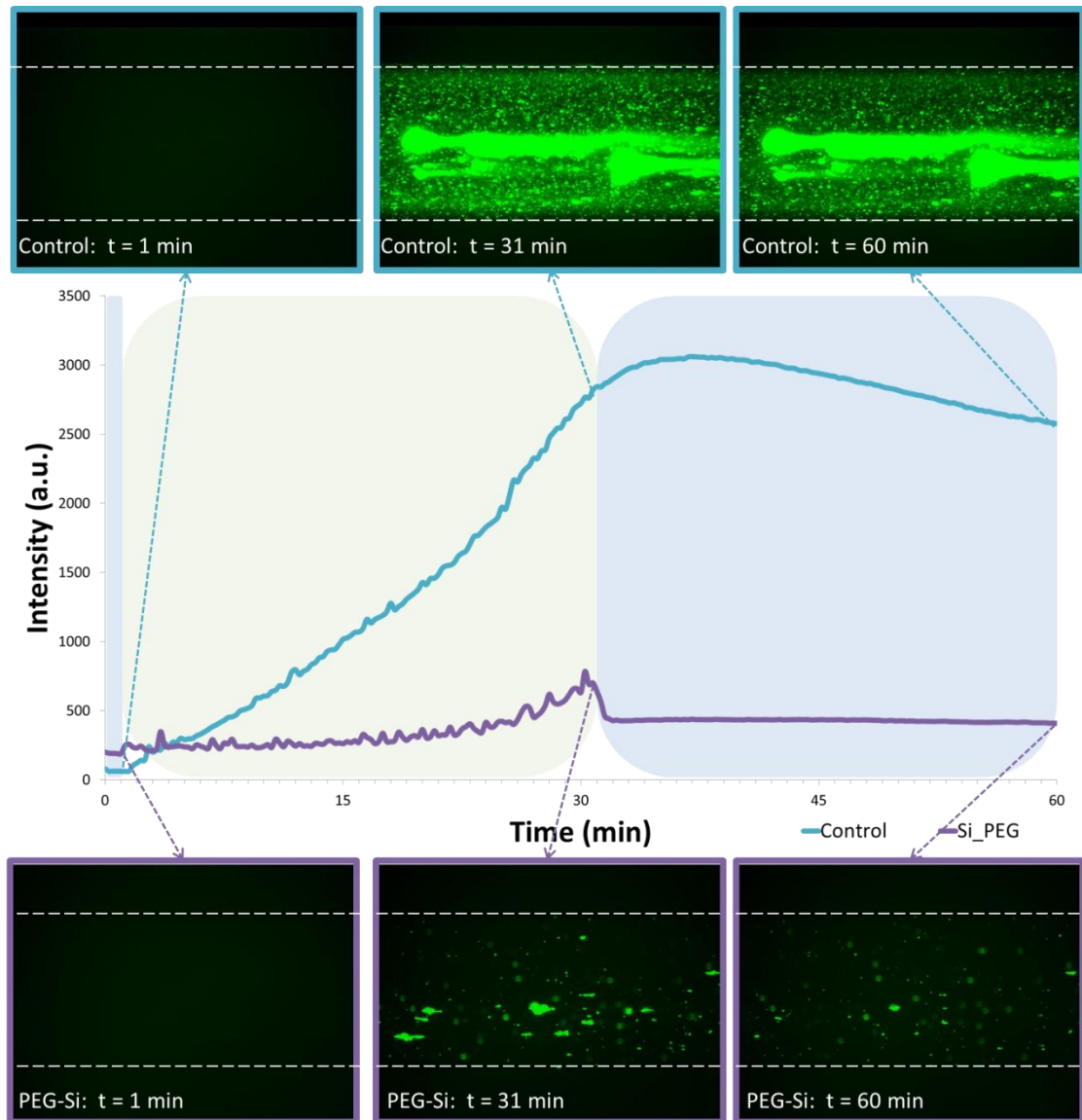


Figure 2.8 Insulin treatment of silanized PDMS channels. PDMS channels were perfused FITC-insulin for 30 minutes (green), followed by 30 minutes of rinsing with Ringer's solution (blue). The top three fluorescent images show the surface bound insulin at 1 min, 31 min and 60 min, with the bottom three images corresponding to the surface modified channels. Silanized PDMS channels (purple line) retain (at maximum) only 25% of the total insulin retained by untreated PDMS.

collect a time point. The cell suspension must be centrifuged for 2 minutes, the supernatant removed, and the cell pellet resuspended in new media. The length of time required for this media change is on the same order of the time points taken with the integrated platform. Repeated centrifuging and pellet aspiration can introduce unnecessary stress to the cells, which may produce an exometabolomic profile resulting from both the media exposure and additional cell stress.

One downside compared to liquid chromatography data is the absence of retention time information. While the solid phase extraction desalter uses a column similar to those found in an LC system, any slight timing discrepancy from one file collection to the next prevents the use of any retention time data. Confounding this issue is the fact that processing data within the Waters Masslynx software without retention time data available prevents the option for the removal of isotopes from the data. While this is a hindrance in some respects (roughly 3 times more peaks, redundant data, etc.), it can prevent the accidental removal of isobaric peaks of interest from the study.

## 2.4.2 Cocaine Metabolism in Naïve and Experienced T cells

### 2.4.2.1 *Online Cellular Analysis*

Two populations of Jurkat T cells were compared in this study: naïve T cells that had never been exposed to cocaine and experienced T cells that had been incubating in cocaine at 60 µg/ml in RPMI 1640 for 4 hours prior to online experimentation. As shown in Figure 5, a high degree of variance was observed based not only on what type of media was present in the bioreactor (*i.e.*, plain RPMI media or cocaine RPMI media), but also whether the cells experienced cocaine earlier in the day (*i.e.*, whether the cells were experienced or naïve to cocaine exposure). The major unique contributors to group separation between naïve and

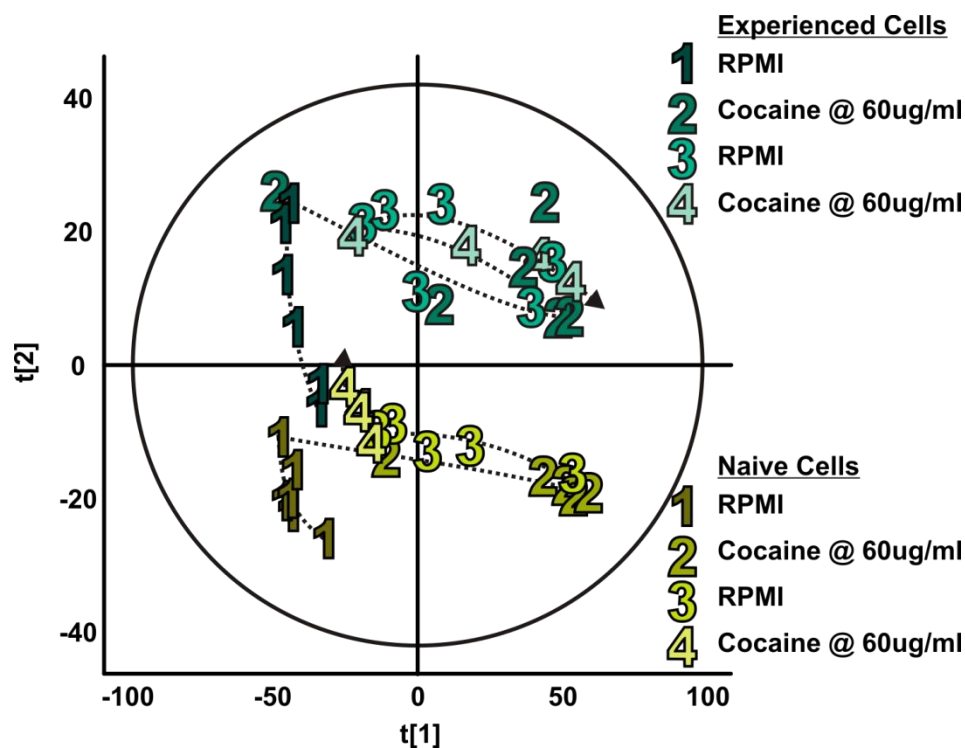


Figure 2.9 Walking principal component analysis of exometabolomic profiles of naïve (shades of yellow) and cocaine-experienced (shades of turquoise) Jurkat T cells obtained with on-line cellular analysis. Each numerically labeled data point represents a 9-minute column elution, with 6 data points collected per step (all marked with the step number and connected in order of collection with the dotted line). In steps 1 and 3, both cell populations received plain RPMI. In steps 2 and 4, both received cocaine in RPMI at 60  $\mu\text{g}/\text{ml}$ . As profiles switch from RPMI to cocaine exposure, the data points move towards the right and vice versa, with the exception of naïve cell step 4, which stays closer to step 1. Further analysis of the data reveals this inconsistency may be explained by the death of the cells. Data were grouped not only based on the experimental step, but also by the experience level of the cells, as the cells receiving a 4-hour pre-incubation in cocaine group separately from those that did not receive this dose.

experienced exometabolomic profiles included  $m/z$  283,  $m/z$  187,  $m/z$  399,  $m/z$  157, and  $m/z$  337 (all at elevated abundance in the experienced group compared to the naïve group). The metabolites contributing to group separation between type of media to which cells were exposed in the MTNP consisted of  $m/z$  312,  $m/z$  182,  $m/z$  304,  $m/z$  290, and  $m/z$  150. Though

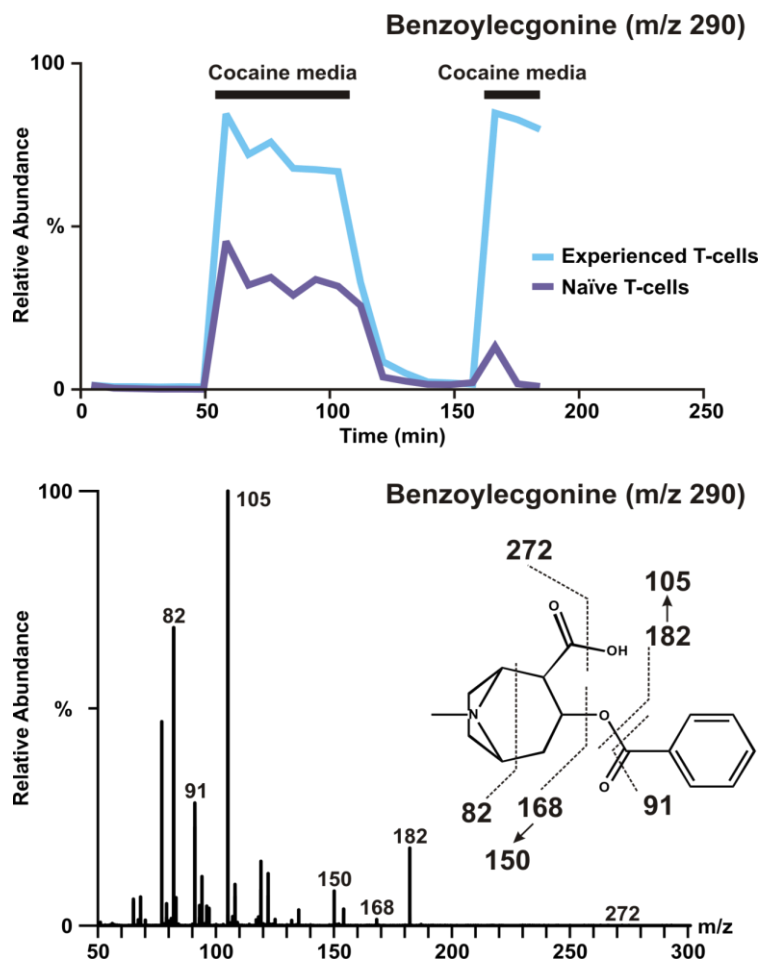


Figure 2.10 Top: Benzoyllecgonine (BE) time course data for experienced (blue) and naïve (purple) cells. While data were gathered sequentially, plots are overlaid to highlight the increased abundance of BE in experienced cells. The absence of the expected increase in BE corresponding to step 4 (the last step of cocaine exposure) provides further evidence of cell death due to lack of cocaine metabolism. Bottom: The fragmentation spectra of BE are shown with parent ion of  $m/z$  290.

the data analysis pipeline prevented removal of isotopes, any  $m/z$  present in the list of top contributors negated the inclusion of their respective isotopes from these lists.

Benzoyllecgonine ( $m/z$  290 as  $[M+H]^+$ ,  $m/z$  312 as  $[M+Na]^+$ ), a primary metabolite of cocaine, was identified as a contributing factor to the separation between the cocaine exposure steps and plain RPMI steps as well as to naïve cells and experienced cells. Analysis of this



metabolite over the time course of the experiment revealed an expected increase during cocaine exposure steps, but also showed a significant increase from naïve to experienced cells ( $p$  value =  $5.7E^{-4}$ ) (Figure 2.10). Fragmentation spectra revealed fragment ions  $m/z$  82,  $m/z$  91,  $m/z$  105,  $m/z$  150,  $m/z$  168,  $m/z$  182 and  $m/z$  272, as shown in Figure 6. Analysis of the remaining top three contributors to separation based on media revealed cocaine at  $m/z$  304, anhydroecgonine methyl ester (AEME) at  $m/z$  182 (produced from dehydration of ecgonine methyl ester (EME) rather than the pyrolysis of cocaine), and ecgonine aldehyde, the decomposition product of EME, at  $m/z$  150.

To verify that this increased BE abundance was not purely a result of non-enzymatic hydrolysis of cocaine to BE in aqueous solutions over the time course of the experiment, an experiment replicating the naïve and experienced cell experimental time course was performed with the omission of the Jurkat T cells. In order to compare the experiment with cells to that without cells, we normalized the BE intensity to the cocaine intensity. On average, the percent of the total normalized BE from non-enzymatic hydrolysis was 34.1% in step 2 of the naïve cell experiment while the corresponding percentage for step 2 of the experienced cell experiment was 34.5%.

The time course of additional metabolites is provided in Figure 2.11, including cocaine metabolites anhydroecgonine (AHE) ( $m/z$  168) and hydroxybenzoylecgonine (HOBE) ( $m/z$  306), as well as several unknown metabolites ( $m/z$  330,  $m/z$  475,  $m/z$  678). Some of these additional metabolites have higher abundance in the cocaine-experienced population while others have no overall change in abundance. Overall, BE, AHE, and  $m/z$  645 show significant increases from naïve to experienced cell population ( $p$ - values =  $5.7E^{-4}$ ,  $1.12E^{-3}$ , and  $1.60E^{-3}$  respectively). While AHE is a typical product of AEME (the pyrolysis product of cocaine), some reports have shown the metabolic pathway from cocaine into AEME and AHE could result from loss of water of EME

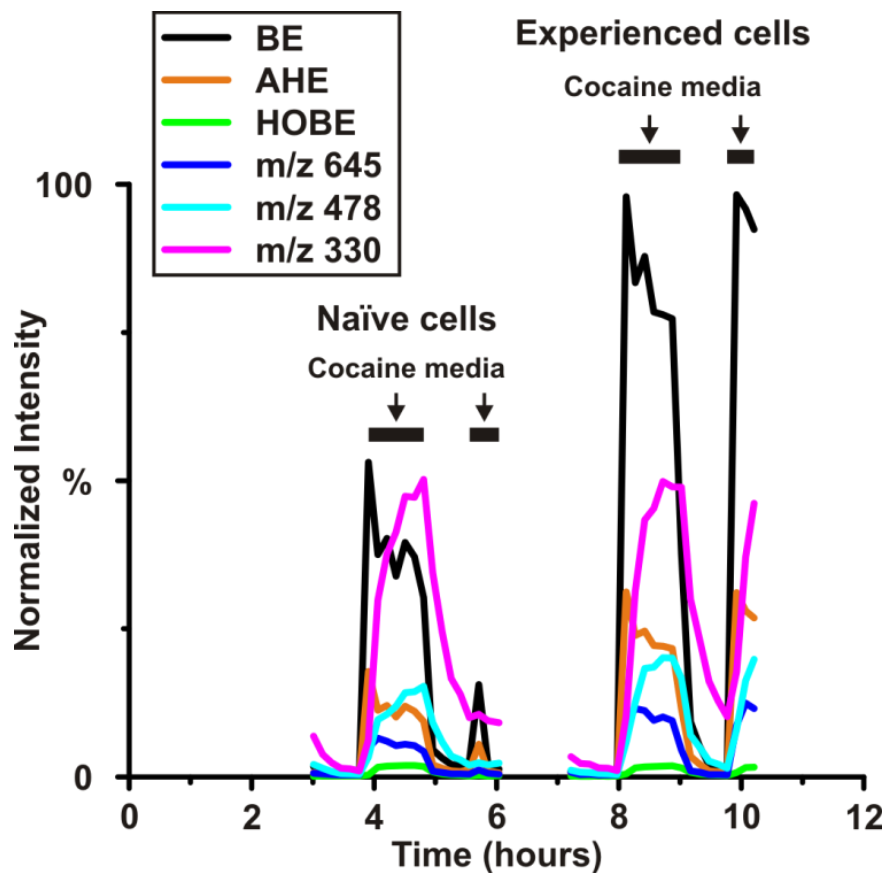


Figure 2.11 Additional metabolite time course data are shown compared to BE. Experimental conditions for each group of cells are shown above the graph with solid black lines indicating exposure to cocaine media. Anhydroecgonine (AHE) and hydroxybenzoylecgonine (HOBE), two additional metabolites of cocaine, provide examples of both variation between naïve and experienced cell groups in the case of AHE and consistency between these two groups in the case of HOBE. The increases in BE and AHE from naïve to experienced groups are statistically significant with respective  $p$  values of  $5.7E^{-4}$  and  $1.12E^{-3}$ . Three unidentified  $m/z$  645,  $m/z$  478, and  $m/z$  330 that contribute to the separation between media exposure groups are also shown.  $m/z$  330 and  $m/z$  478 show no statistical significance between naïve and experienced cell groups while the increase in  $m/z$  645 is statistically significant ( $p = 1.6E^{-3}$ ).

or ecgonine (EG)<sup>23</sup>. While there is much evidence that AEME and AHE can form as a result of the analysis technique, this is typical of gas chromatography separations that require vaporization of compounds, thus risking alteration of thermolabile compounds such as cocaine and its

metabolites<sup>24</sup>. Electrospray ionization is utilized when this type of compound is under investigation.

Exometabolomic profiles in the form of differential heat maps, created by the Metabolite Expression Dynamics Inspector, were created to demonstrate the temporal distinctions present between the naïve and experienced T cells. 30917 metabolites (including isotopes) were organized by random tile assignment into heat maps corresponding to each 9 min data file. After the respective media background peaks were subtracted, the naïve time

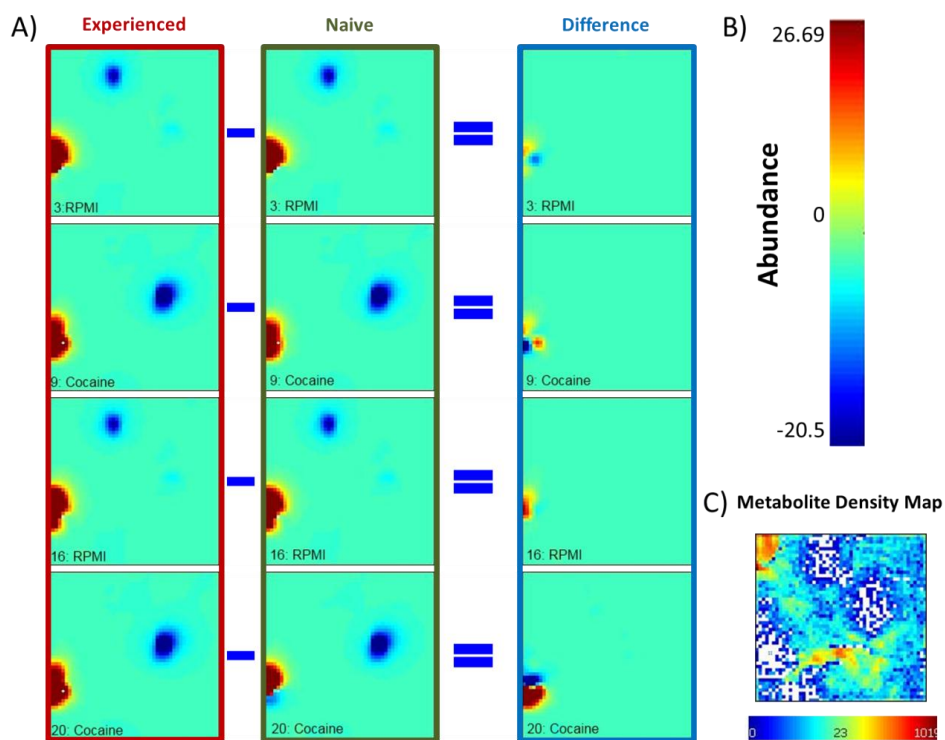


Figure 2.12 Metabolite Expression Dynamics Inspector heat maps demonstrating grouping of metabolites with similar trends in each of 2550 tiles. A) Each heat map represents a time point in the middle of the time course for each experimental step (RPMI or cocaine exposure). For instance, step one of RPMI exposure resulted in heat maps corresponding to data files 1 through 6, with the heat map corresponding to data file 3 shown. The difference between the experienced cells profiles (red) and naïve cells profiles (green) is calculated in the blue column. B) The color scale for the map ranges from -20.5 (showing a decrease in abundance of a particular group of analytes) to 26.69 (for an increased abundance of other analytes). C) The metabolite density map shows the distribution of 30917 metabolites.

course data was subtracted from the experienced time course. A sample of these differential metabolic profiles denoting the middle time point in each media exposure step is shown in Figure 2.12. A full set of time course heat maps for both the naïve and experienced groups are available in Appendix C.

#### *2.4.2.2 In Culture Cellular Analysis*

To compare this instrumentation platform, as well as the resulting biological data of naïve and cocaine-experienced T cells, with the current standard in mass spectrometry analysis of biological samples, the online experiment was replicated in culture and samples analyzed with UPLC-ESI-IM-MS. Figure 2.13 shows the PCA plot demonstrating sufficient variance when comparing steps 1 and 3 (plain RPMI 1640 exposure) with steps 2 and 4 (cocaine exposure). Unlike the online experiment, separation between cocaine experienced cells and naïve cells is not achieved with exception of the initial RPMI exposure of the naïve cell populations. While once major difference is the number of time points per step of media exposure, as discussed previously, replicating the 9 minute time point sampling of the online system would confound the length of time needed for media switching, as well as add unnecessary stress to the cells.

## 2.5 Conclusions

### 2.5.1 Platform Capabilities and Shortcomings

We have described the analysis and proof of concept of a technology platform for near real-time detection of the cellular exometabolome based on the combination of a microfluidic bioreactor, an online SPE desalting arrangement, and mass spectrometry. A great strength of this platform is in its adaptability to different cell types and experimental conditions. Microfluidic cell trapping devices can be customized to the size of any adherent or non-adherent

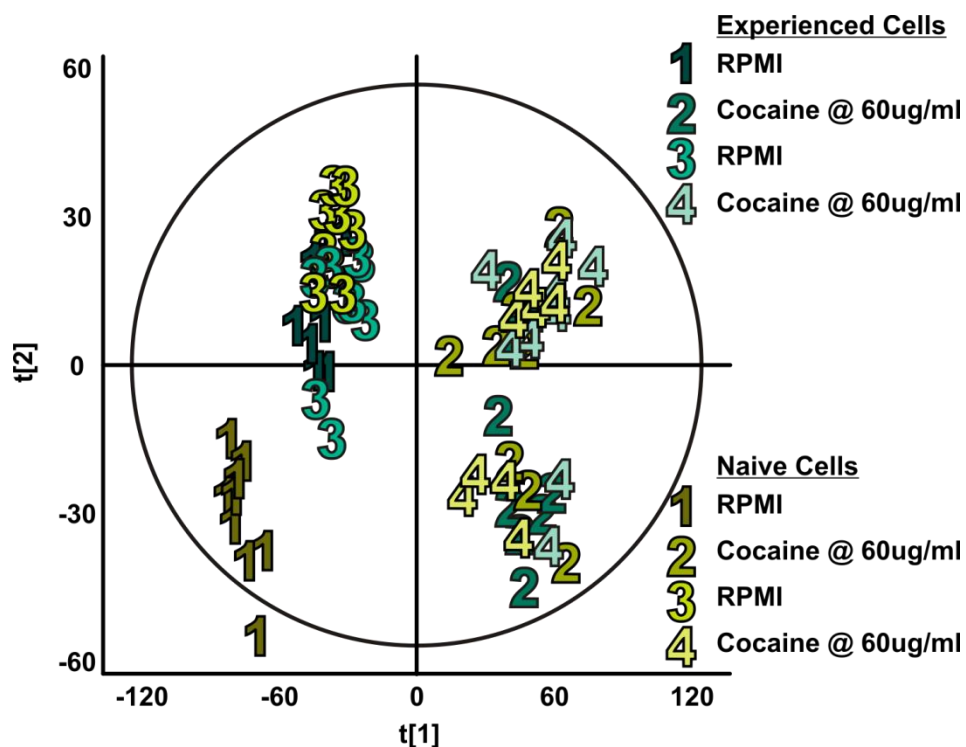


Figure 2.13 In-culture principal component analysis of exometabolomic profiles of naïve (shades of yellow) and cocaine experienced (shades of turquoise) Jurkat T cells. Each numerically labeled data point represents the end point of a 54 minutes exposure to the indicated media. As with the online experiment, during steps 1 and 3 both cell populations received plain RPMI, while during steps 2 and 4 both received cocaine in RPMI at 60 µg/ml. Variance between step1 and 3 and steps 2 and 4 result in unsupervised grouping according to media exposure type. Separation between naïve and experienced cell groups, particularly when under cocaine exposure, does not occur to the same degree as yellow and turquoise points corresponding to steps 2 and 4 are heavily intermixed.

cell type. In this work, we demonstrate cell trapping and experimentation on naïve and cocaine-experienced Jurkat T cells. While this work shows only one model system based around cocaine exposure, the environmental stimuli are limited only by the number of pumps one has available for providing variable perfusion conditions and the temperature change and gas exchange rates an incubator is capable of generating. The online SPE desalting arrangement allowed for sufficient desalting to permit a temporal resolution of 9 minutes. While this temporal resolution

is not by any means a significant advance for cellular chemical detection methods, because it is dictated by the analyte abundance and detection capabilities of the TOF mass analyzer, it is (depending on the mass analyzer) the best resolution possible for this biological system using mass spectrometry. Because it is trivial to scale the loading time in this arrangement based on detection power, we believe a technology platform of this general system will be of considerable utility to the biological community, particularly as mass analysis detectors improve in the coming years.

### 2.5.2 Cellular Memory of Cocaine Experience

Cocaine metabolism in naïve and experienced Jurkat T cells was investigated with this near-real time platform developed for the study of the cellular exometabolome. While it is well known that cocaine has an effect on immune cells, there has been no prior demonstration (though the idea has been suggested)<sup>25</sup> of even a short-term immune cell memory of prior cocaine exposure. With the advent of this innovative platform, unique metabolic profiles are obtained that are absent from the “in-culture” data or perhaps lost due to the increased sample processing and UPLC analysis time. Upregulation of cocaine metabolism into benzoylecgonine in experienced cells demonstrates one contributor to the unique exometabolomic profile resulting from previous cocaine experience. Anhydroecgonine, as well as unknown metabolites  $m/z$  645 and  $m/z$  478, are also upregulated in cell populations with prior cocaine exposure, leading to the possibility of indicators of immune cell memory of cocaine other than cocaine metabolites alone.

While there is a previously reported non-enzymatic degradation rate of cocaine into benzoylecgonine at physiological temperatures and  $pH^{22}$ , we were able to confirm a rate specific to this platform. Through comparison of the BE to cocaine ratios from naïve and experienced

cell experiments, as well as the platform absent of cells, it is evident that the portion of BE abundance from non-enzymatic degradation does not entirely explain the significant increase in BE during the cocaine exposure steps in the experienced cells, indicating the response is due to a unique exometabolomic profile of T cells with prior cocaine exposure. Further analysis of cellular memory of cocaine exposure is warranted based upon these findings.

## 2.6 References

1. Kell, D. B. *et al.* Metabolic footprinting and systems biology: the medium is the message. *Nature Reviews Microbiology* **3**, 557–565 (2005).
2. Faley, S. *et al.* Microfluidic platform for real-time signaling analysis of multiple single T cells in parallel. *Lab Chip* **8**, 1700–1712 (2008).
3. Warnement, M. R., Faley, S. L., Wikswo, J. P. & Rosenthal, S. J. Quantum Dot Probes for Monitoring Dynamic Cellular Response: Reporters of T Cell Activation. *NanoBioscience, IEEE Transactions on* **5**, 268–272 (2006).
4. Faley, S. L. *et al.* Microfluidic single cell arrays to interrogate signalling dynamics of individual, patient-derived hematopoietic stem cells. *Lab Chip* **9**, 2659–2664 (2009).
5. Zhou, J., Ellis, A. V. & Voelcker, N. H. Recent developments in PDMS surface modification for microfluidic devices. *Electrophoresis* **31**, 2–16 (2010).
6. Wong, I. & Ho, C.-M. Surface molecular property modifications for poly(dimethylsiloxane) (PDMS) based microfluidic devices. *Microfluid Nanofluid* **7**, 291–306 (2009).
7. Yates, J. R. Mass spectrometry: from genomics to proteomics. *Trends in Genetics* **16**, 5–8 (2000).
8. Han, X. & Gross, R. W. Global analyses of cellular lipidomes directly from crude extracts of biological samples by ESI mass spectrometry: a bridge to lipidomics. *J. Lipid Res.* **44**, 1071–1079 (2003).
9. Zaia, J. Mass spectrometry of oligosaccharides. *Mass Spectrometry Reviews* **23**, 161–227 (2004).
10. Chan, J. H., Timperman, A. T., Qin, D. & Aebersold, R. Microfabricated Polymer Devices for Automated Sample Delivery of Peptides for Analysis by Electrospray Ionization Tandem Mass Spectrometry. *Analytical Chemistry* **71**, 4437–4444 (1999).
11. Jiang, Y., Wang, P.-C., Locascio, L. E. & Lee, C. S. Integrated Plastic Microfluidic Devices with ESI-MS for Drug Screening and Residue Analysis. *Analytical Chemistry* **73**, 2048–2053 (2001).



12. Chen, Q., Wu, J., Zhang, Y. & Lin, J.-M. Qualitative and Quantitative Analysis of Tumor Cell Metabolism via Stable Isotope Labeling Assisted Microfluidic Chip Electrospray Ionization Mass Spectrometry. *Anal. Chem.* **84**, 1695–1701 (2012).
13. Enders, J. R. *et al.* Towards monitoring real-time cellular response using an integrated microfluidicsmatrix assisted laser desorption ionisation/ nanoelectrospray ionisation-ion mobility-mass spectrometry platform. *IET Systems Biology* **4**, 416–427 (2010).
14. Bagasra, O. & Forman, L. Functional analysis of lymphocytes subpopulations in experimental cocaine abuse. I. Dose-dependent activation of lymphocyte subsets. *Clinical and Experimental Immunology* **77**, 289–293 (1989).
15. Roth, M. D., Whittaker, K. M., Choi, R., Tashkin, D. P. & Baldwin, G. C. Cocaine and {sigma}-1 receptors modulate HIV infection, chemokine receptors, and the HPA axis in the huPBL-SCID model. *J Leukoc Biol* **78**, 1198–1203 (2005).
16. Chao, C. *et al.* Recreational drug use and T lymphocyte subpopulations in HIV-uninfected and HIV-infected men. *Drug and Alcohol Dependence* **94**, 165–171 (2008).
17. Pellegrino, T. & Bayer, B. M. In vivo effects of cocaine on immune cell function. *Journal of Neuroimmunology* **83**, 139–147 (1998).
18. Kubera, M. *et al.* The effect of cocaine sensitization on mouse immunoreactivity. *European Journal of Pharmacology* **483**, 309–315 (2004).
19. Duffy, D. C., McDonald, J. C., Schueller, O. J. A. & Whitesides, G. M. Rapid Prototyping of Microfluidic Systems in Poly(dimethylsiloxane). *Analytical Chemistry* **70**, 4974–4984 (1998).
20. Enders, J. R., Marasco, C. C., Wikswa, J. P. & McLean, J. A. A Dual-Column Solid Phase Extraction Apparatus for the Online Collection and Preparation of Continuously Flowing Effluent Streams for Mass Spectrometry.
21. Anderson, N. L. & Anderson, N. G. The Human Plasma Proteome: History, Character, and Diagnostic Prospects. *Mol Cell Proteomics* **1**, 845–867 (2002).
22. Warner, A. & Norman, A. B. Mechanisms of cocaine hydrolysis and metabolism in vitro and in vivo: a clarification. *Ther Drug Monit* **22**, 266–270 (2000).

23. Xia, Y., Wang, Bartlett, M. G., Solomon, H. M. & Busch, K. L. An LC–MS–MS Method for the Comprehensive Analysis of Cocaine and Cocaine Metabolites in Meconium. *Anal. Chem.* **72**, 764–771 (2000).
24. Fandiño, A. S., Toennes, S. W. & Kauert, G. F. Studies on Hydrolytic and Oxidative Metabolic Pathways of Anhydroecgonine Methyl Ester (Methylecgonidine) Using Microsomal Preparations from Rat Organs. *Chem. Res. Toxicol.* **15**, 1543–1548 (2002).
25. PACIFICI, R. *et al.* Cell-Mediated Immune Response in MDMA Users After Repeated Dose Administration. *Annals of the New York Academy of Sciences* **965**, 421–433 (2002).

## CHAPTER III

### 3 PROGRESS TOWARDS A HETERODYNE FRAMEWORK FOR THE GENERATION AND DETECTION OF OSCILLATORY CHEMICAL SIGNALS IN NONLINEAR LIGHT-PRODUCING SYSTEMS

Christina C. Marasco<sup>1,2,3</sup>, Madeleine S. Durkee<sup>1,2,3</sup>, Ayeeshik Kole<sup>4</sup>, Loi Hoang<sup>1,2</sup>, Jie Zhou<sup>1,5</sup>, Ryan Planchard<sup>3</sup>, Ron Reiserer<sup>1</sup>, Philip C. Sampson<sup>1</sup>, and John P. Wikswo<sup>1,2,3,5,6</sup>

<sup>1</sup>Vanderbilt Institute for Integrative Biosystems Research and Education, Vanderbilt University,  
Nashville, TN

<sup>2</sup>The Searle Systems Biology and Bioengineering Undergraduate Research Experience, Vanderbilt  
University, Nashville, TN

<sup>3</sup>Department of Biomedical Engineering, Vanderbilt University, Nashville, TN

<sup>4</sup>Indiana University School of Medicine, Purdue University, Bloomington, IN

<sup>5</sup>Departments of Physics & Astronomy, Vanderbilt University, Nashville, TN

<sup>6</sup>Molecular Physiology & Biophysics, Vanderbilt University, Nashville, TN

### 3.1 Abstract

The complexities of biological regulatory networks (oscillations, feedback loops, etc.) provide motivation for the development of mathematical and physical models for the exploration of nonlinear reaction dynamics. When considering even single biochemical reactions comprising these networks, simplifications of the reaction mechanism are often unavoidable or even made out of ignorance as nonlinear production of potentially unstable chemical intermediates potentiates a problem that may be nearly impossible to overcome. Within this work we present a novel analytical method based on the radio signal processing technique 'heterodyning' to explore the existence and rate of generation of previously undetectable chemical intermediates. We have developed instrumentation for sinusoidal concentration generation, a microfluidic mixer for the combination of two or more unique chemical frequencies, a detector for quantifying the generation of reaction products, and a data analysis technique for processing the output signal into the frequency domain. This work will describe the heterodyne technique, detail the initial efforts in developing the hardware framework, show preliminary results from the use of the technique on nonlinear chemical reactions, and detail further experiments needed to fully benchmark the heterodyne framework. The development of these methods and their application to biological regulatory networks could provide a means of more closely regulating and interpreting complex cell signaling and metabolic response.

### 3.2 Introduction

Central to the field of systems biology is the effort to both model and understand the complex cell signaling pathways that govern biological networks. Table 3.1 lists the various types of cellular signaling that comprise the breadth of response of a cell to its environment. Experimental and computational biologists alike often use wiring diagram analogies to represent these molecular interaction networks. Biological regulatory networks have been shown to be

Table 3.1. Methods of Cellular Communication

<b>Intercellular Signaling Method</b>	<b>Target</b>	<b>Example</b>
Endocrine	Distant cells	Insulin on hepatocytes
Paracrine	Nearby cells	Coagulation factors in platelets
Juxtacrine	Adjacent cells	Membrane-bound growth factor
Autocrine	Emitting cell	Interleukin-2 in T cells
Intracrine	Intracellular receptor	Renin-angiotensin system in cardiac fibroblasts

comprised of simple motifs, such as cycles and cascades, controlled by positive and negative feedback loops, described by linear, hyperbolic, sigmoidal, and oscillatory signal-response dynamics, which when taken together to form an integrated network, can drive the parametric state of the cell into one or more attractor states<sup>1,2</sup>. With such complexities in signaling systems, experimental determination of dynamical properties must be coupled with mathematical models to minimize error in the interpretation of the results. The dynamics of nonlinear biochemical networks under oscillatory stimulus conditions has been modeled by Ingalls as an extension of metabolic control analysis<sup>3</sup>. Tyson describes a means of combining simple signal-

response elements consisting of sigmoidal switches, transient responses, hysteretic switches and oscillators to computationally model any complex regulatory network<sup>2</sup>. Interested readers are directed towards numerous excellent reviews<sup>1,2,4-6</sup> that have been written detailing the finer points of cell signaling, state stability and modeling of complex networks that are tangential to the scope of this work.

Paramount to this work is in the exploration of sinusoidal signaling dynamics. Sinusoidal stimulus-response has been shown to provide valuable information in dynamical biological systems ranging from neuronal networks<sup>7-11</sup> and the human visual response<sup>12-15</sup> to insulin secretion in pancreatic islets<sup>16-18</sup> and yeast regulation<sup>19-23</sup>. Oscillatory glucose levels have been shown to synchronize pancreatic islets in vitro<sup>24</sup>. Bird et al. report constant frequency sinusoidal calcium oscillations resulting from the stimulation of mouse lacrimal acinar cells with submaximal methacholine dose which are dependent on a negative feedback loop driven by protein kinase C<sup>25</sup>. Berthoumieux et al. reported oscillatory concentration dynamics on a three state enzyme system following Michaelis-Menten kinetics<sup>26</sup>.

### 3.3 Heterodyne Chemistry Theory

Heterodyning is a radio frequency processing technique developed within the telecommunications industry for the shifting of signals from one frequency to another through nonlinear mixing in a diode or transistor. When two or more signals at unique frequencies (Figure 3.1A) are combined in a linear manner, the resulting frequencies include only the input frequencies (Figure 3.1B). In contrast, when these same input signals are combined in a nonlinear fashion, new frequencies are generated, called heterodynes, that correspond to the summation and differences of the input frequencies (Figure 3.1C-E). These heterodynes are similar to musical “beats”. As the complexity of the nonlinear signal combination varies

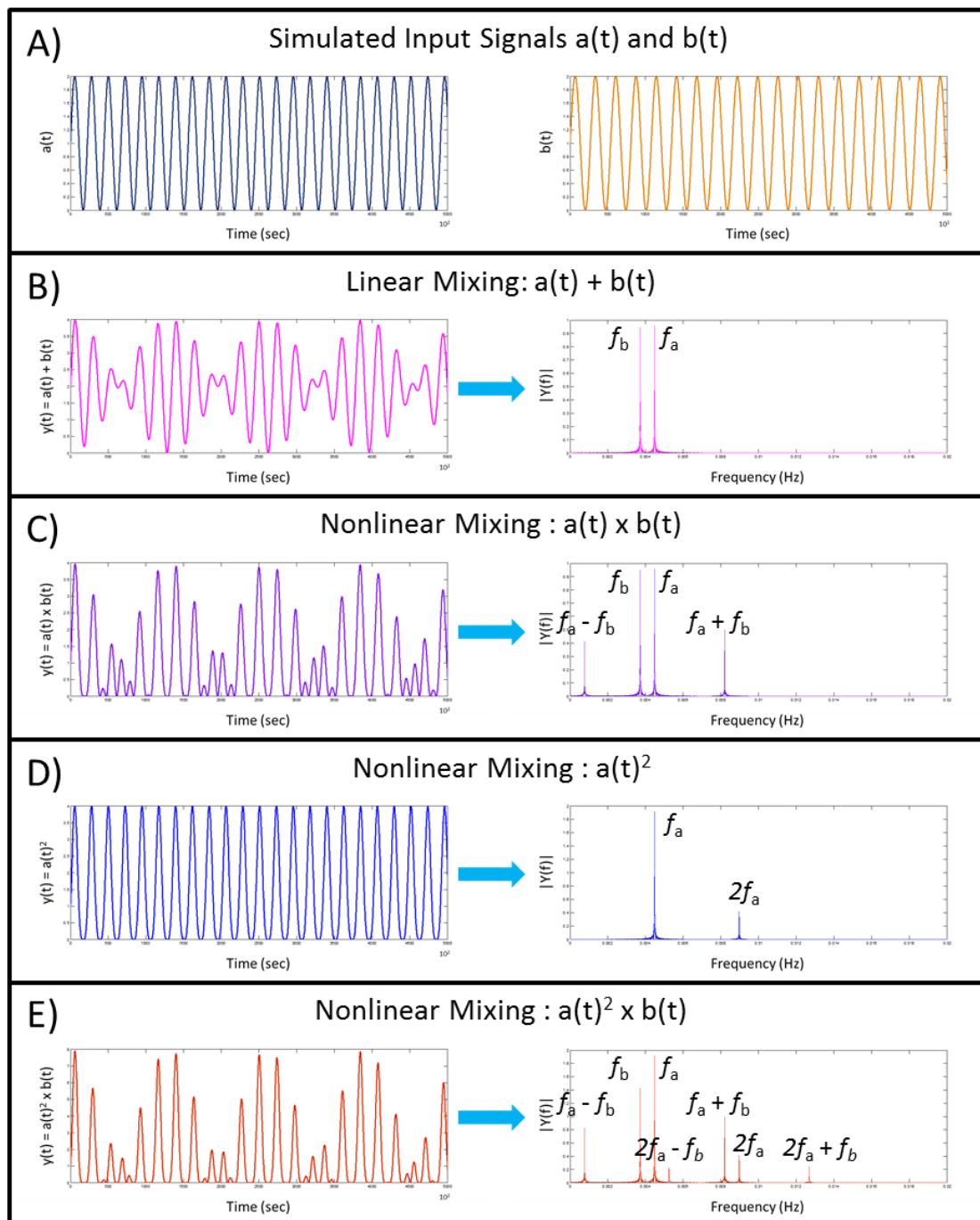


Figure 3.1 Heterodyne chemistry basics. A) contains two simulated signals  $a(t)$  and  $b(t)$  with periods of 223 seconds and 269 seconds. B) When these signals are combined linearly and analyzed in the frequency domain only the two input frequencies are seen. C), D), and E) When nonlinear combinations of these same two frequencies ( $f_a$  and  $f_b$ ) occur, the production of additional frequencies, as annotated, are seen. These new frequencies are referred to as heterodyne frequencies.

the number of heterodyne frequencies also varies. For instance, nonlinear mixing resulting in the product of the two input signals ( $a(t) \times b(t)$ ) results in the formation of two heterodyne frequencies: the summation and difference, while  $a(t)^2$  returns only one heterodyne and  $a(t)^2 \times b(t)$  returns five heterodyne frequencies:  $f_a - f_b$ ,  $2f_a - f_b$ ,  $f_a + f_b$ ,  $2f_a$ , and  $2f_a + f_b$ . Through the knowledge of the particular heterodyne frequencies present, one can potentially infer the combination of the input signals, though contributing system nonlinearities may complicate this analysis. It should also be possible to learn even more through the analysis of the spectral amplitudes.

When considering the application of this technique to chemical reaction schemes, the mixing of radio or television signals translates to the mixing of chemical species. If the reaction is nonlinear (i.e. second order or higher reaction kinetics), the mixing of reactants will result in the production of heterodyne frequencies. Discrepancies between previously determined reaction models and experimental data arising from this technique, in terms of the presence or absence of certain heterodyne frequencies, might illuminate any disagreements in the kinetics controlling the reaction and the presence of formerly unknown reaction intermediates. This technique, therefore, has the potential to clarify chemical reaction schemes, as well as the kinetics governing those reactions.

While the application of this signal elucidation technique to the analysis of oscillating chemical signals in a biological network may be tantalizing, the complexities of the response may produce unexplainable, contradictory data without the *a priori* knowledge of oscillatory chemical signals on a simplified chemical reaction. In order to validate this platform and analysis technique on a chemical reaction, two non-cellular reaction networks will be used, specifically heavy metal quenching of fluorescein and peroxyoxalate chemiluminescence. As the product of



both of these reactions is light, an optical read-out can be used, thus avoiding any intrusive reaction monitoring methods.

The basis for this heterodyne technique lies in the conversion of time domain data into the frequency domain, which can be done through a Fourier transform. For the analysis of discrete data sampled from a continuous source, such as light emission, the Fast Fourier transform (FFT) is used, specifically with the Cooley-Tukey algorithm<sup>27-29</sup>. With the powerful capabilities of the FFT, it is possible to assess reaction product data in the frequency domain.

### 3.3.1 Heterodyne Models of Nonlinear Reactions

Chemical reaction models for both fluorescein quenching and peroxyoxalate chemiluminescence were created in Matlab for verification of data analysis techniques and experimental data comparison.

#### *3.3.1.1 Fluorescence Quenching Model*

Fluorescence excitation, emission, non-radiative decay and quenching are regularly represented with the set of equations shown in Figure 3.2. With low concentrations of the quenching agent, the reaction has been shown to follow the Stern-Volmer relationship

$$\frac{I_0}{I} = 1 + k_Q \tau_0 [Q] \quad (1)$$

where  $k_Q$  is the rate constant of the quenching reaction,  $I$  is the fluorescence intensity under steady-state conditions,  $I_0$  is the fluorescence intensity in absence of the quencher,  $\tau_0$  is the fluorescence lifetime, and  $[Q]$  is the quencher concentration. This relationship indicates a linear correlation between quencher concentration and fluorescence intensity, providing  $k_Q$  is not

dependent on the quencher concentration. However, fluorescence quenching has been shown to behave nonlinearly under circumstances with high concentrations of the quencher<sup>30</sup>. While several mechanisms of fluorescence quenching have been described<sup>31,32</sup>, including collisional

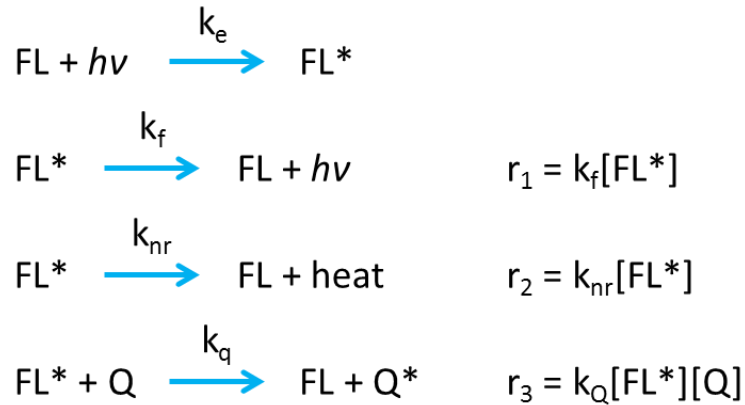


Figure 3.2 Reaction Rate Equations for fluorescein excitation, emission, non-radiative decay and quenching.

electron transfer, excited complex formation, and static quenching, a method of fully describing the complex reaction kinetics of fluorescence quenching has not yet been developed.

Heavy metal quenching of fluorescein with iodide was selected as the specific quenching relationship to inspect<sup>33,34</sup>. Matlab was utilized to create a model of fluorescein quenching with iodide based on the equations shown in Figure 3.2 (excitation was not included) along with rate constants  $k_f$  and  $k_{nr}$  as described by Arik et al.,<sup>35</sup> and  $k_q$  approximated as

$$k_q \approx k_{diff} = \frac{4\pi RND}{1000}, \quad (2)$$

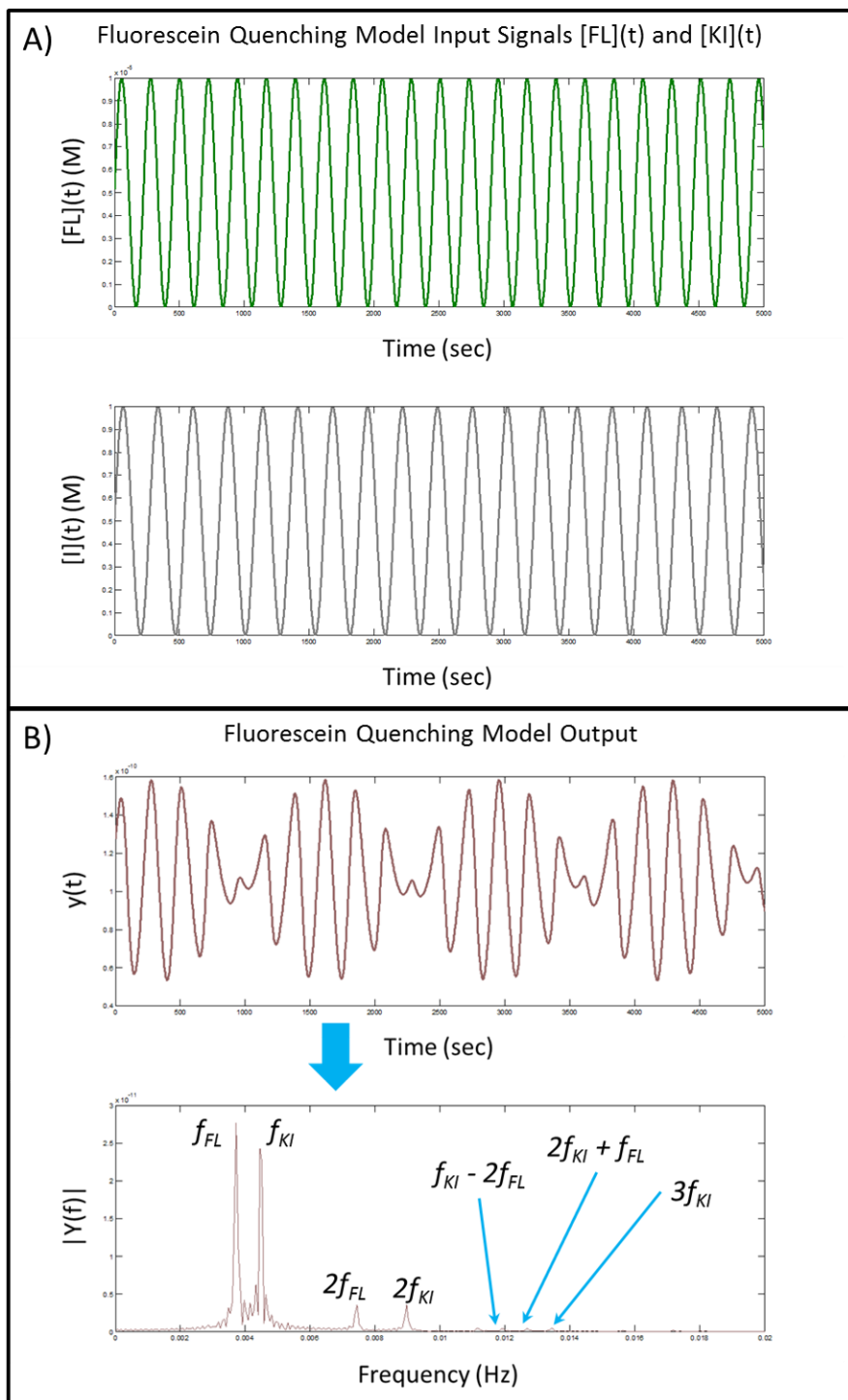


Figure 3.3 Fluorescein Quenching Model A) Input sinusoidal concentration profiles for fluorescein (green) and potassium iodide (grey). The periods of KI and FL were 223 seconds and 269 seconds. B) Display of simulated raw data for a fluorescein quenching reaction with the frequency domain of this simulated raw data set revealing the drive frequencies as well as a few summation and difference frequencies (values with assignments appear in Table 3.2.

where  $R$  is the sum of the molecular radii of the fluorophore and quencher,  $N$  is Avogadro's number, and  $D$  is calculated from the sum of the diffusion coefficients of the fluorophore and quencher<sup>35</sup>. Each concentration vector was specified by a sinusoidal concentration wave, either according to non-constant flow or constant flow. The amplitude, frequencies,  $y$  offset and phase offset were modeled to replicate the experimental conditions. The resulting simulated data for the rate of light emittance over time for a two pump, variable flow setup is displayed in Figure 3.3A. The FFT of this simulated raw data was taken and peaks were annotated as shown in Figure 3.3B and Table 3.2. While this model only considers the reaction kinetics and thus, does not incorporate the channel dimensions or diffusion of chemical species, it does provide theoretical verification of the heterodyne technique.

Table 3.2 Fluorescein quenching drive and heterodyne frequencies corresponding to the data shown in Figure 3.3.

Frequency (Hz)	Assignment
0.003719	$f_{FL}$
0.004482	$f_{KI}$
0.007439	$2f_{FL}$
0.008965	$2f_{KI}$
0.01192	$f_{KI} + 2f_{FL}$
0.01268	$2f_{KI} + f_{FL}$
0.01345	$3f_{KI}$

### 3.3.1.2 Peroxyoxalate Chemiluminescence Model

Peroxyoxalate chemiluminescence can be described with the equations shown in Figure 3.4 in which hydrogen peroxide ( $\text{H}_2\text{O}_2$ ) reacts with bis(2,4,6-trichlorophenyl) oxalate (TCPO) to produce an intermediate (D), which then dissociates further into intermediates C and E. Intermediate E transfers electrons to a fluorophore, Rubrene (Rub), causing it to become excited and emit light. This reaction is the basis for glow sticks. Peroxyoxalate chemiluminescence has been defined by second order chemical kinetics for both reaction 1 and 2 and would be expected to produce a complicated frequency spectrum of heterodynes based upon the summations and differences of the three reactants.

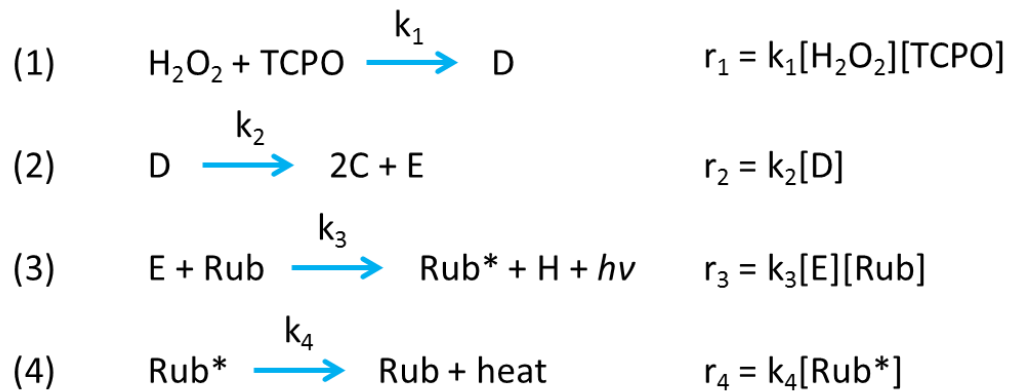


Figure 3.4 Reaction rate equations for peroxyoxalate chemiluminescence in which species C, D and E are reaction intermediates.

A Matlab model of the peroxyoxalate chemiluminescence reaction was created based on the equations in Figure 3.4, along with rate constants as described by Comstock et al.<sup>36</sup>. Sinusoidal concentration profiles for Rubrene, TCPO and  $\text{H}_2\text{O}_2$  were specified with parameters consistent with those of the physical experiment. The periods of Rubrene, TCPO, and  $\text{H}_2\text{O}_2$  were set as 223 seconds, 269 seconds, and 307 seconds to mimic the physical experiment as well. The

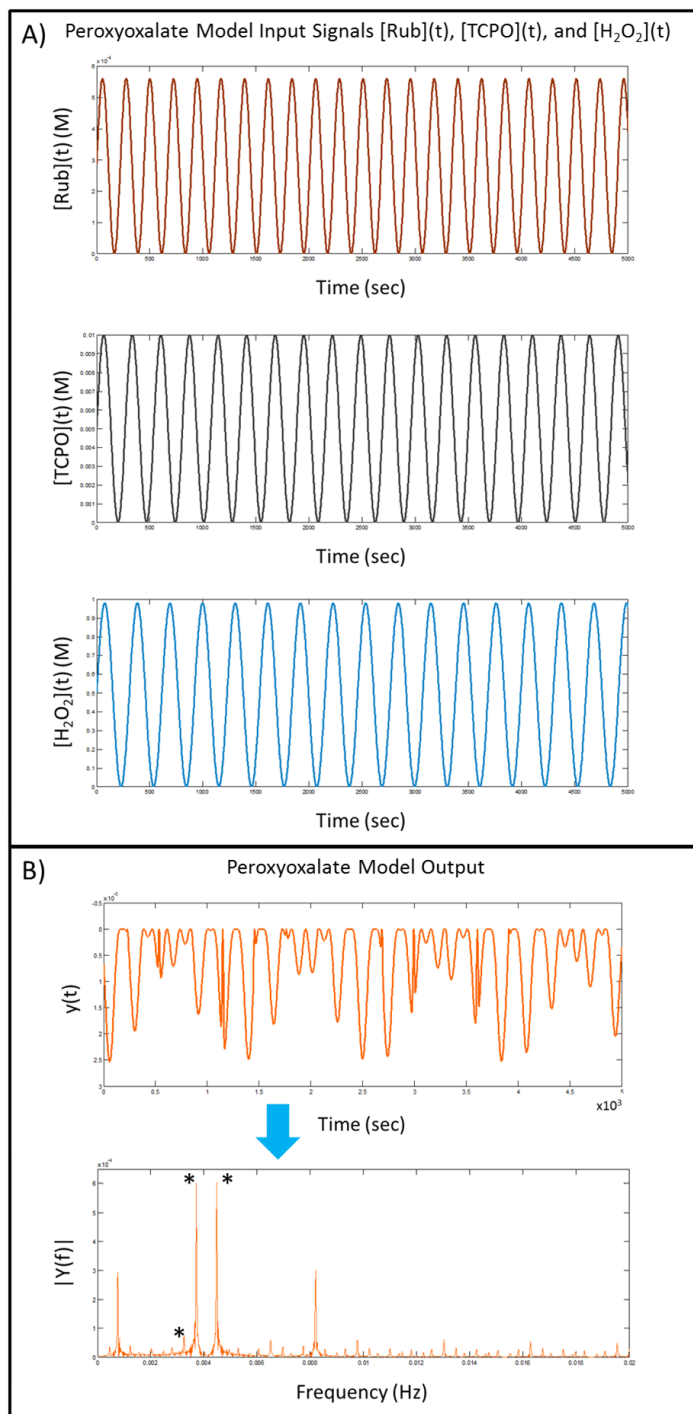


Figure 3.5 Peroxyoxalate Chemiluminescence Model. A) Input sinusoidal concentration profiles for Rubrene, TCPO, and H<sub>2</sub>O<sub>2</sub> oscillating at periods of 223, 269, and 307 seconds. B) The simulated raw chemiluminescence data is shown with the fluorescence signal scale inverted to adhere to the experimental data convention of increase in signal intensity in the downward direction. Exploring the frequency domain returns many heterodyne frequencies as listed in Table 3.3. The amplitude of the drive frequency of H<sub>2</sub>O<sub>2</sub> is much lower than expected. Drive frequencies are labeled with an asterisk.

Table 3.3 Peroxyoxalate chemiluminescence drive and heterodyne frequencies corresponding to the data shown in Figure 3.5.

Frequency (Hz)	Assignment
0.0004578	$f_{TCPO} - f_{H2O2}$
0.000763	$f_{Rub} - f_{TCPO}$
0.001240	$f_{Rub} - f_{H2O2}$
0.002022	$2f_{H2O2} - f_{Rub}$
0.002804	$2f_{H2O2} - f_{TCPO}$
0.003262	$f_{H2O2}$
0.003719	$f_{TCPO}$
0.004482	$f_{Rub}$
0.004959	$f_{Rub} + f_{TCPO} - f_{H2O2}$
0.006065	$3f_{H2O2} - f_{TCPO}$
0.006523	$2f_{H2O2}$
0.006981	$f_{TCPO} + f_{H2O2}$
0.0077744	$f_{Rub} + f_{H2O2}$
0.008202	$f_{Rub} + f_{TCPO}$
0.009766	$3f_{H2O2}$
0.01022	$3f_{Rub} - f_{H2O2}$
0.01055	$2f_{TCPO} + f_{H2O2}$
0.01101	$f_{Rub} + 2f_{H2O2}$
0.01146	$f_{Rub} + f_{TCPO} + f_{H2O2}$
0.01226	$2f_{Rub} + f_{H2O2}$

resulting simulated raw data along with the FFT of this data is shown in Figure 3.19. The drive (bold) and heterodyne frequencies are labeled. As this model requires three reactants compared to the two for the fluorescein quenching model, the data has an added degree of complexity as three drive frequencies combine to produce the frequency spectrum (sum and difference frequencies are a combination of a, b, and c instead of just a and b).

This model, like that of the fluorescein quenching, lacks the added complexity of diffusion and laminar flow in the serpentine mixer used for the physical experiment. Though only concerned with the reaction itself, the model does provide insight into the heterodyne data analysis techniques for nonlinear chemical reactions with three reactants. Further model manipulations including varying the reaction rate constants and the initial concentrations are available in Appendix D along with the Matlab code for the models. We find that alterations in the reactant concentrations and reaction rate constants demonstrate a change in peak amplitude in the frequency domain, though no shift in peak frequencies are seen. Further analysis of these and additional simulations should be completed to fully understand the dependence of the peak amplitudes on the concentrations and rate constants.

#### 3.4 Development of Hardware and Data Analysis Methods for Heterodyne Chemistry

The heterodyne-based platform developed herein for the study of these oscillatory chemical signals must include instrumentation for modulating sinusoidal concentration via flow rate, a microfluidic mixer for the combination of two or more unique chemical frequencies, a detector for acquiring reaction product data, and a data analysis technique for processing the output signal into the frequency domain.



### 3.4.1 Sinusoidal Concentration Generation

The generation of sinusoidal concentration profiles is paramount to this work. While a variety of options is possible, in theory, a low-volume, low-cost, highly adaptable option is desirable. To achieve these desired criteria, we turn to microfluidic-based approaches.

#### *3.4.1.1 Literature Examples*

The generation of sinusoidal concentration profiles for simulating in vivo non-linear dynamics requires sophisticated and expensive flow systems. Several groups have pioneered work on producing microfluidic variable concentration generators, often incorporating valves and pumps (examples shown in Figure 3.6). Mosadegh et al. produced a microfluidic oscillator using switch valves and check valves to convert a constant infusion of fluid into an oscillating output<sup>37</sup>. Azizi and Mastrangelo created a microfluidic pulsed waveform generator capable of simulating rat striatum dopamine release, beta cell intracellular calcium oscillations and beta cell extracellular insulin secretion<sup>38</sup>. A microfluidic device for the production of sinusoidal glucose concentrations has been shown to allow for the entrainment of pancreatic islets<sup>24,39</sup>. The same research group has also produced a microfluidic multi-analyte gradient generator capable of independent sinusoidal control of up to four different chemical species<sup>40</sup>. Through the use of these or similar non-linear concentration generators, it is possible to more closely simulate upstream signaling dynamics, leading to a cellular response to stimulus that more closely mimics the in vivo response. With a sinusoidal concentration generator paired with a method of analyzing cell response data, the influence of the sinusoidal signal component could be revealed, providing another tool for describing, modeling and analyzing complex biological systems.

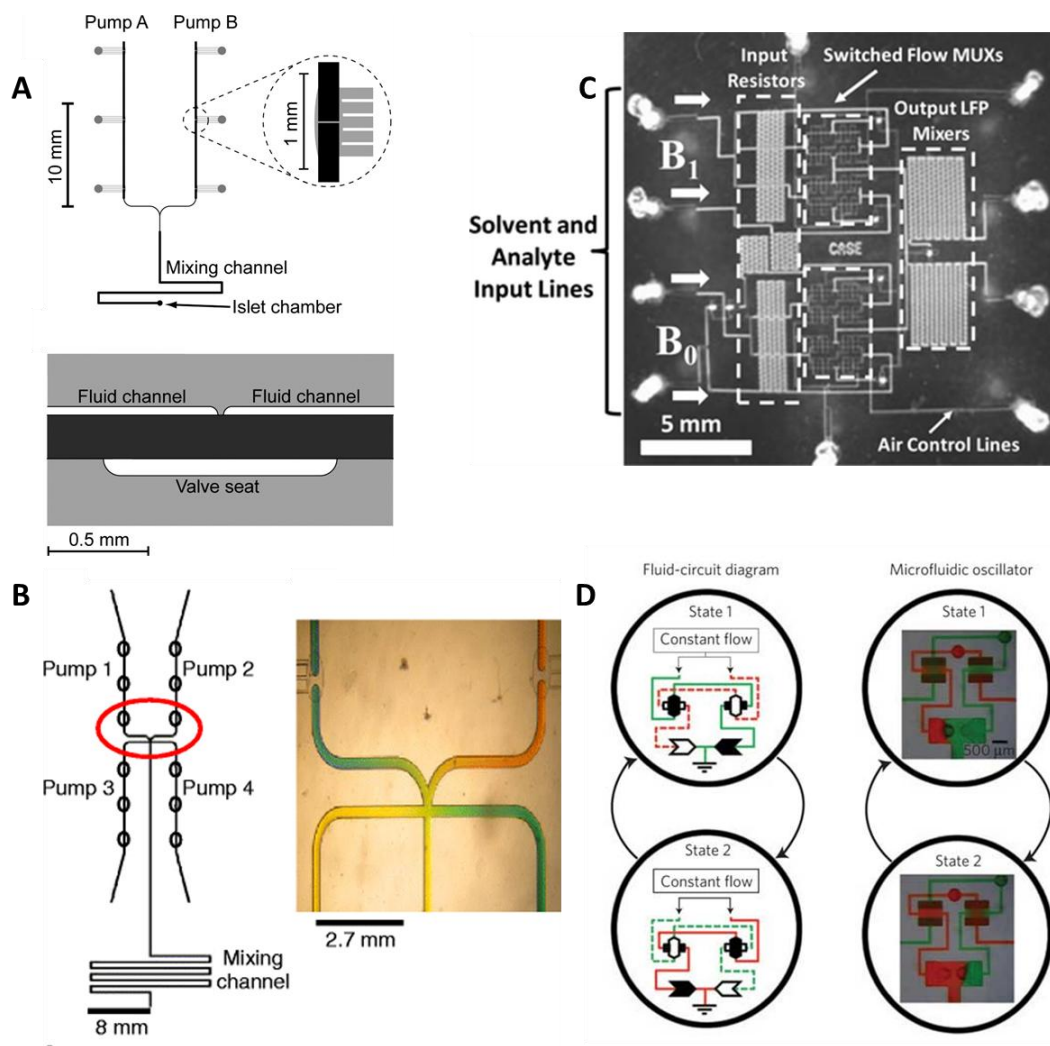


Figure 3.6. Examples of microfluidic sinusoidal concentration generators. (A) and (B) are designs from the same group incorporating pumps and a series of valves to produce independently controllable sinusoidal concentrations<sup>24,39,40</sup>. (C) employs a pulse code modulator comprised of a multiplexer with a low pass filter and digitally encoded clock signals to generate a variety of waveforms<sup>38</sup>. (D) depicts a design for a microfluidic oscillator capable of converting constant flow into an oscillating output through the use of both switch valves and check valves<sup>37</sup>.

### 3.4.1.2 Ideal Pumps

While the production of sinusoidal concentration profiles, as described above, has been described by a number of different groups, an additional means of generating these

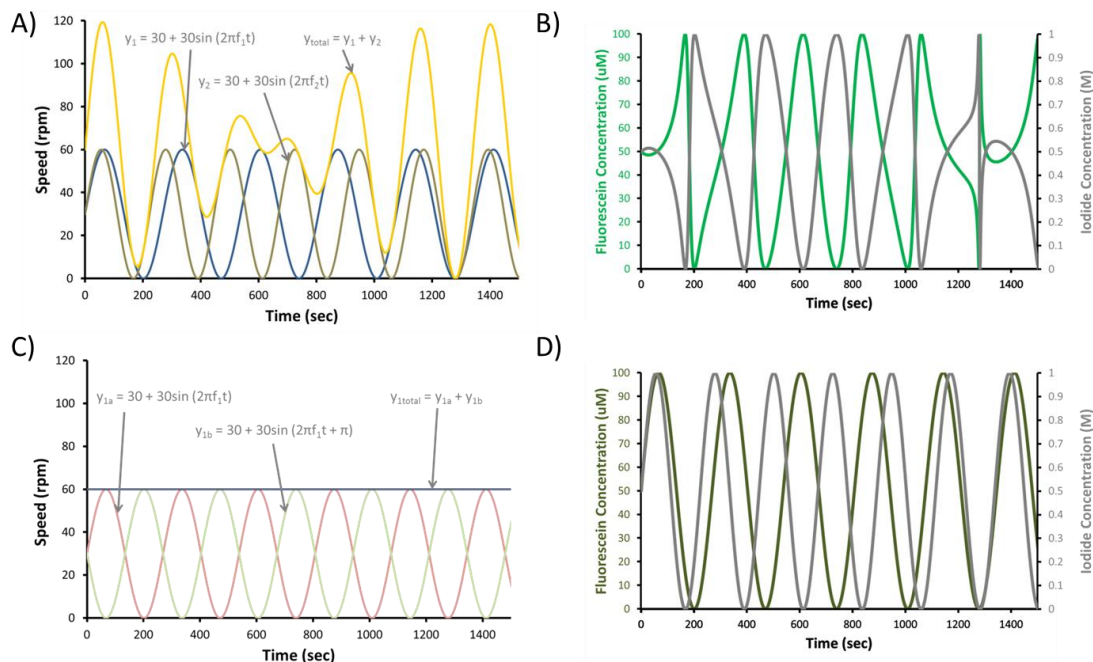


Figure 3.7 Multiple Pump Sinusoidal Concentration Profile Generation. A) Predicted individual (blue and gold) and pumps speeds (yellow) for a 2 pump setup driven sinusoidally at different frequencies with an amplitude of 30 rpm, y offset of 30 rpm.  $y_1$  (blue) has a period of 223 seconds, while  $y_2$  has one of 269 seconds. The total speed (yellow) is calculated from the sum of the individual speed profiles, indicating a non-constant total speed. B) The concentration profiles resulting from variable total flow rates are predicted for fluorescein and iodide based on initial concentrations of 100  $\mu\text{M}$  and 1 M, respectively. C) Using two pumps per reactant (red and green) run 180 degrees out of phase (with y offset = amplitude = 30 rpm), a constant total flow can be achieved. D) The resulting simulated concentration profiles for fluorescein and iodide are sinusoidal.

concentration gradients could be done solely through the use of pumps, thereby preventing limitations on the downstream applications of these variable flows.

Sinusoidal flow alone does not produce sinusoidal concentration profiles. Predicted speeds of a two pump system (blue and gold curves), with each pump running at a different frequency, can be seen in Figure 3.7A. The total speed calculated as the summation of the two sinusoidal speeds is variable (yellow curve) and will, as a result, fail to produce true sinusoidal

concentration profiles. Variable flow concentration profiles are predicted for fluorescein and iodide as shown in Figure 3.7B.

In order to generate sinusoidal concentration profiles, two pumps are required per reactant with these pairs of pumps run with the same sinusoidal flow parameters, but 180 degrees out of phase from each other. Figure 3.7C predicts the speeds of two pumps (red and green curves) run in this manner, with the resulting summation of the speeds (blue curve) a constant. To achieve a sinusoidal concentration profile with this two-pump per reactant setup, one pump should contain the actual reactant, while the other should contain the solvent of the reactant. The resulting concentration profiles, predicted for fluorescein and iodide, with two pumps per reactant (a total of four pumps needed), are shown in Figure 3.7D. Both the variable total flow and constant total flow assume the need for a  $\gamma$  offset preventing the theoretical

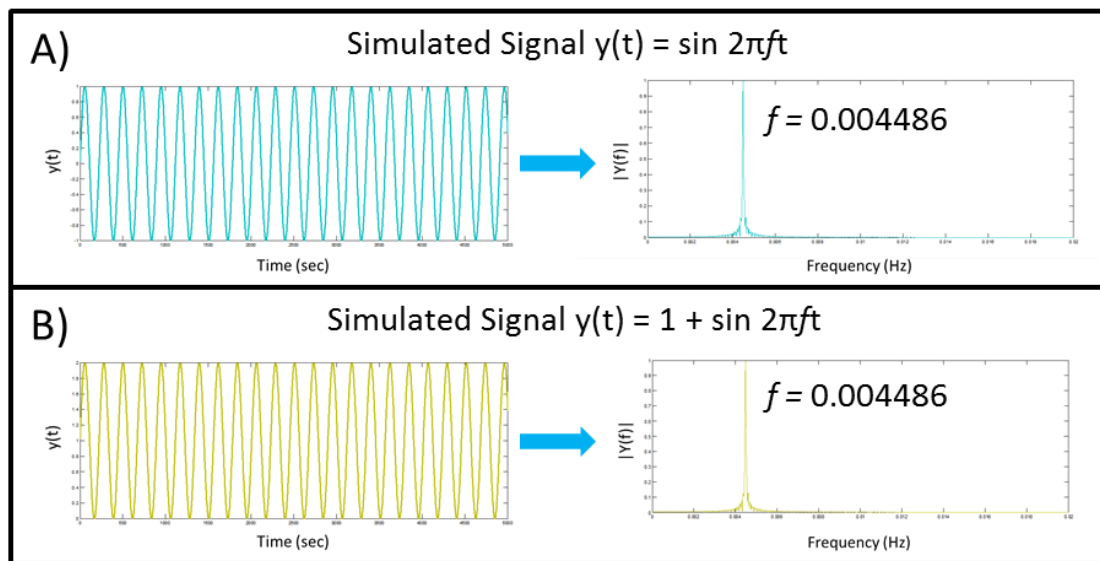


Figure 3.8  $\gamma$  offset contributions to frequency spectrum. A) Simulated signal for  $y(t) = \sin 2\pi ft$ , with  $f = 0.004484$  Hz, along with the frequency domain data showing the drive frequency. B) Simulated signal for  $y(t) = 1 + \sin 2\pi ft$ , with  $f = 0.004484$  Hz. The frequency domain data reveals no change upon the use of a  $\gamma$  offset. The magnitude of the drive frequencies are also the same (0.9973).

production of negative concentrations. By selecting a y offset equal to or greater than the amplitude, negative flows can be avoided. This y offset addition does not lead to any unforeseen discrepancy when analyzing the data in the frequency domain as evidenced by Figure 3.8. The FFT of a single sinusoidal signal with and without a y offset was performed, resulting in identical peaks at 0.004486 Hz (with identical magnitudes 0.9973) in the frequency domain.

Variable flow concentration profiles (Figure 3.7B) can be corrected to true sinusoidal profiles (Figure 3.9D) by adjusting by the total variable flow rate divided by a constant flow rate.

$$[FL](t)_{corrected} = [FL](t)_{variable} \times \frac{A \times (2 + \sin(2\pi f_1) + \sin(2\pi f_2))}{4A}, \quad (3)$$

where A is the amplitude of the speed profile (assuming A = y offset) and  $f_1$  and  $f_2$  are the frequencies of the pump driving fluorescein and the pump driving iodide. This correction factor can convert a single reactant's concentration profile. Correcting resulting light emission based on a second-order kinetic model, requires a slightly different application of this factor

$$[light](t)_{corrected} = [light](t)_{variable} \times \left( \frac{A \times (2 + \sin(2\pi f_1) + \sin(2\pi f_2))}{4A} \right)^2, \quad (4)$$

with variables as described above and a square of the correction factor to account for  $[light](t) = f[FL][I]$ . This correction factor allows data to be collected from variable flow conditions with one pump per reactant as described in Figure 3.7A (with subsequent correction) in addition to constant flow conditions described by Figure 3.7C with two pumps per reactant.

### 3.4.1.3 Rotary Planar Peristaltic Pumps

Rotary Planar Peristaltic Pumps (RPPM, VIIBRE, Vanderbilt University), as previously described<sup>41</sup>, are comprised of a NEMA-17 stepper motor, shaft collar, PDMS washer, thrust bearing, 5-channel PDMS device, and polycarbonate plate as shown in Figure 3.9. Pump construction begins with fabrication of silicon masters through photolithography techniques according to the manufacturer's specifications. 1) SU-8 2010 resist (MicroChem) was spun on a clean silicon wafer; 2) the wafer with resist was then soft baked; 3) the edge bead was removed;

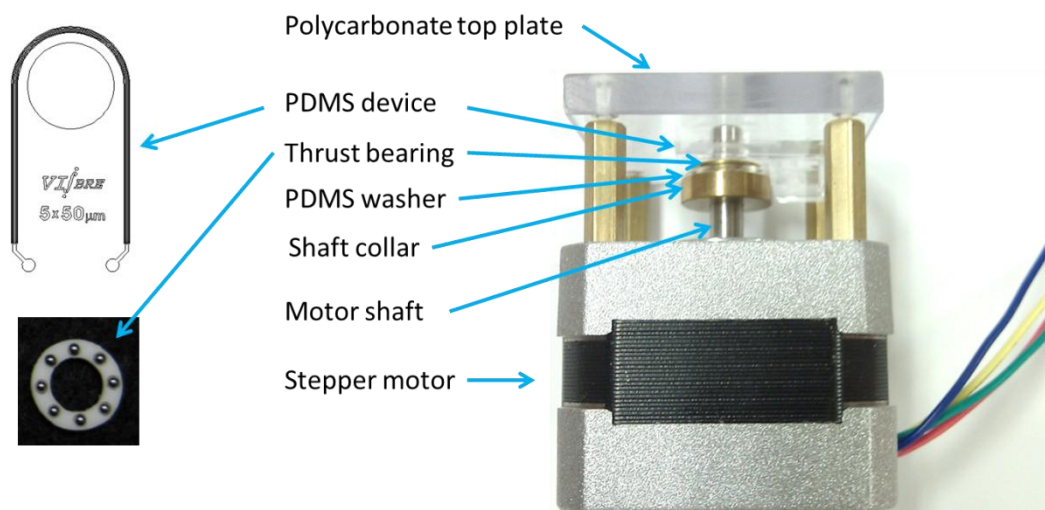


Figure 3.9 Rotary planar peristaltic micropump, shown in side view on the right is comprised of a stepper motor with its shaft coupled through a collar to a PDMS washer and thrust bearing that drive fluid flow through a PDMS device with 5, 50 $\mu$ m W x 20 $\mu$ m H channels.

4) the resist was exposed to UV light through the desired mask; 5) the wafer was again baked to finalize the crosslinking; 6) the patterned wafer was developed until non-cross-linked resist was fully removed; 7) then a final bake was performed to reduce stress in the remaining SU-8. PDMS (Sylgard Elastomer 184, Dow Corning, Midland, MI, in a 10:1 polymer to curing agent ratio) was spun onto the silicon master at 500 rpm for 1 minute and cured on a hot plate at 110°C. To

create a thicker region for punching inlet and outlet ports, a 2 mm x 7 mm x 13.5 mm solid PDMS punch layer was bonded to the cured, spun on PDMS channel layer by treating both surfaces with O<sub>2</sub> plasma (Harrick Plasma Cleaner, Ithaca, NY) and baking for 10 minutes at 110°C to complete the PDMS-PDMS bond. The channel and punch layer were cut and removed from the master and inlet and outlet ports created with a sharpened 25 gauge blunt tip. The device was then bonded to a 2 mm x 13.5 mm x 27 mm solid PDMS base layer by O<sub>2</sub> plasma treatment followed by baking for 10 minutes at 110°C and overnight at 70°C. 6 mm biopsy punches were used to create holes in the microfluidic device for the motor shaft. Devices were aligned to the polycarbonate plate and then assembled onto the stepper motor with shaft collar, PDMS washer and thrust bearing through the application of four screws to the top of the polycarbonate plate. Channels were aligned overtop of the ball bearings with the aid of a microscope. A compression trapeze was used to apply 3.9 N (400 g with gravity) to the area in contact with the ball bearings. Alignment was reconfirmed post-compression. Inlet and outlet ports were intubated with polyether ether ketone tubing (PEEK, 150 µm ID, 360 µm OD, Upchurch Scientific).

RPPMS were controlled with a custom stepper motor driver platform, consisting of an Arduino Duemilanove capable of controlling up to four Schmalzhaus EasyStepper boards, thus providing an integrated module capable of driving up to four RPPMs. In-house developed Arduino code allows for the generation of sinusoidal flow rates through the specification of the direction, half maximum speed in RPM (or half amplitude), y offset, phase offset, period and duration. Annotated code can be found in Appendix E. For verification of sinusoidal flow and calibration to overcome pump-to-pump variability, the Upchurch Scientific Nano Flow Sensor and software package was used.

### 3.4.1.4 Problems and Solutions

To provide verification for the sinusoidal concentration generation, the predicted speed profile, based on the Arduino stepper motor code, when driven sinusoidally was produced (Figure 3.10A). A noticeable discrepancy in the period was produced, resulting in the input frequency to predicted output frequency calibration curve in Figure 3.10B revealing a 0.56% error between the frequency input to the code and the predicted output. An RPPM was then driven with the same input parameters and the resulting flow rate was measured with the NanoFlow sensor (shown in Figure 3.10C). In addition to a larger period discrepancy, the

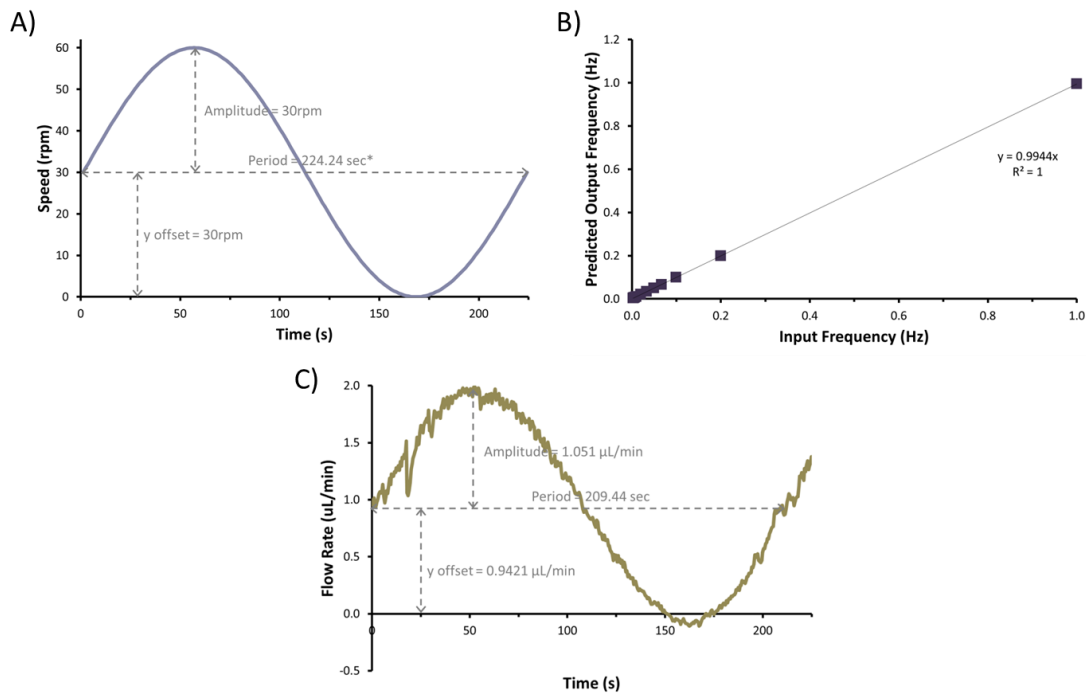


Figure 3.10 Single pump sinusoidal flow rate. A) One period of predicted sinusoidal pump speed profile with an amplitude of 30 rpm, y offset of 30 rpm and an input period of 223 seconds. The resulting output period is 224.24 seconds. B) Predicted output frequency based on 0.56% timing discrepancy in the Arduino code. C) Actual flow sinusoidal flow profile of a single pump with an input amplitude of 30 rpm, input y offset of 30 rpm and input period of 223 seconds. The resulting flow measured with the NanoFlow sensor indicates an amplitude of 1.051  $\mu\text{L}/\text{min}$ , a y offset of 0.9421  $\mu\text{L}/\text{min}$  and a period of 209.44 seconds.



amplitude and y offset drift apart leading a brief time of negative flow. While the NanoFlow sensor has a notoriously difficult time with calibration to zero flow, the negative speed leading to the negative flow rates can be observed by eye as the motor will reverse direction for a very brief time. To avoid this region of negative flow, the y offset can be adjusted 3 or 4 intergers above the set amplitude.

#### 3.4.1.4.1 Inter-pump Variation

Pump assembly, alignment and compression were highly scrutinized under magnification to achieve the most consistent results. Flows from seven RPPMs (1, 2a, 2b, 3a, 3b, 4a, 4b) were monitored with the NanoFlow sensor and software. Pumps are numbered as such indicating that, for example, the fluidic component of pump 2a and 2b are true replicates with precise dimensional control; likewise are pump fluidics 3a and 3b and 4a and 4b identical. This matching of pump fluidics is intended for reducing variation between pairs of pumps, though there are still differences as evidenced by Figure 3.11A. Table 3.4 shows the average output flow rates for each pump run at a constant speed of 79 rpm, as well as the resulting standard deviations. Resultant Analysis of Variance (ANOVA, single factor) performed on this pump data demonstrates statistically significant differences between pumps (results can be found in Appendix G). From the average output flow rate data, it is in theory possible to calibrate the pumps in order to control the output flow rate. Figure 3.11B displays the flow rates of six sinusoidally driven pumps with input amplitude of 41 rpm, y offset of 43 rpm and period of 37 seconds. The input and output parameters are shown in Table 3.5. The amplitude is calculated as half the peak to trough and reveals that the pumps do not trend in perfect agreement with the constant flow rate calibration scheme.

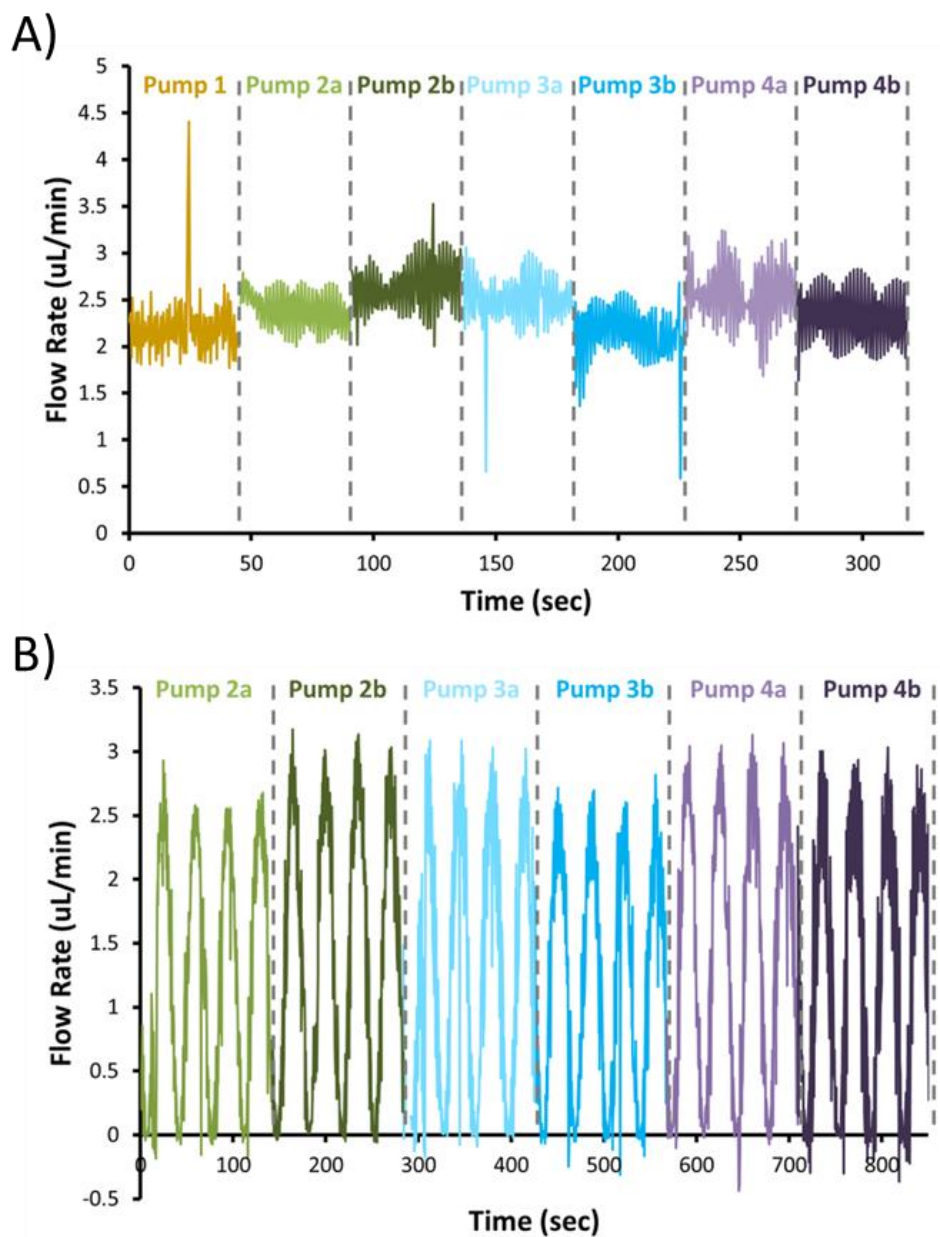


Figure 3.11 Pump Calibration. A) The variation in flow rate (as recorded by the NanoFlow sensor) between seven pumps set at the same constant speed (79rpm) is shown with average flow rates listed in Table 3.3. B) Six pumps driven sinusoidally each with an amplitude of 41 rpm, y offset of 43 rpm, and period of 37 seconds Pump 1 in this experimental setup always runs at a constant speed and was not analyzed for sinusoidal flow. The peak and trough flow rates, along with the output amplitude and y offset are reported in Table 3.4.

Table 3.4 Input speed and average resulting flow rates for constant speed calibration corresponding to Figure 3.11A.

	Input	Output	
	Speed [rpm]	Q [ $\mu\text{L}/\text{min}$ ]	St Dev [ $\mu\text{L}/\text{min}$ ]
<b>Pump 1</b>	79	2.199	0.346
<b>Pump 2a</b>	79	2.342	0.199
<b>Pump 2b</b>	79	2.644	0.300
<b>Pump 3a</b>	79	2.520	0.304
<b>Pump 3b</b>	79	2.151	0.308
<b>Pump 4a</b>	79	2.553	0.339
<b>Pump 4b</b>	79	2.317	0.322

Table 3.5 Input and output parameters for sinusoidal calibration corresponding to Figure 3.11 B.

	Input		Output			
	A [rpm]	y offset [rpm]	$Q_{\text{max}}$ [ $\mu\text{L}/\text{min}$ ]	$Q_{\text{min}}$ [ $\mu\text{L}/\text{min}$ ]	A [ $\mu\text{L}/\text{min}$ ]	y offset [ $\mu\text{L}/\text{min}$ ]
<b>Pump 2a</b>	41	43	2.688	-0.1439	1.416	1.272
<b>Pump 2b</b>	41	43	3.090	-0.0343	1.562	1.528
<b>Pump 3a</b>	41	43	3.060	-0.0759	1.568	1.492
<b>Pump 3b</b>	41	43	2.709	-0.1941	1.452	1.258
<b>Pump 4a</b>	41	43	3.074	-0.1473	1.611	1.463
<b>Pump 4b</b>	41	43	2.968	-0.2963	1.632	1.336

#### 3.4.1.4.2 Matched Pump Pair Calibration

As mentioned previously, flow must be kept constant to produce a sinusoidal concentration profile. Figure 3.12A depicts a two pump setup in which both pumps run with the same amplitude, y offset and period, but one pump has a phase offset of 180 degrees. The

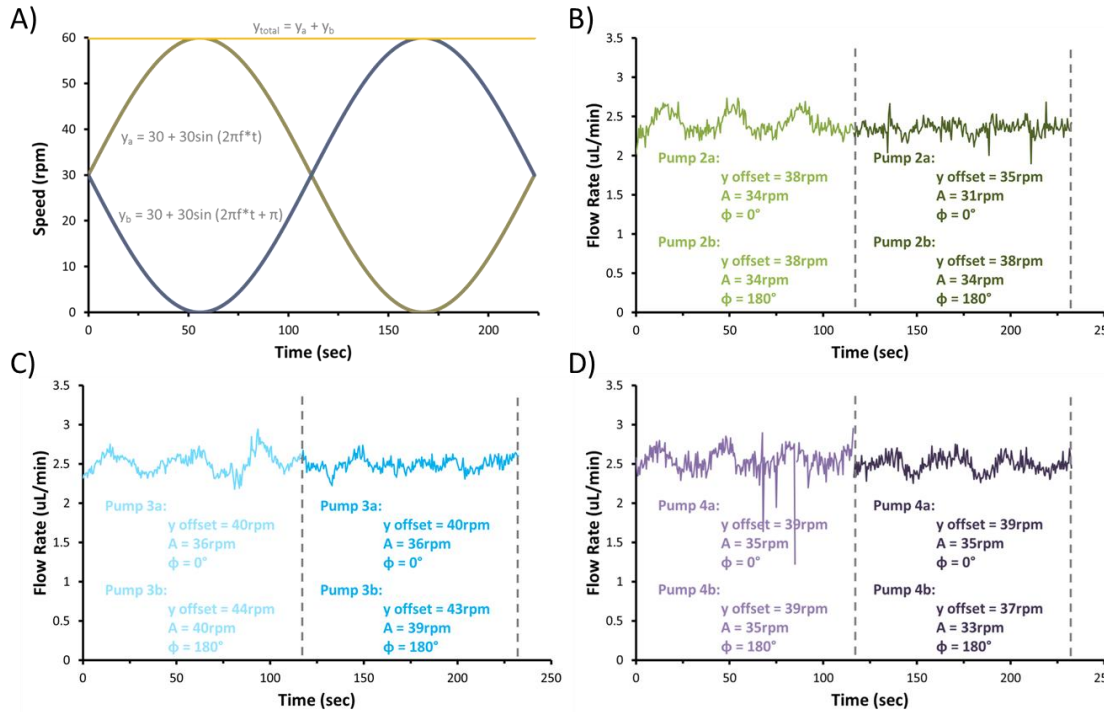


Figure 3.12 Sinusoidal Pump Calibration. A) The predicted speed profile in a 2 pump setup with pump b (blue) running 180 degrees out of phase from pump a (gold) with an amplitude of 30 rpm, a y offset of 30 rpm and a period of 223 seconds for both pumps. The summation of these two speed profiles produces a constant total speed. B), C) and D) show the pump calibration under sinusoidal control for each pair of pumps. For instance, pump 2a and 2b have the same input conditions, except 2b is offset by 180 degrees. The total theoretical flow rate produced should be constant. Yet the left half of B) shows oscillations. Pump 2a was adjusted to reduce the oscillations (right). The same procedure was used with pumps 3a and 3b and 4a and 4b, though the latter set was problematic in that the oscillations could not be alleviated entirely.

summation of these two speed profiles (blue and gold) produce a constant speed output (yellow). This sum of sinusoidal flows can be utilized in the calibration method as well. In order to calibrate sinusoidally driven pumps, flows from pairs of pumps with matching fluidic components were mixed together prior to entrance into the NanoFlow sensor. The expected flow rate is constant, providing the pumps are of the same flow rate. Figure 3.12B-D show an initial flow summation for each pair of pumps in which oscillations occur (left half of each

subplot). Once the amplitude and y offset are tuned properly, the oscillations diminish (right half of each subplot). Pump pair 4a and 4b, Figure 3.12D, was problematic as the oscillations could not be completely reduced.

#### 3.4.2 Chemical Signal mixing with a Microfluidic Reactor

Microfluidic reactors were designed with AutoCAD 2004It and sent to Infinite Graphics (Minneapolis, MN) for production of a mylar mask bearing the designs. Silicon masters were created by standard photolithography procedures. SU-8 2010 resist (MicroChem) was spun on a clean silicon wafer and baked. It was then exposed to UV light through a mask to crosslink the resist in the desired pattern. After baking again, the coated wafer was developed to remove any un-cross-linked resist. The finished master was then poured with Sylgard Elastomer 184 (Dow Corning, Midland, MI) in a 10:1 polymer to curing agent ratio and allowed to cure at 60°C. Cured polydimethylsiloxane (PDMS) was cut and removed from the wafer and inlet and outlet ports created. After treatment with O<sub>2</sub> plasma (Harrick Plasma Cleaner, Ithaca, NY), the PDMS was permanently bonded to glass cover slips. This process is shown pictorially in Figure 3.13.

#### 3.4.3 Detection of Light as Reaction Products

A detection strategy similar to that of flow injection analysis was designed to pair with continuous flow through a microfluidic reactor and the subsequent generation of light from the test chemical reactions chosen. While flow injection setups utilize a valve to control the introduction of a sample into a reagent flow stream for subsequent detection with or without reaction with the reagent, the desired design for the current analysis technique controls multiple reactant flow streams with pumps alone. This provides a means of controlling each

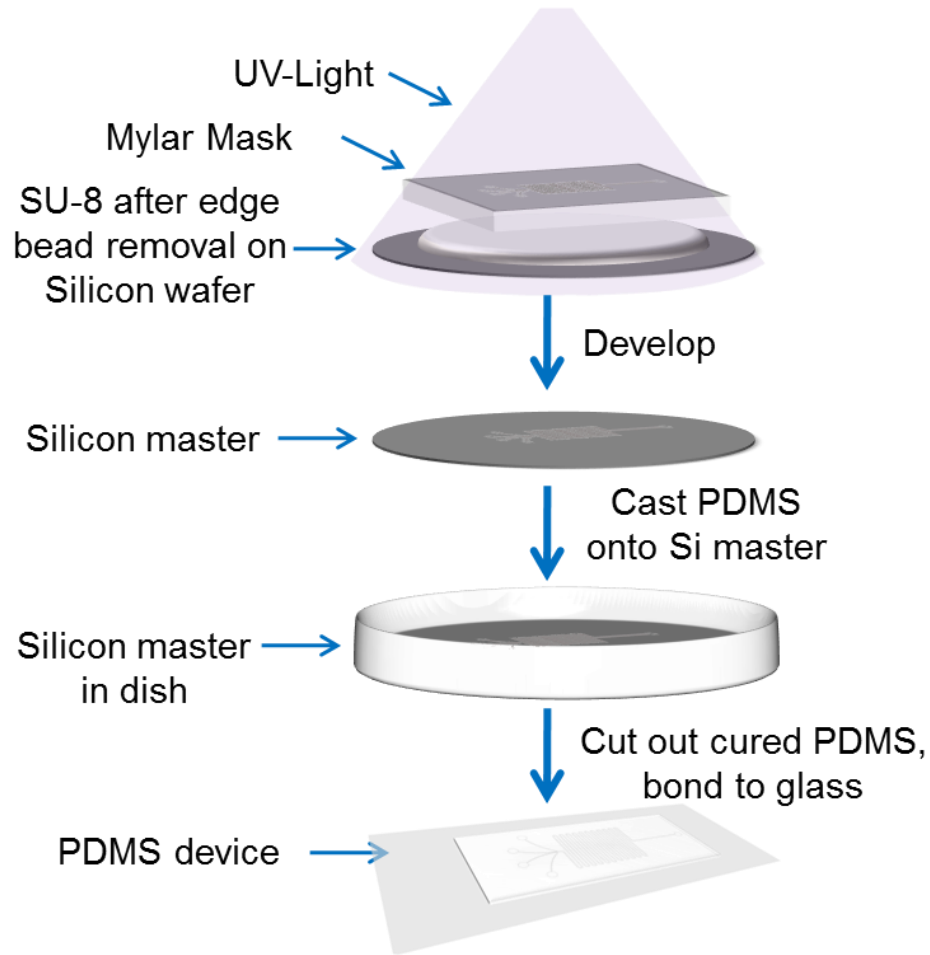


Figure 3.13 Microfabrication procedures for the production of microfluidic reactors involving photolithography and replica molding techniques.

individual reactant separately. Once reactants are mixed, the light produced can be detected.

The experimental setup as shown in Figure 3.14 includes a 20x objective (LD A-Plan 20x/0.3 Ph1, Zeiss) coupled to a photomultiplier tube (PMT, H5784-20, Hamamatsu). PMT output was amplified (20 dB boost, gain of 7-8), filtered (low pass at 20Hz) and collected for analysis by a USB data acquisition card (NI USB-6009, National Instruments). Labview 10 (National Instruments) was used for acquiring data. Fluorescence excitation was accomplished through the use of a 440 nm Solid State, Diode Pumped, Continuous Wave 25 mW Laser (Crystal

Laser) coupled with a narrow band 442 nm excitation filter set with bandpass emission (Chroma Z442BP). Control of the flow of reactants through the microfluidic reactor was achieved by computer controlled microfluidic Rotary Planar Peristaltic Pumps (RPPM, VIIBRE, Vanderbilt University). Flow was conducted through polyether ether ketone (PEEK, 150  $\mu\text{m}$  ID, 360  $\mu\text{m}$  OD, Upchurch Scientific) from reservoirs, through the RPPMs and into the microfluidic reactor. Pump flow rates were under sinusoidal control to vary the concentrations of reactants in the device. Prime number sine wave periods were selected to minimize overlap of the harmonics during the course of the experiment.

The Continuous Flow Photometer (CFP) was successfully developed for both fluorescence and chemiluminescence applications. The fluorescence applications involved the

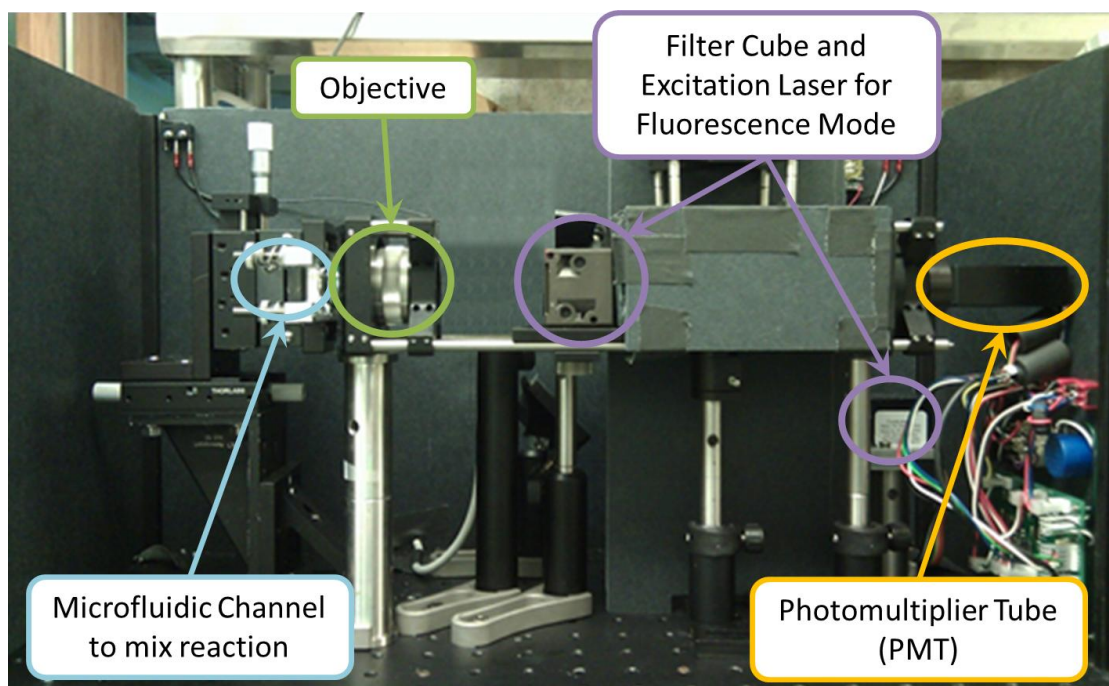


Figure 3.14 Continuous Flow Photometer (CFP) for both chemiluminescence and fluorescence studies with the inclusion of excitation laser and filter set specific to fluorescence measurements of fluorescein.

use of a filter set and excitation laser specific for fluorescein, while the chemiluminescence applications do not. To investigate the capabilities of the CFP for detecting varying concentrations of fluorescent signal, several fluorescein standards (0  $\mu\text{M}$ , 50  $\mu\text{M}$ , 66.7  $\mu\text{M}$ , 80  $\mu\text{M}$  and 100  $\mu\text{M}$ ) were run at a constant rate to produce a standard curve (shown in Figure 3.15A). To test the CFP for sinusoidal fluorescence applications, a single RPPM was sinusoidally driven with a period of 269 seconds or 223 seconds and the FFT was taken of resulting raw data to produce frequency spectra (Figure 3.15B, C respectively). The output drive frequency is bolded and errs from the input frequency according to the calibration plot in figure 3.15E. The ability of the CFP to determine inter-pump variability by means of the drive frequency output was investigated. Upon performing an FFT on the raw voltage time series data produced by driving two pumps under the exact same conditions, a greater shift from the expected output frequency is revealed perhaps as a result of inter-pump variability. The data analysis techniques are robust in that regardless of the shift in output frequency, the harmonics calculated based upon this output drive frequency are exact matches (0.06% error based on the peaks in B-D) for those found in the spectra (Figure 3.15D).

To further investigate the discrepancy with the period, the experimental data from the fluorescein quenching experiments incorporating the use of the CFP were used to produce a curve of input frequencies and actual output frequencies (Figure 3.15E). This data reveals an even greater discrepancy in pump period at 5.83%. Since the periods are selected as prime numbers between 3 and 6 minutes to avoid overlapping harmonics, the actual value of these numbers lacks significance beyond this. Adjusting the input frequency based on this curve is futile to a certain extent as the Arduino stepper motor code requires intergers, preventing the production of an actual 223 second period. To test for the CFP's performance with sinusoidal concentration profiles, a pair of pumps was driven with amplitudes and y offsets based upon the



calibration work. One pump was set to run out of phase from the other. The raw data and resulting frequency spectrum of a very short data set are show in Figure 3.16.

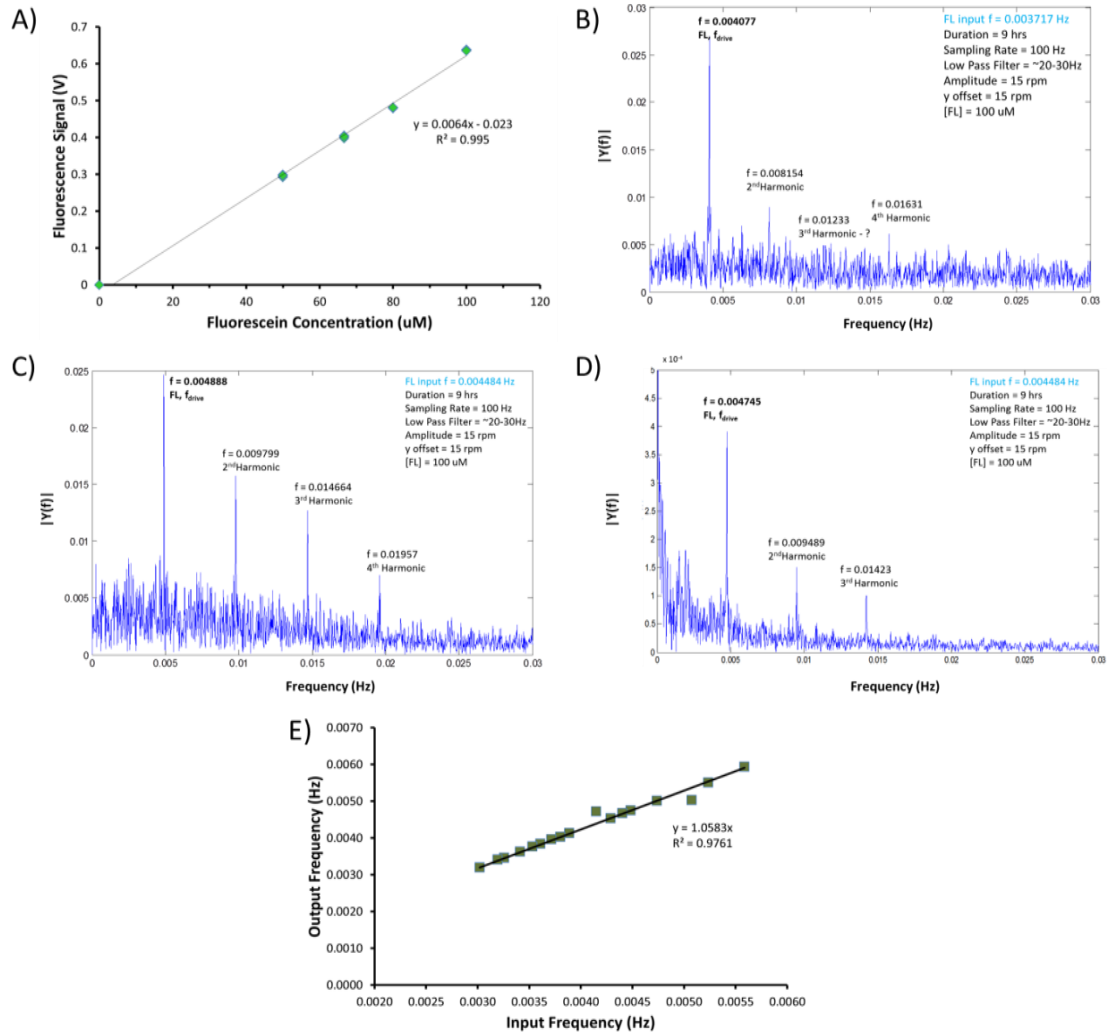


Figure 3.15 CFP evaluation. A) Standard curve for varying concentrations of fluorescein (0  $\mu\text{M}$ , 50  $\mu\text{M}$ , 66.7  $\mu\text{M}$ , 80  $\mu\text{M}$  and 100  $\mu\text{M}$ ) run at constant flow rates. B) and C) show single pump sinusoidal flow (constant concentration) frequency spectra with periods of 269 seconds and 223 seconds and input parameters as indicated. D) Two non-calibrated pumps were run under identical parameters (sinusoidal flow, constant concentration), including the periods, to determine differences in the frequency spectrum as a result of inter-pump variability. The output drive frequency has shifted from that of the input frequency = data (from 0.004888 Hz to 0.004745 Hz). E) Actual output frequencies based on experimental data showing a 5.83% discrepancy between input frequency parameters and resulting frequencies in the experimental data.

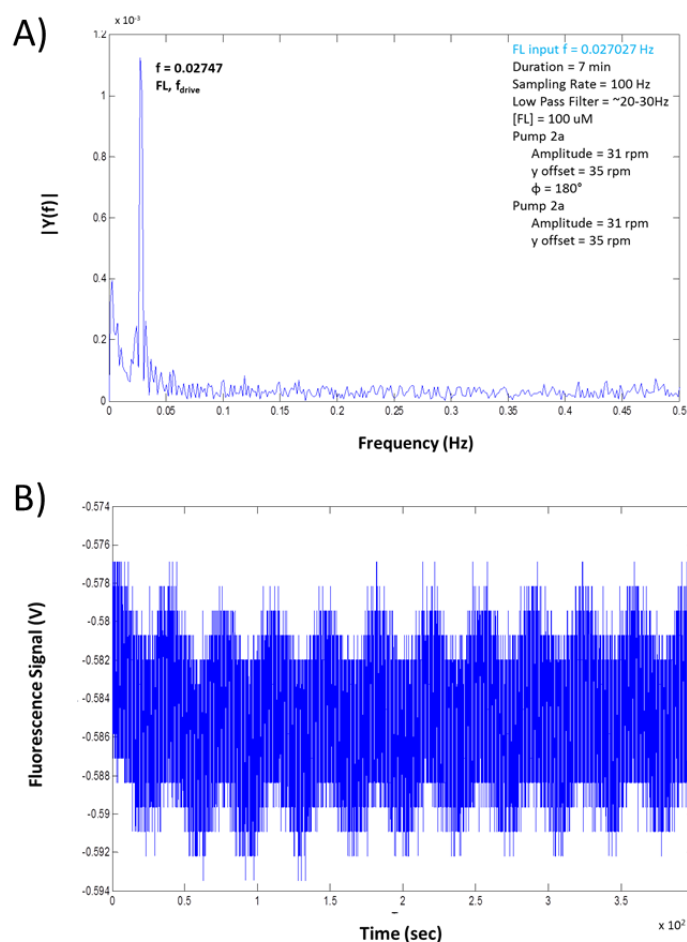


Figure 3.16 CFP detection of sinusoidal concentration profiles. A) The frequency output expected from a 37 second period of oscillations produced an output frequency of 0.02747 Hz (error of 1.6% from the theoretical value). B) shows the raw data of the 400 second data acquisition.

#### 3.4.4 Fourier Transform Analysis

In order to achieve sufficient resolution of the frequency spectra, experiment durations were selected so as to collect at least 100 periods of the reactant driven at lowest frequency. Raw voltage data collected by the PMT and read and digitized by Labview (as a 63 bit .tdms file) was converted to Matlab with an in-house developed TDMS reader capable of down-converting the data into 16 bits without decimation and loss of resolution. Data were detrended (or zero

meaned) and a fast Fourier transform was then performed using Matlab's built in FFT function. All Matlab data analysis scripts are available in Appendix F. Resulting frequency domain data were processed for peaks at least three times greater than the noise level and assigned a peak descriptor as matched to calculated values in the McLaurin series expansion of nonlinear mixing (addition of multiple sin waves) based on the two or three output drive frequencies. 3D and surface plots of swept frequencies were constructed for data visualization. All errors reported were calculated based on the following equation.

$$\%Error = \left( \frac{\text{Measured}-\text{Actual}}{\text{Actual}} \right) \times 100\% \quad (5)$$

### 3.5 Nonlinear Chemical Reaction Exploration

Two chemical reactions were utilized to test the hardware system described in the previous section: fluorescence quenching and peroxyoxalate chemiluminescence. As this system is in its infancy, this data is considered highly preliminary and at most qualitative comparisons can be made between the model data and this experimental data.

#### 3.5.1 Fluorescence Quenching

##### *3.5.1.1 Experimental Parameters and Setup*

Fluorescence quenching was accomplished with 1 M potassium iodide (KI) and 100  $\mu\text{M}$  fluorescein (FL) in water (all chemicals from Sigma Aldrich). Two RPPMs connected to a microfluidic reactor housed in the CFP were first primed with ethanol and a background file with the laser engaged at 10 mW was collected. Reservoirs were replaced with the reactants, which were allowed to flow through at constant rates. Data sets for fluorescein quenching were

collected with the pump speeds of KI and FL sinusoidally varying from 0 to 60 rpm with an amplitude of 30 rpm (to prevent negative speeds) and periods ranging from roughly 3 to 6 minutes. Data was collected for 7-10 hours.

A two pump sinusoidal flow setup was used on all the fluorescein quenching experiments. As indicated previously, this type of two pump sinusoidal flow addition produces a variable total flow rate leading to a concentration profile as shown in Figure 3.18A. However, the correction methods described in section 3.4.1.2 can be applied to transform the data into those produced by concentration profiles that were true sinusoids. Pump one drew fluid from a reservoir of 100  $\mu$ M fluorescein in water, while pump 2 drew fluid from a reservoir of 1 M KI in water. After the two sinusoidal flows combine in the mixer (a 500  $\mu$ m W x 100  $\mu$ m H x 2 cm L microfluidic channel), the laser excitation and fluorescence detection occur within the same field of view of the objective ( $\sim$ 1 mm x 1 mm) (as shown in Figure 3.17). The time delay for this setup with two pumps running at 1  $\mu$ L/min each is 11 minutes from the pump to the measurement point.

#### *3.5.1.2 Data*

Fluorescein was run with a period of 269 seconds, while KI was run with a period of 223 seconds. Both had an amplitude of 30 rpm and y offset of 30 rpm. The oscillatory concentration profiles of both fluorescein and KI are shown in Figure 3.18A. The full time course of the experiment was 8 hours, though only a 1.4 hour section of the full time course data is shown to demonstrate the trends in the fluorescence signal (Figure 3.18B). After importing the raw data into Matlab, detrending and performing the FFT, the drive frequencies and heterodyne frequencies were annotated as shown in Figure 3.18B and Table 3.6 based on McLaurin series expansion. Both sum and difference frequencies are detected. Tabular forms of the theoretical

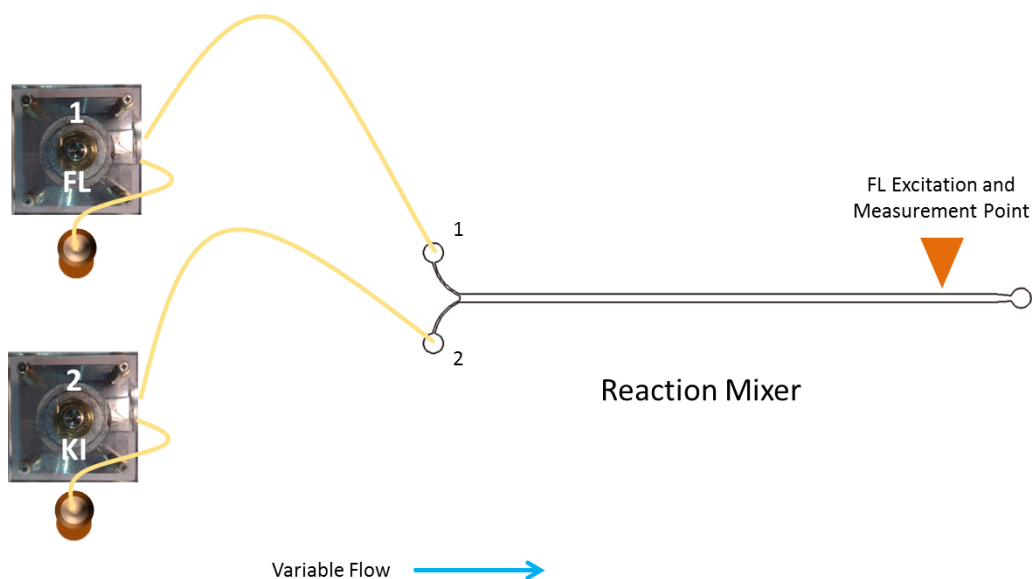


Figure 3.17 Experimental setup for fluorescein quenching with two RPPMs pumping FL and KI at a sinusoidal speed into a mixer (a  $500\ \mu\text{m}$  W x  $100\ \mu\text{m}$  H x  $2\ \text{cm}$  L microfluidic channel) that combines the flows into a variable total flow. The reaction mixer device is held in place on the CFP as shown in Figure 3.14. Laser excitation occurs through the objective on the CFP and fluorescence emission travels through the objective and the filter cube to the PMT for detection. The signal is converted to a voltage and is recorded in Labview 10 Signal Express.

heterodyne sum and difference frequencies specific to these experimental output frequencies are available in Appendix H. Comparing the actual heterodyne frequencies to those calculated based on the output drive frequencies results in a 0.03% average error.

Correction of this fluorescence data produced in a variable flow setup by means discussed in section 3.4.1.2 (equation 4) provides a method of converting the variable total flow results to constant total flow ones, and thus producing data corresponding to that collected in experiments with constant total flow. The corrected data set analogous to Figure 3.18 is shown in Figure 3.19. The annotated drive frequencies (**bold**) and heterodyne frequencies (Table 3.7) do not change upon data correction. Though the time-dependence of the raw data amplitudes are adjusted by this correction, the overall heterodyne and drive frequencies remain unaltered.

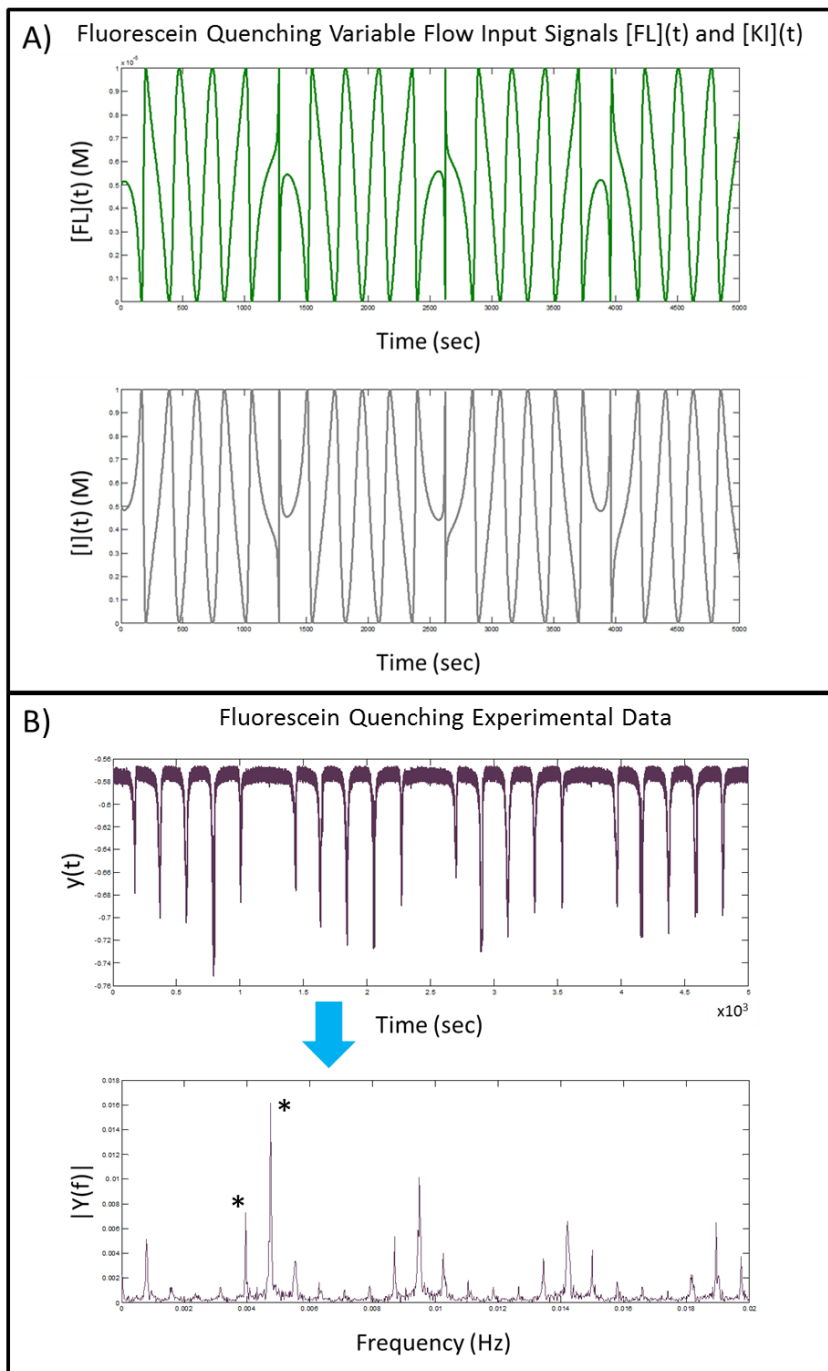


Figure 3.18 Fluorescein quenching sample data set with sinusoidal flow A) Fluorescein at 100  $\mu\text{M}$  was run with a period of 269 seconds, while KI at 1 M was run with a period of 223 seconds. Variable flow concentration profiles result. B) A portion of the raw fluorescence data from an 8 hour fluorescein quenching experiment with a two pump, sinusoidally driven, variable total flow setup is shown. After performing the FFT of the raw data, resulting heterodyne frequencies can be annotated as shown in Table 3.6 based on calculated values from the output driving frequencies with McLaurin series expansion. Drive frequencies are labeled with an asterisk.

Table 3.6 Fluorescein quenching experimental variable flow drive and heterodyne frequencies corresponding to the data shown in Figure 3.18.

Frequency (Hz)	Assignment
0.0007868	$f_{KI} - f_{FL}$
0.001597	$4f_{FL} - 3f_{KI}$
0.002360	$3f_{KI} - 3f_{FL}$
0.003147	$4f_{KI} - 4f_{FL}$
0.003958	$f_{FL}$
0.004745	$f_{KI}$
0.005555	$5f_{FL} - 3f_{KI}$
0.006294	$8f_{KI} - 8f_{FL}$
0.007105	$4f_{KI} - 3f_{FL}$
0.007915	$2f_{FL}$
0.008702	$f_{KI} + f_{FL}$
0.009489	$2f_{KI}$
0.010250	$8f_{KI} - 7f_{FL}$
0.011040	$9f_{KI} - 8f_{FL}$
0.011850	$5f_{KI} - 3f_{FL}$
0.012660	$2f_{FL} + f_{KI}$
0.013450	$2f_{KI} + f_{FL}$
0.014210	$8f_{KI} - 6f_{FL}$
0.015000	$4f_{KI} - f_{FL}$
0.015810	$5f_{KI} - 2f_{FL}$
0.016590	$6f_{KI} - 3f_{FL}$
0.017400	$2f_{KI} + 2f_{FL}$
0.018190	$3f_{KI} + f_{FL}$
0.018950	$9f_{KI} - 6f_{FL}$
0.019740	$5f_{KI} - f_{FL}$
0.020550	$6f_{KI} - 2f_{FL}$

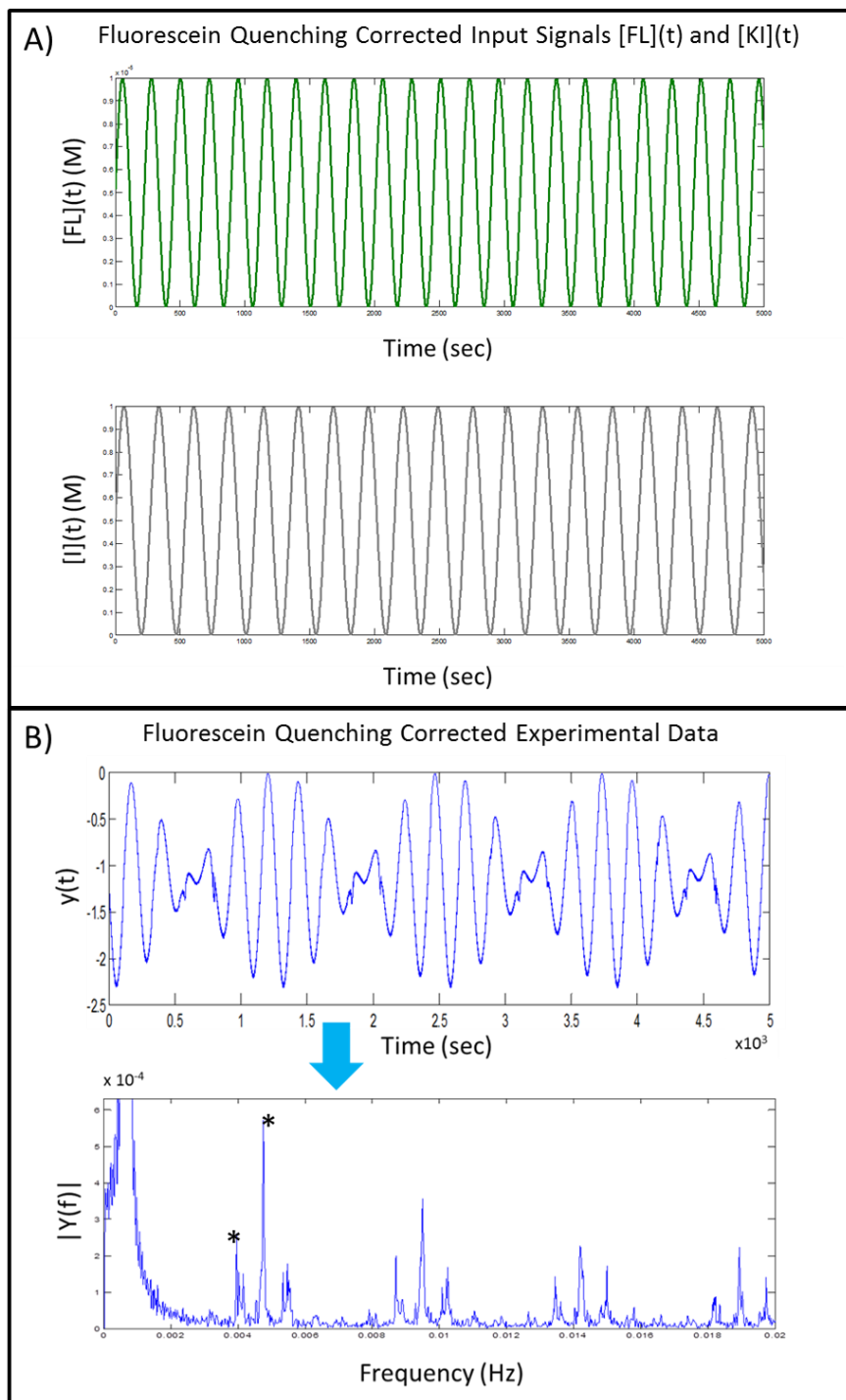


Figure 3.19 Fluorescein quenching sample data set corrected to correspond to sinusoidal concentration inputs. A) The input concentration profiles for FL and KI (periods of 269 and 223 seconds) shown in Figure 3.18A were corrected using equation (3) to show the conversion of oscillatory concentration profiles to sinusoidal ones. B) The data shown in Figure 3.18 was corrected using equation (4). The frequency domain of the corrected raw data reveals heterodyne and drive frequencies analogous to the non-corrected data set (Table 3.7). A large amplitude artifact of the DC offset appears, overshadowing the expected difference frequencies. Drive frequencies are labeled with an asterisk.



Table 3.7 Fluorescein quenching experimental corrected drive and heterodyne frequencies corresponding to the data shown in Figure 3.19.

Frequency (Hz)	Assignment
0.0007868	$f_{KI} - f_{FL}$
0.001597	$4f_{FL} - 3f_{KI}$
0.002360	$3f_{KI} - 3f_{FL}$
0.003147	$4f_{KI} - 4f_{FL}$
0.003958	$f_{FL}$
0.004745	$f_{KI}$
0.005555	$5f_{FL} - 3f_{KI}$
0.006294	$8f_{KI} - 8f_{FL}$
0.007105	$4f_{KI} - 3f_{FL}$
0.007915	$2f_{FL}$
0.008702	$f_{KI} + f_{FL}$
0.009489	$2f_{KI}$
0.010250	$8f_{KI} - 7f_{FL}$
0.011040	$9f_{KI} - 8f_{FL}$
0.011850	$5f_{KI} - 3f_{FL}$
0.012660	$2f_{FL} + f_{KI}$
0.013450	$2f_{KI} + f_{FL}$
0.014210	$8f_{KI} - 6f_{FL}$
0.015000	$4f_{KI} - f_{FL}$
0.015810	$5f_{KI} - 2f_{FL}$
0.016590	$6f_{KI} - 3f_{FL}$
0.017400	$2f_{KI} + 2f_{FL}$
0.018190	$3f_{KI} + f_{FL}$
0.018950	$9f_{KI} - 6f_{FL}$
0.019740	$5f_{KI} - f_{FL}$
0.020550	$6f_{KI} - 2f_{FL}$

As the frequencies are unchanged upon correction, the same average error of 0.03% describes the accuracy of the corrected data set as with the uncorrected spectrum.

Fluorescein quenching experiments with the two pump setup were explored with periods of fluorescein ranging from 179 seconds to 331 seconds, while keeping the period of KI constant at 223 seconds. The FFT frequency and amplitude are plotted against the swept frequencies of FL as shown in 3.20. As the data correction left the heterodyne and drive frequencies unchanged, the uncorrected data was used to construct the 3D plot to avoid the large amplitude DC offset component present after correction.

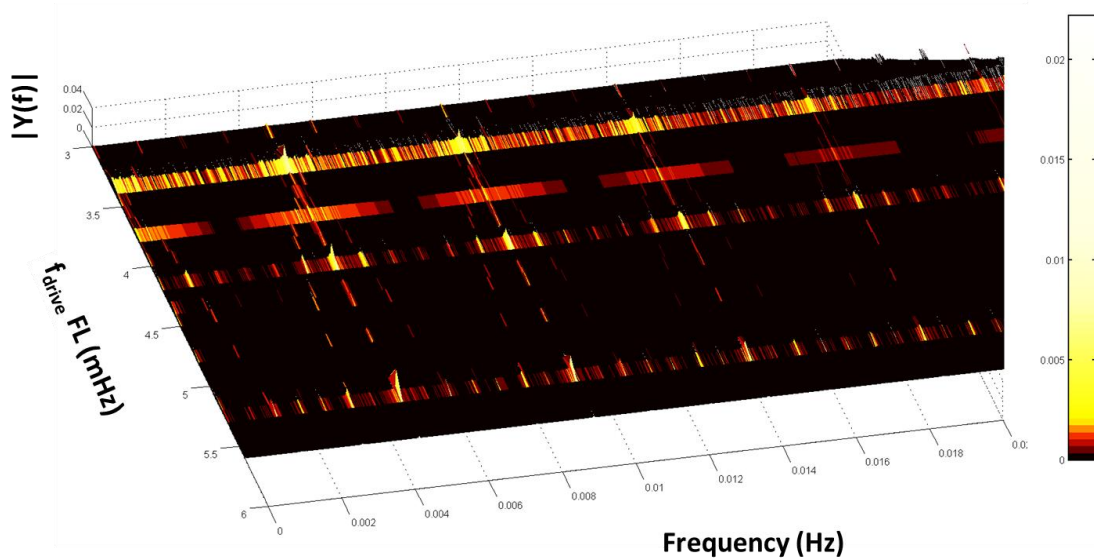


Figure 3.20 3D plot of varying FL drive frequencies from 0.005587 Hz to 0.003021 Hz with KI drive frequency held constant at 0.004484 Hz. The largest amplitude peaks represent the drive frequencies of FL and KI. The color scale bar is available on the right.

### 3.5.1.3 Interpretation, Problems, and Solutions

Fluorescein quenching, though modeled as a more simplistic model of higher order chemical kinetics, reveals heterodyne frequencies indicative of chemical intermediates in both the experimental data and the simulated data. Though these experiments were performed with a two pump setup incapable of producing constant flow rates, even upon correction of this data to mimic constant flow, the heterodyne frequencies remained unchanged; a phenomenon also verified through the same correction method utilized on the simulated variable flow data. As the experimental fluorescein quenching data reveals a richer frequency domain spectrum than the simulated data, it is possible that the model created was oversimplified and further exploration into this occurrence should be conducted. This may also indicate that the nonlinear dynamics of fluorescein quenching are more complex than initially expected. Regardless, the presence of the heterodyne frequencies in these variable flow experiments with non-calibrated pumps demonstrates the robustness of the platform for heterodyne analysis, in general, as the inherent noise generated by pump inconsistencies and non-sinusoidal waveform concentration profiles, does not interfere with the detection of heterodyne frequencies.

## 3.5.2 Peroxyoxalate Chemiluminescence

### 3.5.2.1 Experimental Conditions and Setup

For the peroxyoxalate chemiluminescence reaction, seven reservoirs were filled with 10 mM Bis(2,4,6-trichlorophenyl) oxalate (TCPO) in Diethyl Phthalate (DEP), 0.56 mM Rubrene (Rub) in Dimethyl Formamide (DMF), 0.98 M H<sub>2</sub>O<sub>2</sub>, 0.8 M Imidazole with 2% Pluronic F-68 in water, DEP, DMF, and H<sub>2</sub>O (all chemicals from Sigma Aldrich) as shown in Table 3.8. Seven pumps were used to drive fluids from these seven reservoirs. The RPPMs and the microfluidic reactor were primed with ethanol and a background file was collected. The reservoirs were

Table 3.8 Pump Reservoir Contents and Sample Input Parameters for Peroxyoxalate Reaction

	Contents	Sample Input Parameters			
		A [rpm]	y offset [rpm]	Period [s]	Phase offset
Pump 1	0.8M IMI, 2% Pluronic	59 (constant)	--	--	--
Pump 2a	0.98M H <sub>2</sub> O <sub>2</sub>	31	35	307	0
Pump 2b	H <sub>2</sub> O	34	38	307	180
Pump 3a	0.56mM Rub	36	40	223	0
Pump 3b	DMF	39	43	223	180
Pump 4a	10mM TCPO	35	39	269	0
Pump 4b	DEP	33	37	180	269

switched to those with the reactants and allowed to flow at a constant rate to flush the reactor of ethanol. The pump driving the flow of pluronic and imidazole was held constant at 59 rpm, while the remaining six pumps were driven sinusoidally based on their calibrated values (sample input parameters shown in Table 3.8). The periods of TCPO and Rub were held constant while that of H<sub>2</sub>O<sub>2</sub> was varied over the course of separate experiments from 3 to 6 minutes. Data for each experiment was collected for 7-10 hours.

With pairs of pumps used to define the concentration profile for each of the three reactants (0.98 M H<sub>2</sub>O<sub>2</sub>, 0.56 mM Rubrene and 10 mM TCPO), sinusoidal concentration profiles were possible and no post-collection data correction techniques were necessary. Each pump conducted the flow of fluid from its respective reservoir and the sinusoidal variable flows from each pair of pumps were summed in the pump mixers (a 100 μm W x 70 μm H x 12.8 cm L microfluidic serpentine channel) producing a constant total flow rate with a sinusoidal concentration profile for that reactant. This process was performed for each pair of pumps. The flow from the three pump mixers, along with the constant flow catalyst and pluronic mixture

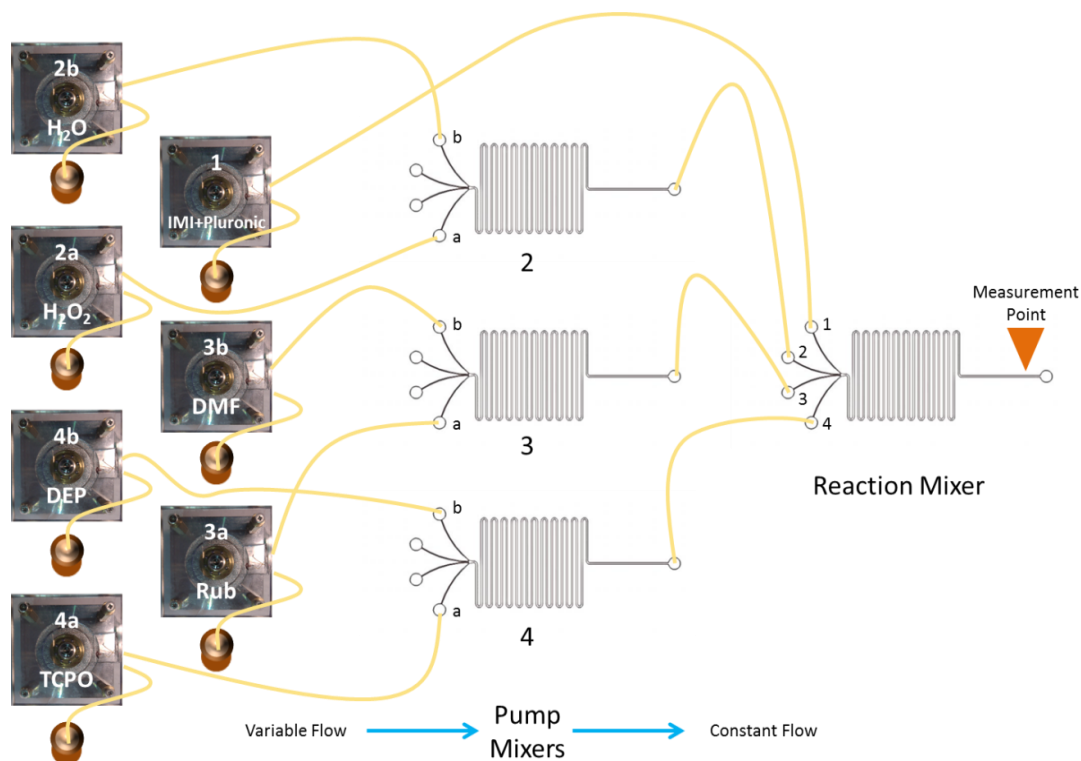


Figure 3.21 Experimental setup for seven pump sinusoidal concentration chemiluminescence reactions. Each pump drives the flow of one of the three reactants, three solvents, or catalyst with pluronic (details shown in Table 3.7). With two pumps running 180 degrees out of phase controlling the concentration profile of the reactant through their combination in the pump mixers, it is possible to achieve both constant flow and sinusoidal concentrations.

were combined in the reaction mixer (100  $\mu\text{m}$  W x 70  $\mu\text{m}$  H x 12.8 cm L microfluidic serpentine channel) and chemiluminescence detection occurs within the field of view of the objective (~1 mm x 1 mm). This experimental setup is as depicted in Figure 3.21.

### 3.5.2.2 Data

Figure 3.22 compares raw time-domain data and frequency domain data for the seven-pump setup before (orange) and after (green) calibration. The period of Rubrene, TCPO, and  $\text{H}_2\text{O}_2$  were 223, 269, and 307 seconds in both sets of data. The pre-calibration setup used a y offset and an amplitude of 30 rpm for all pumps, with half the pumps run with a phase offset of

180 degrees. In the post calibration experiment, each pump pair was calibrated to its pair such that the total flow rate remained constant while each individual pump ran at a variable flow rate. The length of the data sets was equalized prior to FFT analysis to prevent any unnecessary modifications to the data due to differences in experiment duration. A side-by side comparison of the drive frequencies and heterodyne frequencies, as shown in Figure 3.22B and C and Table 3.9, revealed subtle distinctions in the raw data pattern between the pre-calibration experiment and the post-calibration experiment. Both raw data sets are on the same scale. The respective frequency domain data comparison provides a richer source of variation between pre- and post-calibration data. While the same drive frequencies were employed for Rubrene, TCPO and H<sub>2</sub>O<sub>2</sub> (as well as for their respective 180 degree out of phase solvent pump counterpart), the output frequencies vary. For example, the input drive frequency for Rubrene is 0.004484 Hz (223 second period), however, the pre-calibration data returns a Rubrene drive frequency of 0.004745 Hz (5.8% error) while the post-calibration data returns a frequency of 0.004506 Hz (0.5% error). Pump calibration affords a 10% reduction in error from the theoretical frequency values. Pump calibration can take up to 30 minutes per pair of pumps, so a trade-off in this reduction in error exists.

Aside from the accuracy of the frequency values, the post-pump calibration data has reduced noise compared to the pre-calibrated data, allowing for the detection and identification of a greater number of heterodyne frequencies. The error in the location of the heterodyne frequencies for both the pre- and post-calibration data is on average 0.10% and 0.15%, respectively, indicating that, though the accuracy of the frequency values in the pre-calibration data is lower than that of the post-calibration data, the heterodyne frequencies remain accurate within a given experiment when compared to the heterodyne frequencies calculated from the actual output drive frequencies. It is also worth noting that the pattern of the annotated

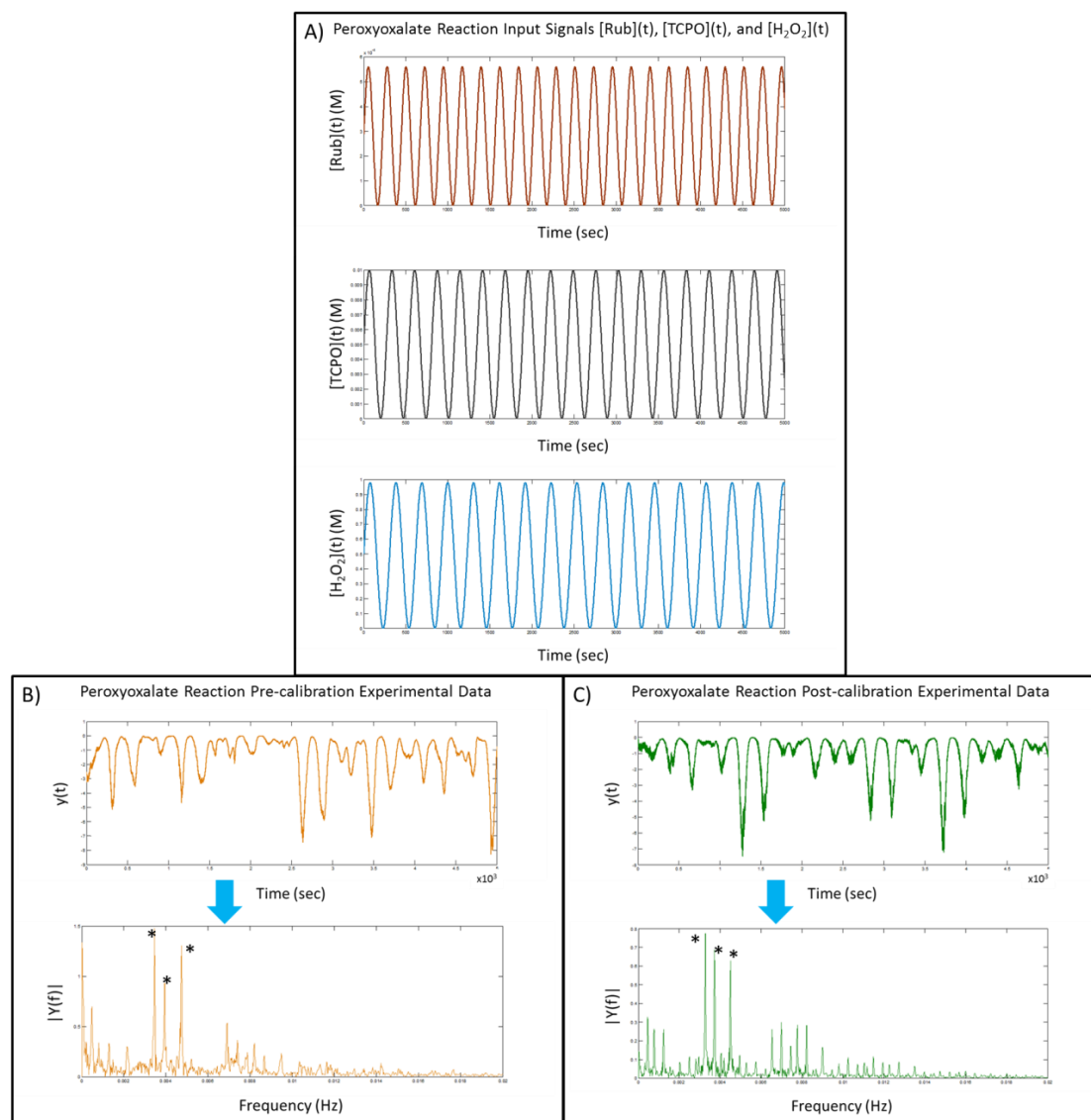


Figure 3.22 Pre- and post-calibration peroxyoxalate chemiluminescence experimental data. An experiment was performed prior to calibration of the seven pump setup for the purposes of comparison to data post-calibration. A) Rubrene, TCPO and  $\text{H}_2\text{O}_2$  were driven with constant flow, sinusoidal concentration with periods of 223 seconds, 269 seconds and 307 seconds. B) A portion of the raw data set (full time course was 6.8 hours) as well as the frequency spectrum for the pre-calibration experiment is shown adjacent to the analogous experiment performed post-pump calibration along with the respective frequency spectrum (C). The resulting frequencies for each experiment are compared in Table 3.9. Drive frequencies are labeled with an asterisk.

Table 3.9 Side-by-side pre- and post-calibration results for peroxyoxalate reaction heterodyne and drive frequencies with assignments, corresponding to the experimental data in Figure 3.22B and C.

Pre-calibration		Post-calibration	
Frequency (Hz)	Assignment	Frequency (Hz)	Assignment
0.0004768	$f_{TCPO} - f_{H2O2}$	0.000453	$f_{TCPO} - f_{H2O2}$
0.000811	$f_{Rub} - f_{TCPO}$	0.000763	$f_{Rub} - f_{TCPO}$
0.001287	$f_{Rub} - f_{H2O2}$	0.001240	$f_{Rub} - f_{H2O2}$
0.002146	$2f_{H2O2} - f_{Rub}$	0.002027	$2f_{H2O2} - f_{Rub}$
0.003457	$f_{H2O2}$	0.002813	$2f_{H2O2} - f_{TCPO}$
0.003934	$f_{TCPO}$	0.003266	$f_{H2O2}$
0.004745	$f_{Rub}$	0.003719	$f_{TCPO}$
0.006914	$2f_{H2O2}$	0.004053	$f_{Rub}$
0.007391	$f_{TCPO} + f_{H2O2}$	0.004959	$f_{Rub} + f_{TCPO} - f_{H2O2}$
0.007868	$2f_{TCPO}$	0.005746	$2f_{Rub} - f_{H2O2}$
0.008202	$f_{Rub} + f_{H2O2}$	0.006533	$2f_{H2O2}$
0.008678	$f_{Rub} + f_{TCPO}$	0.006986	$f_{TCPO} + f_{H2O2}$
0.009489	$2f_{Rub}$	0.007439	$2f_{TCPO}$
		0.007772	$f_{Rub} + f_{H2O2}$
		0.008225	$f_{Rub} + f_{TCPO}$
		0.009012	$2f_{Rub}$
		0.009799	$3f_{H2O2}$
		0.010250	$3f_{Rub} - f_{H2O2}$
		0.010700	$2f_{TCPO} + f_{H2O2}$
		0.011040	$f_{Rub} + 2f_{H2O2}$
		0.011490	$f_{Rub} + f_{TCPO} + f_{H2O2}$
		0.011940	$f_{Rub} + 2f_{TCPO}$
		0.012250	$2f_{Rub} + f_{H2O2}$
		0.012730	$2f_{Rub} + f_{TCPO}$



heterodyne frequencies is the same, even if the frequency values differ, between the pre- and post-calibrated data as noticeable by examination of Table 3.9. The distinction between the pre- and post-calibration data is evident from inspecting Figure 3.22B and C as well as Table 3.9. The frequencies detectable in the post-calibration set that are not detectable in the pre-calibration set include:  $2f_{H_2O_2} - f_{TCPO}$ ,  $f_{Rub} + f_{TCPO} - f_{H_2O_2}$ ,  $2f_{Rub} - f_{H_2O_2}$ ,  $3f_{H_2O_2}$ ,  $3f_{Rub} - f_{H_2O_2}$ ,  $2f_{TCPO} + f_{H_2O_2}$ ,  $f_{Rub} + 2f_{H_2O_2}$ ,  $f_{Rub} + f_{TCPO} + f_{H_2O_2}$ ,  $f_{Rub} + 2f_{TCPO}$ ,  $2f_{Rub} + f_{H_2O_2}$ , and  $2f_{Rub} + f_{TCPO}$ .

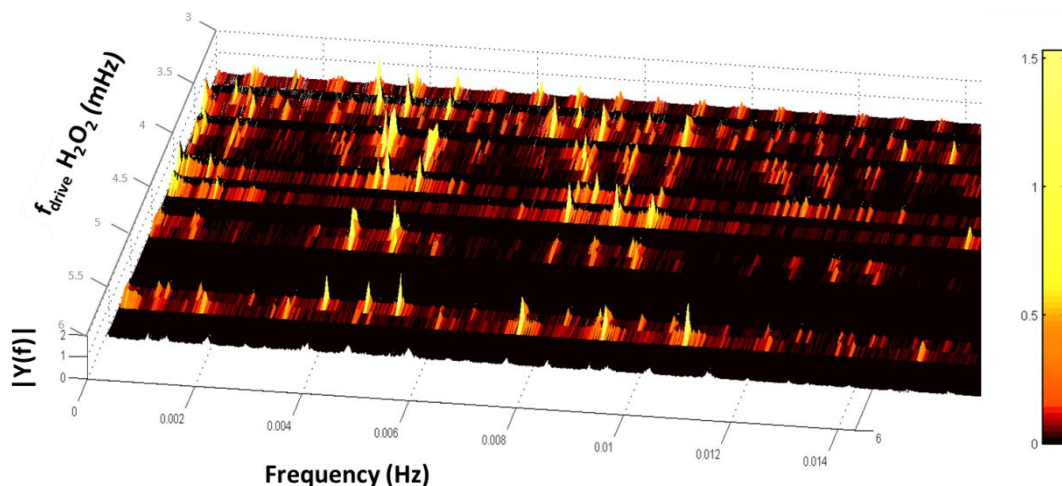


Figure 3.23 3D plot of varying  $H_2O_2$  drive frequencies from 0.005587 Hz to 0.003021 Hz with Rubrene and TCPO drive frequencies held constant at 0.004484 Hz and 0.003719 Hz. With this view it is possible to see the repeating frequency patterns. The color scale bar is available on the right.

The seven pump peroxyoxalate reaction was conducted with varying periods of  $H_2O_2$  from 179 seconds to 331 seconds, while maintaining the periods of rubrene (223 seconds) and TCPO (269 seconds). Data were collected for the same length of time and analyzed in the frequency domain for detection of heterodyne frequencies. The resulting 3D plot sweeping the  $H_2O_2$  frequency is shown in Figure 3.23.

### 3.5.2.3 Interpretation, Problems, and Solutions

For the peroxyoxalate chemiluminescence reaction utilizing calibrated RPPMs in pairs driven 180 degrees out of phase from one another (to accurately generate a sinusoidal concentration profile for each reactant), heterodyne frequencies were also detected in abundance and are comparable to those produced in the simulated data (Figure 3.24). As this

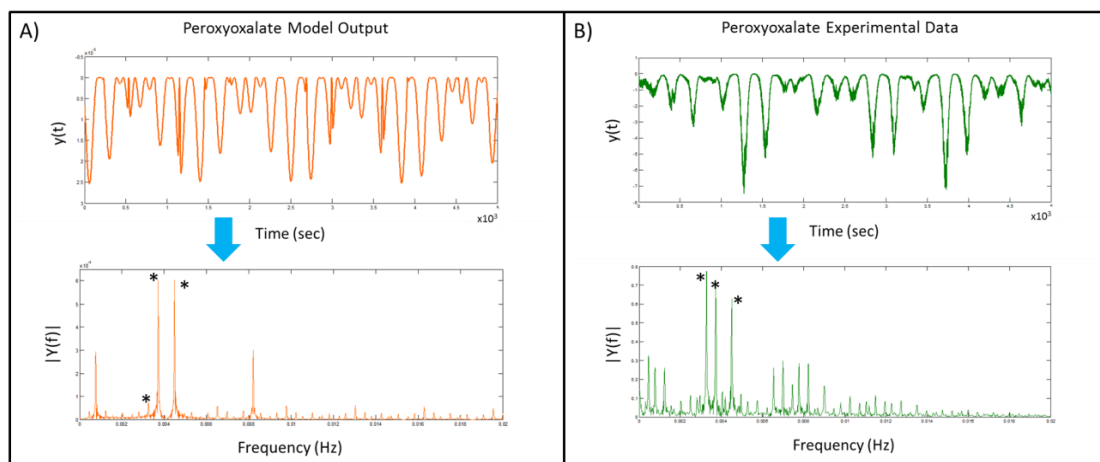


Figure 3.24 Model versus experimental peroxyoxalate chemiluminescence A) Simulated light emission data and frequency domain data for the same parameters used in the experiment producing the data and resulting frequency spectrum in B). Tabular comparison of model and experimental frequencies are available in Table 3.10. Drive frequencies are labeled with an asterisk.

reaction is comprised of three reactants, the McLaurin series expansion becomes more rigorous and peak assignments a lengthier process. However, the accuracy of the assignments of the detected frequencies withstands regardless of the difficulty in making the assignments. Table 3.10 compares the detected frequencies in the simulated and experimental data sets and reveals differences between the model and experimental. This indicates that the model does not completely predict the physical experiment; though deciphering this discrepancy produces additional challenges. A possible explanation for these differences is that the reaction rate

Table 3.10 Side-by-side comparison of frequencies detected from model and experimental peroxyoxalate reaction corresponding to the data in Figure 3.24A and B.

Model		Experimental	
Frequency (Hz)	Assignment	Frequency (Hz)	Assignment
0.0004578	$f_{TCPO} - f_{H2O2}$	0.000453	$f_{TCPO} - f_{H2O2}$
0.000763	$f_{Rub} - f_{TCPO}$	0.000763	$f_{Rub} - f_{TCPO}$
0.001240	$f_{Rub} - f_{H2O2}$	0.001240	$f_{Rub} - f_{H2O2}$
0.002022	$2f_{H2O2} - f_{Rub}$	0.002027	$2f_{H2O2} - f_{Rub}$
0.002804	$2f_{H2O2} - f_{TCPO}$	0.002813	$2f_{H2O2} - f_{TCPO}$
0.003262	$f_{H2O2}$	0.003266	$f_{H2O2}$
0.003719	$f_{TCPO}$	0.003719	$f_{TCPO}$
0.004482	$f_{Rub}$	0.004053	$f_{Rub}$
0.004959	$f_{Rub} + f_{TCPO} - f_{H2O2}$	0.004959	$f_{Rub} + f_{TCPO} - f_{H2O2}$
0.006065	$3f_{H2O2} - f_{TCPO}$	0.005746	$2f_{Rub} - f_{H2O2}$
0.006523	$2f_{H2O2}$	0.006533	$2f_{H2O2}$
0.006981	$f_{TCPO} + f_{H2O2}$	0.006986	$f_{TCPO} + f_{H2O2}$
0.0077744	$f_{Rub} + f_{H2O2}$	0.007439	$2f_{TCPO}$
0.008202	$f_{Rub} + f_{TCPO}$	0.007772	$f_{Rub} + f_{H2O2}$
0.009766	$3f_{H2O2}$	0.008225	$f_{Rub} + f_{TCPO}$
0.01022	$3f_{Rub} - f_{H2O2}$	0.009012	$2f_{Rub}$
0.01055	$2f_{TCPO} + f_{H2O2}$	0.009799	$3f_{H2O2}$
0.01101	$f_{Rub} + 2f_{H2O2}$	0.010250	$3f_{Rub} - f_{H2O2}$
0.01146	$f_{Rub} + f_{TCPO} + f_{H2O2}$	0.010700	$2f_{TCPO} + f_{H2O2}$
0.01226	$2f_{Rub} + f_{H2O2}$	0.011040	$f_{Rub} + 2f_{H2O2}$
		0.011490	$f_{Rub} + f_{TCPO} + f_{H2O2}$
		0.011940	$f_{Rub} + 2f_{TCPO}$
		0.012250	$2f_{Rub} + f_{H2O2}$
		0.012730	$2f_{Rub} + f_{TCPO}$

equations, based on the chemical equations, do not adequately predict the physical phenomenon. However, to make this claim, further experimentation is required to rule out additional causes first. Alternate explanations could include nonlinear mixing contributions from the RPPMs and insufficient mixing. As this reaction combines reactants dissolved in both organic and aqueous solvents, even in the presence of pluronic, the mixing is imperfect. Adaptations to the model equating to lower reaction efficiency, as an approximation of insufficient mixing, should be performed. The nonlinear contributions of the pumps should also be explored through further modeling and experimentation.

### 3.6 Summary, Pitfalls, and Problems

The work described herein demonstrates progress toward the development of a robust technique for the investigation of oscillatory chemical signals in the form of light produced by reactions (fluorescein quenching and peroxyoxalate chemiluminescence) with sinusoidal reactant concentration profiles. It has involved the incorporation of 1) instrumentation for modulating sinusoidal concentration through flow rate as driven by the rotary planar peristaltic micropumps, 2) a microfluidic mixer for the combination of two or more unique chemical frequencies, 3) a detector for acquiring data from the light producing reactions in the form of the Continuous Flow Photometer, and 4) a data analysis technique involving Matlab's Fast Fourier Transform for translating the raw data into the frequency domain where heterodyne frequencies are able to be detected. In order to assess the progress in the development of this heterodyne chemistry hardware framework, a set of metrics were developed as shown in Table 3.10 along with comments regarding the status of each metric. The following discussion provides additional commentary regarding the performance metrics.

Table 3.11 Heterodyne chemistry hardware performance metrics

<b>System Component</b>	<b>Metric</b>	<b>Status</b>
<b><i>Rotary Planar Peristaltic Micropumps</i></b>	Long-term functionality with two pump setup	Maintained continuous experimental data collection for 20 days with three pump fluidic changes.
	Long-term functionality with seven pump setup	Maintained continuous experimental data collection for 11 days with four pump fluidic changes.
	Increased frequency domain resolution with pump calibration	Post-calibration data contained more significant (> 3x noise) heterodyne frequencies than analogous pre-calibration data.
<b><i>Microfluidic Mixers</i></b>	Microfluidic device stability	Minimal device changes required with no device clogging or delamination events.
	Mixing efficiency	Peroxyoxalate reaction mixing increased with the addition of 2% pluronic solution in a serpentine mixer. Fluorescein quenching may need additional mixing time.
<b><i>Continuous Flow Photometer</i></b>	Calibration curve for four fluorescein concentrations	Completed with concentrations tested in the linear region of the detector.
	Long-term fluorescence and/or chemiluminescence acquisition	Continuous data collection possible with no discernible time limit.
<b><i>Data Collection and Analysis</i></b>	Long-term data collection with Labview 10	Labview failed three times over three months as a result of too many data logs saved to the project.
	Rapid conversion (less than 5 seconds) of large Labview data files into Matlab	Conversion of >3million point .tdms data sets achieved in under 5 seconds with Matlab file converter and a 1.73GHz, 4GB, 32-bit i7 processor.
	Fast Fourier transform in Matlab of large data files in less than 5 seconds	Matlab processed the FFT of >3million data points in under 5 seconds with a 1.73GHz, 4GB, 32-bit i7 processor.
	Data correction for variable total flow conditions	Data correction completed successfully with sample pre- and post-correction data provided.

The validation of this platform involved assessing the sinusoidal concentration generation with the RPPMs, verifying the fluorescence and chemiluminescence detection capabilities of the CFP, and confirming the data analysis techniques through comparison with expected heterodyne frequencies calculated from McLaurin series expansion. The use of models of the chemical reactions was also utilized for comparison to the experimental data and for testing variable flow data correction methods. Finally, the platform was utilized to collect swept frequency data of fluorescein for the fluorescein quenching reaction and H<sub>2</sub>O<sub>2</sub> for the peroxyoxalate chemiluminescence reaction.

Assessments indicated the need for pairs of pumps running 180 degrees out of phase from one another in order to generate a sinusoidal concentration profile. Inter-pump variable led to the incorporation of pump calibration schemes. Constant flow pump calibration of matched fluidic pumps pairs reveals issues beyond channel dimensional differences that are contributing to the statistically significant inter-pump variation. The assembly, alignment and compression processes are highly subject to the user's discretion, particularly during the alignment procedure. Further, alignment, even under magnification, can be problematic due to the tolerance of the thrust bearing cage (machined in house out of Teflon) which leads to the misalignment of less than half of the thrust bearings. (Misalignment of half of the ball bearings or greater is due to insufficient alignment of the channels and rarely an issue with the thrust bearing.)

Discrepancies were found when attempting to convert the constant flow calibration to sinusoidal pump rates, necessitating the need for pumps intended to be run sinusoidally, to be calibrated under such conditions. However, a multipoint constant flow calibration was not performed and may provide results in agreement with the sinusoidal flow calibration.

Comparing data sets of pre- and post-pump calibration experiments revealed that pump calibration in the seven pump setup provides reduced noise in the frequency domain, allowing for enhanced heterodyne frequency determination and minimized error compared to theoretical frequency values. The benefits of pump calibration come at the expense of time as the current calibration procedures can take up to 30 minutes per pair of pumps. Additionally, extreme care must be taken while calibrating to minimize the stopping of the pumps controlled by the same Arduino board, but yet are not the object of the current calibration. While the calibration of the pumps allows for the detection of an increased number of heterodyne frequencies, the lack of a calibration does not invalidate the data as the values of the frequencies detected are highly accurate when compared to those calculated from the output drive frequencies for that experiment.

The detection of these heterodyne frequencies under known reactant profile conditions allows for the verification of the analysis technique. Though the output drive frequencies err from the input frequencies, even without prior knowledge of the driving frequencies of the reactants, it is possible to assign identities with high accuracy to each frequency detected (i.e.  $(a+b)$ ,  $(2a-c)$ ,  $(a+b+c)$ ) based on the most abundant peaks in the spectrum. Through this method, it is possible to extrapolate the frequencies with which the reactants were run.

While this work may appear to be oriented towards chemical kinetics, this strategy has potential applicability to a variety of complex nonlinear biological networks including those characterized by oscillatory chemical signals. Through the extension of these techniques into biochemical signaling networks, a new level of understanding may arise and lead to the discovery of unknown upstream chemical interactions as detected by the frequency domain pattern of downstream products.

### 3.7 Future Solutions

While this work represents a significant amount of progress in the development of a heterodyne technique, additional work must be completed to accurately ascertain the cause(s) of the discrepancies between the model frequency spectra and the experimental frequency spectra. The Arduino code driving the motors needs to be refined to eliminate any internal delays or frequency discrepancies. Suggestions for tests to determine the cause of the observed heterodyne frequencies include the following. 1) Further calibration of the detector response under constant flow of only fluorescein, in particular low flow conditions may allow for visualization of any photo-bleaching that may occur. 2) Next, pump pairs driven with water and fluorescein with the same frequency, so as to produce a sinusoidal concentration profile of fluorescein, can be utilized to view the resulting oscillatory fluorescence signal detected. This will allow for the assessment of the accuracy and consistency of the sinusoidal concentrations produced. All pairs of pumps can be tested in this manner. Pumps can be adjusted based on the oscillatory fluorescence signal produced. Additionally, any resulting heterodyne peaks when tests are performed under conditions that exclude photo-bleaching can be concluded to be artifacts of the pumping or the fluorescence excitation. It is highly recommended that the pumps first be calibrated either with the method discussed in this work (the addition of two sinusoidal flows 180 degrees out of phase from each other add to a constant flow) or with the automated calibration methods currently under development within VIIBRE. 3) The next test that can be performed is similar to step 2, except fluorescein is in all reservoirs. This setup will result in a constant fluorescein concentration and constant fluorescence signal. Any remaining oscillations in the fluorescence signal will indicate issues with the pump calibration. 4) To test for the congruency of the pump phases and any discrepancies between pairs of pump, two pairs of pumps can be run with the same frequency and with fluorescein and water in the reservoirs.



In order to have the fluorescein concentration sum to a constant, as well as the resulting fluorescence signal, one pair of pumps should drive fluorescein with a zero degree phase offset, while the second pair of pumps should drive fluorescein with a 180 degree offset. Any noticeable oscillations in the resulting signal will indicate variations between the pairs of pumps or discrepancies in the phase offsets. After successful completion of this pump and detector calibration with fluorescein, quenching experiments can continue. 5) The Stern-Volmer relationship can be explored and calibrated on a spectrophotometer with a range of fluorescein and KI concentrations. While a high quencher concentration (known to be in the nonlinear range of the Stern-Volmer) has been used in the experiments discussed in this work, exploring the concentration space may result in a set of concentrations that will demonstrate the reaction nonlinearities to an even greater extent. 6) A similar concentration space exploration can also be performed with the RPPM-mixer-CFP setup so as to investigate the Stern-Volmer relationship on the instrumentation that will be utilized in future experiments. Through comparison of this data set to that gained in step 5, it may be possible to detect any instrumentation-specific issues that could cause experimental results to vary. 7) Next, fluorescein quenching experiments with pairs of pumps driven at the same frequency can be conducted over a range of frequencies. 8) Finally, fluorescein quenching experiments can be performed with pairs of pumps driven at different frequencies. Resulting heterodyne frequencies can be compared to those discovered in step 2 above in order to rule out heterodyne frequencies caused by the pumps or the excitation. Statistical assessment of the assignments of each heterodyne peak must also be performed. Remaining heterodyne frequencies that differ from the mathematical models can be more confidently contributed to the physical quenching phenomenon and modifications to the model can be made in order to mimic the experimental results.

### 3.8 References

1. Kholodenko, B. N. Cell-signalling dynamics in time and space. *Nature Reviews Molecular Cell Biology* **7**, 165–176 (2006).
2. Tyson, J. J., Chen, K. C. & Novak, B. Sniffers, buzzers, toggles and blinkers: dynamics of regulatory and signaling pathways in the cell. *Current Opinion in Cell Biology* **15**, 221–231 (2003).
3. Ingalls, B. P. A Frequency Domain Approach to Sensitivity Analysis of Biochemical Networks. *J. Phys. Chem. B* **108**, 1143–1152 (2003).
4. Ferrell, J. E. & Xiong, W. Bistability in cell signaling: How to make continuous processes discontinuous, and reversible processes irreversible. *Chaos: An Interdisciplinary Journal of Nonlinear Science* **11**, 227–236 (2001).
5. Eungdamrong, N. J., Iyengar, R., Eungdamrong, N. J. & Iyengar, R. Modeling Cell Signaling Networks, Modeling Cell Signaling Networks. *Biology of the Cell, Biology of the Cell* **96, 96**, 355–362, 362 (2004).
6. Huang, S., Eichler, G., Bar-Yam, Y. & Ingber, D. E. Cell Fates as High-Dimensional Attractor States of a Complex Gene Regulatory Network. *Phys. Rev. Lett.* **94**, 128701 (2005).
7. Szűcs, A., Elson, R. C., Rabinovich, M. I., Abarbanel, H. D. I. & Selverston, A. I. Nonlinear Behavior of Sinusoidally Forced Pyloric Pacemaker Neurons. *J Neurophysiol* **85**, 1623–1638 (2001).
8. Denker, M., Szucs, A., Pinto, R. D., Abarbanel, H. D. I. & Selverston, A. I. A network of electronic neural oscillators reproduces the dynamics of the periodically forced pyloric pacemaker group. *Biomedical Engineering, IEEE Transactions on* **52**, 792–798 (2005).
9. Abarbanel, H. D. I. & Rabinovich, M. I. Neurodynamics: nonlinear dynamics and neurobiology. *Current Opinion in Neurobiology* **11**, 423–430 (2001).
10. Montana, D. J. & Davis, L. Training feedforward neural networks using genetic algorithms. *Proceedings of the 11th international joint conference on Artificial intelligence - Volume 1* 762–767 (1989).at <<http://dl.acm.org/citation.cfm?id=1623755.1623876>>

11. Hastings, H. M. & Pikelney, R. Stochastic information processing in biological systems. *Biosystems* **15**, 155–168 (1982).
12. Regan, D. & Heron, J. R. Clinical Investigation of Lesions of the Visual Pathway: A New Objective Technique. *J Neurol Neurosurg Psychiatry* **32**, 479–483 (1969).
13. Regan, D. & Regan, M. P. Objective evidence for phase-independent spatial frequency analysis in the human visual pathway. *Vision Research* **28**, 187–191 (1988).
14. Regan, D. & Regan, M. P. Nonlinearity in human visual responses to two-dimensional patterns, and a limitation of fourier methods. *Vision Research* **27**, 2181–2183 (1987).
15. Regan, M. P., Regan, D. & He, P. An audio-visual convergence area in the human brain. *Experimental Brain Research* **106**, 485–487 (1995).
16. Gilon, P., Shepherd, R. M. & Henquin, J. C. Oscillations of Secretion Driven by Oscillations of Cytoplasmic Ca<sup>2+</sup> as Evidences in Single Pancreatic Islets. *J. Biol. Chem.* **268**, 22265–22268 (1993).
17. Pørksen, N. The in vivo regulation of pulsatile insulin secretion. *Diabetologia* **45**, 3–20 (2002).
18. Porksen, N. *et al.* Pulsatile Insulin Secretion: Detection, Regulation, and Role in Diabetes. *Diabetes* **51**, 245S–254 (2002).
19. Bennett, M. R. *et al.* Metabolic gene regulation in a dynamically changing environment. *Nature* **454**, 1119–1122 (2008).
20. Miller, J., Nawarathna, D., Warmflash, D., Pereira, F. & Brownell, W. Dielectric Properties of Yeast Cells Expressed With the Motor Protein Prestin. *Journal of Biological Physics* **31**, 465–475 (2005).
21. Nawarathna, D. *et al.* SQUID-Based Biosensor for Probing Ion Transporters in Cell Suspensions and Tissue. *IEEE Transactions on Applied Superconductivity* **17**, 812–815 (2007).

22. Nawarathna, D. *et al.* Harmonic generation by yeast cells in response to low-frequency electric fields. *Phys. Rev. E* **73**, 051914 (2006).
23. Mettetal, J. T., Muzzey, D., Gomez-Uribe, C. & van Oudenaarden, A. The Frequency Dependence of Osmo-Adaptation in *Saccharomyces cerevisiae*. *Science* **319**, 482–484 (2008).
24. Zhang, X., Grimley, A., Bertram, R. & Roper, M. G. Microfluidic System for Generation of Sinusoidal Glucose Waveforms for Entrainment of Islets of Langerhans. *Analytical Chemistry* **82**, 6704–6711 (2010).
25. Bird, G. S., Rossier, M. F., Obie, J. F. & Putney, J. W. Sinusoidal Oscillations in Intracellular Calcium Requiring Negative Feedback by Protein Kinase C. *J. Biol. Chem.* **268**, 8425–8428 (1993).
26. Berthoumieux, H., Antoine, C., Jullien, L. & Lemarchand, A. Resonant response to temperature modulation for enzymatic dynamics characterization. *Phys. Rev. E* **79**, 021906 (2009).
27. Brigham, E. O. & Morrow, R. E. The fast Fourier transform. *Spectrum, IEEE* **4**, 63–70 (1967).
28. Cooley, J. W. & Tukey, J. W. An Algorithm for the Machine Calculation of Complex Fourier Series. *Mathematics of Computation* **19**, 297–301 (1965).
29. Frigo, M. & Johnson, S. G. The Design and Implementation of FFTW3. *Proceedings of the IEEE* **93**, 216–231 (2005).
30. Keizer, J. Nonlinear fluorescence quenching and the origin of positive curvature in Stern-Volmer plots. *J. Am. Chem. Soc.* **105**, 1494–1498 (1983).
31. Sikorski, M., Krystkowiak, E. & Steer, R. P. The kinetics of fast fluorescence quenching processes. *Journal of Photochemistry and Photobiology A: Chemistry* **117**, 1–16 (1998).
32. Mataga, N., Chosrowjan, H. & Taniguchi, S. Ultrafast charge transfer in excited electronic states and investigations into fundamental problems of exciplex chemistry: Our early studies and recent developments. *Journal of Photochemistry and Photobiology C: Photochemistry Reviews* **6**, 37–79 (2005).

33. Umberger, J. Q. & LaMer, V. K. The Kinetics of Diffusion Controlled Molecular and Ionic Reactions in Solution as Determined by Measurements of the Quenching of Fluorescence<sup>1,2</sup>. *J. Am. Chem. Soc.* **67**, 1099–1109 (1945).
34. Watt, R. M. & Voss, E. W. Solvent perturbation of the fluorescence of fluorescein bound to specific antibody. Fluorescence quenching of the bound fluorophore by iodide. *J. Biol. Chem.* **254**, 1684–1690 (1979).
35. Arık, M., Çelebi, N. & Onganer, Y. Fluorescence quenching of fluorescein with molecular oxygen in solution. *Journal of Photochemistry and Photobiology A: Chemistry* **170**, 105–111 (2005).
36. Comstock, N., Gurman, N. & Folger, H. S. Chemiluminescence Web Module. *Elements of Chemical Reaction Engineering* at <<[http://www.engin.umich.edu/~cre/web\\_mod/new/glowsticks/index.htm](http://www.engin.umich.edu/~cre/web_mod/new/glowsticks/index.htm)>>
37. Mosadegh, B. *et al.* Integrated elastomeric components for autonomous regulation of sequential and oscillatory flow switching in microfluidic devices. *Nature Physics* **6**, 433–437 (2010).
38. Azizi, F. & Mastrangelo, C. H. Generation of dynamic chemical signals with pulse code modulators. *Lab on a Chip* **8**, 907 (2008).
39. Zhang, X. & Roper, M. G. Microfluidic Perfusion System for Automated Delivery of Temporal Gradients to Islets of Langerhans. *Anal. Chem.* **81**, 1162–1168 (2008).
40. Cao, L., Zhang, X., Grimley, A., Lomasney, A. & Roper, M. Microfluidic multi-analyte gradient generator. *Analytical and Bioanalytical Chemistry* **398**, 1985–1991 (2010).
41. Gould, P. A. *et al.* Rotary Planar Peristaltic Micropump. *in preparation*

## CHAPTER IV

### 4 SUMMARY, FUTURE WORK AND ETHICAL IMPACT

The previous chapters have described work on the following projects: *Real-time Cellular Exometabolome Analysis with a Microfluidic-Mass Spectrometry Platform* and *Heterodyne Framework for the Generation and Receiving of Oscillatory Chemical Signals in Nonlinear Light-Producing Systems*. At first read, these projects may appear disconnected; however, they are highly related and intertwined as each contributes to the movement towards a system for automated biology. With the success of the integrated microfluidic-ion mobility-mass spectrometry platform, rapid progress has been made towards the analysis of cell states under varying environmental conditions as evidenced by the differential cocaine metabolism of naïve and experienced cells demonstrated in **Chapter II**. Additionally, the development of the heterodyne framework, based on the radio frequency deconvolution methodology, has successfully generated sinusoidal concentration profiles, combined these together in a mixer, received the subsequent light-based signal and analyzed the resulting data in the Fourier domain to detect heterodyne (sum and difference) frequencies.

While both the microfluidic-mass spectrometry platform and the heterodyne techniques are still in their infancy, they share a common characteristic of expansive potential for the advancement of biological studies. With the ability to detect distinct cellular phenotypes or states based on the exometabolomic profile of a given cell population, honing in on key features causing separation between various states, there is limitless potential for discovery in the realm of complex cellular, biochemical networks. For instance, through further investigation into the identity of the unknown features found in the naïve and experienced Jurkat T cell cocaine

exposure experiment, along with the pathways that may be affected by the challenge, new insight may be gleaned relating to the long-term effects of cocaine exposure on the immune system. As the heterodyne techniques develop and extend beyond chemical reaction test systems, the power of the two platforms can be combined with an upstream sinusoidal concentration profile generator feeding oscillator chemical signals into the bioreactor. As mass spectrometry technology advances along with desalting techniques for true real-time desalting, the detector of the mass spectrometer may have the potential to serve as the heterodyne receiver for numerous oscillatory chemical signals at once. Extreme caution is advised as species abundance as recorded by the detector is highly dependent on the ionization which can vary as the composition of complex sample changes. Targeted studies, utilizing a constant concentration standard addition to the media, possibly with stable isotope labeling, may provide an initial starting point for these heterodyne biology experiments incorporating the two platforms discussed in this work. Though a future goal of the combination of these two projects into a unified system is possible, each individual system has further refinements that should be undertaken before the merger is attempted. A thorough analysis of the two platforms along with suggestions for further enhancement is provided.

#### 4.1 MF-SPE-nESI-IM-MS

This online platform for analysis of the cellular exometabolome consists of a microfluidic bioreactor, a solid phase extraction desalter, and nanoelectrospray ionization-ion mobility-mass spectrometry. As described in **Chapter II**, the system has been successfully integrated and utilized for the analysis of naïve and cocaine-experienced T cells with a dynamic stimulus of cocaine. Though these results provide initial evidence of differential cocaine metabolism between these two cell populations, continued work is desirable on both the platform and this

particular biological investigation. Future users of this platform are directed to Appendix B for a complete use and troubleshooting guide.

#### 4.1.1 Microfluidic Device Design and Control

The signal intensities achievable upon downstream detection are related to the size of the cell population on which experiments are conducted. Any desired increase in signal from lower concentration species would require a greater number of cells. Two options exist for increasing the size of the cell population: 1) multiple devices in parallel and 2) increasing the size of the device and number of traps. Using multiple MTNPs in parallel could be an option, though they require a greater number of syringes and expensive syringe pumps. The second option of increasing the size of the device is perhaps a better option as any new device design could be easily adapted from current designs and would not require any increase in the number of pumps and syringes, providing this new, larger device is designed appropriately to function with only three or four inlets.

#### 4.1.2 Online Desalting

In the current arrangement, the solid phase extraction desalter produces small batches of desalted effluent. In the experiments reported, effluent filled a sample loop for 9 minutes (4.5 $\mu$ L at 500nL/min) and was then directed by the flow of aqueous solvent over the column at a rate of 0.9 $\mu$ L/min. This setup provides a 1.5 $\mu$ L aqueous column equilibration volume followed by the 4.5 $\mu$ L of sample effluent load and then an additional 2.1 $\mu$ L of aqueous salt removal. Further fine tuning of these flow rates, the size of the sample loop and its fill time, and the column length could result in higher efficiency desalting with a shorter time averaging tradeoff. The low sample flow rate negatively affects the ability to compare downstream and upstream salt



concentrations as necessary dilution to larger volumes, in addition to sample evaporation during its collection, skews the measurements. A strategy for quantifying salt removal in the current setup could be paramount in fine tuning the desalter.

Additional strategies for desalting are currently underway. For instance, a microdialysis desalter is presently being refined and tested. While this method for salt removal will provide an actual real-time signal, it does so with several tradeoffs. The use of commercially manufactured dialysis membranes is limiting due to the few selections in pore size of molecular weight cut-off. A 13kDa cutoff is the lower bound of the currently available products, which clearly is significantly larger than the molecular weight of most salts and relies upon the higher diffusivity of salts in aqueous solutions in order to achieve sufficient salt removal without the loss of precious sample. The overall size of the membrane tube diameter (as this microdialysis setup uses countercurrent sheath flow around a cylindrical shell membrane with the sample flow inside the dialysis membrane and buffer flow external to the membrane) is likewise limited and is an order of magnitude larger than the typical tubing used to direct sample effluent from the bioreactors creating a nozzle effect that greatly increases the timing delay from bioreactor to detector. Preliminary tests for packing this inner dialysis tubing with beads were promising and should be considered for this microdialysis desalting strategy.

An analytical column as part of the current desalter setup has already been considered, though it has not yet been incorporated. This additional column, along with a gradient elution, would provide increased chromatographic separation of species similar to LC. However, the system timing would have to be tightly controlled in order to allow for the use of retention time data to be included. Without tight control of the timing, the retention time for a given  $m/z$  would shift from data file to data file, preventing inclusion of this information in the data analysis scheme.

#### 4.1.3 Data Analysis

The integrated platform produces data at an insurmountable rate for a single individual to handle. For typical online cellular studies that last 4-8 hours in length, data correction and peak detection with Markerlynx can require nearly as long as the experiment took to perform. Providing one is satisfied with the method used and resulting detection of peaks, an infinite amount of time may then be spent performing careful interrogation of the data, particularly when attempting to identify unknown features. In the meantime, while attempting to analyze this single set of experimental data, each day that passes produces an additional data set in need of similar analysis (particularly since these experiments are run back to back over the course of several weeks). For instance, in the course of developing this platform, 16 biologically valuable data sets were collected and processed with Markerlynx, each with sufficient complexity that would require a researcher's sole attention for a minimum of 3 months in order to confidently glean biologically relevant information. This data avalanche and overwhelming time requirement spurs the need, not only for ever increasing data storage space, but also for parallel researchers or a perhaps, the more highly desirable, data analysis automation. At a minimum, future endeavors should entail continued analysis of the remaining 15 data sets produced from the online platform (as only one, the naïve and experienced T cell cocaine exposure, was analyzed thoroughly for the purposes of an initial manuscript detailing the capabilities of the platform). Enough data exists for potentially six additional publications solely using data that has already been collected. It is suggested that incoming mass spectrometry graduate student researchers be given the opportunity to learn data analysis and feature identification methods with these data sets, followed by the production of a manuscript relaying the pertinent biological findings. This serves not only to allow students early in their careers to gain valuable skills in mass spectrometry data analysis, but also provides the opportunity to

acquire a first author publication without having to develop, troubleshoot, and perform additional experiments.

#### 4.1.4 MTNP-SPE-nESI-IM-MS

Seven unique biological experiments were performed using the online cellular analysis platform, though only one of these experiments was utilized for the purposes of this dissertation. The additional experimental data, though it has been processed through Markerlynx and preliminary analysis shows distinctions between different exposure sample groups, was not included to prevent any undesirable effects upon the release of this document to the public prior to completion of the data analysis and publication of those experimental results.

This system is poised for conducting endless possibilities of biological experiments. In its current state, particularly concerning the data analysis, biological studies with anticipated exometabolomic components lower the high threshold for feature identification as determining the presence of expected compounds is significantly less convoluted.

As the cellular memory of cocaine exposure is a unique biological question with interesting initial results, continued investigation is critical. The experienced population was created with a short-term period of cocaine exposure immediately followed by online experimentation. Experimental variations of particular interest would be extending the exposure incubation time and also incorporating a period of incubation in regular media (without serum) prior to online analysis. The length of time between the initial cocaine exposure in culture and the online analysis of those experienced cells should be increased to determine the time course of cocaine exposure memory. These same experimental concepts should also be applied to primary white blood cell populations from rat models of addiction. While this was

attempted in collaboration with Dr. Schramm-Sapyta at Duke University, the initial methods determined for blood sample transfer resulted in too few cells per sample for loading into a microfluidic device. If work with her group continues, separation of white blood cells from whole blood should be requested prior to freezing and shipping samples in order to provide sufficient population sizes for analysis with the online platform.

Overall, this system for real-time elucidation of cellular response stands to revolutionize cell-based research, clinical laboratory testing and drug discovery and development. While it is in its infancy, I believe it has a bright future ahead providing it receives the necessary attention from researchers and funding agencies. Without additional attention from graduate students, post-docs and PIs, this potentially powerful technology will end up in the basement of the Stevenson Center building 6.

#### 4.2 Heterodyne Framework

Successful creation, integration and validation of a sinusoidal concentration generator, a mixer for combining multiple oscillating signals, a receiver for collection of the resulting product of the mixing, and a data analysis technique utilizing the fast Fourier transform for detection of high accuracy heterodyne frequencies has been performed. Underlying frequency oscillations, aside from those of the oscillating input signals, are indicative of frequencies of production of reaction intermediates that cause modulation of product formation. While this technique has been proven for two higher order light-producing chemical reactions and will be of interest to the analytical chemistry community, an offshoot of the technique for applications relevant to biological systems should be explored. Improvements on the current framework, in addition to suggestions for optimizing it for biological application, will be included in this section.

#### 4.2.1 Sinusoidal Concentration Generation

Rotary planar peristaltic micropumps have been adapted for generation of sinusoidal concentration profiles. While the RPPMs have many strengths for use in heterodyne chemistry experiments, issues exist with pulsatility of the flow, inter-pump variation, and intra-pump variation over time. Attempts at reducing the flow pulsatility for sinusoidal flow rates with a microfluidic flow depulsitizer, characterized by compliant area with a thin membrane, was futile as the desired oscillations were dampened, in addition to the undesirable pulses, due to the compliance of the depulsitizer. Further work into alternate schemes for reducing pulsatile flow is already underway and could stand to reduce the noise in the experimental light production data, and therefore, the noise in the frequency domain.

Inter-pump variation is addressable through rigorous calibration procedures, though from the findings in **Chapter III**, constant flow calibration was not applicable to sinusoidal flow schemes. A multipoint constant calibration procedure should be tested prior to abandoning this technique as an option. Calibration, while reducing inter-pump variability to a certain extent, requires a significant time commitment (at least 30 minutes per pump currently) in the short lifetime of the pump (one week on average). The calibration procedure can also contribute to a reduced lifetime of the pumps as the repeated stopping and starting is problematic. To achieve the longest possibly lifetime out of a pump, it is recommended to maintain continuous flow through the pumps with minimal stopping. This prevents evaporation of fluids through the thin membrane as well as clogging of the channels. Automated pump calibration efforts are in progress and may serve to rectify these concerns with the current calibration procedure.

While a pump may be driven at a constant flow, over lengthy periods of time (multiple hours to days), the actual flow rate may change due to bubble formation, changes in the PDMS membrane upon rigorous and continuous mechanical deformation, clogged channels, and slight

misalignments of the channels with the thrust bearing that potentiate over time. Reducing the formation of bubbles is challenging as the cause is yet to be confidently assigned. Possibilities include intake of air through the thin membrane resulting from incomplete channel closure in square profile channels, intake of air around the punch hole due to splits in the PDMS or lack of a tight seal between the PEEK tubing and the PDMS, or intake of air through dissolved gas in the reservoir fluids. The first can be rectified through construction of rounded channels as opposed to square, though initial testing with a rounded channel device produced undesirable results in terms of the amount of bubbles generated. The second can be overcome by creating inlet and outlet ports with sharper punches or sealing the tube to the PDMS. In many cases, using a drop of high viscosity oil can provide an adequate seal. This can break down in some circumstances, causing the oil to enter the channels which leads to pump failure. Glue or PDMS can also be used to seal the PEEK tubing into the inlet, but is permanent, requiring disposal of either the device or inlet tubing should one or the other fail. The third can be overcome, as discovered by VIIBRE researchers, by heating and degassing the solutions under vacuum, yet some solutions (i.e. peroxide) will degrade rapidly with heat. Bubble formation, however, is only one cause of pump variation over time. PDMS deformation is unavoidable in this setup and can only be altered through the membrane thickness and ratio of curing agent to base polymer. Clogged channels are inevitable, particularly when using oil as a sealant, but also when stopping and starting the flow repeatedly with minutes or hours of time in between the periods of use. Continuous running is suggested, which complies with repeated trial heterodyne experiments. In the case where the pumps must be stopped for a significant periods of time, ethanol should be used to purge and pumps should be stored with no compression of the channels to prevent the formation of permanent indentations. A final contributor to pump variation over time may be due to an initial misalignment or a shift in alignment over time. Rigorous initial alignment is

required to reduce alignment issues, however, even a slight shift of the thrust bearing due to uneven wear of the PDMS washer or PDMS device can lead to an alteration in the alignment. Regular replacement of the PDMS washers could aid in alleviating this issue temporarily, while fixing the location of the thrust bearing could provide a more robust, long-term solution. Though significant, these pump weaknesses can be overcome satisfactorily to use them for the generation of sinusoidal concentration profiles.

In order to generate a true sinusoidal concentration profile with a constant flow rate, a pair of pumps must be used to define the profile for each reactant. This quickly scales a three reactant experiment to six pumps, increasing the difficulty significantly as maintaining six working pumps instead of three is more than twice the challenge. While the work in Chapter III resulted in reduced noise in data produced with true sinusoidal concentration profiles, variable flow data still contained rich heterodyne frequencies that were of similar accuracy to those produced under constant flow regimes. Future endeavors should repeat the Fluorescein quenching experiments with a constant flow setup for a truer comparison of variable and constant flow.

#### 4.2.2 Upstream Chemical Signal Mixing

A simple serpentine mixer with four inlets was utilized as the reaction chamber in the peroxyoxalate chemiluminescence reaction. As this reaction requires the “mixing” of aqueous with non-aqueous solutions, a 2% pluronic solution driven at a constant flow rate was incorporated to aid in the mixing and diminish the oil in water droplet formation that occurs in its absence. Refinement of the pluronic concentration, as well as the dimensions of the serpentine mixer may result in higher efficiency mixing. The cross section of the mixer was 100

$\mu\text{m}$  W x 70  $\mu\text{m}$  H, though a channel that is taller than it is wide will decrease the relative diffusional distance, promoting more thorough mixing.

The fluorescein quenching reaction was performed in a straight channel as both solutions were aqueous. Bubble formation in these experiments was significant and device designs have already been created to allow for bubbles to exit the device through a separate outlet by taking advantage of the vertical channel orientation (fluid moves toward the bottom of the channel, while bubbles stay at the top). These devices should be constructed and tested with the Fluorescein quenching setup.

#### 4.2.3 Downstream Chemical Signal Detection

Signal detection by the Continuous Flow Photometer produces consistent data whether in chemiluminescence or fluorescence mode. The background signal caused by the excitation laser drifts over time, but by less than 50mV, which causes little issue with the data. The light-tightness of the enclosure box should be improved as a change in the ambient room light (lights on or off, opening of nearby refrigerator) can be detected, though are currently mitigated by leaving the lights on and blocking the side of the enclosure facing the refrigerator. Additional improvements could include a controllable internal light source for instrument calibration, particularly for application to low signal setups.

#### 4.2.4 Data Analysis Techniques

Matlab, with its built in Fast Fourier Transform, is utilized for the analysis of the raw data sets. It remains unclear exactly how this FFT, based on the Cooley-Tukey algorithm, is implemented for long data sets. Work is ongoing by members of VIIBRE to create a Fourier transform with known implementation scheme with which to process these data sets. Once



complete, the frequency domain data output from Matlab should be compared to that from this developed FFT technique.

#### 4.2.5 Modeling Heterodyne Chemistry

Models of the Fluorescein quenching and peroxyoxalate chemiluminescence with sinusoidal concentration profiles for each reactant were constructed in Matlab. These models, solely based upon the reaction kinetics, lack the diffusion and flow components of the physical experiment. Constant concentration models of both reaction systems, along with their particular reaction mixer, have been constructed in Comsol Multiphysics 4.2a and include laminar flow, transport of dilute species, and chemical reaction modules. This model, for the purpose of the manuscript, will be altered to sinusoidal concentration profiles. It was not completed for this dissertation as the completion of this model assigned to a student to provide them the opportunity to be included as an author.

#### 4.2.6 Probing Biochemical Reactions

Extension of this framework into biologically relevant areas should be a priority. While the current setup utilizes a detector for light produced by a reaction, the possibilities of using fluorescently labeled reactants could provide a biochemical application with the existing setup. Exploration of biochemical reactions, particularly those that follow Michaelis-Menten kinetics, should follow the completion of the Fluorescein quenching and peroxyoxalate chemiluminescence.

APPENDIX A

A Alphabetical List of Contributors

Brian Akselrad	Jennifer McKenzie
Stephen Arndt	Dave McLean
Eric Bankaitis	John McLean
Frank Block	Rafael Montenegro
Tommy Byrd	Amy Ostrowski
David Cliffel	Ryan Planchard
Erica Curtis	Ravi Rao
Madeliene Durkee	Ron Reiserer
Jeff Enders	Phil Samson
Alex Garza	David Schaffer
Cody Goodwin	Nicole Schramm-Sapyta
Parker Gould	Joe Scherrer
Doug Hall	Kevin Seale
Rachel Harvey	Stacy Sherrod
Loi Hoang	Raghav Venkataraman
Ayeeshik Kole	Erik Werner
Daniel Ly	John Wikswo
Dmitry Markov	Danny Winder
Jody May	Jie Zhou

## APPENDIX B

### B MTNP-SPED-NEI-IM-MS USE AND TROUBLESHOOTING GUIDE

This manual provides documentation of all aspects of the current microfluidic-mass spectrometry platform (Figure B.1) for real-time analysis of the cellular exometabolome as discussed in Chapter II. Please consult this guide for part numbers, instrumentation settings, and protocols.

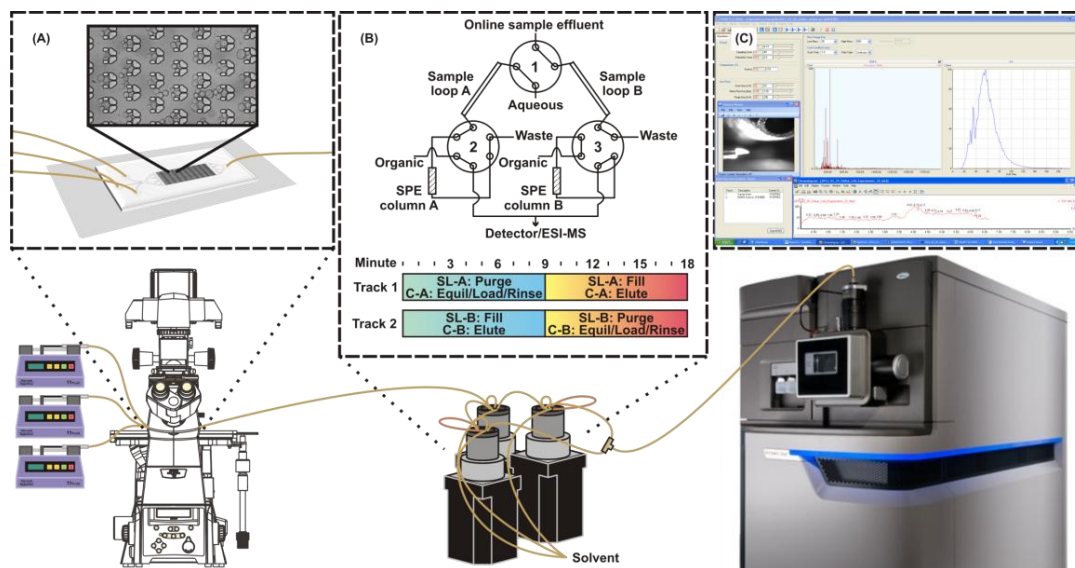


Figure B.1 MTNP-SPE-nESI-IM-MS platform with Harvard Apparatus syringe pumps, Nikon Eclipse Ti-e with stage incubator, solid phase extraction desalter with Eksigent and nanoAcquity pumps for solvent flow control, nanoelectrospray ionization source for continuous flow sample analysis in the Waters Synapt G2 ion mobility-mass spectrometer. Beyond the initial experimental setup, all components are fully automated and capable of running multi-hour experiments limited by the lifetime of cells in the MTNP.

## B.1 Liquid Management

### B.1.1 Fittings and Connectors

Common thread types of fittings and connectors are shown in Figure B.2. 10-32 thread type will most often be encountered when using 1/16" PEEK tubing for high-volume/high-flowrate applications. In order to use 10-32 1/16" PEEK connectors (as shown in top left), one



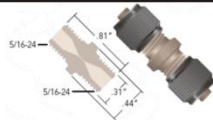


Image	Thread Type	Parts' Uses
	10-32 (Coned)	IDEX: F-120, P-659, P-770, P-727, P-742
	Luer Lock (Male)	IDEX: P-662, P-659
	5/16-24 (Female nut and male screw)	IDEX: P-662, P-888, P-772, front of Eksigent system
	2-56 (Male screws and female union)	VICI: C360UPKG4, C360NFPKG, C360PPK
	6-32	IDEX: F-124S, P-770, M-135, M-520, M-120x, M-130x

Figure B.2 Common fittings and part numbers used in this instrumentation setup.

must use IDEX Health and Science 'Green sleeves' (IDEX Health and Science F-242X). From IDEX: "Silica SealTight Sleeves are designed to connect 70  $\mu\text{m}$  – 1mm OD capillary tubing to any standard 10-32 coned port normally intended for 1/16" OD tubing. The 1.6" long Silica SealTight sleeves withstand up to 50°C and can be finger tightened to hold up to 5,000 psi when using the NanoTight fittings". Luer lock connections will most often be used to connect 360  $\mu\text{m}$  OD tubing

to syringes for liquid perfusion. The use of 5/16-24 fittings involves a male part (e.g., IDEX PN: P-888), which has threads on the outside, a female nut (IDEX PN: P-416), which has threads on the inside, and a ferrule piece (IDEX PN: F-152, for 360  $\mu\text{m}$  OD tubing) which goes between those two parts. The ferrule receives force as the female nut is tightened and in doing so causes the ferrule to crimp the 360  $\mu\text{m}$  OD PEEK or fused silica tubing. Fittings with 2-56 thread are common to VICI-Valco type fittings and will most commonly be used on VICI unions (VICI PN: C360UPK(G)4), and for valve fitting connectors (VICI PN: C360NFPKG, C360PPK, *See Valves*). Thread type 6-32 is found on coned nuts (e.g., IDEX PN: F-124S) and is similar to ferrules (F-152) in the sense that it crimps 360  $\mu\text{m}$  tubing directly. **CAUTION:** When using connectors on tubing and using finger tightening it is generally not recommended to tighten very strongly when direct connector-to-tubing combinations are used. For example, when using an IDEX P-888 (5/16-24) union, where a PEEK ferrule directly crimps the 360  $\mu\text{m}$  OD tubing, one should tighten just tight enough to not let the tubing pull out under moderate force. Tightening past this point leads to occlusion of the line (especially for PEEK tubing). When using fittings that require a 1/16" sleeve to connect to 360  $\mu\text{m}$  OD tubing, more force can be used to tighten the fitting as the pressure applied must first penetrate the green sleeve before crimping the underlying 360  $\mu\text{m}$  OD tubing.

### B.1.2 Syringe Pumps

Media perfusion of microfluidic devices was carried out using a Harvard Apparatus Model '11' Plus Dual Syringe Pump with Serial Communication (MA1-70-2212). The syringe pumps drive the plunger of a syringe at a rate that is directly dependent on the user's inputted syringe inside diameter. Common syringe diameters can be found in the manual. When operating the syringe pumps, the 'pusher block brackets' (small black bars that screw into place to hold the disc shaped end of the syringe plunger) are often removed to provide a more level

surface for the edge of the syringe plunger to rest against. Infusion can be performed manually using the pump's interface and LED screen, or automatically using the RS-232 data connection cables and either the pump control buttons or a macro written in *NIS Elements*. When operating manually the choice between infusion and withdraw can be selected based on the direction of the “←FLOW→” button. If operated using software and then disconnected and used manually, occasionally the “←FLOW→” button can become reversed. When operating the syringe pump it may become customary to press on the pusher block to expedite flow, however, after pressing on the block, the pump driving mechanism will ‘kick’ back, causing cessation of flow immediately thereafter. Use of syringe retainer is recommended, however, use of the syringe block bracket is not necessary. It is important to be sure the “Infuse limit switch adjuster” is placed at the maximum position (as shown on page 6 of the instruction manual) and tightened often (as use of the pump seems to loosen this adjuster). The pump manual is included in this work.

### B.1.3 Syringes

Commonly, 250  $\mu\text{L}$  (Hamilton 81120 250  $\mu\text{L}$ , Model 1725 TLL) or 500  $\mu\text{L}$  (Hamilton 81220 500  $\mu\text{L}$ , Model 1750 TLL) glass syringes are used to infuse media through microfluidic devices. Syringe-to-360  $\mu\text{m}$  tubing connections are made using a PEEK female Luer adapter assembly (IDEX Health and Science, P-662, 5/16-24 thread port connection, 0.006 in thru hole). This results in less leaking than that experienced when using 10-32 PEEK female Luer lock adapter (IDEX Health and Science, P-659, 10-32 thread port connection, coned Female).

#### B.1.4 Tubing

Typically polyether ether ketone (PEEK) tubing is used wherever possible. An OD of 360  $\mu\text{m}$  with varying ID's (IDEX Health and Science, 1574, 1570, 1573, 1571) will be used for most applications (with 1/16" tubing being required very infrequently). Polymer tubing cutters (IDEX Health and Science, A-327, Standard Polymer Tubing Cutter for 1/16" and 1/8" tubing) are used to cut PEEK tubing to best ensure the severed end is not occluded. A main drawback to PEEK is the fact that noticeably large amounts of sample and biomolecular material have potential to adhere (reversibly and irreversibly) to its surfaces. This has been seen to cause, at times, massive tailing and memory effects. For this reason fused silica is used on sections of long uninterrupted tubing due to the glass's less adherent surface properties. Teflon tubing is available from IDEX as well (PNs: 1930, 1931, 1932, and 1933) in 360  $\mu\text{m}$  OD and 50-150  $\mu\text{m}$  IDs. Teflon is recommended as being compatible with all type of solvents, which could lead one to believe that chemical reactivity with this material is low relative to other types of tubing.

### B.2 Microfluidic Device

#### B.2.1 Device Design

Microfluidic devices such as the MTNP in Figure B.3 are designed in 2D through the use of AutoCAD or similar computer-aided design software. Designs are compiled by VIIBRE staff engineer (David Schaffer) and sent to Advanced Reproductions for creation of a chrome mask. It can take anywhere from two weeks to several months for a mask to be sent out and to arrive depending on how full the mask design is when drawings are submitted.

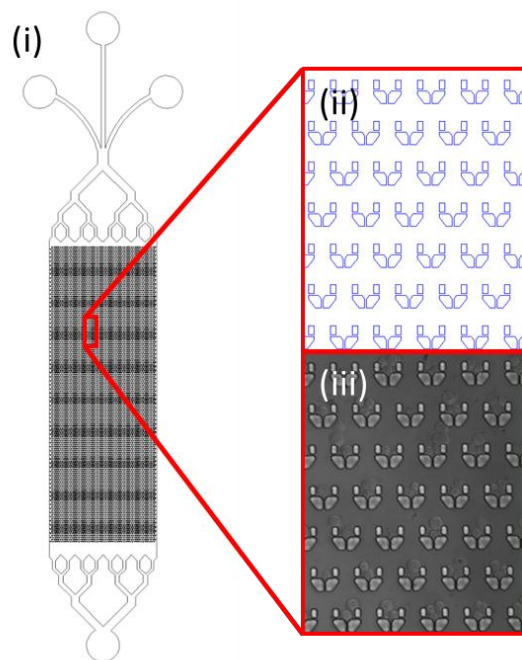


Figure B.3 Design of the MTNP (i) with  $18\ \mu\text{m} \times 12\ \mu\text{m}$  cell traps (ii) capable of trapping 2-3 cells each (iii) in a device with a 234 nL volume and 7056 cells traps.

### B.2.2 Photolithography

A master can be created from the chrome mask through photolithography techniques.

The protocol for a  $\sim 12\ \mu\text{m}$  high T12 trap design such as those on Mask 38iii in the mask repository is as follows:

1. silicon wafers are rinsed with acetone then isopropanol, dried under a stream of nitrogen, dehydration baked for 5 minutes at  $180^\circ\text{C}$  and allowed to cool to  $<60^\circ\text{C}$ .
2. SU-8 2010 is spun on clean wafers for 10 seconds at 500 rpm (acceleration of 2) followed by 35 seconds at 2500 rpm (acceleration of 5).
3. The wafer with SU-8 is then covered, soft baked under a ramped temperature from 50 to  $95^\circ\text{C}$  (2 min at  $95^\circ\text{C}$ ), and allowed to cool to  $<60^\circ\text{C}$ .



4. The edge bead is then removed by spinning under a stream of edge bead remover.
5. The mask is positioned ovetop of the SU-8 coated master with uncovered portions covered by ruby tape and exposed for 20-45 seconds at a  $45 \text{ J/cm}^2$  dose.
6. The master is then covered, post-exposure baked with a temperature ramp of  $180^\circ\text{C/hr}$ , baked for 5 minutes at  $95^\circ\text{C}$ , and allowed to cool to  $<60^\circ\text{C}$ .
7. The master is then developed on the spinner for 3 minutes or until rinsing with isopropanol is completely clear.

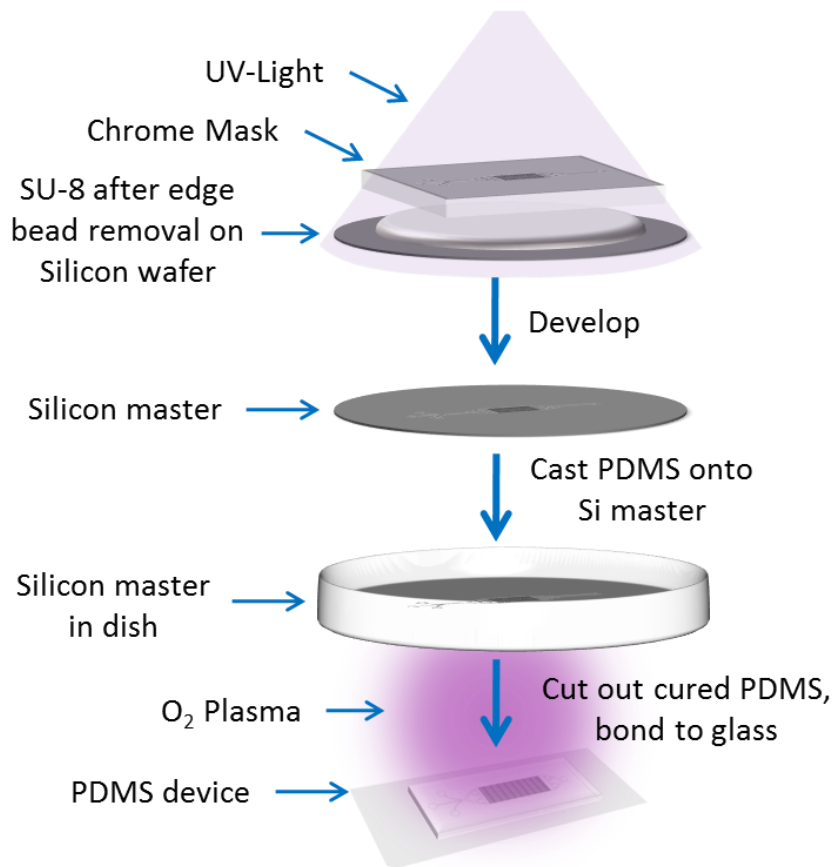


Figure B.4. Sequence of steps in photolithography and replica molding.

8. The master is hard baked with a temperature ramp of 120°C/hr, baked for 30 minutes at 180°C, and allowed to cool completely.

### B.2.3 Soft Lithography and Device Silanization

PDMS devices on glass coverslips are constructed through replica molding and silanized with a PEG-silane to prevent non-specific metabolite, peptide and protein adsorption. The protocol is as follows:

1. The cooled master is placed in a round petri dish, poured with mixed 10:1 Sylgard 84 elastomer: curing agent (until roughly 3-4mm deep), and degassed under vacuum until bubbles are gone.
2. PDMS is allowed to cure for 4 hours at 60°C.
3. Patterned areas are then cut with a scalpel and removed from the master.
4. Inlet and outlet ports are created by inserting a sharpened biopsy punch through the cut PDMS, patterned side up, with a sacrificial PDMS layer underneath to protect the punch, NOTE: Cores should be removed after each punch and can be aided by keeping a piece of wire inserted into the shaft of the punch stopping a few millimeters before the tip.
5. Both sides of the PDMS are cleaned with tape and coverslips are cleaned with acetone and IPA.
6. The device is placed patterned side up along with one of the coverslips on a 2"x3" glass slide and placed in the chamber of the Harrick Plasma cleaner about 3 inches from the back of the chamber.
7. Device and coverslip are then plasma activated under vacuum for 30-45 seconds, removed from the chamber and the device is placed patterned side down on the coverslip,

NOTE: Tweezers can be used to lightly press on the top of the PDMS to assist with bonding if needed.

8. Immediately after bonding, the PEG-Silane solution (2% in 95% EtOH, 5% H<sub>2</sub>O, 10 mM acetic acid) is flowed through the device from the outlet until it just comes out the inlets.

9. Devices are allowed to sit at room temperature for at least 10 minutes and are then rinsed with EtOH and H<sub>2</sub>O.

10. Devices are then incubated at 110°C for 10 minutes and allowed to cool.

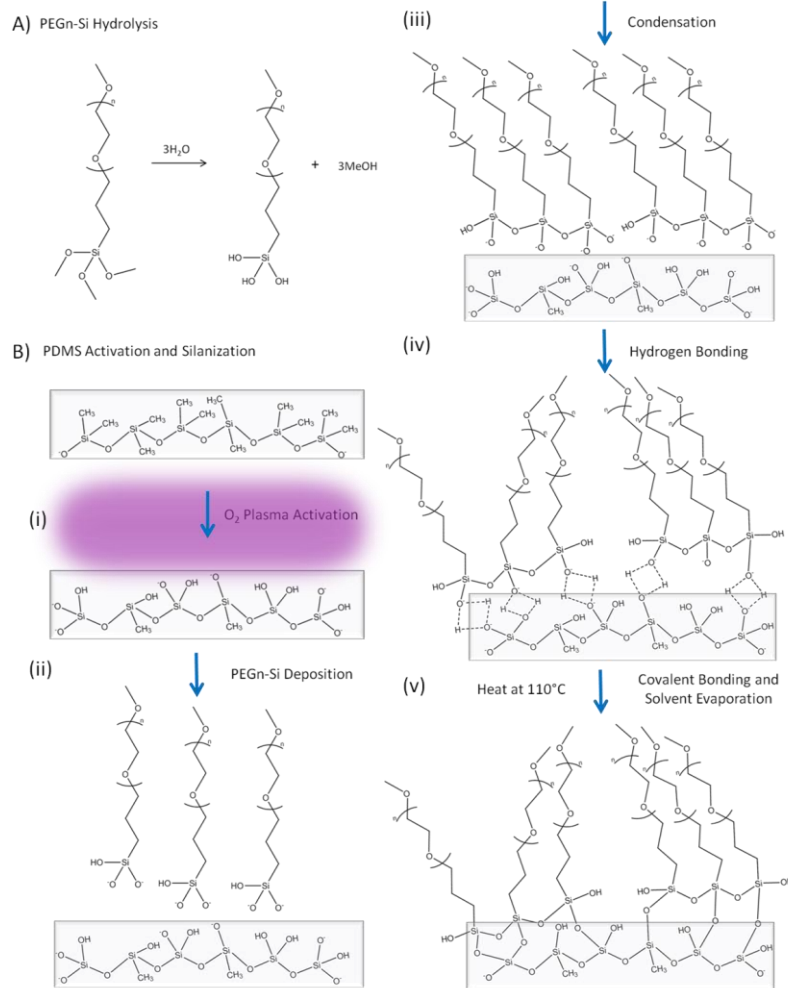


Figure B.5. PDMS Silanization Procedure.

#### B.2.4 Priming

Prior to experiment, the microfluidic device is primed by first putting a drop of methanol on the outlet port, allowing it to move by capillary action through the device. If it does not easily move, gently flick one end of the cover slip against the bench top. Devices that do not easily allow ethanol to flow in this way should not be used. The outlet can then be intubated with PEEK tubing attached to a syringe containing the basic media for the experiment (i.e. RPMI or Running buffer) and the plunger can be depressed until beads of media form on the inlets. The outlet and inlets should be covered with a drop of the same media before removing the PEEK tubing from the outlet.

### B.3 Cells

#### B.3.1 Culture

Cells should be cultured according to supplier's instructions. Techniques will not be addressed herein as many cell culture resources exist.

#### B.3.2 Loading

An aliquot of cells is obtained just prior to the experiment. For non-adherent cells, ~500  $\mu$ L of cell suspension is dispensed into a clear or light-colored microcentrifuge tube (dark colors are difficult to see through under the microscope). These cells can be used almost any day during the culturing procedure and volume dispensed adjusted to account for changing cell density. For adherent cells, subculturing procedures are followed to detach cells from surfaces of the culture flask. When cell suspensions are transferred to a centrifuge tube for trypsin removal, an aliquot is placed in an additional tube that is destined for the experiment. Cells are

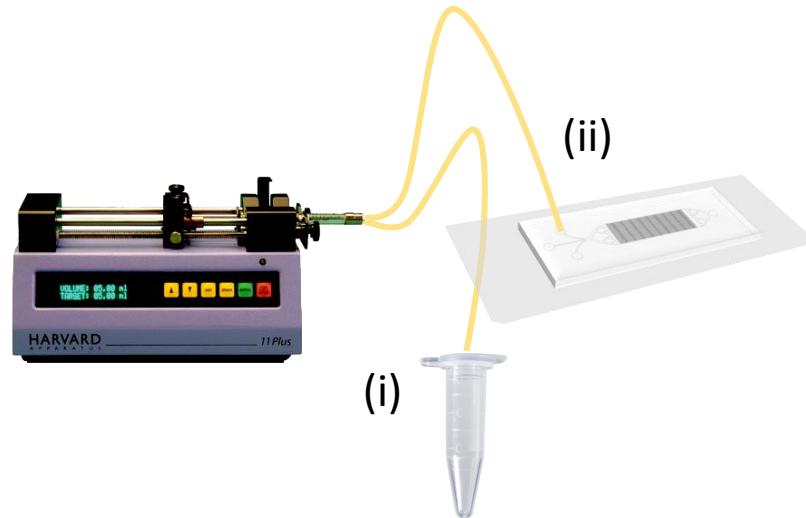


Figure B.6 Cell Loading Diagram

centrifuged according to culture instructions (typically low speed,  $\sim 100xg$ , is best). Media/trypsin is removed from the cell pellet and the aliquot for the experiment is resuspended in the desired media at the desired cell density (recommended at full density of split flask or greater). The cell suspension is transferred to a clear or light-colored microcentrifuge tube. For either adherent or non-adherent cell suspensions, aliquots are centrifuged at 1200 rpm for 2 minutes in the McLean lab centrifuge (Eppendorf Minispin Plus) just prior to cell loading.

The tube of pelleted cells is placed in the orange foam tube holder and onto the stage insert, fitting over the four pegs on the insert. The microscope and software are both ready for use (see below for instructions) and all syringes have been prepared and set to run forward on syringe pumps. The DIC optical configuration in NIS Elements is selected and the Ti-pad is checked for the halogen shutter to be open with the lamp in the on position and at 3V. The light will be physically visible if the settings are correct. The stage is then positioned with the light immediately overtop of the open tube containing cells. Looking into the eye piece, the focus is adjusted to bring some portion of cells into focus. This can be tricky at first, but with experience

it becomes easy to quickly bring cells into focus. The light path can be switched from the eye piece to the camera and play button hit to view the cells on the monitor. The end of the PEEK tubing into which the cells are to be loaded is then placed in the microcentrifuge tube (fluid should always be exiting the tubing when inserting into the cells to avoid any air bubbles) and pushed down towards the bottom to contact the cell pellet. It is useful to put a small kink in the tubing about 1.5 inches from the end, but keep the bend <90 degrees. The plunger of the syringe attached to this tubing can be clamped to the pusher and the pump flow direction can then be reversed to withdraw cells into the PEEK tubing. There is a delay when the flow is reversed before suction occurs. For a flow rate of 500 nL/min, it is around 1.5 minutes. The PEEK tubing should be constantly held in order to manipulate the location of the end relative to the cells. It is helpful during the loading process to adjust the exposure as needed and to move in and out of focus of the tubing end in order to view moving cells. Once cell movement into the tube is visually confirmed, loading continues for 3 minutes at 500 nL/min with a 2 ft PEEK tubing length with an inner diameter of 50  $\mu\text{m}$ . If the tubing length, ID or the flow rate is altered, the amount of time for loading should be recalculated. Once the desired loading time has been achieved, the pump is reversed and plunger unclamped from the pusher. Again, there will be a delay before the flow is in the forward direction. During this time, the device should be intubated with tubing from the remaining forward flowing syringes. If the cells need to avoid the contents of the syringe, the pump can be stopped right before the tubing is intubated, but a drop of liquid should be on the end while inserting the tubing to prevent air bubbles. The tubing containing the cells can then be intubated as well to begin the loading. The outlet tubing is also connected at this time. Note that if a given pump is stopped while cells are loaded into the device, some back flow of cells into those lines may occur. One way to prevent this is by putting crimped plugs of PEEK tubing into the remainder of the inlet ports during loading, then

intubating with syringe tubing post-cell loading. Cells are allowed to load the device completely while the device is carefully moved into the stage incubator. Outlet tubing should not be connected until the rate of cells exiting the device has slowed significantly.

## B.4 Microscopy

### B.4.1 Nikon Eclipse Ti-e

The startup procedure must be followed or connection to the microscope/camera will not work correctly. Startup procedure is as follows:

1. If the computer has been shut down or logged off, it is started, logged into and allowed to load completely.
2. Power to all microscope components (except for the mercury arc lamp and the camera) is achieved by turning on the power strip on the back right of the cart.
3. If fluorescence images are to be taken, the mercury arc lamp power must be turned on separately from its power switch.
4. Once the initialization procedure has completed, the camera can be turned on from its power switch.
5. NIS Elements is then started.

A common issue results from the software not loading the camera driver. In the event of this error message, close the software, wait and try to reopen again. This problem is just as likely a result of a faulty shut down procedure as it is from the startup procedure. Shut down procedure is as follows:

1. All desired image files are saved.

2. NIS Elements is closed.
3. The camera power is turned off from its specific power switch.
4. If the mercury arc lamp is on, its power switch can be set to off.
5. The power strip is then turned off.

#### B.4.2 NIS Elements

For detailed instructions on the use and capabilities of NIS Elements, consult the user guide located in the NIS Elements folder.

#### B.4.3 Stage Incubator

Temperature, gas and humidity control can be achieved using the stage incubator. Its control box will turn on and off with the power strip on the back right of the cart. The gas line with Luer lock fitting is attached to the incubator for CO<sub>2</sub> control, the tank turned on and the stop valve and needle valve on the back of the cart are adjusted appropriately. (The end of the tubing can be placed in a beaker filled with water to check the gas flow rate.) Once the device has been intubated and loading has begun, the device is carefully moved onto the stage incubator. It is important to have the stage incubator pressed into place on the stage before transferring the device. The clips are screwed into place to hold the cover slip, the side channels are filled with water to maintain humidity, and the lid of the incubator is placed carefully on top, allowing inlet and outlet tubing to rest between the top and bottom pieces. The incubator channel is then set to 37°C. Once the experiment is completed, the channel is set to off and the gas turned off. The control box power is turned off with the microscope power strip.



## B.5 Desalter Apparatus

### B.5.1 Inline Filters

Inline filters have been used to prevent cellular debris escaping from the microfluidic device from entering the valves and column setup, where clogging is much more likely and problematic. Two types of inline filters are primarily used: black 0.5  $\mu\text{m}$  PEEK frit inline filters (IDEX PN: M-120X) and natural colored 1  $\mu\text{m}$  SST filter screen (IDEX PN: M-130X). Typically, these filters were replaced every experiment because it can be difficult to assess their level of occlusion.

### B.5.2 Eksigent/Desalting Pumps

An Eksigent Nanoflow Metering System is used to supply the organic-based elution solvent. The Eksigent system is capable of flowing from 10-500 nL/minute from each of four independent channels, all of which are gas driven by 100psi of either air or nitrogen. Typically the organic solvent is perfused through the desalting apparatus at 500 nL/min. This flowrate was chosen to match the flow of the microfluidic bioreactors but also due to typical pressure constraints with regards to downstream columns and frits. To track this pressure, one must create a "Run Manager" flow profile. While this is running the pressure information is automatically collected and displayed on the chart on the main window of the Eksigent software. Maintenance and calibration must be performed routinely to ensure the pumps work efficiently and without the complications of air bubbles.

### B.5.3 Waters NanoAcquity UPLC Pump

The NanoAcquity pump is used to perfuse the desalting apparatus with aqueous solvent for the purpose of rinsing the columns of salt contaminants. The NanoAcquity pump is controlled through the Binary Solvent Manager portion of the MassLynx program and set to a flow rate of 0.9 $\mu$ L/min in arrangement 2.

### B.5.4 Valves

Three 10-port Nanovolume UPLC Valves with 360  $\mu$ m fittings, C72MH-4690ED (VICI Valco Instruments Co. Inc., Houston, TX), were arranged as seen in Figures B.8 and B.10. These valves connect to the computer through a RS-232 daisy chain cable to the “2-position actuator control module”. The “manual controller”, the valve itself and the power supply cable also all connect to this control module (see Figure B.7). It is important to note that there are different models of controller modules and using the incorrect part will cause valves to malfunction.

### B.5.5 Columns

Columns are comprised of three components: the fused silica tubing, the chemically interactive silica packing phase, and the frit, which prevents the phase from escaping with the solvent flow. Columns are made from 360  $\mu$ m OD fused silica tubing. The ID of the tubing is chosen based on the size of the packing phase particles that are going to be used to pack the column. The packing phase used in these exometabolomic experiments was 3  $\mu$ m C18 silica phase (Jupiter 3  $\mu$ m C18 300 Å bulk packing phase, PN: 04A-4263, 404951-1, Phenomenex) and typically fused silica with 100  $\mu$ m ID and 360  $\mu$ m OD.

Column frits are made by using the following protocol:

1. Mix 170  $\mu\text{L}$  of KASIL (PQ  $\text{\textcircled{R}}$  KASIL $\text{\textcircled{R}}$  1 Potassium Silicate Solution) and 30  $\mu\text{L}$  of formamide (F9037 SIGMA) in an eppendorf tube. Vortex mixture.
2. Spin mixture down for <2min at a moderate RPM in a benchtop centrifuge. Yields a semi-solid lower layer of unusable polymerized material, and an upper layer of mixed unpolymerized material.

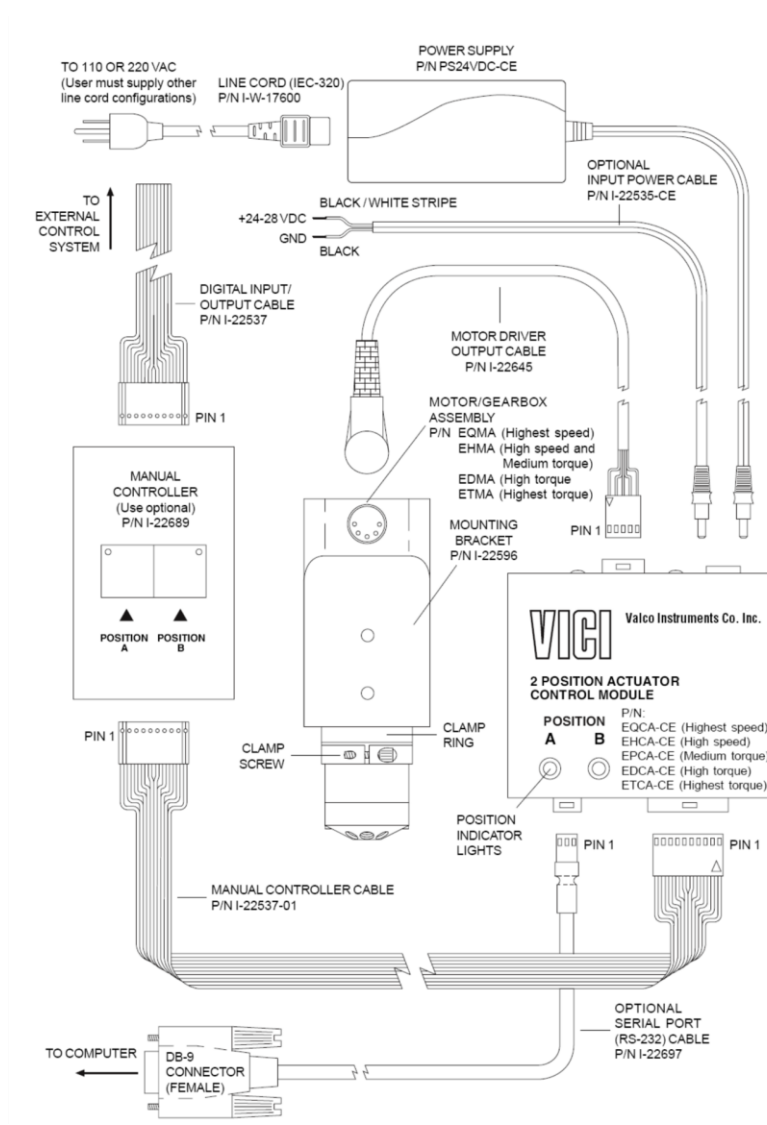


Figure B.7 Wiring and connection diagram for VICI/Valco/Cheminert actuated valves.

3. Dip pre-cut fused silica tubing into liquid upper layer for ~5-10 seconds. Liquid will rise into tubing due to capillary action.
4. Remove tubing from liquid and, keeping as still as possible, bake the fritted ends under a heating block for >3 hours/overnight at 100°C (Setting of 4.5 (high) on the VWR analog heatblock).
5. Cut frit to a few millimeters or shorter (depending on back pressure desired). Typical length for these experiments was a 2mm frit

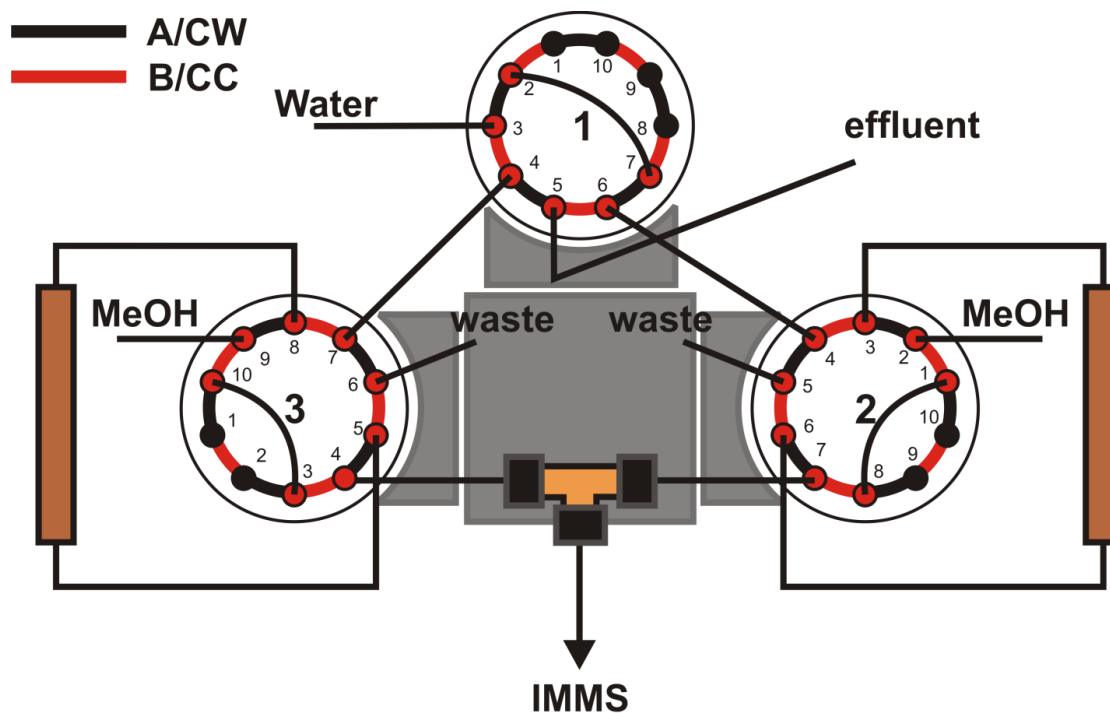
Columns are bomb loaded using a New Objective Nanobomb apparatus (New Objective PIP-500 Pressure Injection System). The Nanobomb accepts in incoming air/nitrogen pressure of 1000 psi to generate the necessary pressure to drive the beads into the tubing. It not necessary to use ultra-pure nitrogen as the gas is only used as a pressure source. Follow standard protocol for the Nanobomb and always wear eye protection.

#### B.5.6 Sample Loop

The sample loops in this experiment were made from fused silica tubing with the dimensions: 360  $\mu\text{m}$  OD and 250  $\mu\text{m}$  ID. This large ID allowed the sample loops to be much shorter.

#### B.5.7 Desalter Arrangements

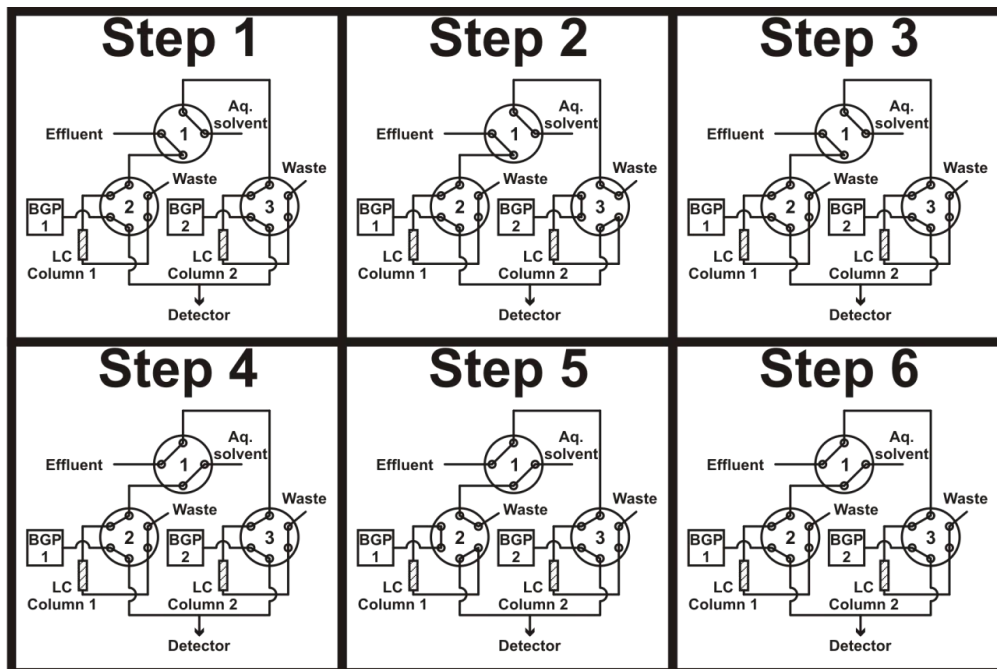
There are two primary valve arrangements that have been used to desalt a continuous bioreactor sample stream. The first arrangement is a six-step arrangement, as depicted in Figure B.8, which was used for multiple years and was used for collecting most the preliminary data for the system. This cycle provides a constant loading condition, ensuring that all analyte material in



## Valve Arrangement 1

Figure B.8. Valve arrangement 1. This arrangement incorporated a 6-step valve cycle to achieve online SPE desalting. This arrangement was entirely capable of performing online desalting of a continuous sample stream, but suffered from back pressure problems when used for online desalting of PDMS bioreactor effluent.

the online sample effluent is collected. In addition, contaminants were rinsed from the SPE columns during a purge step which is directed to waste. Valve cycle steps can be scaled in time uniformly to yield a cycle which is better for detecting high frequency oscillations (short step durations) or one which is better for detecting very low abundance analytes (long step durations). Figure B.9 outlines the valve switching scheme for online sample preparation. In step 1, the valve orientation was as pictured in Figure B.9, such that SPE column A was loaded with online sample effluent and SPE column B was desalting a sample plug and sending salts to waste. Valve 3 was switched such that SPE column A was receiving sample effluent and SPE



Valve Positions  
(CC - Counter clockwise, CW - Clockwise)

	① Step 1	③ Step 2	③ Step 3	① Step 4	② Step 5	② Step 6
Valve 1						
Valve 2						
Valve 3						

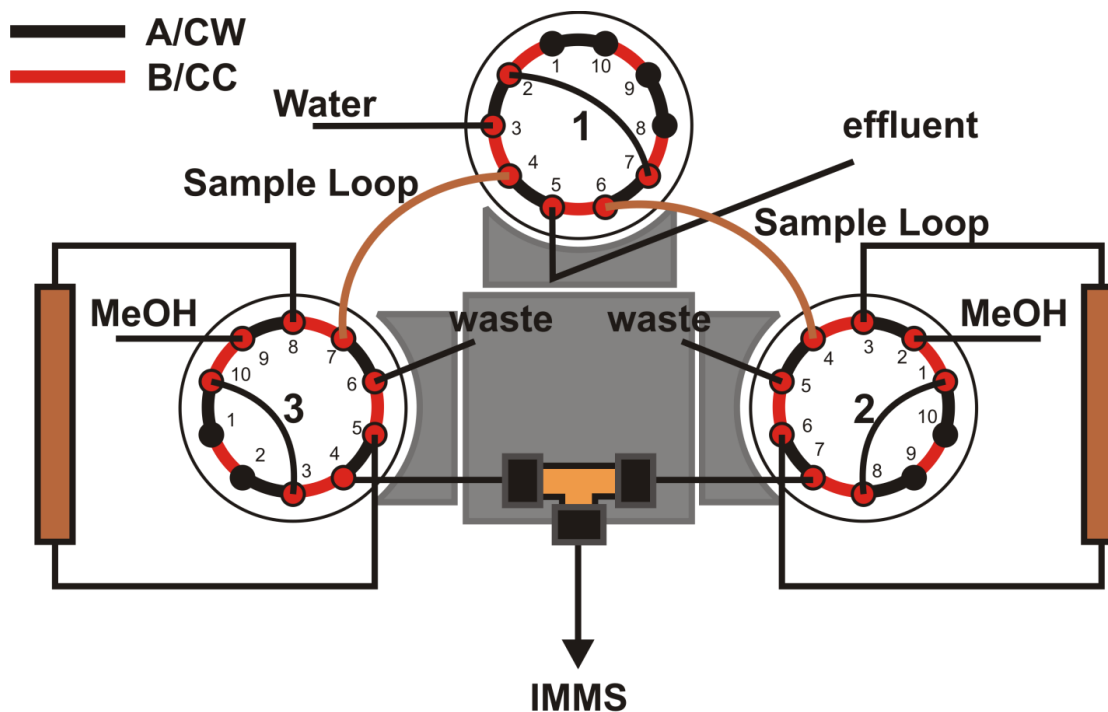
Figure B.9. Stepwise depiction of the 6-step desalting method using valve arrangement 1. The top portion shows the valve positions during each step. The chart in the bottom portion shows a graphical representation of these valve position during each step, where the number in the circle between each step (at the top of the chart) is indicative of which valve is switching to achieve the next step.

column B was eluted and directed towards the MS for ion detection. Because this is the first time through the cycle, column B has not actually been loaded with any analytical material at this time and so this elution is blank. After this, valve 3 was switched so that SPE column B was

equilibrated with aqueous solvent in preparation for its subsequent loading step. SPE column A continued to load sample throughout the equilibration of SPE column B. Next, valve 1 was switched such that the online sample effluent was directed to the newly equilibrated SPE column B. SPE column A was purged with water at this step allowing for desalination of the sample collected on the column. Valve 2 switched and SPE column A was eluted with organic solvent, while SPE column B was left in the loading position. Lastly, valve 2 was switched to equilibrate SPE column A and the SPE apparatus started the entire cycle again.

This arrangement suffered from constant problems associated with back pressure. As aqueous solvent was perfused over the columns, when using the first arrangement, a high back pressure, usually on the order of 2000-3000 psi, was generated immediately preceding the columns. Because there was a direct “line of sight” between the SPE columns and the microfluidics, when the valves switched back to load from the microfluidics, this enormous back pressure plug would travel backwards and cause the PDMS device to delaminate from the glass cover slip.

The second arrangement was designed in response to the frequent problems experienced with back pressure when using the first arrangement. This second arrangement was designed to ensure that the microfluidics never had a direct “line of sight” with the SPE columns. In Figure B.10, it can be seen that the arrangement is almost identical to the previous design except for the incorporation of sample loops. This addition simplified the valve switching scheme required by shortening it to only two steps. To explain the arrangement: sample loops, which were made of 360  $\mu\text{m}$  OD/250  $\mu\text{m}$  ID tubing, were 12.2cm long, providing a sample loop volume of 6  $\mu\text{L}$ . The continuous sample stream was diverted into each sample loop for exactly 9 min at 500 nL/min, thus filling the sample loop 75% of the way. Because water was always flowing through these sample loops immediately prior to sample flow, a plug of 1.5  $\mu\text{L}$  of water

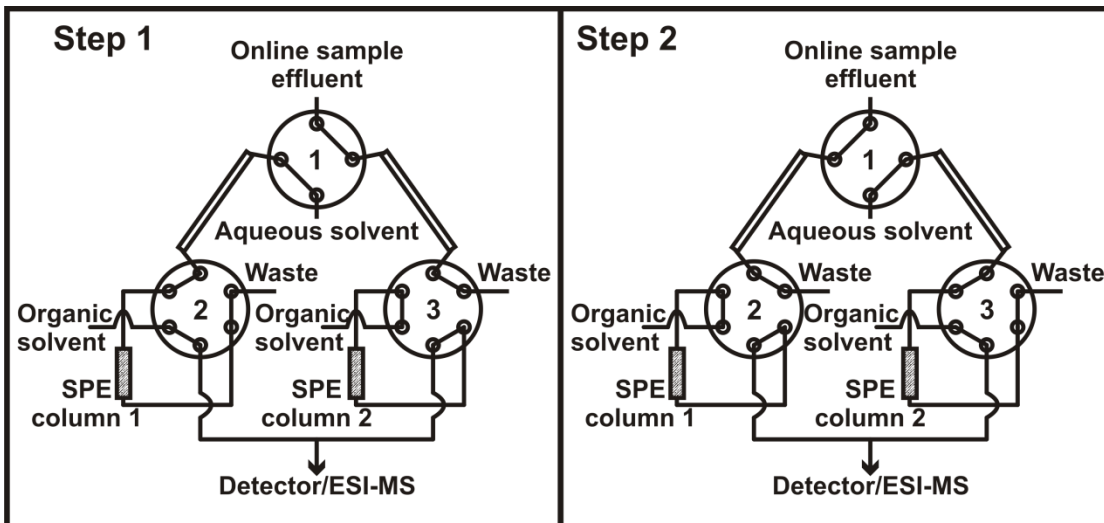


## Valve Arrangement 2

Figure B.10. Valve arrangement 2. This valve arrangement was a simplification of valve arrangement 1 and negated the effects of back pressure on the microfluidics by providing a waste port to vent excessive pressure. This arrangement incorporated a 2-step valve switching cycle to achieve online SPE desalting.

preceded each sample effluent plug. This plug served to quickly and roughly equilibrate the column with an aqueous solvent. Once the loop was filled to 75% with online sample effluent, the small water plug and sample effluent were passed over the column, using the aqueous solvent line to generate the necessary backpressure. Once the effluent had cleared the sample loop and had been entirely passed over the column, an additional 2.3 min or 2.1  $\mu\text{L}$  of aqueous solvent (H<sub>2</sub>O with 0.1% formic acid) was run over the column to serve as the rinsing/purging step to remove residual salts. Following the salt purge, the column was eluted with organic solvent (90% Methanol, 10% H<sub>2</sub>O, 0.1% formic acid). Whenever effluent was filling through a





**Valve Positions**  
(CC - Counter clockwise, CW - Clockwise)

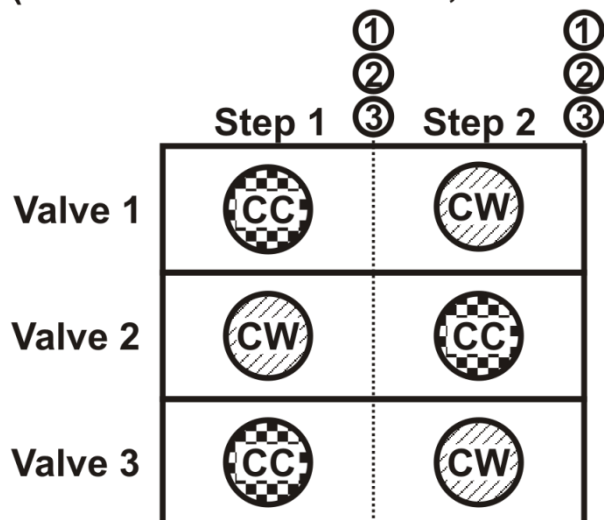


Figure B.11. Stepwise depiction of the 2-step desalting method using valve arrangement 2. The top portion shows the valve positions during each step. The chart in the bottom portion shows a graphical representation of these valve position during each step, where the number in the circle between each step (at the top of the chart) is indicative of which valve is switching to achieve the next step.

sample loop, the other end of the sample loop was open to a waste port. This allowed any residual back pressure that may have been generated by the pumping of water over the

columns to be alleviated out of the waste port instead of traveling upstream and delaminating the PDMS device.

## B.6 Mass Spectrometry Data Acquisition

### B.6.1 nESI Source

The nano-electrospray ionization (nESI) source is a probe “door” for the Waters Synapt G2. The nESI source can produce a sufficient spray so long as the incoming flow is in the range of 200nL/min to 2  $\mu$ L/min. The output line of the online SPE desalter is connected directly to the nESI source. The incoming tube is connected with a PEEK fitting to a stainless steel union. The nanospray capillary connects to the other end of the union. This union and also the nanospray

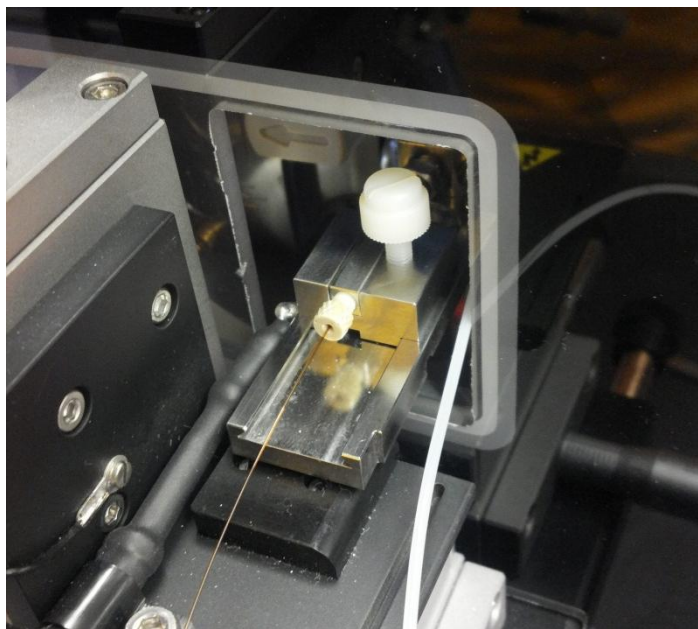


Figure B.12 The nESI source as it appears during normal operating conditions.

capillary are very susceptible to clogging when analyzing complex sample matrices such as bioreactor effluent.

#### B.6.2 Sample List

Continuous collection of discrete “samples” of data for processing in MarkerLynx is accomplished by creating a sample list within MassLynx, analogous to UPLC type sample collection. Each sample is a set length of continuously running analytes eluted off of the columns. For the medium length sample loops (12.2 cm), an 8.8 minute data file is collected, allowing for delay time between each sample. Analogous data file length for the long sample loops (24.5 cm) is 17.8 minutes. Samples are named chronologically to prevent confusion. Once samples are ready to be acquired, the sample list can be saved and started.

#### B.6.3 Method File/Data Dependent Analysis

When performing online, real-time analyses, data collection can be quite onerous. In traditional discreet sample analysis, such as might be performed with LC or just by direct infusion, it may be customary to acquire a preliminary data file and search through this file to find the pertinent feature/peaks and then during a second acquisition, set up the instrument to fragment or better accentuate these features/peaks. When performing online, real-time analyses, it can be difficult to setup the instrument to collect the information most pertinent to your study because there is no indication of when this material will show up and it may only show up once and perhaps only for a very short period of time. For this reason it was quickly decided to acquire data using Data Dependent Analysis (DDA). MassLynx provides the option for this type of experiment in the MS method portion of the software. Within the DDA profile there are many options that can be used to tailor this type of acquisition to the experiment being

performed. The following DDA profile settings were used for most online cellular effluent acquisitions:

<u>2012_03_06_ENDERS_880_ONLINE_MS_DDA_LOCK_FILE_trapCE_50.EXP</u>			
[ACQUISITION]		[COLLISION ENERGY]	
Survey Start Time	0.00	Using MS Auto Trap Collision Energy (eV)	
Survey End Time	8.80	4.000000	
		Using MS Auto Transfer Collision Energy (eV)	
		0.000000	
[MS SURVEY]		[CONE VOLTAGE]	
Survey Start Mass	50.0000	Survey Use Tune Page CV	YES
Survey End Mass		MSMS CV Ramp Start Voltage	0.0
2000.0000		MSMS CV Ramp End Voltage	80.0
Discard uninteresting scans	NO	[INCLUDE]	
Switch to MS/MS when rising	Intensity	Precursor Selection	Included
	above	Masses Take Priority	
	threshold	Use Include Masses List	YES
Intensity Threshold	15.0	Include Mass Range	600-
Survey Scan Time	1.000	1200	
Survey Interscan Time	0.024	Use Include File Masses	NO
Survey Data Format		Include Window +/- (mDa)	100.0
Continuum		Include Retention Time Window	10.0
ADC Sample Frequency (GHz)	3.0		
[MS/MS]		[EXCLUDE]	
MSMS Start Mass	50.0	Detected Precursor Inclusion	Using
MSMS End Mass	2000.0	Real Time Exclusion	
Number of components	1	Detected Precursor Inclusion	Include
Switchback threshold (intensity / second)	10.0	After Time	
Use MSMS to MS Switch After Time	NO	Include After Time (s)	120.0
Use MSMS to MS Switch After 1 Scan	NO	Use Exclude Masses List	NO
Use MSMS to MS Switch After N Scans	YES	Use Exclude File Masses	NO
MSMS Switch After Scans	1.0	Exclude Window +/- (mDa)	100.0
MSMS Scan Time (sec)	1.000	FragmentationMode	CID
MSMS Interscan Time (sec)	0.024	[MOBILITY]	
MSMS Data Format		Use Precursor Drift Times	NO
Continuum		Maintain Mobility Separation	YES
Use MS/MS ipr File	NO	Calibration	Dynamic
		1	
[PEAK DETECTION]			
Use Intensity based Peak Detection	YES		
Peak Detection Window	3.0		
Deisotope Peak Selection	YES		
Charge State Tolerance Window	3.0		
Charge State Extraction Window	2.0		
Deisotope Tolerance Window	3.0		
Deisotope Extraction Window	2.0		

## B.7 Mass Spectrometry Data Analysis

Once data files are collected, they can be transferred to a data analysis computer, aligned through MassLynx and processed with MarkerLynx and GEDI, if desired.

### B.7.1 MassLynx Data Alignment

Data collected in the method described above does not correct, on-the-fly, or collect data to allow for a lock spray collection. To align the data, a peak of reasonable intensity and presence in all samples is chosen, commonly HEPES + Na<sup>+</sup> (m/z = 261.0888 Da). Data is aligned by first opening any file in the data set in Chromatogram to set the file path, then in the MassLynx window selecting 'Tools', 'Automated Mass Measure'. In the AFAMM box, files desired to be aligned are double-clicked to change the red '✗' to a green '✓'. 'Automatic Peak Detection' parameters are set such that the lockspray mass is 261.0888, if aligning to HEPES, mass window is +/-0.150 and background subtraction is not selected. Samples are then processed. Once complete an additional, centroided data file is created with the name as set in the 'Automatic Peak Detection' parameters. The sample list is then altered to include these new file names along with any standards that may be ideal to incorporate into the data processing. A method file for processing must be created within MassLynx by selecting 'Tools', 'Edit Method'. For this type of non-chromatographic data, 'Combined Scan Range' is selected, with a threshold of 1000 and mass tolerance of 0.05. Deisotoping of the data is not possible in the 'Combined Scan Range' feature. The method file is then saved.

### B.7.2 MarkerLynx

Once data is aligned and centroided, it can be processed with MarkerLynx for detection of peaks across the samples within the sample list. Data is processed by selecting 'MarkerLynx' from within the MassLynx window. In the box that appears, the appropriate project file which contains the data set to be processed, the altered sample list, and the method file are selected. The output file is named, all boxes checked, and data processed (a time-consuming process). Once the MarkerLynx file is created, samples are labeled both in terms of the experimental

condition(s) and order of experiment for a “walking Principal Component Analysis (PCA)”. For statistical analysis of the data, the ‘XS’ button is selected. This creates an Extended Statistics report (if not already produced during the data processing). Within Extended Statistics, the template is changed to PCA with pareto scaling and applied. Any plot can be double-clicked to enter the plots and something window. Data labels are changed to reflect given labels and desired plots and data lists are saved for further analysis. Groups are selected to produce OPLS-DA plots if needed for the particular data set.

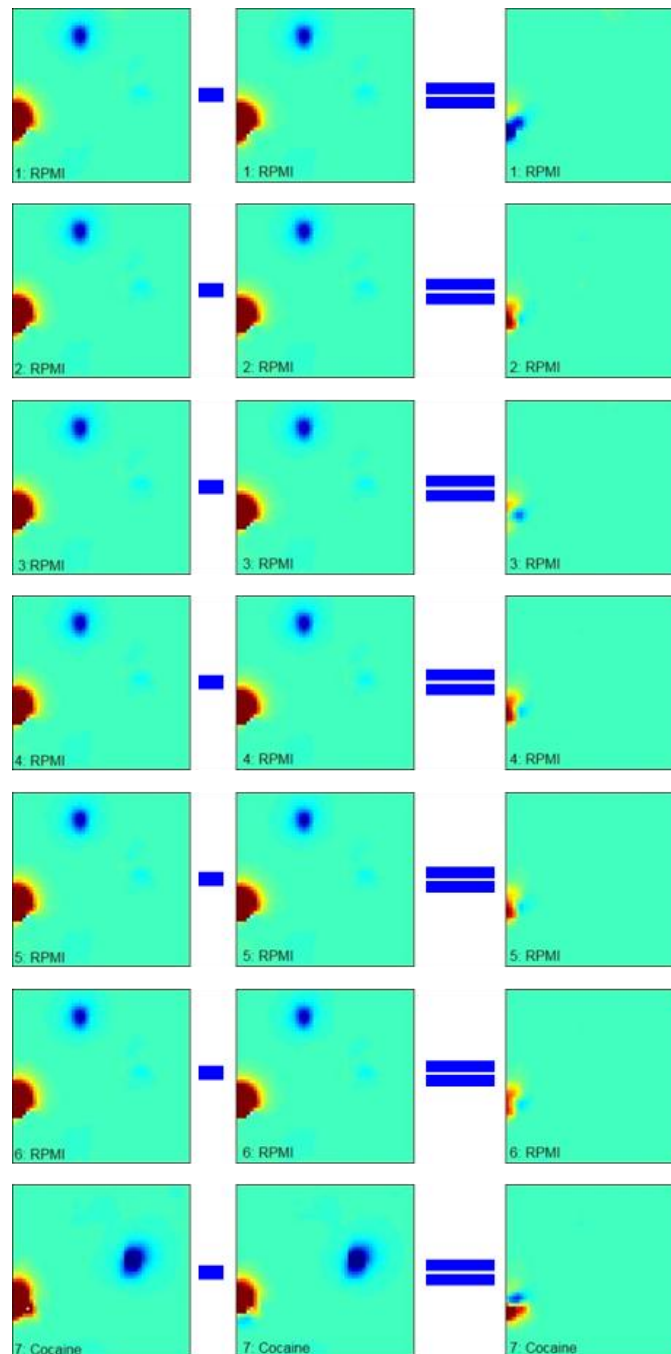
### B.7.3 Metabolite Expression Dynamics Identification (MEDI)

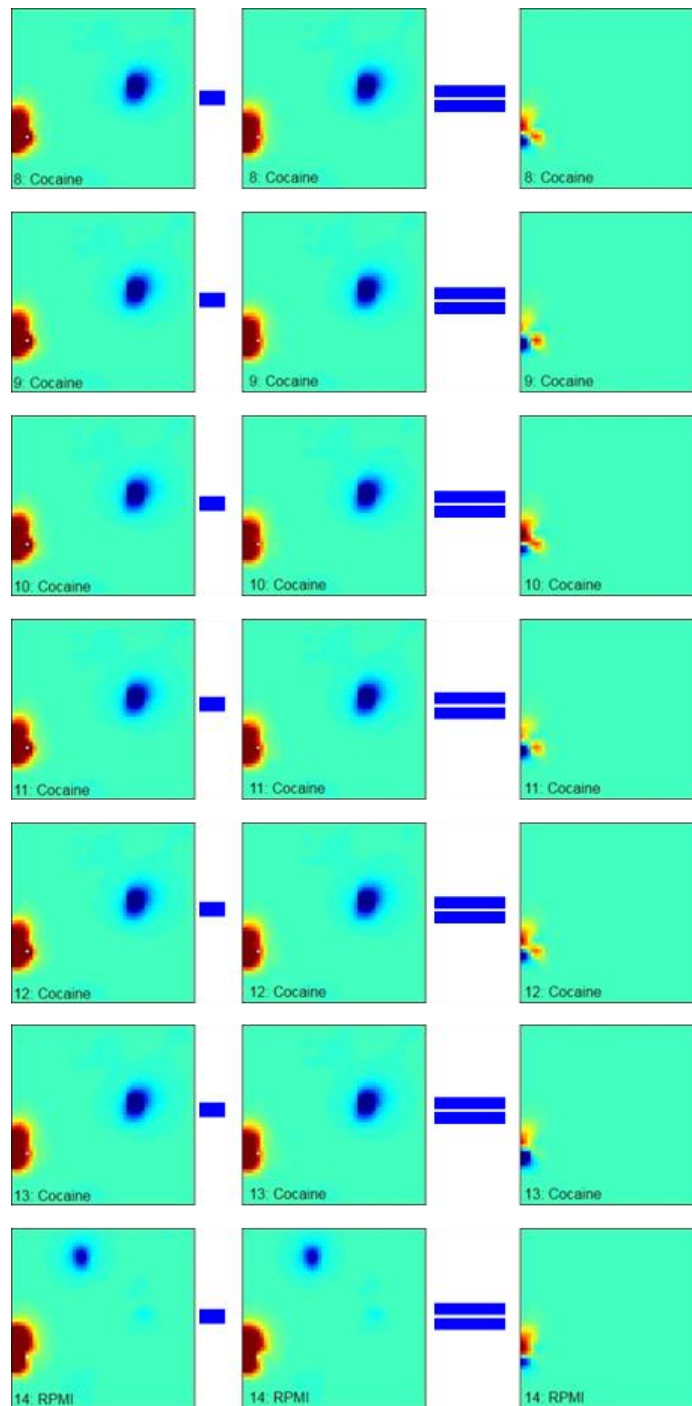
If desired, data sets can be exported from Extended Statistics and processed with MEDI for the production of heat map style plots for enhanced data visualization. MEDI, along with documentation and instructions, is free for download. For large data sets (>16,000 columns), data cannot be copied or opened within Excel prior to transposition. To transpose data, it is first saved in Extended Statistics as a .dif file, and then opened as a new project. Within this new project area, the data can be transposed, selected, copied and then pasted in Excel. Once in Excel, the header is adjusted to comply with MEDI input format and the file is saved as a tab delimited text file. If standards are to be subtracted, the data must be run as ‘Static’ even though it is dynamic data. From with MEDI, this file can be selected, and settings altered to those desired, typically 50 x 51 tiles, Random Selection, Pearson Correlation, and 10 Seed something. MEDI is then set to analyze. Once finished, averages of standards are calculated and subtracted from samples. Heat maps are then incorporated into figures as desired.

## APPENDIX C

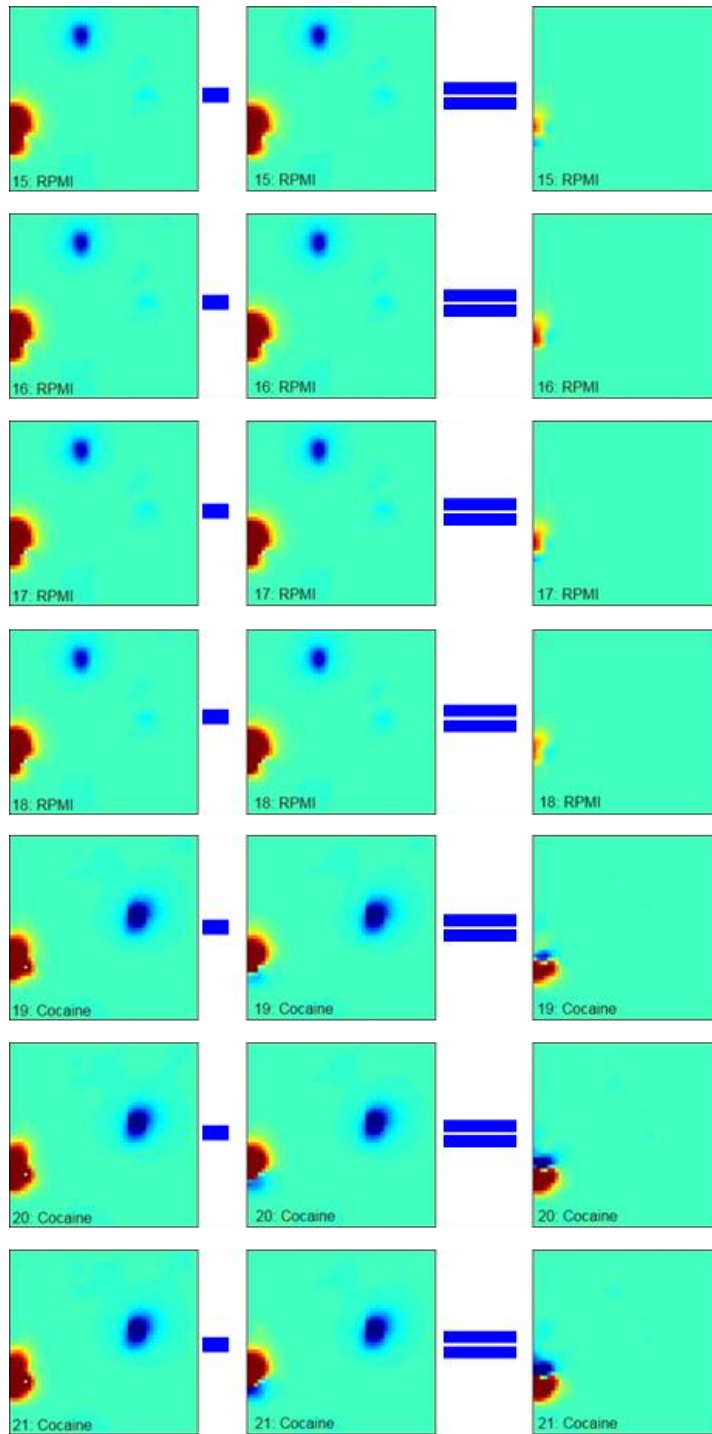
### C MEDI HEAT MAPS

MEDI heat maps showing the differences (right) in metabolite profile between cocaine experienced (left) and naïve (middle) cells.









## APPENDIX D

### D CHEMICAL REACTION MODELS

#### D.1 Fluorescein Quenching

fquenching.m

```
% Reaction of fluoro
% Efluoro====> Fluoro + E, kf(light emission)=0.24e-9;
% Efluoro====> Fluoro + heat, knr(non-radiative decay)=3.8e-11;
% Efluoro + KI ==> Fluoro+EKI, kq(quenching)=1.8e-9;
%df/dt=-(kf+knr)*Ef-kq*KI*Ef;
%dKI/dt=-kq*KI*Ef;
%dE/dt=kf*Ef;
%dH/dt=knr*Ef;
%dEKI=kq*KI*Ef;

function dy=fquenching(t,y)

kf=0.24e-9;
knr=3.8e-11;
kq=1.8e-9;

y1=y(1);
y2=y(2);
y3=y(3);

r1 = kf*y1;
r2 = knr*y1;
r3 = kq*y1*y2;

dy=zeros(3,1);
dy1=-r1-r2-r3; %-(kf+knr)*y(1)-kq*y(1)*y(2);% Ef
dy2=-r3;% KI
dy3=r1;% E
dy = [dy1 dy2 dy3]';
```

fquenchingfaster\_2.m

% Simulation for Heterodyne Chemistry for Fluorescent Quenching

f1=1/223; % KI input  
f2=1/269; % FL input

Ef0=0.00001;  
K10=1;  
ic=zeros(3,1);  
ic(1)=Ef0;  
ic(2)=K10;  
ic(3)=0;

T=100;%223\*269\*307;  
%data=zeros(1,T);  
counter = 0;  
parfor t= [0:0.5:T];  
    counter = (i\*10)+1;  
%    t=i;  
    flow1=30\*(1+sin(2\*pi\*f1\*t));  
    flow2=30\*(1+sin(2\*pi\*f2\*t));  
    flowtotal=flow1+flow2;  
    CF0 =0.00001\*flow1; %0.00001 mol/liter Fluorescein  
    C10 = 1\*flow2;%1 mol/liter KI

C0 = [CF0 C10 0 ]/flowtotal;

t0 = 0; % initial volume for solving  
tf = 3600; % .003 microliter -- final volume, volume of reactor

trange = [t0 tf]; % range of simulation variable

% Apply Matlab ODE solver to equations, initial condition

% ode113 returns two vectors  
% v = vector of volume steps  
% f = matrix of flows, one row per v step.

options = odeset('RelTol',1e-8,'AbsTol',1e-9);  
[T,Y] = ode15s(@fquenching,trange,C0,options); %[T,Y] = ode15s(@fquenching,[0 3600],ic,options);  
%[time,f] = ode113(@TCPO,trange,C0);

QY = .88;  
data(counter)=Y(end,1).\*(0.24e-9)\*QY; %Compensation for Scale rEMIT  
end

fquenching\_constant.m

% Simulation for Heterodyne Chemistry for Fluorescein Quenching - constant flow

f1=1/223; % KI input  
f2=1/269; % FL input

```

Ef0=0.0001;
Kl0=1;
ic=zeros(3,1);
ic(1)=Ef0;
ic(2)=Kl0;
ic(3)=0;

T=28800;%223*269*307;28800
datac=zeros(1,T);
counter = 0;
for i=(0:0.1:T);
    counter = counter + 1;
    t=i;
    % flow1(counter)=30*(1+sin(2*pi*f1*t));
    % flow2(counter)=30*(1+sin(2*pi*f2*t));
    % flow3(counter)=30*(1-1*sin(2*pi*f1*t));
    % flow4(counter)=30*(1-1*sin(2*pi*f2*t));
    % flowtotal(counter)=flow1(counter)+flow2(counter)+flow3(counter)+flow4(counter);
    % CF0(counter) =0.00001*flow1(counter)./(flowtotal(counter)); %0.00001 mol/liter Fluorescein
    % Cl0(counter) = 1*flow2(counter)./(flowtotal(counter));%1 mol/liter KI
    CF0 = 0.00001*(sin(2*pi*f1*t)+1);%.8 ; % micromol/microliter H2O2
    Cl0 = 1*(sin(2*pi*f2*t)+1);%

    C0 = [CF0 Cl0 0 ];

t0 = 0; % initial volume for solving
tf = 3600; % .003 microliter -- final volume, volume of reactor

trange = [t0 tf]; % range of simulation variable

% Apply Matlab ODE solver to equations, initial condition
% ode113 returns two vectors
% v = vector of volume steps
% f = matrix of flows, one row per v step.

options = odeset('RelTol',1e-8,'AbsTol',1e-9);
[T,y] = ode15s(@fquenching,trange,C0,options); %[T,Y] = ode15s(@fquenching,[0 3600],ic,options);
%[time,f] = ode113(@TCPO,trange,C0);

QY = .88;
datac(counter)=y(end,1).*(0.24e-9)*QY; %Compensation for Scale rEMIT
end
% T=32768;
% d=fft(data(1:32768),T);
% Pd=d.*conj(d)/T;
% Y=1/T*(1:(T+1)/2);
% plot(Y(:),Pd(2:(T+3)/2));
% title('light Emmison');
% axis([0 0.025 -0.001 2]);
% xlabel('Frequency');
% ylabel('FFT magnitude');
% [X,Y]=find(Pd>0.1);

```

```
% Y=Y/T;
% plot(Y);

%plot(datac);figure(gcf);
```

## D.2 Peroxyoxalate Chemiluminescence

TCPO.m

```
function y = TCPO(v,f)
```

```
k1 = 1.485; % (dm^3/mol)/s
k2 = 0.1485; % 1/s
k3 = 0.00891; % (dm^3/mol)/s
k5 = 0.001111; % 1/s
```

```
fa = f(1);
fb = f(2);
fc = f(3);
fd = f(4);
fe = f(5);
ff = f(6);
fh = f(7);
fk = f(8);
```

```
% rates of formation
r1 = k1*fa*fb;
r2 = k2*fd;
r3 = k3*fe*ff;
r5 = k5*fk;
```

```
ya = -(r1);
yb = -(r1);
yc = (r1+r2);
yd = (r1 - r2);
ye = (r2 - r3);
yf = (r5 - r3);
yh = (2*r3);
yk = (r3 - r5);
```

```
% Return vector of derivatives
y = [ya yb yc yd ye yf yh yk]';
```

run\_TCPO\_constant.m

```
w1=2*pi/223;% fluorophore
w2=2*pi/269;% TCPO
w3=2*pi/307;% H2O2
T=28800
data2=zeros(1,T);
```

```

counter = 0;
for i=1:0.1:T;
    counter = counter + 1;
    t=i;
    CF0 =0.00056*(sin(w1*t)+1); %micromol/microliter Fluorophore
    CA0 = 0.98*(sin(w3*t)+1);%.8 ; % micromol/microliter H2O2
    CB0 =0.01*(sin(w2*t)+1);%.7 ; % micromol/microliter TCPO

    C0 = [CA0 CB0 0 0 0 CF0 0 0];

t0 = 0; % initial volume for solving
tf = 60; % .003 microliter -- final volume, volume of reactor

trange = [t0 tf]; % range of simulation variable

% Apply Matlab ODE solver to equations, initial condition
% ode113 returns two vectors
% v = vector of volume steps
% f = matrix of flows, one row per v step.

[time,f] = ode113(@TCPO,trange,C0);
QY = 12964;
data2(counter)=f(end,5).*f(end,6).*(.00891)*QY; %Compensation for Scale rEMIT
end

```

### D.3 Additional Simulations

<i>Simulation Summary</i>								
<b>Figure</b>	<b>Table</b>	<b>[Rub]</b>	<b>[TCPO]</b>	<b>[H2O2]</b>	<b>k1</b>	<b>k2</b>	<b>k3</b>	<b>k4</b>
		<b>(mM)</b>	<b>(mM)</b>	<b>(M)</b>	<b>(L/mole)/s)</b>	<b>(1/s)</b>	<b>(L/mole)/s)</b>	<b>(1/s)</b>
3.5	3.3	0.56	10	0.98	1.485	0.1485	0.00891	0.00111
D.1	D.1	560	10	0.98	1.485	0.1485	0.00891	0.00111
D.2	D.2	0.56	10000	0.98	1.485	0.1485	0.00891	0.00111
D.3	D.3	0.56	10	9.8	1.485	0.1485	0.00891	0.00111
D.4	D.4	0.56	10	0.98	14.85	0.1485	0.00891	0.00111
D.5	D.5	0.56	10	0.98	1.485	1.485	0.00891	0.00111
D.6	D.6	0.56	10	0.98	1.485	0.1485	0.0891	0.00111
D.7	D.7	0.56	10	0.98	1.485	0.1485	0.00891	0.0111

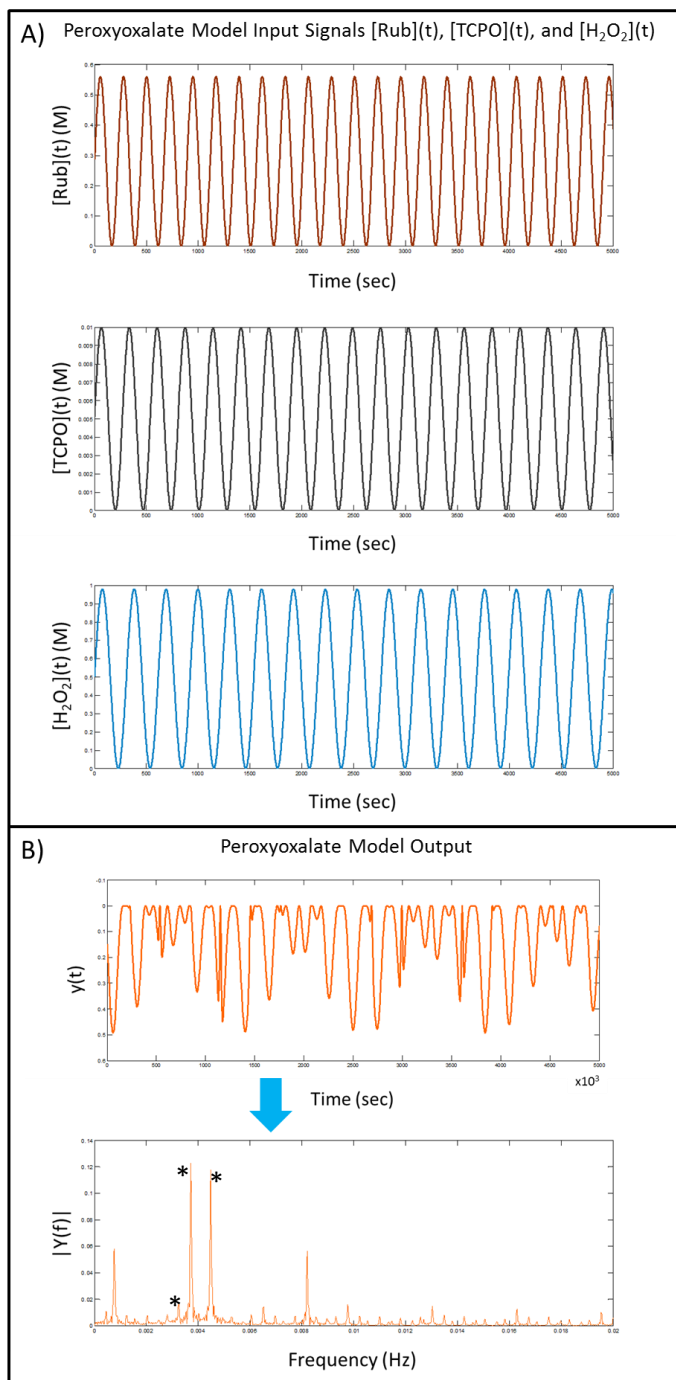


Figure D.1 Peroxyoxalate Chemiluminescence Model. A) Input sinusoidal concentration profiles for Rubrene, TCPO, and H<sub>2</sub>O<sub>2</sub> oscillating at periods of 223, 269, and 307 seconds. Rubrene concentration is 1000x original (0.56 mM). B) The simulated raw chemiluminescence data is shown with the fluorescence signal scale inverted to adhere to the experimental data convention of increase in signal intensity in the downward direction. Exploring the frequency domain returns many heterodyne frequencies as listed in Table D.1. The amplitude of the drive frequency of H<sub>2</sub>O<sub>2</sub> is much lower than expected.

Table D.1 Peroxyoxalate chemiluminescence drive and heterodyne frequencies corresponding to the data shown in Figure D.1.

Frequency (Hz)	Assignment
0.0004578	$f_{TCPO} - f_{H2O2}$
0.0007629	$f_{Rub} - f_{TCPO}$
0.001221	$f_{Rub} - f_{H2O2}$
0.002045	$2f_{H2O2} - f_{Rub}$
0.002808	$2f_{H2O2} - f_{TCPO}$
0.003265	$f_{H2O2}$
0.003723	$f_{TCPO}$
0.004486	$f_{Rub}$
0.004944	$f_{Rub} + f_{TCPO} - f_{H2O2}$
0.006042	$3f_{H2O2} - f_{TCPO}$
0.006531	$2f_{H2O2}$
0.006989	$f_{TCPO} + f_{H2O2}$
0.007751	$f_{Rub} + f_{H2O2}$
0.008209	$f_{Rub} + f_{TCPO}$
0.009766	$3f_{H2O2}$
0.01022	$3f_{Rub} - f_{H2O2}$
0.01053	$2f_{TCPO} + f_{H2O2}$
0.01099	$f_{Rub} + 2f_{H2O2}$
0.01147	$f_{Rub} + f_{TCPO} + f_{H2O2}$
0.01227	$2f_{Rub} + f_{H2O2}$



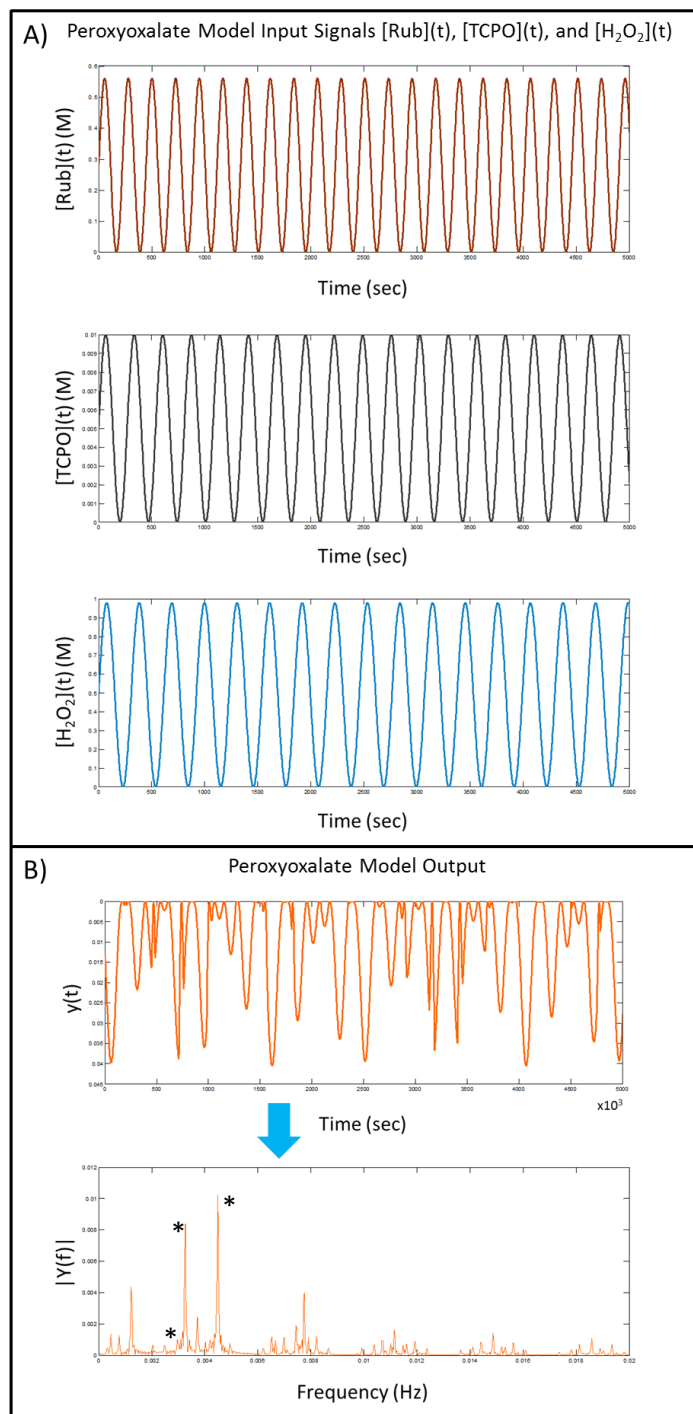


Figure D.2 Peroxyoxalate Chemiluminescence Model. A) Input sinusoidal concentration profiles for Rubrene, TCPO, and  $\text{H}_2\text{O}_2$  oscillating at periods of 223, 269, and 307 seconds. TCPO concentration is 1000x original (10 mM). B) The simulated raw chemiluminescence data is shown with the fluorescence signal scale inverted to adhere to the experimental data convention of increase in signal intensity in the downward direction. Exploring the frequency domain returns many heterodyne frequencies as listed in Table D.2.

Table D.2 Peroxyoxalate chemiluminescence drive and heterodyne frequencies corresponding to the data shown in Figure D.2.

Frequency (Hz)	Assignment
0.0004578	$f_{TCPO} - f_{H2O2}$
0.0007629	$f_{Rub} - f_{TCPO}$
0.001221	$f_{Rub} - f_{H2O2}$
0.002045	$2f_{H2O2} - f_{Rub}$
0.00296	$2f_{H2O2} - f_{TCPO}$
0.003265	$f_{H2O2}$
0.003723	$f_{TCPO}$
0.004486	$f_{Rub}$
0.004944	$f_{Rub} + f_{TCPO} - f_{H2O2}$
0.006042	$3f_{H2O2} - f_{TCPO}$
0.006531	$2f_{H2O2}$
0.006989	$f_{TCPO} + f_{H2O2}$
0.007751	$f_{Rub} + f_{H2O2}$
0.008209	$f_{Rub} + f_{TCPO}$
0.009918	$3f_{H2O2}$
0.01038	$3f_{Rub} - f_{H2O2}$
0.01071	$2f_{TCPO} + f_{H2O2}$
0.01114	$f_{Rub} + 2f_{H2O2}$
0.01147	$f_{Rub} + f_{TCPO} + f_{H2O2}$
0.01236	$2f_{Rub} + f_{H2O2}$

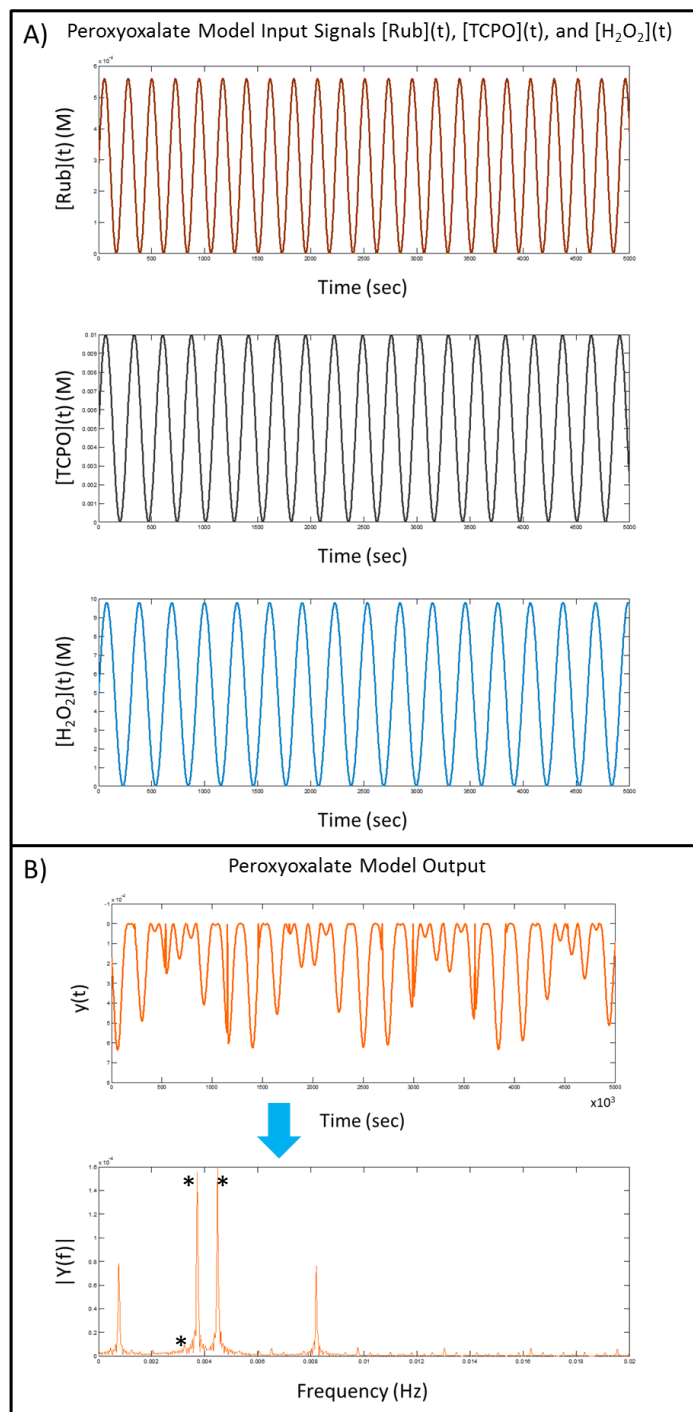


Figure D.3 Peroxyoxalate Chemiluminescence Model. A) Input sinusoidal concentration profiles for Rubrene, TCPO, and H<sub>2</sub>O<sub>2</sub> oscillating at periods of 223, 269, and 307 seconds. H<sub>2</sub>O<sub>2</sub> concentration is 10x original (0.98 M). B) The simulated raw chemiluminescence data is shown with the fluorescence signal scale inverted to adhere to the experimental data convention of increase in signal intensity in the downward direction. Exploring the frequency domain returns many heterodyne frequencies as listed in Table D.3.

Table D.3 Peroxyoxalate chemiluminescence drive and heterodyne frequencies corresponding to the data shown in Figure D.3.

Frequency (Hz)	Assignment
0.0007629	$f_{Rub} - f_{TCPO}$
0.003235	$f_{H2O2}$
0.003723	$f_{TCPO}$
0.004486	$f_{Rub}$
0.006042	$3f_{H2O2} - f_{TCPO}$
0.006531	$2f_{H2O2}$
0.006958	$f_{TCPO} + f_{H2O2}$
0.0077221	$f_{Rub} + f_{H2O2}$
0.008209	$f_{Rub} + f_{TCPO}$
0.009766	$3f_{H2O2}$
0.01025	$3f_{Rub} - f_{H2O2}$
0.01053	$2f_{TCPO} + f_{H2O2}$
0.01102	$f_{Rub} + 2f_{H2O2}$
0.01135	$f_{Rub} + f_{TCPO} + f_{H2O2}$
0.01227	$2f_{Rub} + f_{H2O2}$

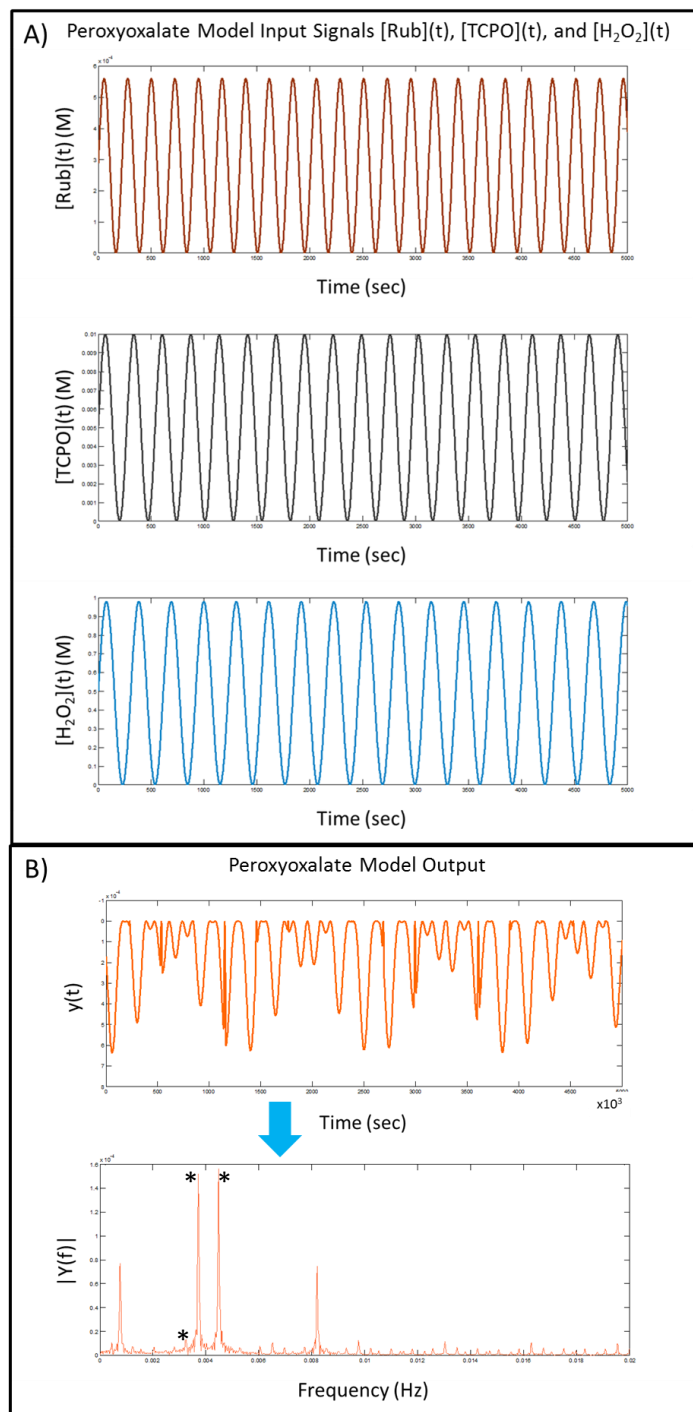


Figure D.4 Peroxyoxalate Chemiluminescence Model. A) Input sinusoidal concentration profiles for Rubrene, TCPO, and  $\text{H}_2\text{O}_2$  oscillating at periods of 223, 269, and 307 seconds. The value of  $k_1$  was increased by 10. B) The simulated raw chemiluminescence data is shown with the fluorescence signal scale inverted to adhere to the experimental data convention of increase in signal intensity in the downward direction. Exploring the frequency domain returns many heterodyne frequencies as listed in Table D.4.

Table D.4 Peroxyoxalate chemiluminescence drive and heterodyne frequencies corresponding to the data shown in Figure D.4.

Frequency (Hz)	Assignment
0.0004578	$f_{TCPO} - f_{H2O2}$
0.0007629	$f_{Rub} - f_{TCPO}$
0.001251	$f_{Rub} - f_{H2O2}$
0.002045	$2f_{H2O2} - f_{Rub}$
0.002808	$2f_{H2O2} - f_{TCPO}$
0.003265	$f_{H2O2}$
0.003723	$f_{TCPO}$
0.004486	$f_{Rub}$
0.006042	$3f_{H2O2} - f_{TCPO}$
0.006531	$2f_{H2O2}$
0.006989	$f_{TCPO} + f_{H2O2}$
0.007751	$f_{Rub} + f_{H2O2}$
0.008209	$f_{Rub} + f_{TCPO}$
0.009766	$3f_{H2O2}$
0.01022	$3f_{Rub} - f_{H2O2}$
0.01053	$2f_{TCPO} + f_{H2O2}$
0.01099	$f_{Rub} + 2f_{H2O2}$
0.01135	$f_{Rub} + f_{TCPO} + f_{H2O2}$
0.01227	$2f_{Rub} + f_{H2O2}$

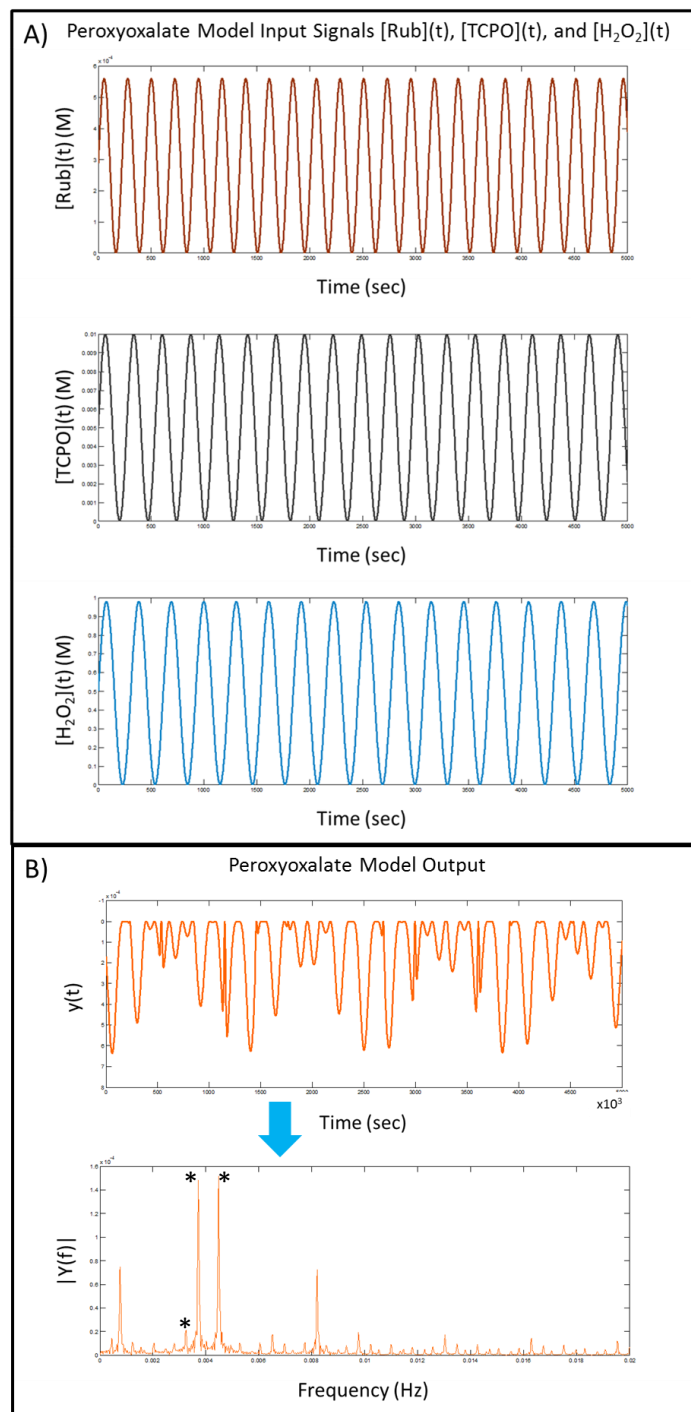


Figure D.5 Peroxyoxalate Chemiluminescence Model. A) Input sinusoidal concentration profiles for Rubrene, TCPO, and H<sub>2</sub>O<sub>2</sub> oscillating at periods of 223, 269, and 307 seconds. The value of  $k_2$  was increased by 10. B) The simulated raw chemiluminescence data is shown with the fluorescence signal scale inverted to adhere to the experimental data convention of increase in signal intensity in the downward direction. Exploring the frequency domain returns many heterodyne frequencies as listed in Table D.5.

Table D.5 Peroxyoxalate chemiluminescence drive and heterodyne frequencies corresponding to the data shown in Figure D.5.

Frequency (Hz)	Assignment
0.0004578	$f_{TCPO} - f_{H2O2}$
0.0007629	$f_{Rub} - f_{TCPO}$
0.001251	$f_{Rub} - f_{H2O2}$
0.002045	$2f_{H2O2} - f_{Rub}$
0.002808	$2f_{H2O2} - f_{TCPO}$
0.003265	$f_{H2O2}$
0.003723	$f_{TCPO}$
0.004486	$f_{Rub}$
0.006042	$3f_{H2O2} - f_{TCPO}$
0.006531	$2f_{H2O2}$
0.006958	$f_{TCPO} + f_{H2O2}$
0.007751	$f_{Rub} + f_{H2O2}$
0.008209	$f_{Rub} + f_{TCPO}$
0.009766	$3f_{H2O2}$
0.01022	$3f_{Rub} - f_{H2O2}$
0.01053	$2f_{TCPO} + f_{H2O2}$
0.01102	$f_{Rub} + 2f_{H2O2}$
0.01135	$f_{Rub} + f_{TCPO} + f_{H2O2}$
0.01227	$2f_{Rub} + f_{H2O2}$



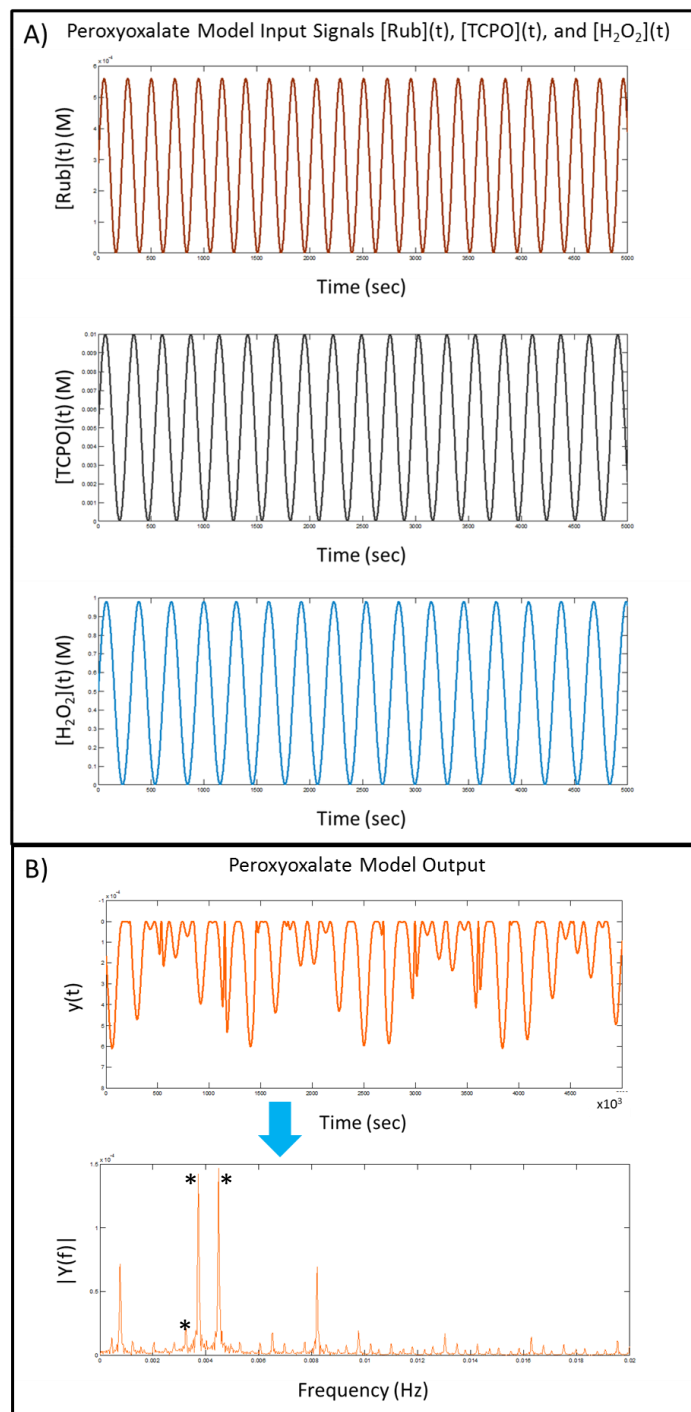


Figure D.6 Peroxyoxalate Chemiluminescence Model. A) Input sinusoidal concentration profiles for Rubrene, TCPO, and H<sub>2</sub>O<sub>2</sub> oscillating at periods of 223, 269, and 307 seconds. The value of  $k_3$  was increased by 10. B) The simulated raw chemiluminescence data is shown with the fluorescence signal scale inverted to adhere to the experimental data convention of increase in signal intensity in the downward direction. Exploring the frequency domain returns many heterodyne frequencies as listed in Table D.6.

Table D.6 Peroxyoxalate chemiluminescence drive and heterodyne frequencies corresponding to the data shown in Figure D.6.

Frequency (Hz)	Assignment
0.0004578	$f_{TCPO} - f_{H2O2}$
0.0007629	$f_{Rub} - f_{TCPO}$
0.001251	$f_{Rub} - f_{H2O2}$
0.002045	$2f_{H2O2} - f_{Rub}$
0.002808	$2f_{H2O2} - f_{TCPO}$
0.003265	$f_{H2O2}$
0.003723	$f_{TCPO}$
0.004486	$f_{Rub}$
0.006042	$3f_{H2O2} - f_{TCPO}$
0.006531	$2f_{H2O2}$
0.006958	$f_{TCPO} + f_{H2O2}$
0.007751	$f_{Rub} + f_{H2O2}$
0.008209	$f_{Rub} + f_{TCPO}$
0.009766	$3f_{H2O2}$
0.01022	$3f_{Rub} - f_{H2O2}$
0.01053	$2f_{TCPO} + f_{H2O2}$
0.01099	$f_{Rub} + 2f_{H2O2}$
0.01132	$f_{Rub} + f_{TCPO} + f_{H2O2}$
0.01227	$2f_{Rub} + f_{H2O2}$

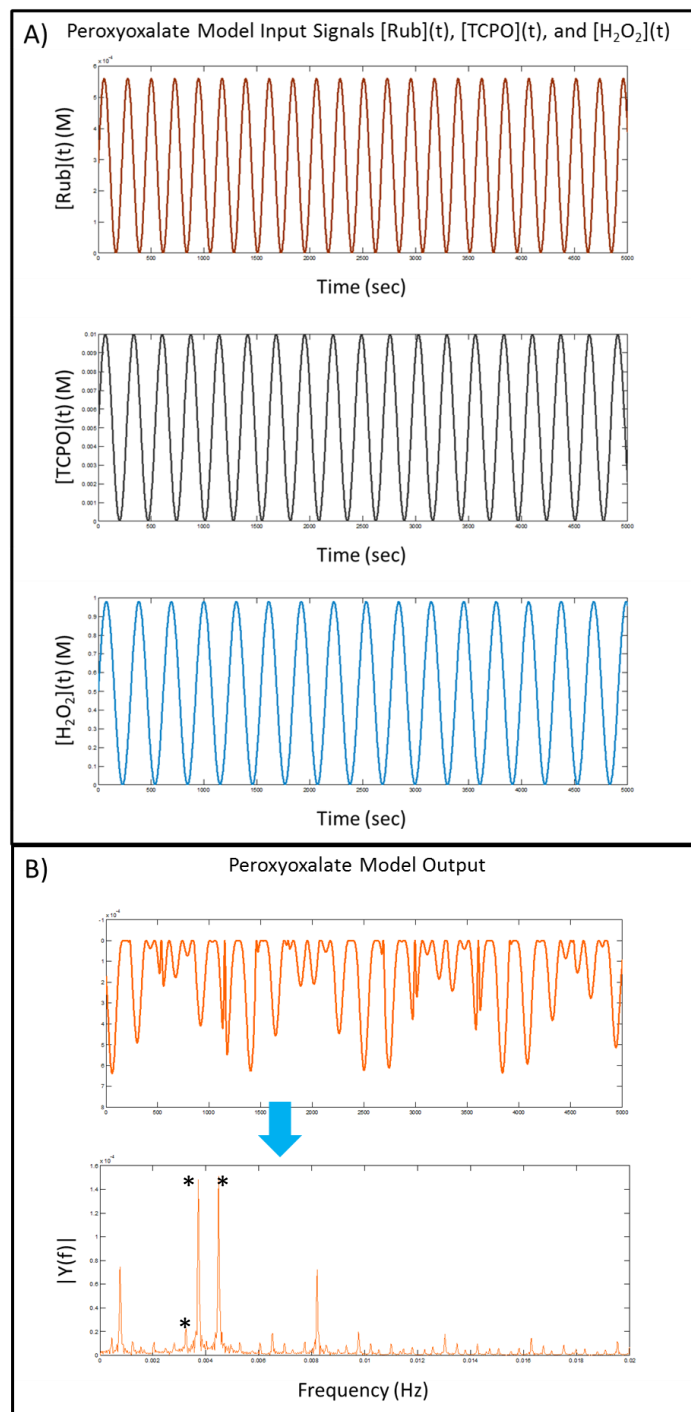


Figure D.7 Peroxyoxalate Chemiluminescence Model. A) Input sinusoidal concentration profiles for Rubrene, TCPO, and H<sub>2</sub>O<sub>2</sub> oscillating at periods of 223, 269, and 307 seconds. The value of  $k_4$  was increased by 10. B) The simulated raw chemiluminescence data is shown with the fluorescence signal scale inverted to adhere to the experimental data convention of increase in signal intensity in the downward direction. Exploring the frequency domain returns many heterodyne frequencies as listed in Table D.7.

Table D.7 Peroxyoxalate chemiluminescence drive and heterodyne frequencies corresponding to the data shown in Figure D.7.

Frequency (Hz)	Assignment
0.0004578	$f_{TCPO} - f_{H2O2}$
0.0007629	$f_{Rub} - f_{TCPO}$
0.001251	$f_{Rub} - f_{H2O2}$
0.002045	$2f_{H2O2} - f_{Rub}$
0.002808	$2f_{H2O2} - f_{TCPO}$
0.003265	$f_{H2O2}$
0.003723	$f_{TCPO}$
0.004486	$f_{Rub}$
0.006042	$3f_{H2O2} - f_{TCPO}$
0.006531	$2f_{H2O2}$
0.006958	$f_{TCPO} + f_{H2O2}$
0.007751	$f_{Rub} + f_{H2O2}$
0.008209	$f_{Rub} + f_{TCPO}$
0.009766	$3f_{H2O2}$
0.01022	$3f_{Rub} - f_{H2O2}$
0.01053	$2f_{TCPO} + f_{H2O2}$
0.01099	$f_{Rub} + 2f_{H2O2}$
0.01132	$f_{Rub} + f_{TCPO} + f_{H2O2}$
0.01227	$2f_{Rub} + f_{H2O2}$

## APPENDIX E

### E RPPM CODE

```
/*  
Author: Loi Hoang  
Date: 03/20/2012  
Edited by FBlock 12 June 2012  
Edited again by E Werner 28 June 2012
```

Arduino code for running up to 4 stepper motors at constant or sinusoidal speeds.

Syntax:

Setting parameters:

```
set (motor number) (mode, 1 for sin, 0 for constant) (dir, 0 or 1) (rpm) (duration in minutes)  
  (yOffset) (phaseOffset) (period)
```

- \* space bar can be used as delimiter
- \* Duration can be left out for continuous running time. yOffset, phaseOffset, and period can be left out if running in constant mode.
- \* Typical values for RPM are on the order of 60 (30 for sin wave)
- \* Duration has not worked reliably
- \* yOffset should be > RPM (i.e. RPM=30, yOffset>33 to prevent long runtimes when speeds are slow and move distance is great)
- \* phaseOffset of sine wave in degrees
- \* period of sine wave (i.e. number of periods of sine wave between 0 and 180 degrees)

To Run:

```
go (integer)
```

Integer is a four digit number consisting of 1 or 0. 1 represent that the respective motor is to be run. Ex: "go 1000" to start the first motor, or "go 0001" to start the fourth motor

```
*/  
//////////////////////////////////<Definitions>//////////////////////////////////  
#include <AccelStepper.h> // Needed for access to the AccelStepper library, an "improved" library of  
functions for stepper motor control.  
#define int MAX_RPM = 150, STEP_PER_REV = 200; //Defines a max speed and steps per revolution of the  
stepper. Initialized in all motors.  
float CONVERSION_RPM_TO_STEP_SEC = STEP_PER_REV/60.0; // float conversion of RPMs to revolutions  
int DIR[5], STEP[5], MS1[5], MS2[5], SLEEP[5]; //Create arrays to store output pins for direction, step,  
microstep, and sleep for each motor.  
#define double pi = 3.1415926535897932;  
  
//////////////////////////////////</Definitions>//////////////////////////////////  
//////////////////////////////////<Constructor>//////////////////////////////////
```

```

AccelStepper stepper[] = { //Constructor five stepper objects. Note pin assignments are for easy driver,
not arduino board. i.e. 4 is step pin, 5 is drive pin*/
  AccelStepper(1,99,99),AccelStepper(1,4,5), //stepper 0 is an extra to make the array indices easier for
the feeble-minded
  AccelStepper(1,6,7),AccelStepper(1,8,9),
  AccelStepper(1,10,11)};
//the syntax for AccelStepper(1,X,Y) is 1 means a stepper driver with step and direction pins, X is step pin,
and Y is direction pin
char input_str[255]; //declares an array of input strings
char *token; //declares token as a pointer to char and points it at a string literal which is non-modifiable.
int offset = 0;
int motorParam[5][7] = {0}; // 0 = sin or const, 1 = dir, 2 = rpm, 3 = duration(0 = inf), 4 = y offset, 5 = phase
offset, 6 = period
//////////////////////////////////</Constructor>//////////////////////////////////
void setup()
{
  Serial.begin(9600); // open the serial connection, BAUD rate set at 9600bps
  Serial.flush(); //flushes serial buffer. In arduino 1.0+, this function has changed to flush the serial
output buffer, so it is no longer useful in this application.
  delay(100);

  //setting PINS for stepper[1] (the first stepper motor)
  DIR[1] = 5;
  STEP[1] = 4;
  SLEEP[1] = 12;
  MS1[1] = 3;
  MS2[1] = 2;
  //By default these pins are output. This double checks.//////////////////////////////////
  pinMode(DIR[1], OUTPUT); //output on pin 5////////////////////////////////// MS1 MS2 Resolution    ///
  pinMode(STEP[1], OUTPUT); //output on pin 4////////////////////////////////// L L Full step (2 phase) //
  pinMode(SLEEP[1], OUTPUT); //output on pin 12 ////////////////////////////////// H L Half step    //
  pinMode(MS1[1], OUTPUT); //output on pin 3////////////////////////////////// L H Quarter step    //
  pinMode(MS2[1], OUTPUT); //output on pin 2////////////////////////////////// H H Eighth step    //
  ////////////////////////////////////////////////////////////////////
  //executes to begin with motor off (i.e. sleep function is turned on for one motor)
  digitalWrite(SLEEP[1], HIGH); //turn motor off

  ///Now repeat the procss to setup the other three steppers
  DIR[2] = 7;
  STEP[2] = 6;
  // SLEEP[2] = 9;
  // MS1[2] = 10; // PIN 12 = MS1
  // MS2[2] = 11; // PIN 13 = MS2
  pinMode(DIR[2], OUTPUT); // set pin 4 to output
  pinMode(STEP[2], OUTPUT); // set pin 5 to output
  // pinMode(SLEEP[2], OUTPUT); // set pin 9 to output
  // pinMode(MS1[2], OUTPUT); // set pin 12 to output
  // pinMode(MS2[2], OUTPUT); // set pin 13 to output
  // digitalWrite(SLEEP[2], LOW); // saves power

  DIR[3] = 9;
  STEP[3] = 8;

```

```

//SLEEP[3] = 12;
pinMode(DIR[3], OUTPUT);
pinMode(STEP[3], OUTPUT);
// pinMode(SLEEP[3], OUTPUT);
// digitalWrite(SLEEP[3], LOW);

DIR[4] = 11;
STEP[4] = 10;
// SLEEP[4] = 13;
pinMode(DIR[4], OUTPUT);
pinMode(STEP[4], OUTPUT);
// pinMode(SLEEP[4], OUTPUT);
// digitalWrite(SLEEP[4], LOW);

//set max speeds converted properly for accellstepper format
stepper[1].setMaxSpeed(MAX_RPM*CONVERSION_RPM_TO_STEP_SEC);
stepper[2].setMaxSpeed(MAX_RPM*CONVERSION_RPM_TO_STEP_SEC);
stepper[3].setMaxSpeed(MAX_RPM*CONVERSION_RPM_TO_STEP_SEC);
stepper[4].setMaxSpeed(MAX_RPM*CONVERSION_RPM_TO_STEP_SEC);

}
//////////END OF SETUP

void loop()
{
  while (Serial.available() > 0) //checks for bytes in the buffer. Serial.available() returns the number of
  bytes waiting.
  {

    char c = Serial.read(); //read a byte from the serial line
    Serial.print(c); // Echo each character, print out what is received
    if ((c == '\n') || (c == '\r') || (c == 'X')) //if character entered is new line, return, or "X" then parse the
    string
    {
      Serial.println();

      input_str[offset] = 0;    // Terminate string with a 0

      parse_str();    // Parse input through our own parse_str() function
      memset(input_str,0,sizeof(input_str)); // Reset input char array
      offset=0; // Reset offset
      return;
    }
    if (offset < 255)
      input_str[offset++] = c;

  }
}
//////////END OF MAIN LOOP//////////

void parse_str()
{
  char* token;

```

```

if (!strncmp(input_str,"set",3)) //if the user inputs set as this function
{
  //Parse the input string and convert characters to integers for accelstepper (atoi = alphanumeric to
integer)
  token = strtok(input_str(),".-");
  set( atoi(strtok(NULL,") ,.-"),atoi(strtok(NULL,") ,.-")),//this is a giant call to the SET function with the
parsed string
  atoi(strtok(NULL,") ,.-"),atoi(strtok(NULL,") ,.-"),
  atoi(strtok(NULL,") ,.-"),atoi(strtok(NULL,") ,.-"),
  atoi(strtok(NULL,") ,.-"),atoi(strtok(NULL,") ,.-"));
}
else if (!strncmp(input_str,"go",2))
{
  //this handles the go function
  token = strtok(input_str(),".-");
  go(atoi(strtok(NULL,") ,.-"));
}
}
//END OF OUR FUNCTION PARSE STRING for interpreting keyboard input to drive the motors

```

```

void set( int motor, int mode, int dir, int rpm, int duration, int yOffset, int phaseOffset, int period)
{
  //each motor has its own array of motor parameters, we are setting the attributes of each motor below
  motorParam[motor][0] = mode; // 1 for sin, 0 for constant
  //we are omitting direction, that is handled below
  motorParam[motor][2] = rpm;
  motorParam[motor][3] = duration; //duration is in minutes!!
  motorParam[motor][4] = yOffset;
  motorParam[motor][5] = phaseOffset;
  motorParam[motor][6] = period;
  if(dir == 0) //direction cannot be set to either 0 or 1, we set the correct syntax for accelstepper below
  {
    motorParam[motor][1] = -1;
  }
  else
  {
    motorParam[motor][1] = 1;
  }
}
//END OF OUR SET FUNCTION

```

```

void go(int motor) //starts the inputted motor number
{
  bool flag1 = false, flag2 = false, flag3 = false, flag4 = false, //initializes all run and constant/sin booleans as
"false"
  constInf1 = false, constInf2 = false, constInf3 = false, constInf4 = false;
  int ii = 0, jj = 0, kk = 0, ll = 0; ///prepare variables for an array which is used in our sine functions. 180
sample iterations

  if( motor >= 1000) //////////////////////////////////starting the first motor; input from keyboard is "go 1000"

```



```

{
  stepper[1].setCurrentPosition(0); ///initializes the first stepper motor at position 0
  flag1 = true; ///sets flag1 true, we are using this motor
  if(motorParam[1][0] == 0) ///checking to see if constant or sine mode operating
  {
    stepper[1].setSpeed(CONVERSION_RPM_TO_STEP_SEC*motorParam[1][1]*motorParam[1][2]);///sets
speed to the direction * rpm converted properly
    if(motorParam[1][3] == 0) //if duration = 0 then run forever
    {
      constInf1 = true; //run forever
    }
    else
    {
      //sets number of revolutions to make if not running forever

stepper[1].move(CONVERSION_RPM_TO_STEP_SEC*motorParam[1][1]*motorParam[1][2]*motorParam[
1][3]); //if not set to run forever, move the motor the direction * rpm * duration
    }
  }
}
if( motor % 1000 >= 100) //this is for the second motor, all comments same as above
{
  stepper[2].setCurrentPosition(0); //initiliaze second motor
  flag2 = true; //sets flag2 to true, we are using this motor as well
  if(motorParam[2][0] == 0)
  {
    stepper[2].setSpeed(CONVERSION_RPM_TO_STEP_SEC*motorParam[2][1]*motorParam[2][2]);
    if( motorParam[2][3] == 0)
    {
      constInf2 = true;
    }
    else
    {
stepper[2].move(CONVERSION_RPM_TO_STEP_SEC*motorParam[2][1]*motorParam[2][2]*motorParam[
2][3]);
    }
  }
}

if( motor % 100 >= 10) //this is for the 3rd motor
{
  stepper[3].setCurrentPosition(0);
  flag3 = true;
  if(motorParam[3][0] == 0)
  {
    stepper[3].setSpeed(CONVERSION_RPM_TO_STEP_SEC*motorParam[3][1]*motorParam[3][2]);
    if( motorParam[3][3] == 0)
    {
      constInf3 = true;
    }
    else
    {

```

```

stepper[3].move(CONVERSION_RPM_TO_STEP_SEC*motorParam[3][1]*motorParam[3][2]*motorParam[
3][3]);
    }
}
}

if( motor % 10 >= 1) //this is for the 4th motor
{
stepper[4].setCurrentPosition(0);
flag4 = true;
if(motorParam[4][0] == 0)
{
stepper[4].setSpeed(CONVERSION_RPM_TO_STEP_SEC*motorParam[4][1]*motorParam[4][2]);
if( motorParam[4][3] == 0)
{
constInf4 = true;
}
else
{

stepper[4].move(CONVERSION_RPM_TO_STEP_SEC*motorParam[4][1]*motorParam[4][2]*motorParam[
4][3]);
    }
}
}
//END OF IF BLOCK to setup motors

//run the motors as long as one flag is set to true
while(flag1 || flag2 || flag3 || flag4)
{
if (flag1 && stepper[1].distanceToGo() == 0 && !constInf1) //as long as we are not finished running
{
if (motorParam[1][0] == 1) //if sin mode THIS IS THE SINE MODE CODE!!! set to define first motor here
{

//here we are setting the speed of our motor, speed is variable depeding on our sine curve

stepper[1].setSpeed(CONVERSION_RPM_TO_STEP_SEC*(motorParam[1][4]+(motorParam[1][1]*motorPa
ram[1][2]*sin(((ii*2*motorParam[1][6])+motorParam[1][5]*pi/180))));
//ALTERED from original version to
//= yOffest + (direction)* RPM * [sin((ii*2*period + phaseOffset * (pi/180)))]
//this includes our conversion factor; ii is set to 0 initially

//here we are instructing our motor to move, variable with respect to our sine curve

stepper[1].move(CONVERSION_RPM_TO_STEP_SEC*(motorParam[1][4]+(motorParam[1][1]*motorParam
[1][2]*
sin(((ii*2*motorParam[1][6])+motorParam[1][5]*pi/180)))*(1.0/180.0));
//this is set to = yOffest + (direction)* RPM * [sin((ii*2*period + phaseOffset * (pi/180)))] * (1/180)
//including our conversion factor

```

```

    ii++; //incrementing ii

    if( motorParam[1][3] != 0 && ii >= 180.0*motorParam[1][3]/motorParam[1][6] //if motor is not set
to run indefinately and 180 * duration / period is less than ii
    {
        flag1 = false; //disable motor 1
    }
}
else
{
    flag1 = false; //end running the motor if no sine function
}
}
//this is the if block for the second motor
if (flag2 && stepper[2].distanceToGo() == 0 && !constInf2)
{
    if (motorParam[2][0] == 1) //if sin mode
    {

stepper[2].setSpeed(CONVERSION_RPM_TO_STEP_SEC*(motorParam[2][4]+(motorParam[2][1]*motorPa
ram[2][2]*sin(((jj*2*motorParam[2][6])+motorParam[2][5]*pi/180))));

stepper[2].move(CONVERSION_RPM_TO_STEP_SEC*(motorParam[2][4]+(motorParam[2][1]*motorParam
[2][2]*
        sin(((jj*2*motorParam[2][6])+motorParam[2][5]*pi/180)))*(1.0/180.0));
        jj++;
        if( motorParam[2][3] != 0 && jj >= 180.0*motorParam[2][3]/motorParam[2][6])
        {
            flag2 = false;
        }
    }
}
else
{
    flag2 = false;
}
}
//if block for 3rd motor
if (flag3 && stepper[3].distanceToGo() == 0 && !constInf3)
{
    if (motorParam[3][0] == 1) //if sin mode
    {

stepper[3].setSpeed(CONVERSION_RPM_TO_STEP_SEC*(motorParam[3][4]+(motorParam[3][1]*motorPa
ram[3][2]*sin(((kk*2*motorParam[3][6])+motorParam[3][5]*pi/180))));

stepper[3].move(CONVERSION_RPM_TO_STEP_SEC*(motorParam[3][4]+(motorParam[3][1]*motorParam
[3][2]*
        sin(((kk*2*motorParam[3][6])+motorParam[3][5]*pi/180)))*(1.0/180.0));
        kk++;
        if( motorParam[3][3] != 0 && kk >= 180.0*motorParam[3][3]/motorParam[3][6])
        {
            flag3 = false;
        }
    }
}
}

```

```

    }
    else
    {
        flag3 = false;
    }
}
//if block for 4th motor
if (flag4 && stepper[4].distanceToGo() == 0 && !constInf4)
{
    if (motorParam[4][0] == 1) //if sin mode
    {
        stepper[4].setSpeed(CONVERSION_RPM_TO_STEP_SEC*(motorParam[4][4]+(motorParam[4][1]*motorParam[4][2]*sin(((ll*2*motorParam[4][6])+motorParam[4][5])*pi/180))));

        stepper[4].move(CONVERSION_RPM_TO_STEP_SEC*(motorParam[4][4]+(motorParam[4][1]*motorParam[4][2]*
            sin(((ll*2*motorParam[4][6])+motorParam[4][5])*pi/180)))*(1.0/180.0));
        ll++;
        if( motorParam[4][3] != 0 && ll >= 180.0*motorParam[4][3]/motorParam[4][6])
        {
            flag4 = false;
        }
    }
    else
    {
        flag4 = false;
    }
}
////////////////////Calls the run function of accel stepper. Run should be called as often
as possible////////////////////////////////
if(flag1) stepper[1].runSpeed();
if(flag2) stepper[2].runSpeed();
if(flag3) stepper[3].runSpeed();
if(flag4) stepper[4].runSpeed();

}
Serial.println("Finished Running.");
Serial.println("Ready for new command."); //end of running motors
}
//END OF OUR "GO" FUNCTION

//END OF PROGRAM.

```

## APPENDIX F

### F HETERODYNE DATA ANALYSIS

Readfile.m

```
clc;
%% environment variables (first three need to be set for each PC)
NI_TDM_DLL_Path = 'C:\Users\Seniors\Desktop\RV TDMS read\dev\bin\32-bit\nilibddc.dll'
NI_TDM_H_Path = 'C:\Users\Seniors\Desktop\RV TDMS read\dev\include\32-bit\nilibddc_m.h'

% NI_TDM_DLL_Path = strcat([pwd '\nilibddc.dll'])
% NI_TDM_H_Path = strcat([pwd '\nilibddc_m.h'])
libname = 'nilibddc'

%Recreate needed property constants defined in nilibddc_m.h
DDC_FILE_NAME = 'name';
DDC_FILE_DESCRIPTION = 'description';
DDC_FILE_TITLE = 'title';
DDC_FILE_AUTHOR = 'author';
DDC_FILE_DATETIME = 'datetime';
DDC_CHANNELGROUP_NAME = 'name';
DDC_CHANNELGROUP_DESCRIPTION = 'description';
DDC_CHANNEL_NAME = 'name';

%% Check if the paths to 'nilibddc.dll' and 'nilibddc_m.h' have been
%selected. If not, prompt the user to browse to each of the files.
if exist('NI_TDM_DLL_Path','var')==0
    [dllfile,dllfolder]=uigetfile('*dll','Select nilibddc.dll');
    libname=strtok(dllfile, '.');
    NI_TDM_DLL_Path=fullfile(dllfolder,dllfile);
end
if exist('NI_TDM_H_Path','var')==0
    [hfile,hfolder]=uigetfile('*h','Select nilibddc_m.h');
    NI_TDM_H_Path=fullfile(hfolder,hfile);
end

%% Prompt the user to browse to the path of the TDM or TDMS file to read
[filepath,filefolder]=uigetfile({'*.tdms'; '*.tdm'}, 'Select a TDM or TDMS file');
Data_Path=fullfile(filefolder,filepath);

%Load nilibddc.dll (Always call 'unloadlibrary(libname)' after finished using the library)
loadlibrary(NI_TDM_DLL_Path,NI_TDM_H_Path);

%Open the file (Always call 'DDC_CloseFile' when you are finished using a file)
fileIn = 0;
[err,dummyVar,dummyVar,file]=calllib(libname,'DDC_OpenFileEx',Data_Path,',',1,fileIn);

%Read and display file name property
filenamelenIn = 0;
```

```

%Get the length of the 'DDC_FILE_NAME' string property
[err,dummyVar,filenamelen]=calllib(libname,'DDC_GetFileStringPropertyLength',file,DDC_FILE_NAME,file
namelenIn);
if err==0 %Only proceed if the property is found
    %Initialize a string to the length of the property value
    pfilename=libpointer('stringPtr',blanks(filenamelen));

[err,dummyVar,filename]=calllib(libname,'DDC_GetFileProperty',file,DDC_FILE_NAME,pfilename,filename
len+1);
    setdatatype(filename,'int8Ptr',1,filenamelen);
    disp(['File Name: ' char(filename.Value)]);
end

%Read and display file description property
filedesclenIn = 0;
%Get the length of the 'DDC_FILE_DESCRIPTION' string property
[err,dummyVar,filedesclen]=calllib(libname,'DDC_GetFileStringPropertyLength',file,DDC_FILE_DESCRIPTIO
N,filedesclenIn);
if err==0 %Only proceed if the property is found
    %Initialize a string to the length of the property value
    pfiledesc=libpointer('stringPtr',blanks(filedesclen));

[err,dummyVar,filedesc]=calllib(libname,'DDC_GetFileProperty',file,DDC_FILE_DESCRIPTION,pfiledesc,file
desclen+1);
    setdatatype(filedesc,'int8Ptr',1,filedesclen);
    % disp(['File Description: ' char(filedesc.Value)]);
end

%Read and display file title property
filetitlelenIn = 0;
%Get the length of the 'DDC_FILE_TITLE' string property
[err,dummyVar,filetitlelen]=calllib(libname,'DDC_GetFileStringPropertyLength',file,DDC_FILE_TITLE,filetitl
elenIn);
if err==0 %Only proceed if the property is found
    %Initialize a string to the length of the property value
    pfiletitle=libpointer('stringPtr',blanks(filetitlelen));

[err,dummyVar,filetitle]=calllib(libname,'DDC_GetFileProperty',file,DDC_FILE_TITLE,pfiletitle,filetitlelen+1)
;
    setdatatype(filetitle,'int8Ptr',1,filetitlelen);
    disp(['File Title: ' char(filetitle.Value)]);
end

%Read and display file author property
fileauthlenIn = 0;
%Get the length of the 'DDC_FILE_AUTHOR' string property
[err,dummyVar,fileauthlen]=calllib(libname,'DDC_GetFileStringPropertyLength',file,DDC_FILE_AUTHOR,fil
eauthlenIn);
if err==0 %Only proceed if the property is found
    %Initialize a string to the length of the property value
    pfileauth=libpointer('stringPtr',blanks(fileauthlen));

```

```

[err,dummyVar,fileauth]=calllib(libname,'DDC_GetFileProperty',file,DDC_FILE_AUTHOR,pfileauth,fileauthl
en+1);
    setdatatype(fileauth,'int8Ptr',1,fileauthlen);
    disp(['File Author: ' char(fileauth.Value)]);
end

%Read and display file timestamp property
yearIn = 0;
monthIn = 0;
dayIn = 0;
hourIn = 0;
minuteIn = 0;
secondIn = 0;
msecondIn = 0;
wkdayIn = 0;
[err,dummyVar,year,month,day,hour,minute,second,msecond,wkday]=calllib(libname,'DDC_GetFilePrope
rtyTimestampComponents',file,DDC_FILE_DATETIME,yearIn,monthIn,dayIn,hourIn,minuteIn,secondIn,ms
econdIn,wkdayIn);
if err==0 %Only proceed if the property is found
    disp(['File Timestamp: ' num2str(month) '/' num2str(day) '/' num2str(year) ', ' num2str(hour) ':'
num2str(minute) ':' num2str(second) ':' num2str(msecond)]);
end
%% process
%Get channel groups
%Get the number of channel groups
numgrpsIn = 0;
[err,numgrps]=calllib(libname,'DDC_GetNumChannelGroups',file,numgrpsIn);
%Get channel groups only if the number of channel groups is greater than zero
if numgrps>0
    %Initialize an array to hold the desired number of groups
    pgrps=libpointer('int32Ptr',zeros(1,numgrps));
    [err,grps]=calllib(libname,'DDC_GetChannelGroups',file,pgrps,numgrps);
end
% for i=1:numgrps %For each channel group
for i=1:1 %reads 2 while there is but one dataset?
    %Get channel group name property
    grpnamelenIn = 0;

[err,dummyVar,grpnamelen]=calllib(libname,'DDC_GetChannelGroupStringPropertyLength',grps(i),DDC_C
HANNELGROUP_NAME,grpnamelenIn);
    if err==0 %Only proceed if the property is found
        %Initialize a string to the length of the property value
        pgrpname=libpointer('stringPtr',blanks(grpnamelen));

[err,dummyVar,grpname]=calllib(libname,'DDC_GetChannelGroupProperty',grps(i),DDC_CHANNELGROUP
_NAME,pgrpname,grpnamelen+1);
        setdatatype(grpname,'int8Ptr',1,grpnamelen);
    else
        grpname=libpointer('stringPtr','');
    end

    %Get channel group description property

```

```

grpdesclenIn = 0;

[err,dummyVar,grpdesclen]=calllib(libname,'DDC_GetChannelGroupStringPropertyLength',grps(i),DDC_CHAN
ANNELGROUP_DESCRIPTION,grpdesclenIn);
    if err==0 %Only proceed if the property is found
        %Initialize a string to the length of the property value
        pgrpdesc=libpointer('stringPtr',blanks(grpdesclen));

[err,dummyVar,grpdesc]=calllib(libname,'DDC_GetChannelGroupProperty',grps(i),DDC_CHANNELGROUP_
DESCRIPTION,pgrpdesc,grpdesclen+1);
    end

% figure('Name',char(grpname.Value));
% hold on;

%Get channels
numchansIn = 0;
%Get the number of channels in this channel group
[err,numchans]=calllib(libname,'DDC_GetNumChannels',grps(i),numchansIn);
%Get channels only if the number of channels is greater than zero
if numchans>0
    %Initialize an array to hold the desired number of channels
    pchans=libpointer('int32Ptr',zeros(1,numchans));
    [err,chans]=calllib(libname,'DDC_GetChannels',grps(i),pchans,numchans);
end

channames=cell(1,numchans);

for j=1:numchans %For each channel in the channel group
    %Get channel name property
    channamelenIn = 0;

[err,dummyVar,channamelen]=calllib(libname,'DDC_GetChannelStringPropertyLength',chans(j),DDC_CHA
NNEL_NAME,channamelenIn);
    if err==0 %Only proceed if the property is found
        %Initialize a string to the length of the property value
        pchanname=libpointer('stringPtr',blanks(channamelen));

[err,dummyVar,channame]=calllib(libname,'DDC_GetChannelProperty',chans(j),DDC_CHANNEL_NAME,pc
hanname,channamelen+1);
        setdatatype(channame,'int8Ptr',1,channamelen);
        channames{j}=char(channame.Value);
    else
        channames{j}='';
    end

%Get channel data type
typeIn = 0;
[err,type]=calllib(libname,'DDC_GetDataType',chans(j),typeIn);

%Get channel values if data type of channel is double (DDC_Double = 10)
if strcmp(type,'DDC_Double')
    numvalsIn = 0;

```



```

[err,numvals]=calllib(libname,'DDC_GetNumDataValues',chans(j),numvalsIn);
%Initialize an array to hold the desired number of values
pvals=libpointer('doublePtr',zeros(1,numvals));
[err,vals]=calllib(libname,'DDC_GetDataValues',chans(j),0,numvals,pvals);
setdatatype(vals,'doublePtr',1,numvals);

%Add channel values to a matrix. The comment, #ok<AGROW>, at
%the end of the line prevents warnings about the matrix needing
%to allocate more memory for the added values.
chanvals(:,j)=(vals.Value); %#ok<AGROW>
%   chanvals(:,j)=single((vals.Value)); %#ok<AGROW>
end

end
%next line added to halve memory usage - RV
chanvals = single(chanvals);
%% %Plot Data from channels in this group
%test if length is doable - RV
if(length(chanvals)>1000000)
    xIDX = 1:1000:length(chanvals);
    figure
    plot(xIDX, chanvals(xIDX));
else
    figure
    plot(chanvals);
end
% clear chanvals;
% legend(channames);
end

%Close file
err = calllib(libname,'DDC_CloseFile',file);

%Unload nilibddc.dll
unloadlibrary(libname);

hd_zpf.m

function [f,amp]=hd_zpf(datai,Fs,B)
%This function takes an original data signal ('data') and will zero-pad the
%data times B and decimate it by B to keep the same number of points.
%Consequently, the sampling rate (Fs) will go down by a factor of B.
global amp
global f
%Calculate the length of the data and pad the end of the original data
%signal by a factor of B and then decimate to keep the number of data
%points the same.
data=datai;
L=length(data);
data=[data zeros(1,L*(B-1))];
data=decimate(data,B);

```

```

%Filter the data using fftfilt. P is the filter at 48th order
%p=fir1(48,.000005,'low');
%data=fftfilt(p,data);

%Detrend the data (get rid of DC-offset)
data=detrend(data, 0);

% Next power of 2 from length of y and calculate the fft
NFFT = 2^nextpow2(L);
Y = fft(data,NFFT)/L;
Fs=Fsi/B;
f = Fs/2*linspace(0,1,NFFT/2+1);
amp=2*abs(Y(1:NFFT/2+1));

% Plot the original signal, filtered signal, and the single-sided
%amplitude spectrum.
%ORIGINAL SIGNAL%
figure(1);
subplot(2,1,1); plot(1:length(data),data)
title('Time Domain of y(t) [Original]', 'FontWeight', 'bold')
xlabel('Time')
ylabel('V')
        %Filtered SIGNAL%
        %subplot(2,2,2); plot(1:(L/B),data(1:(L/B)))
        %title('Time Domain of y(t) [Filtered]', 'FontWeight', 'bold')
        %xlabel('Time')
        %ylabel('V')
%FFT SIGNAL%
subplot(2,1,2); plot(f,amp)
%xlim(subplot(2,1,2),[0 0.02]);
title('Single-Sided Amplitude Spectrum of y(t)', 'FontWeight', 'bold')
xlabel('Frequency (Hz)')
ylabel('|Y(f)|')

end
hd_zpfcorr.m

function [f,amp]=hd_zpfcorr(datai,Fsi,B, P1, P2)
%This function takes an original data signal ('data') and will zero-pad the
%data times B and decimate it by B to keep the same number of points.
%Consequently, the sampling rate (Fs) will go down by a factor of B.
global amp
global f
%Calculate the length of the data and pad the end of the original data
%signal by a factor of B and then decimate to keep the number of data
%points the same.
data=datai;
t=1:1:length(datai);
%data=zeros(1,length(datai));

% v=zeros(1,length(datai));
for ii=1:1:length(datai)
v(ii)=(2+sin(2*pi*(t(ii)/Fsi)*(1/P1))+sin(2*pi*(t(ii)/Fsi)*(1/P2)))/40; %/40;

```

```

end
% length v
% datai=datai';
% data=datai.*v;
%
L=length(data);
% data=[data zeros(1,L*(B-1))];
% data=decimate(data,B);
for jj=1:length(datai)
    data(jj)=datai(jj)*v(jj);
end

%Filter the data using fftfilt. P is the filter at 48th order
%p=fir1(48,.000005,'low');
%data=fftfilt(p,data);

%Detrend the data (get rid of DC-offset)
data=detrend(data, 0);

% Next power of 2 from length of y and calculate the fft
NFFT = 2^nextpow2(L);
Y = fft(data,NFFT)/L;
Fs=Fs1/B;
f = Fs/2*linspace(0,1,NFFT/2+1);
amp=2*abs(Y(1:NFFT/2+1));

% Plot the original signal, filtered signal, and the single-sided
%amplitude spectrum.
%ORIGINAL SIGNAL%
figure(1);
subplot(3,1,1);
plot(1:length(datai),datai, 'Color','b')
title('Time Domain of y(t) [Original]','FontWeight','bold')
xlabel('Time')
ylabel('V')
    %Filtered SIGNAL%
    %subplot(2,2,2); plot(1:(L/B),data(1:(L/B)))
    %title('Time Domain of y(t) [Filtered]','FontWeight','bold')
    %xlabel('Time')
    %ylabel('V')
subplot(3,1,2);
plot(1:length(data),data, 'Color','m')
title('Time Domain of y(t) [Original]','FontWeight','bold')
xlabel('Time')
ylabel('V')

%FFT SIGNAL%

subplot(3,1,3);
plot(f,amp)
%xlim(subplot(2,1,2),[0 0.02]);

```

```

title('Single-Sided Amplitude Spectrum of y(t)', 'FontWeight', 'bold')
xlabel('Frequency (Hz)')
ylabel('|Y(f)|')

```

```
end
```

```
hd_zpfcorr3.m
```

```

function [f,amp]=hd_zpfcorr(datai,Fsi,B,P1,P2,P3)
%This function takes an original data signal ('data') and will zero-pad the
%data times B and decimate it by B to keep the same number of points.
%Consequently, the sampling rate (Fs) will go down by a factor of B.
global amp
global f
%Calculate the length of the data and pad the end of the original data
%signal by a factor of B and then decimate to keep the number of data
%points the same.
data=datai;
t=1:1:length(datai);
%data=zeros(1,length(datai));

%v=zeros(1,length(datai));
for ii=1:1:length(datai)
v(ii)=(3+sin(2*pi*(t(ii)/Fsi)*(1/P1))+sin(2*pi*(t(ii)/Fsi)*(1/P2))+sin(2*pi*(t(ii)/Fsi)*(1/P3)))/60;
end
% length v
% datai=datai';
% data=datai.*v;
%
L=length(data);
% data=[data zeros(1,L*(B-1))];
% data=decimate(data,B);
for jj=1:length(datai)
    data(jj)=datai(jj)*v(jj);
end

%Filter the data using fftfilt. P is the filter at 48th order
%p=fir1(48,.000005,'low');
%data=fftfilt(p,data);

%Detrend the data (get rid of DC-offset)
data=detrend(data, 0);

% Next power of 2 from length of y and calculate the fft
NFFT = 2^nextpow2(L);
Y = fft(data,NFFT)/L;
Fs=Fsi/B;
f = Fs/2*linspace(0,1,NFFT/2+1);
amp=2*abs(Y(1:NFFT/2+1));

% Plot the original signal, filtered signal, and the single-sided

```

```

%amplitude spectrum.
%ORIGINAL SIGNAL%
figure(1);
subplot(3,1,1);
plot(1:length(datai),datai, 'Color','b')
title('Time Domain of y(t) [Original]','FontWeight','bold')
xlabel('Time')
ylabel('V')
    %Filtered SIGNAL%
    %subplot(2,2,2); plot(1:(L/B),data(1:(L/B)))
    %title('Time Domain of y(t) [Filtered]','FontWeight','bold')
    %xlabel('Time')
    %ylabel('V')
subplot(3,1,2);
plot(1:length(data),data, 'Color','m')
title('Time Domain of y(t) [Original]','FontWeight','bold')
xlabel('Time')
ylabel('V')

    %FFT SIGNAL%

subplot(3,1,3);
plot(f,amp)
%xlim(subplot(2,1,2),[0 0.02]);
title('Single-Sided Amplitude Spectrum of y(t)','FontWeight','bold')
xlabel('Frequency (Hz)')
ylabel('|Y(f)|')

end

fft_corrector_og.m

function [amp,f]=FFT_corrector_og(datai,Fsi,B,w1,w2)
%This function takes an original data signal ('data') and will zero-pad the
%data times B and decimate it by B to keep the same number of points.
%Consequently, the sampling rate (Fs) will go down by a factor of B.
global amp
global f
%Calculate the length of the data and pad the end of the original data
%signal by a factor of B and then decimate to keep the number of data
%points the same

data=(datai);
t=1:1:length(data);
for ii=1:length(datai)
data(ii)=datai(ii)*(2+sin(2*pi*w1*t(ii)/Fsi)+sin(2*pi*w2*t(ii)/Fsi))/40;
end
L=length(data);

```

```

%Filter the data using fftfilt. P is the filter at 48th order
%p=fir1(48,.000005,'low');
%data=fftfilt(p,data);

%Detrend the data (get rid of DC-offset)
%data=detrend(data, 0);

% Next power of 2 from length of y and calculate the fft
NFFT = 2^nextpow2(L);
Y = fft(data,NFFT)/L;
Fs=Fsi/B;
f = Fs/2*linspace(0,1,NFFT/2+1);
amp=2*abs(Y(1:NFFT/2+1));

% Plot the original signal, filtered signal, and the single-sided
%amplitude spectrum.
%ORIGINAL SIGNAL%
figure(1);
subplot(3,1,1);
plot(1:length(data),data, 'Color','b')
title('Time Domain of y(t) [Original]','FontWeight','bold')
xlabel('Time')
ylabel('V')
        %Filtered SIGNAL%
        %subplot(2,2,2); plot(1:(L/B),data(1:(L/B)))
        %title('Time Domain of y(t) [Filtered]','FontWeight','bold')
        %xlabel('Time')
        %ylabel('V')
subplot(3,1,2);
plot(1:length(data),data, 'Color','m')
title('Time Domain of y(t) [Original]','FontWeight','bold')
xlabel('Time')
ylabel('V')

        %FFT SIGNAL%

subplot(3,1,3);
plot(f,amp)
%xlim(subplot(2,1,2),[0 0.02]);
title('Single-Sided Amplitude Spectrum of y(t)','FontWeight','bold')
xlabel('Frequency (Hz)')
ylabel('|Y(f)|')

end

FFT_correcctor_new.m

function [amp,f]=FFT_correcctor_new(datai,Fsi,B,w1,w2)
%This function takes an original data signal ('data') and will zero-pad the
%data times B and decimate it by B to keep the same number of points.

```

```

%Consequently, the sampling rate (Fs) will go down by a factor of B.
global amp
global f
%Calculate the length of the data and pad the end of the original data
%signal by a factor of B and then decimate to keep the number of data
%points the same

data=(datai);
t=1:1:length(data);
for ii=1:length(datai)
v(ii)=(2+sin(2*pi*w1*t(ii)/Fsi)+sin(2*pi*w2*t(ii)/Fsi))/40;
end
L=length(data);

for jj=1:length(datai)
data(jj)=datai(jj)/v(jj);
end

% Next power of 2 from length of y and calculate the fft
NFFT = 2^nextpow2(L);
Y = fft(data,NFFT)/L;
Fs=Fs/B;
f = Fs/2*linspace(0,1,NFFT/2+1);
amp=2*abs(Y(1:NFFT/2+1));

figure(1);
subplot(3,1,1);
plot(1:length(datai),datai,'Color','b')
title('Time Domain of y(t)','FontWeight','bold')
xlabel('Time')
ylabel('V')
    %Filtered SIGNAL%
    %subplot(2,2,2); plot(1:(L/B),data(1:(L/B)))
    %title('Time Domain of y(t) [Filtered]','FontWeight','bold')
    %xlabel('Time')
    %ylabel('V')
%FFT SIGNAL%
subplot(3,1,2);
plot(1:length(data),data,'Color','m')
xlabel('Time')
ylabel('V')

subplot(3,1,3);
plot(f,amp)
%xlim(subplot(2,1,2),[0 0.02]);
title('Single-Sided Amplitude Spectrum of y(t)','FontWeight','bold')
xlabel('Frequency (Hz)')
ylabel('|Y(f)|')

%xlim(subplot(2,1,2),[0 0.02]);
end

```

APPENDIX G

G PUMP CALIBRATION ANOVA

G.1 Raw Data Table

Q2b (uL/min)	Q2a (uL/min)	Q4b (uL/min)	Q4a (uL/min)	Q1 (uL/min)	Q3b (uL/min)	Q3a (uL/min)
Pump 2b	Pump 2a	Pump 4b	Pump 4a	Pump 1	Pump 3b	Pump 3a
2.8184	2.4566	2.3476	2.5064	2.2621	2.1767	2.7635
2.7482	2.607	2.6136	2.7536	2.3611	2.4784	2.7822
2.3179	2.7936	1.6395	2.1137	1.8809	1.562	2.1831
2.6041	2.4735	2.4387	3.1846	2.5238	2.2723	3.0625
2.8517	2.655	2.67	2.6605	2.0218	2.3777	2.7085
2.0152	2.7215	1.9499	2.3018	2.0099	1.3597	2.2359
2.7716	2.4476	2.4969	3.0116	2.3665	2.303	2.9464
2.7934	2.6915	2.5114	2.4273	1.8325	2.3673	2.4115
2.3198	2.5429	1.9704	2.5198	2.3682	1.4521	2.3051
2.8016	2.4523	2.5948	2.6083	2.0775	2.3482	2.9365
2.6291	2.6393	2.4678	2.4959	1.8076	2.3631	2.2816
2.2301	2.414	1.9898	2.7232	2.4816	1.7185	2.6274
2.8624	2.4912	2.6588	2.3808	2.0019	2.4364	2.8019
2.534	2.5849	2.3748	2.5959	2.2669	2.4529	2.4391
2.2983	2.2898	2.0555	2.645	2.0522	1.813	2.3383
2.9737	2.5229	2.7275	2.2156	2.145	2.518	2.6958
2.5001	2.5675	2.2929	2.6667	2.3273	2.1587	2.1815
2.3575	2.196	2.1062	2.5579	1.8135	1.9184	2.6213
2.9142	2.5263	2.7493	2.3371	2.5881	2.5329	2.5287
2.4397	2.3523	2.1908	2.8156	2.0088	2.0752	0.6635
2.4127	2.1998	2.1915	2.3148	2.0663	2.0389	2.606
2.8551	2.6415	2.7791	2.5642	2.3227	2.5088	2.4203
2.4006	2.4111	2.0838	2.8314	1.8487	2.0252	2.3482
2.5219	2.1486	2.2462	2.184	2.3671	2.1604	2.7305
2.7804	2.636	2.7496	2.8651	1.9223	2.4902	2.2962
2.3883	2.3379	2.015	2.7341	2.058	1.9776	2.4059
2.5811	2.1368	2.316	2.1258	2.3223	2.262	2.7529
2.665	2.669	2.7035	3.1227	1.7942	2.4512	2.2674
2.4022	2.2578	1.9488	2.5528	2.3667	1.9445	2.4136
2.6663	2.2342	2.4056	2.2174	2.0461	2.4467	2.6009



2.5456	2.7056	2.6732	3.2434	2.1164	2.3941	2.2658
2.4541	2.177	1.8921	2.3325	2.3981	1.9974	2.5919
2.7245	2.3074	2.4684	2.47	1.8963	2.479	2.5759
2.4036	2.7053	2.588	3.2319	2.4516	2.327	2.2952
2.5262	2.138	1.8746	2.1478	2.0822	1.9746	2.7035
2.7953	2.3531	2.5848	2.8192	2.0787	2.5578	2.5585
2.3911	2.6768	2.5294	3.0702	2.309	2.2387	2.3425
2.6497	2.0588	1.8989	2.0491	2.0482	1.9787	2.6973
2.7892	2.438	2.6795	2.9988	2.5215	2.5868	2.3238
2.3135	2.6434	2.4522	2.725	2.0334	2.1369	2.4296
2.7429	2.0499	1.9097	2.0118	2.274	2.0098	2.7397
2.7867	2.5232	2.747	3.0576	2.4851	2.591	2.24
2.3019	2.5675	2.3754	2.4423	1.817	2.0656	2.575
2.8718	2.0462	1.9391	2.1009	2.5104	2.0544	2.7265
2.7215	2.5956	2.7939	2.934	2.0627	2.572	2.14
2.3177	2.5114	2.2578	2.2646	1.93	1.9902	2.6691
2.9747	1.9989	1.9777	2.3741	2.4643	2.1141	2.6189
2.6259	2.6627	2.825	2.694	1.9325	2.5413	2.089
2.3079	2.4465	2.1502	2.2922	3.4722	1.9222	2.8461
2.9911	2.0871	2.0132	2.47	4.4082	2.1744	2.8967
2.4972	2.7036	2.8349	2.4379	2.1545	2.4934	2.1319
2.3719	2.3525	2.0535	2.402	2.4176	1.8757	2.9802
3.1089	2.14	2.0687	2.4957	2.0621	2.2192	2.5087
2.7179	2.6753	2.8258	2.2464	2.329	2.4008	2.2262
2.4574	2.2571	1.9931	2.6099	2.0074	1.817	3.0282
3.1308	2.2266	2.1319	2.3221	2.3436	2.2609	2.3436
2.3038	2.6297	2.7865	2.2473	2.3367	2.3218	2.2532
2.5433	2.1717	1.9305	2.8913	1.8543	1.7935	3.0019
3.1454	2.3197	2.22	2.0722	2.6215	2.3244	2.2183
2.2321	2.6197	2.7395	2.7858	1.8434	2.2316	2.3944
2.6575	2.1418	1.8864	2.9013	2.0287	1.7955	2.9546
3.112	2.3816	2.3038	1.7725	2.3415	2.3666	2.1047
2.189	2.6075	2.6712	2.5996	1.8286	2.1491	2.5336
2.785	2.0421	1.8685	2.9652	2.3106	1.8086	2.862
3.0421	2.5571	2.3989	1.6858	1.9561	2.4188	2.8993
2.2001	2.4743	2.5917	2.878	2.0028	2.0649	2.5272
2.9095	2.0461	1.856	2.735	2.3152	1.8146	2.6392
3.5236	2.6136	2.4812	1.8233	1.8255	2.4165	2.1568
2.0061	2.3764	2.4846	3.0685	2.316	1.9762	2.8109
2.9745	2.0534	1.8802	2.551	2.0292	1.832	2.5558
2.8243	2.6634	2.5669	2.0781	2.1019	1.9258	2.1527

2.3162	2.3161	2.3806	3.1356	2.4569	2.2674	2.8205
3.0912	2.0882	1.912	2.2824	1.8603	1.8936	2.4234
2.7187	2.6818	2.6415	2.4649	2.4373	2.4022	2.2571
2.4073	2.2452	2.2793	2.9374	2.1173	1.888	2.8173
3.121	2.1275	1.9489	2.1233	2.2395	1.9453	2.3139
2.5546	2.6808	2.6632	2.8752	2.4228	2.3659	2.3765
2.524	2.1902	2.1492	2.7706	1.9751	1.8493	2.7833
3.1203	2.2038	2.0015	2.2088	2.6652	1.9917	2.275
2.4937	2.6525	2.7093	3.1026	2.0592	2.3678	2.4682
2.6815	2.1385	2.0528	2.5314	2.2246	1.8505	2.5843
3.0861	2.2562	2.0735	2.3557	2.5701	2.1225	2.2312
2.3478	2.5621	2.7273	3.1449	1.7676	2.2003	2.5613
2.7497	2.0857	1.9828	2.3499	2.4868	1.9646	2.597
3.0271	2.3092	2.1364	2.5837	2.1256	2.282	2.3156
2.2907	2.4775	2.7022	2.8823	1.8476	2.2057	2.6923
2.9448	2.0728	1.9238	2.2666	2.3395	2.6879	2.4958
2.9563	2.3856	2.2319	2.8341	1.8444	0.5896	2.3602
2.2687	2.4031	2.679	2.5501	2.1341	2.1053	2.7029
3.0471	2.0655	1.8742	2.3207	1.9956	1.9697	2.4187
2.847	2.4384	2.3086	2.9056	2.0002	2.3172	2.4896

## G.2 ANOVA Results

Anova: Single Factor

### SUMMARY

<i>Groups</i>	<i>Count</i>	<i>Sum</i>	<i>Average</i>	<i>Variance</i>
Pump 2b	91	241.0157	2.648524	0.089395
Pump 2a	91	218.2247	2.398074	0.048721
Pump 4b	91	210.8672	2.317222	0.103415
Pump 4a	91	232.9577	2.559975	0.123016
Pump 1	91	200.1993	2.199992	0.128581
Pump 3b	91	195.2694	2.145818	0.101499
Pump 3a	91	227.9487	2.504931	0.100034

### ANOVA

<i>Source of Variation</i>	<i>SS</i>	<i>df</i>	<i>MS</i>	<i>F</i>	<i>P-value</i>	<i>F crit</i>
Between Groups	19.08649	6	3.181082	32.05536	9.98E-34	2.112954
Within Groups	62.5194	630	0.099237			
Total	81.60589	636				

APPENDIX H

H HETERODYNE FREQUENCY TABLES

	2a	3a	4a	5a	6a	7a	8a	9a	10a	11a	12a	13a	14a	15a
0.009490	0.014235	0.018980	0.023725	0.028470	0.033215	0.037960	0.042705	0.047450	0.052195	0.056940	0.061685	0.066430	0.071175	0.075920
0.013448	0.018193	0.022938	0.027683	0.032428	0.037173	0.041918	0.046663	0.051408	0.056153	0.060898	0.065643	0.070388	0.075133	0.079878
0.017406	0.022151	0.026896	0.031641	0.036386	0.041131	0.045876	0.050621	0.055366	0.060111	0.064856	0.069601	0.074346	0.079091	0.083836
0.021364	0.026109	0.030854	0.035599	0.040344	0.045089	0.049834	0.054579	0.059324	0.064069	0.068814	0.073559	0.078304	0.083049	0.087794
0.025322	0.030067	0.034812	0.039557	0.044302	0.049047	0.053792	0.058537	0.063282	0.068027	0.072772	0.077517	0.082262	0.087007	0.091752
0.029280	0.034025	0.038770	0.043515	0.048260	0.053005	0.057750	0.062495	0.067240	0.071985	0.076730	0.081475	0.086220	0.090965	0.095710
0.033238	0.037983	0.042728	0.047473	0.052218	0.056963	0.061708	0.066453	0.071198	0.075943	0.080688	0.085433	0.090178	0.094923	0.099668
0.037196	0.041941	0.046686	0.051431	0.056176	0.060921	0.065666	0.070411	0.075156	0.079901	0.084646	0.089391	0.094136	0.098881	0.103626
0.041154	0.045899	0.050644	0.055389	0.060134	0.064879	0.069624	0.074369	0.079114	0.083859	0.088604	0.093349	0.098094	0.102839	0.107584
0.045112	0.049857	0.054602	0.059347	0.064092	0.068837	0.073582	0.078327	0.083072	0.087817	0.092562	0.097307	0.102052	0.106797	0.111542
0.049070	0.053815	0.058560	0.063305	0.068050	0.072795	0.077540	0.082285	0.087030	0.091775	0.096520	0.101265	0.106010	0.110755	0.115500
0.053028	0.057773	0.062518	0.067263	0.072008	0.076753	0.081498	0.086243	0.090988	0.095733	0.100478	0.105223	0.109968	0.114713	0.119458
0.057080	0.061825	0.066570	0.071315	0.076060	0.080805	0.085550	0.090295	0.095040	0.099785	0.104530	0.109275	0.114020	0.118765	0.123510
0.061032	0.065777	0.070522	0.075267	0.080012	0.084757	0.089502	0.094247	0.098992	0.103737	0.108482	0.113227	0.117972	0.122717	0.127462
0.065084	0.069829	0.074574	0.079319	0.084064	0.088809	0.093554	0.098299	0.103044	0.107789	0.112534	0.117279	0.122024	0.126769	0.131514
0.069136	0.073881	0.078626	0.083371	0.088116	0.092861	0.097606	0.102351	0.107096	0.111841	0.116586	0.121331	0.126076	0.130821	0.135566
0.073188	0.077933	0.082678	0.087423	0.092168	0.096913	0.101658	0.106403	0.111148	0.115893	0.120638	0.125383	0.130128	0.134873	0.139618
0.077240	0.081985	0.086730	0.091475	0.096220	0.100965	0.105710	0.110455	0.115200	0.119945	0.124690	0.129435	0.134180	0.138925	0.143670
0.081292	0.086037	0.090782	0.095527	0.100272	0.105017	0.109762	0.114507	0.119252	0.123997	0.128742	0.133487	0.138232	0.142977	0.147722
0.085344	0.090089	0.094834	0.099579	0.104324	0.109069	0.113814	0.118559	0.123304	0.128049	0.132794	0.137539	0.142284	0.147029	0.151774
0.089396	0.094141	0.098886	0.103631	0.108376	0.113121	0.117866	0.122611	0.127356	0.132101	0.136846	0.141591	0.146336	0.151081	0.155826
0.093448	0.098193	0.102938	0.107683	0.112428	0.117173	0.121918	0.126663	0.131408	0.136153	0.140898	0.145643	0.150388	0.155133	0.159878
0.097500	0.102245	0.106990	0.111735	0.116480	0.121225	0.125970	0.130715	0.135460	0.140205	0.144950	0.149695	0.154440	0.159185	0.163930
0.101552	0.106297	0.111042	0.115787	0.120532	0.125277	0.130022	0.134767	0.139512	0.144257	0.149002	0.153747	0.158492	0.163237	0.167982
0.105604	0.110349	0.115094	0.119839	0.124584	0.129329	0.134074	0.138819	0.143564	0.148309	0.153054	0.157799	0.162544	0.167289	0.172034
0.109656	0.114401	0.119146	0.123891	0.128636	0.133381	0.138126	0.142871	0.147616	0.152361	0.157106	0.161851	0.166596	0.171341	0.176086
0.113708	0.118453	0.123198	0.127943	0.132688	0.137433	0.142178	0.146923	0.151668	0.156413	0.161158	0.165903	0.170648	0.175393	0.180138
0.117760	0.122505	0.127250	0.131995	0.136740	0.141485	0.146230	0.150975	0.155720	0.160465	0.165210	0.169955	0.174700	0.179445	0.184190
0.121812	0.126557	0.131302	0.136047	0.140792	0.145537	0.150282	0.155027	0.159772	0.164517	0.169262	0.174007	0.178752	0.183497	0.188242
0.125864	0.130609	0.135354	0.140099	0.144844	0.149589	0.154334	0.159079	0.163824	0.168569	0.173314	0.178059	0.182804	0.187549	0.192294
0.129916	0.134661	0.139406	0.144151	0.148896	0.153641	0.158386	0.163131	0.167876	0.172621	0.177366	0.182111	0.186856	0.191601	0.196346
0.133968	0.138713	0.143458	0.148203	0.152948	0.157693	0.162438	0.167183	0.171928	0.176673	0.181418	0.186163	0.190908	0.195653	0.200398
0.138020	0.142765	0.147510	0.152255	0.157000	0.161745	0.166490	0.171235	0.175980	0.180725	0.185470	0.190215	0.194960	0.199705	0.204450
0.142072	0.146817	0.151562	0.156307	0.161052	0.165797	0.170542	0.175287	0.180032	0.184777	0.189522	0.194267	0.199012	0.203757	0.208502
0.146124	0.150869	0.155614	0.160359	0.165104	0.169849	0.174594	0.179339	0.184084	0.188829	0.193574	0.198319	0.203064	0.207809	0.212554
0.150176	0.154921	0.159666	0.164411	0.169156	0.173901	0.178646	0.183391	0.188136	0.192881	0.197626	0.202371	0.207116	0.211861	0.216606
0.154228	0.158973	0.163718	0.168463	0.173208	0.177953	0.182698	0.187443	0.192188	0.196933	0.201678	0.206423	0.211168	0.215913	0.220658
0.158280	0.163025	0.167770	0.172515	0.177260	0.182005	0.186750	0.191495	0.196240	0.200985	0.205730	0.210475	0.215220	0.219965	0.224710
0.162332	0.167077	0.171822	0.176567	0.181312	0.186057	0.190802	0.195547	0.200292	0.205037	0.209782	0.214527	0.219272	0.224017	0.228762
0.166384	0.171129	0.175874	0.180619	0.185364	0.190109	0.194854	0.199599	0.204344	0.209089	0.213834	0.218579	0.223324	0.228069	0.232814
0.170436	0.175181	0.179926	0.184671	0.189416	0.194161	0.198906	0.203651	0.208396	0.213141	0.217886	0.222631	0.227376	0.232121	0.236866
0.174488	0.179233	0.183978	0.188723	0.193468	0.198213	0.202958	0.207703	0.212448	0.217193	0.221938	0.226683	0.231428	0.236173	0.240918
0.178540	0.183285	0.188030	0.192775	0.197520	0.202265	0.207010	0.211755	0.216500	0.221245	0.225990	0.230735	0.235480	0.240225	0.244970
0.182592	0.187337	0.192082	0.196827	0.201572	0.206317	0.211062	0.215807	0.220552	0.225297	0.230042	0.234787	0.239532	0.244277	0.249022
0.186644	0.191389	0.196134	0.200879	0.205624	0.210369	0.215114	0.219859	0.224604	0.229349	0.234094	0.238839	0.243584	0.248329	0.253074
0.190696	0.195441	0.200186	0.204931	0.209676	0.214421	0.219166	0.223911	0.228656	0.233401	0.238146	0.242891	0.247636	0.252381	0.257126
0.194748	0.199493	0.204238	0.208983	0.213728	0.218473	0.223218	0.227963	0.232708	0.237453	0.242198	0.246943	0.251688	0.256433	0.261178
0.198799	0.203544	0.208289	0.213034	0.217779	0.222524	0.227269	0.232014	0.236759	0.241504	0.246249	0.250994	0.255739	0.260484	0.265229
0.202851	0.207596	0.212341	0.217086	0.221831	0.226576	0.231321	0.236066	0.240811	0.245556	0.250301	0.255046	0.259791	0.264536	0.269281
0.206903	0.211648	0.216393	0.221138	0.225883	0.230628	0.235373	0.240118	0.244863	0.249608	0.254353	0.259098	0.263843	0.268588	0.273333
0.210955	0.215700	0.220445	0.225190	0.229935	0.234680	0.239425	0.244170	0.248915	0.253660	0.258405	0.263150	0.267895	0.272640	0.277385
0.215007	0.219752	0.224497	0.229242	0.233987	0.238732	0.243477	0.248222	0.252967	0.257712	0.262457	0.267202	0.271947	0.276692	0.281437
0.219059	0.223804	0.228549	0.233294	0.238039	0.242784	0.247529	0.252274	0.257019	0.261764	0.266509	0.271254	0.275999	0.280744	0.285489
0.223111	0.227856	0.232601	0.237346	0.242091	0.246836	0.251581	0.256326	0.261071	0.265816	0.270561	0.275306	0.280051	0.284796	0.289541
0.227163	0.231908	0.236653	0.241398	0.246143	0.250888	0.255633	0.260378	0.265123	0.269868	0.274613	0.279358	0.284103	0.288848	0.293593
0.231215	0.235960	0.240705	0.245450	0.250195	0.254940	0.259685	0.264430	0.269175	0.273920	0.278665	0.283410	0.288155</		